Ultraschnelle transiente Spektroskopie zur Untersuchung des Einflusses der Morphologie auf die Dynamik von Anregungen in organischen und hybriden Halbleitern

Dissertation

zur Erlangung des Grades eines
Doktors der Naturwissenschaften (Dr. rer. nat.)
im Promotionsprogramm
Photophysik synthetischer und biologischer multichromophorer Systeme der Bayreuther Graduiertenschule für Mathematik und Naturwissenschaften

Von der Universität Bayreuth genehmigte Abhandlung von

Thomas Unger

geboren in Lutherstadt Wittenberg

Bayreuth, 2017

Die vorliegende Arbeit wurde in der Zeit von Oktober 2012 bis Juli 2017 am Lehrstuhl für Experimentalphysik II der Universität Bayreuth unter der Betreuung von Prof. Dr. Anna Köhler angefertigt.

Amtierender Direktor der Graduiertenschule: Prof. Dr. Dirk Schüler

Prof. Dr. Stephan Kümmel (bei Einreichung)

Datum der Einreichung: 03.08.2017

Datum des Kolloquiums: 27.11.2017

Erstgutachter: Prof. Dr. Anna Köhler

Zweitgutachter: Prof. Dr. Markus Lippitz

Inhaltsverzeichnis

1 Zusammenfassung

Das Themengebiet organischer ungeordneter Halbleiter hat sich seit den Anfängen, zu Beginn der 90er Jahre, bis heute stetig weiterentwickelt. Organische Leuchtdioden und Feldeffekttransistoren finden sich bereits heute in Handy-Displays beziehungsweise als RFIDs in unterschiedlichsten Bereichen des täglichen Lebens. Bei der Anwenung in Solarzellen zeigen sowohl rein organische Halbleiter als auch hybride organisch-anorganische Perowskit-Materialien zwar ausreichende Effizienzen, jedoch reicht die Lebensdauer noch nicht zur Marktreife aus.

Sowohl in organischen Materialien als auch in hybriden Perowskit-Strukturen für die Solarzellanwendung spielt die Morphologie von Grenzflächen eine besondere Rolle für die Funktionsweise, da sie eng mit den optischen und elektronischen Eigenschaften verknüpft ist. Bei organischen Materialien können dies Grenzflächen zwischen geordneten, aggregierten und amorphen Phasen oder zwischen elektronreichen Donor- und elektronarmen Akzeptor-Komponenten sein. Wohingegen in hybriden Perowskit-Materialien Grenzflächen in polykristallinen Filmen an Korngrenzen entstehen oder durch strukturelle Änderungen aufgrund einer veränderten Stöchiometrie hervorgerufen werden können.

In der vorliegenden Arbeit wird daher mit Hilfe ultraschneller Spektroskopie wie der transienten Absorption die Dynamik der Anregungen an diesen Grenzflächen untersucht. Dazu habe ich zu Beginn meiner Promotion einen Aufbau zur transienten Absorptionsspektroskopie eingerichtet und charakterisiert. Mit einer zeitlichen Auflösung von wenigen hundert Femtosekunden und einem weiten spektralen Messbereich (480-1100 nm) ist es möglich sowohl Lösungen als auch dünne Filme in einem weiten Temperaturbereich (5-500 K) zu untersuchen. Die Charakterisierung und die Beschreibung des Messaufbaus sind in Kapitel 5 der vorliegenden Arbeit zusammengefasst.

Bei den organischen Materialien wird der komplexe Prozess der Exzitonentrennung systematisch aufgeschlüsselt. Dazu werden im ersten Teil dieser Arbeit die entscheidenden Schritte, wie Diffusion innerhalb der Phasen des Donorpolymers oder die Dynamik des Ladungstransfers an der Grenze zwischen Donor und Akzeptor näher beleuchtet. Dagegen fehlt bei Perowskit-Materialien das Verständnis über die Zusammenhänge zwischen Morphologieveränderungen und der Rekombinationsdynamik der Anregungen, was im Fokus des zweiten Teils dieser Arbeit steht.

Bei vielen häufig verwendeten Polymeren, die als Elektrondonor dienen, spielt Aggregation eine wichtige Rolle. Ein Beispiel-Material ist das Polymer MEH-PPV. Im Einzelnen habe ich die Dynamik der Exzitonen an der Grenzschicht unterschiedlicher Konformationsphasen dieses Polymers untersucht. Die Ausprägung der einzelnen Phasen in Lösung können durch Veränderung der Tempratur kontrolliert werden. Amorphe und geordnete Phasenanteile

tragen unterschiedlich zu den zeitabhängigen Spektren bei und überlappen teilweise. Sie lassen sich jedoch anhand von temperaturabhängigen Absorptions- und Photolumineszenz-spektren (PL-Spektren) trennen. Auf diese Weise konnte mittels transienter Absorptionsmessungen ein ultraschneller Energietransfer zwischen beiden Phasen auf einer Zeitskala von unter 1 ps quantifiziert werden. Dies ist nur möglich, wenn beide Phasen in direktem Kontakt zueinander vorliegen. Die Ergebnisse sind in Kapitel 6 zusammengefasst.

In Kapitel 7 wird die Dynamik innerhalb der aggregierten Phase von MEH-PPV unterhalb der Übergangstemperatur betrachtet. Durch Vergleich von Ergebnissen aus 2D-Spektroskopie und transienter Absorptionsspektroskopie zeigt sich, dass die Anregungen auf ultraschneller Zeitskala lokalisieren. Dem folgt ein komplexes Relaxationsverhalten innerhalb der Zustandsdichte der Aggregate über Transferschritte mit variierenden Abständen.
Ein weiterer Aspekt neben der Diffusion sind die Vorgänge an der Grenzfläche zwischen Donor- und Akzeptoreinheiten. In Kapitel 8 wird daher die Anregungsdynamik einer chemischen Dyade in Lösung untersucht. Sie besteht aus kleinen kovalent gebundenen Molekülen, die als Donor (PBI) und Akzeptor (CuPc) dienen. Zeitaufgelöste Messungen im Ultrakurzzeit- und Nanosekundenbereich sowie Strukturdaten aus Simulationen der Moleküldynamik zeigen, dass abhängig vom Konformationszustand der Dyade Tripplettbildung und nichtstrahlender Zerfall dominieren können und so effizienter Ladungstransfer verhindert wird.

Diffusion innerhalb der Donorphase bzw. die Dynamik an der Grenzfläche zwischen Donor und Akzeptor, die in den Kaptiteln 7 und 8 betrachtet wurden, sind für die Ladungsträgertrennung in organischen Solarzellen von Bedeutung.
Aufbauend darauf wird in Kapitel 9 der Prozess der Ladungsträgertrennung in Blend-Filmen untersucht, die die aktive Schicht in organischen Solarzellen darstellen. Diese bestehen jeweils zu gleichen Teilen aus einem Polymer-Donor und dem Akzeptor PCBM. Der Fokus liegt auf dem ersten Schritt der Ladungsträgertrennung, also der Bildung eines ladungsgetrennten Zustands. Es wird systematisch der Einfluss der Temperatur und des Unterschieds in den Energieniveaus beider Materialien auf den Elektronentransfer untersucht. Die Messungen zeigen in allen untersuchten Blend-Systemen eine temperaturunabhängigen effizienten Ladungstransfer, der nicht für alle Materialkombinationen konsistent mit dem häufig angewendeten Marcus-Modell beschrieben werden kann. Es zeigt sich vielmehr, dass Modelle angewendet werden müssen, die quantenmechanische Kopplung von Molekülschwingungen an den Elektronentransfer berücksichtigen. Es wird auch deutlich, dass der Einfluss des Unterschieds der Energieniveaus von Donor und Akzeptor eine untergeordnete Rolle spielt.

Kapitel 10 und 11 fassen Ergebnisse zur Anregungsdynamik an hybriden Perowskit-Filmen ($CH_3NH_3PbI_3$ und $CH_3NH_3PbI_{3-x}Cl_x$) zusammen. Augrund der geringen Bindungsenergie in diesen polykristallinen Strukturen reicht die thermische Energie bei Raumtemperatur aus um direkt freie Ladungsträgerpaare zu erzeugen. Das Hauptaugenmerk liegt daher auf den

Rekombinationsmechanismen direkt nach der optischen Anregung und wie diese durch die Film-Morphologie beeinflusst werden. Kapitel 10 geht der Fragestellung nach wie geringfügige Änderungen der Zusammensetzung der Ausgangsstoffe sich auf die morphologische Struktur des Films und letztlich auf die elektronischen Eigenschaften auswirken. In dieser Teilarbeit wurde ein zusätzlicher Anteil an Bleiiodid (PbI_2) in der Materialkomposition durch Ausheizen der Filme gezielt eingestellt. In Übereinstimmung mit der Literatur steigt die Solarzelleffizienz zunächst mit steigendem Bleiiodid-Anteil an bevor sie sinkt. Dies ist konsistent mit dem beobachteten Anstieg der PL-Intensität mit zunehmendem PbI_2-Gehalt, was auf eine geringere nichtstrahlende Rekombinationsrate der Ladungsträger hinweist. Jedoch führt zusätzliches PbI_2 zu einer geringeren Stabilität der Filme wie aus den Langzeitmessungen an Solarzellen hervorgeht. Damit verknüpft ist auch der Verlauf der PL-Intensität bei Filmen, die über mehrere Tage gelagert wurden. Die Publikation belegt, dass zusätzliches Bleiiodid zwar zu einer Effizienzsteigerung führt aber auch zusätzliche Kristallisationskeime für eine schnellere Zersetzung der Kristallstruktur liefert, wie Röntgenbeugungsdaten und SEM-Aufnahmen bestätigen.

Mögliche Ursachen für den nichtstrahlenden Zerfall werden in Kapitel 11 näher untersucht. Dazu befasst sich das letzte Kapitel durch Nutzung von orts- und zeitaufgelöster PL mit der Ladungsträgerdynamik in dünnen Filmen aus $CH_3NH_3PbI_{3-x}Cl_x$. Ortsaufgelöste PL-Messungen machen die Korngrenzen zwischen Kristalliten sichtbar und zeigen, dass die einzelnen Kristallite unterschiedlich hell leuchten. Einige bleiben sogar für den Zeitraum von wenigen Minuten ganz dunkel, was einem Blinkverhalten entspricht. Eine Vermutung, dass gefangene Elektronen für diesen Dunkelzustand verantwortlich sind, konnte mittels einer zusätzlich aufgedampften Schicht des Akzeptors PCBM bestätigt werden. Die spektroskopischen und ortsaufgelösten Messungen deuten zusammenfassend auf einen Auger-Prozess als zusätzlichen nichtstrahlenden Prozess hin, der von der Fallendichte im Perowskitfilm abhängt.

Summary

Since the beginnings in the early 90s the field of organic semiconductors has shown steady progress. Organic light emitting diodes and field effect transistors can be already found today in cell phone displays or as RFIDs in different aspects of daily life. For solar cell application both organic as well as hybrid organic-inorganic perovskite materials show at least good efficiencies but lifetimes are not long enough to bring them to market.

Both in organic materials and in hybrid Perovskite structures for solar cells the morphology at interfaces plays a crucial role for the functionality because it is intimately linked with the optical and electronic properties. In organic materials these can be interfaces between ordered aggregated and amorphous phases or between donor and acceptor components.

Whereas in hybrid Perovskites interfaces in polycrystalline films form at grain boundaries or by structural changes induced by a changed stoichiometry.

In this thesis with the help of ultrafast spectroscopic methods like transient absorption, the dynamic of excitations at those interfaces is therefore investigated. That is why I built up and characterized a setup for transient absorption at the beginning of my PhD. With a time resolution of a few hundreds of femtoseconds and a wide spectral range (480-1100 nm) it is possible to investigate either solutions or thin films in a wide temperature range (5-500 K). The characterization and the description of the setup are summarized in chapter 5.

In the case of organic systems the complex process of exciton dissociation will be systematically resolved. Therefore in the first part of this work the crucial steps, like diffusion within the phases of the donor polymer or the dynamic of charge transfer at the interface between donor and acceptor are analyzed. Whereas in perovskite materials, knowledge of the relation between changes in morphology and the recombination dynamic is still missing. This lies in the focus of the second part of this work.

For most used polymers, which serve as donor, aggregation plays an important role. One example is the polymer MEH-PPV. In detail, I have investigated the dynamic of the excitons near the interface of different conformations of this polymer. The extension of the different phases can be tuned by changing the temperature. Amorphous and ordered phases contribute differently to the time dependent spectra and partially overlap. But it is possible to spectrally separate them by considering the temperature dependent absorption and PL spectra. In this way by using transient absorption measurements an energy transfer between both phases could be quantified to occur on a timescale smaller than 1 ps. This is only possible if both phases are in direct contact to each other. The results are further described in chapter 6.

In chapter 7 the dynamic within the aggregated phase of MEH-PPV below the transition temperature is considered. It is shown by comparing transient absorption data with the results from 2D spectroscopy measurements that the excitations localize on an ultrafast timescale. This is followed by a complex relaxation behavior within the density of states of the aggregates via transfer steps over a range of distances. Another aspect beside diffusion concerns the processes occurring at the interface between donor and acceptor units.
In chapter 8 therefore the excitation dynamic of a chemical dyad in solution is investigated. It consists of small covalently bounded molecules which act as donor (CuPc) and acceptor (PBI). Time-resolved measurements in the ultrafast and nanosecond region as well as structural data from simulations of molecular dynamics show, that formation of triplet states and non-radiative decay can dominate dependent on the conformational state of the dyad and consequently prevent efficient charge transfer.

Diffusion within the donor phase and the dynamics at the interface between donor and acceptor, which are considered in chapter 7 and 8, respectively, are crucial for charge separation in organic solar cells.
Based on this, in chapter 9 the process of charge separation in blend films is investigated. These films, which represent active layers in organic solar cells, consist of a donor-polymer and the acceptor PCBM to equal parts. The focus lies on the first step of charge separation, which is the formation of a charge separated state. Here the dependence of the difference in energy levels of both materials and temperature on the electron transfer is investigated systematically. The measurements show that in all investigated blend systems there is a temperature independent charge transfer, which cannot be described consistently with the often used Marcus model for all the material systems. It shows that other models must be considered which include quantum mechanical coupling of molecular vibrations to the electron transfer. Furthermore, it gets clear that the influence of the energy levels from donor and acceptor plays a minor role.

Chapter 10 and 11 summarize the results of the measurements on the excitation dynamic of hybrid Perovskite films ($CH_3NH_3PbI_3$ und $CH_3NH_3PbI_{3-x}Cl_x$). Due to the low binding energy in those polycrystalline structures thermal energy at roomtemperature is high enough to directly generate free charges. Therefore the main focus is drawn to recombination mechanisms directly after photo excitation and how they are influenced by the film morphology.

Chapter 10 answers the question how small changes in the composition of the reactants influence the morphologic structure of the films and on the electronic properties. In this part of the work an additional lead iodide (PbI_2) content in the material was specifically changed by additional annealing of the films.
In accordance with literature the solar cell efficiency first increases for additional PbI_2 content before it drops for higher PbI_2 content. This is also in agreement with the measured increase in PL-intensity for increasing PbI_2 content which gives hint to a smaller non-radiative recombination rate of the charge carriers. Conversely, it leads to less stability of the films indicated by long term measurements of solar cells. This is also linked with the trend of the PL-intensity for films which were stored for several days under ambient air conditions.
The publication makes clear that additional lead iodide may lead to an increased efficiency but also delivers seeds for crystallization which accelerate the degeneration of the crystal structure, also evidenced by X-ray scattering data and SEM images.

Possible reasons for non-radiative channels are investigated in chapter 11. Therefore this last chapter deals with the carrier dynamic in $CH_3NH_3PbI_{3-x}Cl_x$ films by using spatially as well as time resolved PL measurements. Spatially resolved measurements display the grain boundaries between crystallites and show that the individual crystallites show different PL intensity. Some even stay completely dark for minutes, which is equivalent to a “blinking”

behavior. It could be verified by adding an additional evaporated layer of PCBM as acceptor that trapped electrons are responsible for the dark state. All in all, the measurements point to an Auger-recombination process as an additional non-radiative channel, which depends on the trap state density.

2 Motivation

Eine zunehmende Bevölkerung mit wachsendem Energiebedarf stellt bei begrenzten fossilen Ressourcen eine der wichtigsten Herausforderung dieses noch jungen Jahrhunderts dar. Photovoltaik kann einen entscheidenden Beitrag zur Lösung beitragen. Heutige Solarzellmodule bestehen fast ausschließlich aus Silizium. Sie werden zwar auch immer günstiger in der Herstellung, aber ihre energetische Armortisationszeit ist zu lang. Hier sind Solarzellen aus organischen[1,2,3] oder hybriden Materialien[4,5,6] interessant. Durch die kostengünstige Prozessierung aus Lösung können sich großflächig gedruckt werden und bilden nicht nur eine günstige Alternative zu Silizium, sondern erschließen auch andere Anwendungsbereiche. Aufgrund ihres geringeren Gewichts und der möglichen Flexibilität der Module können sie beispielsweise als Gestaltungselemente an Gebäudefassaden eingesetzt werden. Reine organische Solarzellen erreichen zur Zeit eine Effizienz von etwa 12 % [5]. Trotz ihrer geringeren Lebensdauer gegenüber den etablierten Silizium-Solarzellen, sind sie bereits für Nischenanwendungen teilweise wirtschaftlich rentabel.

In organischen Solarzellen führt die optische Anregung selten direkt zu getrennten Ladungsträgern. Vielmehr ist es ein komplexer Prozess, der in mehreren Schritten abläuft, von denen jeder Gegenstand aktueller Forschung ist[7,8,9]. Nach der Absorption eines Photons diffundieren die angeregten Zustände zur Kontaktfläche zwischen einem Donor- und einem Akzeptormaterial, wo der Eletronentransfer stattfindet. Sowohl die Diffusionsdynamik als auch die Trennung der erzeugten Exzitonen werden durch den Ordnungsgrad des Donorpolmyers sowie der Morphologie an der Grenzfläche bestimmt[10,11,12]. Strittig bei der Trennung zum Beispiel ist die Bedeutung des Ladungstransferzustands (CT), wie er durch die Morphologie des Donors-Akzeptors Films beeinflusst und in welchem Maße freie Ladungsträger direkt gebildet werden[13]. Nicht geklärt ist auch, ob der erste Transferschritt thermisch aktiviert ist, und somit mit der Marcus-Theorie beschrieben werden kann, oder in welchem Maße quantenmechanisches Tunneln berücksichtigt werden muss[14,15]. Ein wichtiges Werkzeug bei der Untersuchung dieser „ultraschnellen“ Prozesse ist die transiente Absorption im Zeitbereich von Femtosekunden bis Nanosekunden. Daher wurde dafür ein Messaufbau eingerichtet, der nicht nur einen breiten spektralen Bereich (VIS-NIR) sondern auch einen breiten Temperaturbereich von 5-500 K abdeckt und Messungen an dünnen Filmen und Lösung ermöglicht (siehe Kapitel 5).

Erweiternd bieten transiente Photolumineszenz und PLQE die Möglichkeit strahlende und nichtstrahlende Raten zu ermitteln um so mögliche Verlustkanäle in rein organischen Dünnschichtfilmen oder hybriden Perowskit-Strukturen aufzuspüren.

Seit Kojima u.a. 2009 mit einer Perowskit-Solarzelle eine Effizienz von 3.8%[4] erreichten, wurde diese Materialklasse in den letzten Jahren intensiv erforscht und es konnten Effiziensteigerungen auf aktuell 22°%[5] erreicht werden.

Viele Fragen, die den Einfluss der Morphologie auf die Photophysik und die Stabilität der Filme betreffen, sind jedoch noch offen. Hierzu zählen unter anderem Ursachen von Fallenzuständen und deren Einfluss auf die optischen Eigenschaften, sowie die Rekombinationsdynamik der erzeugten Ladungsträger. Um diesen Fragestellungen nachzugehen wurden die Rekombinationsdynamik der erzeugten Ladungsträger und die spektralen Eigenschaften der Filme näher beleuchtet. Die Ergebnisse an den beiden wichtigsten Vertretern, $CH_3NH_3PbI_3$ und $CH_3NH_3PbI_{3-x}Cl_x$, dieser Materialklasse sind in den letzten beiden Kapiteln 10 und 11 zusammengefasst.

3 Einführung in die Konzepte und Stand der Forschung

3.1 π-konjugierte Systeme

In diesem Kapitel führe ich die wichtigsten Begriffe ein, die für die Analyse und Einordnung der Ergebnisse hinsichtlich Ladungsträgertrennung und Rekombination in reinen organsichen Halbleitern und hybriden Perowskit-Materialien benötigt werden. Dies beinhaltet verschiedene Arten angeregter Zustände in organischen Halbleitern sowie die Mechanismen, die deren Dynamik beschreiben.

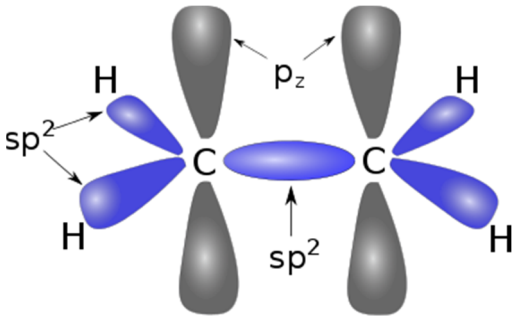

Abbildung 1: konjugierte Systeme, schematische Darstellung benachbarter Kohlenstoffatome in kovalenter Bindung mit sp^2-Hybridisierung, grau unterlegt: p_z-Orbitale, die das π-konjugierte System bilden; angedeutet sind die jeweils pro C-Atom angebundenen Wasserstoffatome, die in dieser Darstellung abwechselnd aus der Zeichenebene heraus bzw. in die Ebene reinragen.

Bei sogenannten π-konjugierten Systemen haben die Kohlenstoffatome meist eine sp^2-Hybridisierung und bilden σ-Bindungen zu ihren Nachbarn aus. Das übrige Valenzelektron besetzt das übrigbleibende p-Orbital, das senkrecht zur Verbindungsachse steht (grau gekennzeichnet in Abb. 1). Der Überlapp dieser p-Orbitale führt zur teilweisen oder sogar vollständigen Delokalisierung der Elektronen über das gesamte Molekül hinweg. Im Grundzustand sind die Orbitale entweder vollständig besetzt oder vollständig unbesetzt. Das höchste besetzte Orbital wird auch HOMO und das niedrigste unbesetzte Orbital auch LUMO genannt. Ihr energetischer Abstand, der grob der optischen Bandlücke entspricht, beträgt zwischen 1 und 4 eV, damit zeigen die Moleküle Eigenschaften eines Halbleiters[16]. Der konjugierte Teil eines kleinen Moleküls oder einer Polymerkette ist das Chromophor. Dabei kann die Chromophorlänge, auch Konjugationslänge genannt, größer sein als die Wiederholeinheit des Polymers, typischerweise 4-10 Wiederholeinheiten[17,18]. Mit steigender Wiederholeinheit sinkt die optische Bandlücke. Für das Modell eines Teilchens in der Kiste würde sie fürs Polymer gegen Null gehen, nach dem Modell von Kuhn für gekoppelte Oszillatoren jedoch sättigt sie bei einem Wert größer Null[19,20].

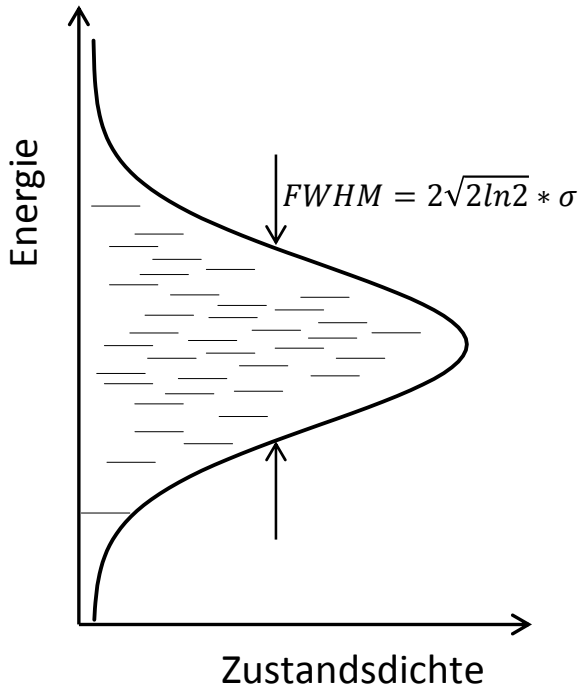

Abbildung 2: schematische Darstellung einer Gaußförmigen Zustandsdichte lokalisierter Zustände

Im gelösten Zustand sind Polymere oder kleine Moleküle von Lösungsmittelmolekülen umgeben. Dabei erfährt jedes Molekül eine etwas andere Polarisationsumgebung, wodurch sich die Energieniveaus der elektronischen Zustände des Chromophors leicht verschieben und um einen Mittelwert schwanken. Des Weiteren gibt es Schwankungen von Torsionswinkeln um Molekülbindungen sowie unterschiedliche Biegungswinkel entlang des Polymergrundgerüsts im amorphen Zustand[21]. In der Summe ergibt sich eine statische Unordnung. Sie hat eine gaußförmige Verteilung und wird mit der Streuung σ quantifiziert (siehe Abb. 2). Ist diese Schwankung der Energiewerte kleiner als die elektronische Kopplung zwischen zwei benachbarten Chromophoren können Anregungen über mehrere delokalisieren und (kohärent) ausgetauscht werden[22]. Ein kohärenter Transport von Anregungen oder Ladungen kann z.B. in organischen Molekülkristallen bei tiefer Temperatur beobachtet werden, sowie in einigen idealisierten 1-dimensionalen Systemen wie zum Beispiel Nanodrähten[23,24] oder Polymerketten[25]. Ist die elektronische Kopplung zwischen den Chromophoren jedoch kleiner als die Streuung σ bleiben die Anregungen oder Ladungen auf einzelnen Chromophoren lokalisiert und können nur durch inkohärentes Hüpfen zwischen benachbarten Chromophoren ausgetauscht werden[26]. Holstein beschreibt diesen Vorgang in seinem „small polaron“ Modell[27] und nimmt dabei die elektronische Kopplung zwischen Molekülen als Störung an[17].

3.2 Anregungen in organischen Halbleitern

Bei der optischen Charakterisierung konjugierter Materialien misst man das Absorptions- und Emissionsspektrum, entweder in Lösung oder im Festkörper in Form eines dünnen Films. In der Absorptionsspektroskopie misst man die Transmissionsänderung durch die Probe bezüglich eines Referenzstrahls. Mit einem Gitterspektrographen zum Beispiel wird die Intensität des transmittierten Lichts wellenlängenabhängig gemessen und anschließend durch die Intensität des Referenzstrahls geteilt. Die optische Dichte errechnet sich dann unter Annahme des Lambert-Beerschen Gesetzes zu:

$$I(x) = I_0 \cdot 10^{-OD} \tag{1}$$

wobei $I(x)$ die Intensität hinter der Probe und I_0 die Intensität des Referenzstrahls ist. Außer der Absorption können auch Reflexion und Streuung die gemessene Transmission beeinflussen. Sie werden aber bei dieser Messmethode vernachlässigt. Falls diese bedeutend sind, muss ein Spektrometer mit Ulbrichtkugel verwendet werden.

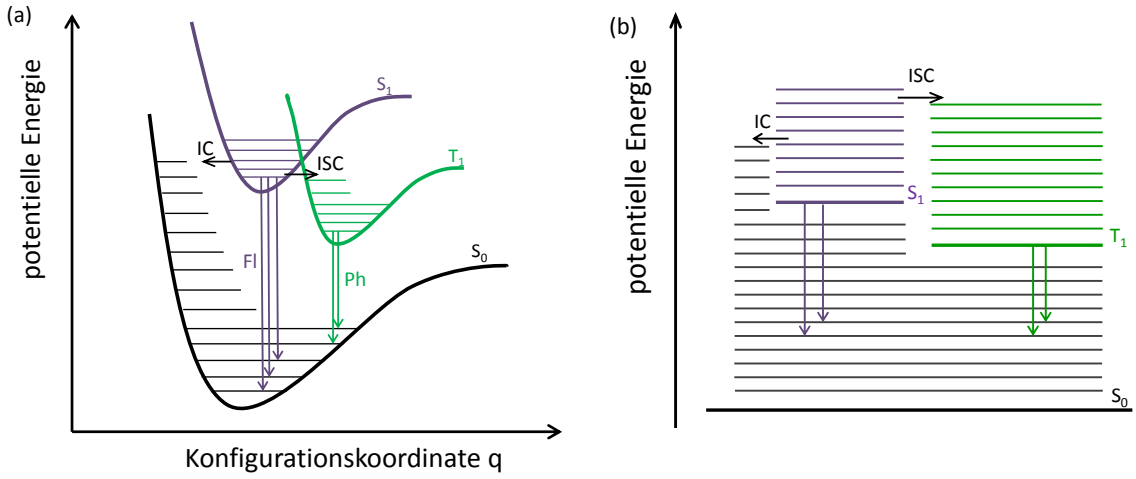

Abbildung 3: (a): Energie-Diagramm der angergten Zustände in organischen Molekülen. S_0 ist der Singulett-Grundzustand, S_1 der erste angeregte Singulett- und T_1 der Triplettzustand. Die Pfeile zeigen mögliche Absorptions- und Emissionsvorgänge an. Phosphoreszenz Ph vom T_1 in den S_0, Fluoreszenz Fl vom S_1 in den S_0 (b) schematisches Jablonski-Diagramm mit interner Konversion IC zwischen Singulettzuständen und Intersystem crossing ISC zwischen Singulett- und Triplettzustand.

Absorption und Emission lassen sich anhand eines Jablonski-Diagramms veranschaulichen (siehe Abb. 3). Vor der Anregung befindet sich das Molekül im Grundzustand. Bei fast allen organischen Materialien ist das Orbital mit der höchsten Energie mit zwei Elektronen besetzt. Diese besitzen Spins mit unterschiedlichen Vorzeichen. Das heißt der Gesamtelektronenspin ist Null und der elektronische Grundzustand ist ein Singulett, der oft mit S_0 bezeichnet wird.

Bei optischer Anregung, also Absorption eines Photons, wird der absorbierende Teil eines Moleküls, das *Chromophor*, in einen angeregten Singulettzustand (S_1 oder S_n) gebracht, da

bei Absorption keine Änderung des Spins stattfindet. Die Photonenenergie liegt im Bereich zwischen 1-4 eV. Bei höheren Zuständen S_n geht es innerhalb weniger Femtosekunden in den untersten angeregten Zustand S_1 über („*Kasha's rule*“)[28,29,30]. Dies ist eine Konsequenz des Energielückengesetzes („*energy-gap law*“). Im ersten angeregten Zustand kann es ebenfalls in einem vibronisch angeregten Schwinungsniveau vorliegen, von wo aus es in das unterste Schwingungsniveau des ersten angeregten elektronischen Zustands relaxiert. Von dort gibt es mehrere Möglichkeiten für das Molekül in den Grundzustand zurückzukehren. Entweder es gelangt über Anregung interner Vibronen über interne Umwandlung („*internal conversion*“) strahlungslos in den untersten Grundzustand S_0 (angedeutet durch einen Pfeil in Abb. 3a und b), oder es nimmt den strahlenden Übergang in den Grundzustand unter Aussendung eines Photons (angezeigt durch lila Pfeile in Abb. 3a und b). Ebenso können auch Übergänge zwischen den Zuständen Singulett und Tripplett durch „*inter-system crossing*“ (*ISC*) stattfinden. Dies geschieht über die Spin-Bahn-Wechselwirkung, bei der quantenmechanisch Singulett- und Triplettzustände gemischt werden. Diese wird entweder durch eine hohe Kernladungszahl beteiligter Atome oder durch Schwingungen des Moleküls hervorgerufen[31,32]. Vom Triplettzustand aus kann das System ebenfalls strahlungslos oder strahlend durch Phosphoreszenz (angedeutet durch einen grünen Pfeil in Abb. 3b) in den Grundzustand übergehen. Dies geschieht jedoch mit kleinerer Rate als beim Singulett, da gleichzeitig eine Änderung des Spins stattfinden muss, was die Wahrscheinlichkeit des Übergangs deutlich verringert. Aus diesem Grund sind auch die Lebenszeiten der Triplettzustände ($\tau \approx \mu s$-s) vieler organischer Halbleiter deutlich höher als die von Singulettzuständen ($\tau \approx 0.1$-10 ns)[17,33,34].

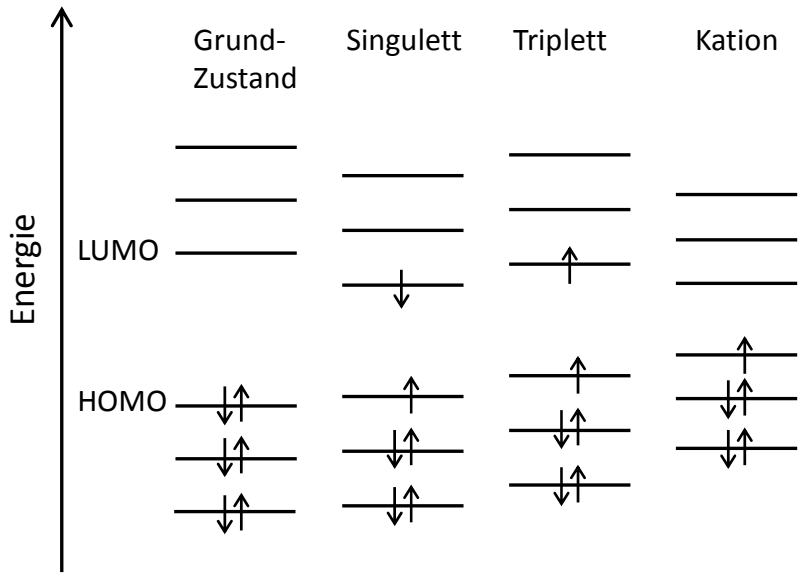

Abbildung 4: mögliche Ein-Elektronenorbital-Darstellungen eines Moleküls im Grundzustand, im neutralen angeregten Zustand (Singulett bzw. Triplett) und im positiv geladenen Dublettzustand (Kation).

In Abbildung 4 sind die unterschiedlichen elektronischen Zustände für den Grundzustand, den angeregten Singulett und Triplett sowie den Polaronzustand in einem Orbitaldiagramm

dargestellt. Diese Orbitaldarstellungen stellen nur die wichtigsten Konfigurationen dieser elektronischen Zustände dar.

Eine solche Darstellung ist eine Näherung, da Orbitale nur Darstellungen von Ein-Elektronen-Zuständen sind und dabei die Elektron-Elektron-Wechselwirkung vernachlässigt wird. Bei der Absorption von Licht geht das Molekül vom Grundzustand in den angeregten Singulettzustand. Dieser kann aufgefasst werden als angeregtes Elektron-Loch-Paar, mit einem Elektron im LUMO und einem verbleibenden Loch im HOMO (siehe Abb. 4). Aufgrund der Coulombwechselwirkung sind Elektron und Loch jedoch weiterhin stark gebunden ist. Dies liegt an der im Vergleich zu anorganischen Materialien geringeren dielektrischen Konstante zwischen[16] ε_r=3-4 so wie an Elektron-Elektron- und Elektron-Phonon-Wechselwirkungen[35]. Die HOMO- und LUMO-Werte lassen sich jeweils mit dem Ionisationspotenzial bzw. der Elektronenaffinität abschätzen. Sie sind zum Beispiel über Cyclovoltammetrie-Messungen oder über die Ultraviolett-Photoelektronenspektroskopie zugänglich. Ihr Abstand entspricht der elektronischen Bandlücke und die Differenz zwischen elektronischer und optischer Bandlücke entspricht der Bindungsenergie des Exzitons, die für organische Halbleitermaterialien zwischen wenigen meV und ca. 1 eV liegen kann[36].

Die Lebensdauer des Exzitons ist intrinsisch begrenzt durch die Kopplung an die Zustandsdichte des Singulett Grundzustands. Das Übergangsdipolmoment bestimmt die radiative Kopplung. Die nicht-radiative Rate hängt von der Bandlücke ab und wird im *„energy gap law“* beschrieben. Sie ergibt sich aus Fermis Goldener Regel und gilt sowohl für Singulett- als auch Triplett-Exzitonen[37,38]. Die Diffusionslänge hängt von der Lebensdauer aber auch vom Mechanismus des Transfers ab. Singuletts diffundieren hauptsächlich über den Förster-Transfer-Mechanismus[29,39], Tripletts über den Dexter-Transfer-Mechanismus[40,29,41]. Beide werden in Abschnitt 3.3 näher erläutert. Landet ein Exziton in einem tiefen Fallenzustand steigt indirekt die nichtstrahlende Rate, wodurch sich die Lebenszeit weiter verkürzt. Bei tiefen Temperaturen werden die Diffusionsprozesse ausgefroren und Exzitonen können nicht zu Fallenzuständen diffundieren, was dann zu einem Anstieg der Lebenszeit führen kann.

Vorgang der Ladungsträgertrennung in Blend-Filmen für organische Solarzellen

In organischen Solarzellen sind typischerweise Donor- und Akzeptormaterial in einem Blend-Film gemsicht. In der Literatur spricht man dann von einer „bulk-heterojunction“. Wird ein Photon von einem Donormolekül absorbiert entsteht ein Exziton. Nach seiner Bildung diffundiert es innerhalb der Donorphase zur Donor-Akzeptor-Grenzfläche. Aufgrund der geringeren Elektronenaffinität wird das Elektron auf ein Akzeptormolekül wechseln[17]. Der Einfluss der Elektronenaffinität auf den Elektronentransfer wird in Kapitel 9 näher untersucht. Nach dem Transferschritt bleibt auf dem Donormolekül ein "Loch" also ein posititv geladenes Polaron (siehe Kation in Abb. 4) zurück. Ein entsprechend großer Unterschied der Elektronenaffinitäten verhindert auch den thermisch aktivierten Rücktransfer auf das Donormolekül. Die Coulombanziehung zwischen Elektron und Loch ist aber wegen ihres geringen Abstands so stark, dass das Elektron-Loch-Paar immer noch als ein gebundener Zustand, beziehungsweise als Quasiteilchen, angesehen werden kann. In der Literatur spricht man dann von einem "*charge-transfer state*" (CT-Zustand). Oft wird er nur im Zusammenhang mit Donor-Akzeptor-Grenzflächen verwendet, jedoch besitzen auch einige Polymere unterschiedlich elektron-affine Einheiten, die Elektronendichte "anziehen" oder "abstoßen". Aus diesem Grund nennt man sie in der älteren Literatur oft auch "*push-pull*-" oder „*low-bandgap*“-Polymere[42,43,44]. Prominente Beispiele dafür sind PCPDTBT oder PCDTBT. Die Abgrenzung des CT-Zustands zum Exziton ist oft fließend, da DFT-Rechnungen zeigen, dass der angeregte Singulett-Zustand auch CT-Charakter haben kann[35, 45]. Im Einklang mit der Literatur wird dieser Zustand im weiteren als intramolekularer CT-Zustand bezeichnet. Ob ein Elektronenübertrag vom angeregten Donor auf ein benachbartes neutrales Akzeptormolekül stattfindet, hängt von vielen Faktoren ab. Für gängige Solarzellsysteme läuft dieser erste Schritt exothermisch ab, da die Änderung der freien Enthalpie ΔG_0kleiner null ist. Sie wird auch als Triebkraft für den Prozess der Ladungsträgertrennung betrachtet und wird in erster Näherung durch den Unterschied der Elektronenaffinitäten von Donor und Akzeptor abgeschätzt. Es hat sich gezeigt, dass für effiziente Solarzellen ein gewisser Wert nötig ist[46, 47], jedoch gibt es auch neuere Beispiele effizienter Systeme mit sehr geringem Unterschied (ca. 0.1 eV)[48, 49]. Allgemein ist daher unklar, welche Rolle dieser bei der Bildung des CT-Zustands spielt und welche weitere Effekte wie elektronische Kopplung und Morphologie an der Grenzfläche die Ladungsträgertrennung begünstigen. Allgemein wird bei vielen organischen Donor-Akzeptor-Solarzellen die Bildung des CT-Zustands innerhalb weniger Femtosekunden (20-<200 fs) beobachtet und ist in den meisten gängigen Systemen sehr effizient[9,50]. Danach besteht die Möglickeit der Trennung in freie Ladungsträger oder des Transfers zurück auf den Donor. Das Onsager-Braun-Modell beschreibt die Raten dafür und berücksichtigt thermische Aktivierung und externe elektrische Felder. Wird der Zustand nicht getrennt, wird er durch "*geminate recombination*", also Rekombination gebundener Ladungsträger, aufgelöst. Dies kann radiativ oder nicht-radiativ geschehen. Gegenstand aktueller Forschung ist dabei der Einfluss der lokalen Morphologie an der Grenzfläche, der Unordnung, der Anregungsdichte und Anregungsenergie. Besonders letztere wird aktuell in der Literatur kontrovers

betrachtet[51,13,9]. Schon Chance et al. zeigten für Molekülkristalle, dass es für eine effiziente Ladungsträgertrennung vor allem auf den elektronischen Zustand, der angeregt wird, ankommt und nicht etwa auf die Anregung von Schwingungsniveaus. Erst bei Anregung des nächst höheren elektronischen Zustands steigt die Effizienz weiter an. Innerhalb des gleichen elektronischen Zustands bleibt die Effizienz bei steigender Anregungsenergie konstant[52]. Für ungeordnete Blendsysteme wird weiterhin diskutiert, ob auch Anregungen von Molekülschwingungen zur Trennung des CT-Zustands beitragen können[9, 53].

3.3 Modelle für Energie- und Ladungstransfer

Die Art der Energieübertragung zwischen einem Donor- und einem Akzeptormolekül lässt sich allgemein schreiben als:

$$D^* + A \rightarrow D + A^* \tag{2}$$

Die elektronische Kopplung bestimmt die Art des Energietransfers und damit auch die Reichweite. Sie besteht aus einem Coulomb- und einem Austauschanteil. Beide können gleichermaßen auftreten und sich ergänzen. Ersterer kann unter bestimmten Voraussetzungen mit dem Modell von Förster beschrieben werden und letzter als Dexter-Transfer.

3.3.1 Förster-Energie-Transfer

Der Coulombanteil beschreibt die Coulombwechselwirkung der Ladungsträgerverteilungen und kann in einer Entwicklung nach Taylor in Dipol-Dipol und Dipol-Quadrupolterme entwickelt werden[54]. Für größere Abstände der Moleküle überwiegen die Terme der Dipol-Dipol-Wechselwirkung. Der angeregte Donor regt so den Dipol des Akzeptors an. Die Transferrate von Gleichung (2) lässt sich dann über Fermis-Goldene-Regel schreiben als [55,56]:

$$k_{Förster}(d) = \frac{1}{\tau_D r^6} \frac{9\ln(10)\kappa^2 \varphi_D}{128\pi^5 N_A n^4} \int_0^\infty F_D(\lambda)\epsilon_A \lambda^4 d\lambda \tag{3}$$

κ ist ein Orientierungsfaktor der beiden Dipole zueinander und wird über die Verteilung im Film oder in Lösung gemittelt. In drei Dimensionen nimmt er den Wert $2/3$ an. φ_D ist hierbei die Quanteneffizienz des Donors, n der Brechungsindex des umgebenden Mediums, F_D das auf die Fläche normierte Emissionsspektrum des Donors und ϵ_A ist der Extinktionskoeffizient des Akzeptors. Für Donor-Akzeptor-Abstände bis zu 10 nm stimmen experimentell gemessene Raten mit den theoretischen gut überein[55,57,58]. Für kleine Abstände (ca. <1 nm), wenn der Abstand r Werte der Ausdehnung der Moleküle annimmt, kommt es hingegen zu starken Abweichungen.

3.3.2 Dexter Energie Transfer

Bei kleineren Abständen gewinnen bei der Coulombwechselwirkung die Quadrupol-Dipol-Terme an Bedeutung. Sie sind jedoch deutlich kleiner als der Einfluss der Austauschwechselwirkung. Diese hängt vom räumlichen Überlapp der Orbitale von Donor und Akzeptor ab, welcher expoentiell mit dem Abstand R abfällt und somit auf wenige Ångström[59] beschränkt ist. Die Transferrate kann geschrieben werden als[22,60,54]:

$$k_{dexter} = KJe^{-2R\gamma} \tag{4}$$

Dabei ist *J* der dimensionslose spektrale Überlapp $J = \int F\varepsilon\lambda^4 d\lambda$, γ der inverse Lokalisationsradius der Orbitale und *K* eine Konstante. Durch den Überlapp der Wellenfunktionen ist es auch möglich, den Energie-Transfer als korrelierten Transfer von Elektronen anzusehen. In diesem Bild wird das angeregte Elektron vom LUMO des Donors auf das LUMO des Akzeptors übertragen und gleichzeitig ein Elektron aus dem HOMO des Akzeptors auf das HOMO des Akzeptors. In diesem Fall ist kein Umklappen des Spins nötig, so dass zum Beispiel ein Triplett von einem Chromophor zum benachbarten übertragen werden kann[61]. Hat der Akzeptor eine niedrigere Energie als der Donor zuvor, so wurde die Energiedifferenz an das umliegende Wärmebad abgegeben.

3.3.3 Das Modell von Miller-Abrahams

Neben Modellen zum Energietransfer gibt es auch verschiedene Modelle zum Ladungstransfer in organischen Halbleiern. Das Modell von Miller und Abrahams beschrieb erstmals Ladungstransport in dotierten inorganischen Halbleitern[62], allerdings zeigt es auch Gültigkeit bei der Beschreibung von organischen Halbleitern[26, 63]. Abweichend vom Bandtransport betrachtet es den Transportprozess als Hüpfen zwischen lokalisierten Zuständen mit unterschiedlichen Energien. Transportprozess meint hier den Elektronentransfer bei dem ein geladenes Donor-Molekül in einen neutralen Zustand übergeht und ein benachbartes Molekül im Abstand r_{ij} vom neutralen in einen einfach geladenen Zustand. Die Elektron-Phonon Kopplung ist klein, so dass polaronische Effekte vernachlässigt werden können, aber groß genug um noch eine Kopplung ans Wärmebad zu gewährleisten[26]. Das Hüpfen wird durch quantenmechanisches Tunneln möglich und durch den elektronischen Wellenfunktionsüberlapp zwischen Donor- und Akzeptoreinheit berücksichtigt. Für Sprünge in Zustände höherer Energie wird ein einzelner Phononen-aktivierter Prozess angenommen. Die Rate zwischen räumlich und energetisch unterschiedlichen Zuständen ergibt sich zu:

$$k_{ij} = v_0 e^{-2\gamma \cdot r_{ij}} \begin{cases} e^{-\frac{\epsilon_j - \epsilon_i}{kT}} & \epsilon_j \geq \epsilon_i \\ 0 & \epsilon_j < \epsilon_i \end{cases} \tag{5}$$

Dabei ist γ der inverse Lokalisationsradius der Elektronenwellenfunktion und υ_0 ist ein Vorfaktor mit Dimension einer Frequenz (*attempt-to-jump frequency*). r_{ij} ist der räumliche Abstand zwischen den Chromophoren. Der Vorfaktor ist ein Parameter, der von Donor- und Akzeptormolekül sowie von deren elektronischer Kopplung abhängt. Er kann aus Mobilitätsmessungen abgeschätzt werden. Bei einem negativen Unterschied der Energieniveaus ist keine thermische Energie nötig, jedoch für eine positive Energiedifferenz, daher wird im letzten Fall ein Boltzmann-Faktor zur Rate multipliziert.

3.3.4 Marcus-Theorie

Ein häufig verwendetes Modell ist das Marcus-Modell. Es geht von einem Prozess in mehreren Schritten aus, der durch Anregung von Phononen unterstützt wird. In Abbildung 5 ist dies schematisch angedeutet durch blaue Pfeile zwischen den Schwingungsniveaus im Potential des neutralen angeregten Zustands (D*-A). Das Modell setzt thermisches Gleichgewicht voraus. Es wurde ursprünglich entwickelt um Ladungstransfer in chemischen Reaktionen zu beschreiben, bei denen keine Bindungen gebrochen oder gebildet werden. Die Rate lässt sich angeben mit[64]:

$$k_{ET} = \frac{{J_{DA}}^2}{\hbar}\sqrt{\frac{\pi}{\lambda \cdot kT}}\, e^{-\frac{(\lambda+\Delta G_0)^2}{4\lambda kT}} \qquad (6)$$

J_{DA} ist dabei die elektronische Kopplung zwischen Donor- und Akzeptormolekül und ΔG_0 die Änderung der freien Enthalpie des Elektronentransfers. Für den Fall, dass Anfangs- und Endzustand die gleiche Energie besitzten aber unterschiedliche Gleichgewichtspositionen q_i und q_f haben, schneiden sich die Potentialkurven bei einer Energie, die dem Viertel der Reorganisationsenergie λ entspricht und ist die Energiebarriere E_A bezüglich der Minima, die das System überwinden muss (siehe Abb. 6a). Zu beachten ist, dass die Potentialkurven jeweils das Gesamtsystem aus Donor, Akzeptor und dem umgebenden Lösungsmittel, bzw. der polarisierbaren Umgebung, berücksichtigen. Unterscheiden sich die Minima um ΔG_0, verändert sich die Energiebarriere E_A entsprechend (siehe Abb. 6b). Die Rate in Gleichung (6) gibt die Wahrscheinlichkeit pro Zeit an, dass bei gegebener thermischer Energie $k_B T$ mit Hilfe von Phononen am Schnittpunkt der Potentialkurven ein Ladungstransfer stattfindet. Da die Rate nach Gleichung (6) eine Parabel beschreibt, gibt es ein Optimum der Rate für den Fall: $\Delta G_{opt} = -\lambda$, bei der der Exponent null und die Rate maximal ist. Ist $-\Delta G_0 > \lambda$ nennt man das den inversen Marcus-Fall. Das Marcus-Modell beschreibt nur den nicht-adiabatischen Fall, also wenn die Kopplungsstärke J_{DA} viel kleiner als die Energiebarriere ist[22].

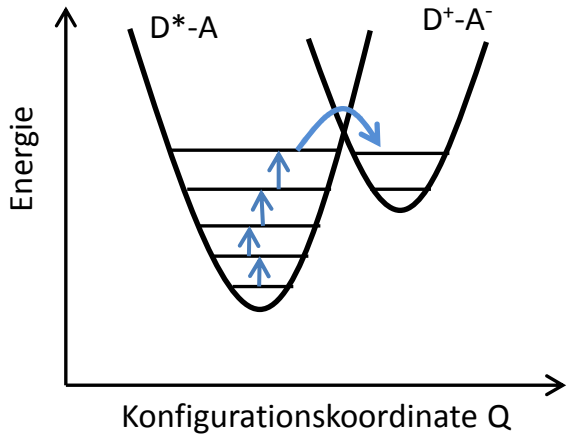

Abbildung 5: Schematische Darstellung der potentiellen Energie des Donor-Akzeptor Systems vor und nach dem Elektronentransfer aufgetragen über die Konfigurationskoordinate Q. Dargestellt ist der thermisch aktivierte Hüpfprozess mittels Phononen angezeigt durch blaue Pfeile. Am Kreuzungspunkt der Parabeln findet der Übergang statt.

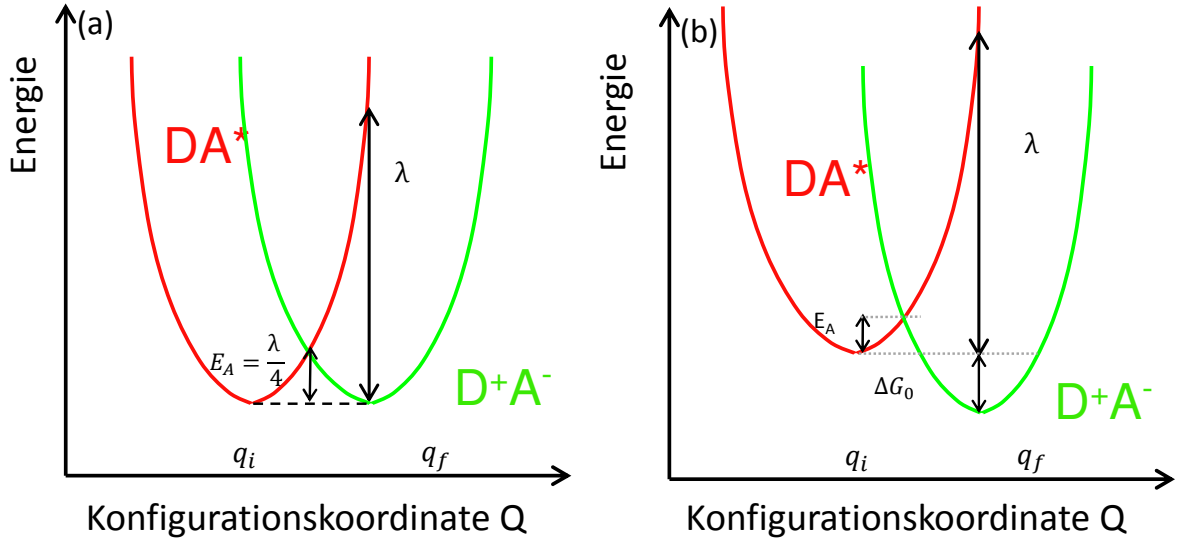

Abbildung 6: potentielle Energiekurve für den Transfer nach Marcus für ein System vor dem Elektronentransfer aus Donor und Akzeptor im angeregten Zustand DA* und danach D^+A^- mit gleicher Energie von Anfangs- und Endzustand (a) und für den Fall mit Energiedifferenz ΔG_0 zwischen Anfangs- und Endzustand (b).

Das Marcus-Modell beschreibt den Elektronentransfer allgemein und übereinstimmend mit experimentellen Daten, unabhängig vom Ausgangszustand des Systems, ob der Transfer zwischen gleichen oder unterschiedlichen Molekülen[65,66,67] oder intramolekular zwischen unterschiedlichen Einheiten eines Moleküls[68,69] stattfindet. Besonders gut passt das Modell bei Ladungstransferraktionen in Lösung, wobei der Beitrag der Reorganisationsenergie durch Umorientierung der Lösungsmittelmoleküle von Bedeutung ist.

Betrachtet man als Ausgangszustand eine Donormolekül im angeregten Singulett-Zustand, ändert das vor allem die freie Enthalpie ΔG_0 und die Reorganisationsenergie λ. Erstere lässt

sich aus der Differenz der Elektronenaffinitäten zwischen Donor und Akzeptor abschätzen[17]. Etwas genauer ist die Rehm-Weller-Gleichung[70,71]:

$$\Delta G_0 = IP_{D^+/D} - EA_{A^-/A} - \Delta E_{00} - E_b \quad (7)$$

$IP_{D+/D}$ und $EA_{A/A-}$ sind das Ionisationspotential des isolierten Donors und die Elektronenaffinität des isolierten Akzeptors. ΔE_{00} ist die adiabatische Energieänderung zwischen D*A und DA, welche der Energie des ersten Singulettzustands entspricht, und E_b der Unterschied der Bindungsenergien von CT-Zustand und Exziton des Donors. Bindungsenergie oder Coulombwechselwirkung hängen jedoch stark von der lokalen Morphologie und Orientierung der Moleküle direkt an der Grenzfläche ab, was ein Vergleich von Rechnungen und experimentellen Ergebnissen erschwert. Zumal der letzte Term nur durch theoretische Kalkulationen zugänglich ist[71]. Aus diesem Grund ist eine Abschätzung von ΔG_0 mit Hilfe der CT-Energie und der Singulettenergie oft sinnvoller:

$$\Delta G_0 = E_{S1} - E_{CT} \quad (8)$$

Die CT-Energie lässt sich aus spektrospektroskopischen Methoden wie EQE- und CT-Emissionsspektren[72] bestimmen und die Singulett-Energie aus PL- und Absorptionsspektren. Die Reorganisationsenergie λ kann durch DFT-Rechnungen abgeschätzt werden[71] oder ebenfalls aus EQE- und CT-Emissionsspektren[51,73] bestimmt werden.

Betrachtet man Gleichung (6) so fällt auf, dass der Exponentialfaktor die größte Temperaturabhängigkeit liefert. Dadurch kann die Rate um Größenordnungen sinken, wie Abbildung 7a zeigt. Nimmt man einen typischen Wert für λ (etwa 200 meV) an, so ergibt sich im Maximum, also für $\Delta G_{opt} = -\lambda$, eine Rate von $k_{max} \approx 10^{14}\ s^{-1}$ bei Raumtemperatur. J_{DA} wurde mit 30 meV abgeschätzt, da es typischerweise zwischen wenigen meV und etwa 30 meV liegt[74,75,76]. Der Wurzelterm macht weniger als eine Größenordnung der Rate aus. Die Theorie wurde zwar für getrennte Donor- und Akzeptor-Moleküle entwickelt, zeigt aber auch für Molekülsysteme mit kovalent gebundenen Donor- und Akzeptoreinheiten Gültigkeit[69].

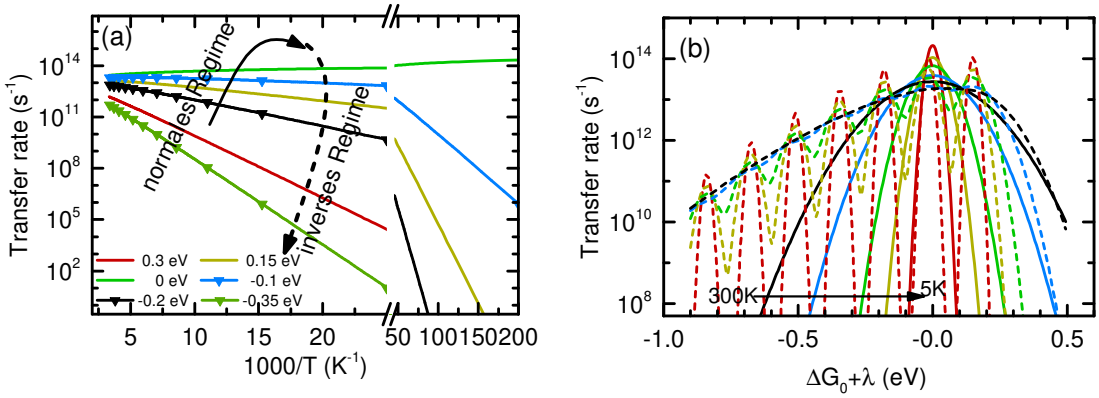

Abbildung 7: (a) Transferrate nach Gl. 6 aufgetragen in Arrheniusdarstellung über 1000/Temperatur für verschiedene Werte von $\Delta G_0 + \lambda$ wie in der Legende angegeben und (b) Transferrate nach Gl. 6 für λ=300 meV, J_{DA}=30 meV aufgetragen über $\Delta G_0 + \lambda$ (feste Linien) und nach Gl. 10 (gestrichelte Linien) für eine vibronische Energie von 165 meV und einem Huang-Rhys-Faktor von S=1.

2.3.4 Erweiterung durch Levich Jortner

Das Modell nach Marcus gilt streng nur bei hohen Temperaturen, wenn $k_B T$ größer ist als die Energie der inneren Schwingungen der beteiligten Moleküle. Eine Erweiterung zum Marcus-Modell, die bei tieferen Temperaturen auch den steigenden Einfluss von quantenmechanischem Tunneln berücksichtigt, wird von Marcus, Levich und Jortner (MLJ) gegeben[77]. Die gesamte Reorganisationsenergie λ besteht aus zwei Teilen: einem internen molekularen Anteil λ_{int}, der die geometrische Relaxation von Donor- und Akzeptormolekül berücksichtigt, und einem polaronischen Anteil des umgebenden Lösungsmittels λ_S[78]:

$$\lambda = \lambda_S + \lambda_{int} \tag{9}$$

In dieser Erweiterung wird nun die vibronische Kopplung an den elektronischen Übergang quantenmechanisch mit dem Huang-Rhys-Faktor $S = \frac{\lambda_{int}}{\hbar\omega}$ berücksichtigt. Dabei meint ω die Moden der internen Vibronen[78] und λ_{int} den internen molekularen Beitrag der zugehörigen effektiven Mode $\hbar\omega$ zur Reorganisationsenergie. Die Rate nach Marcus-Levich-Jortner ergibt sich dann zu:

$$k_{ET} = \frac{{J_{DA}}^2}{\hbar}\sqrt{\frac{\pi}{\lambda_s k_B T}}\sum_{v=0}^{\infty}\frac{\exp(-S)\,S^v}{v!}\,exp\left[-\frac{(\Delta G_0 + \lambda_S + v\hbar\omega)^2}{4\lambda_S k_B T}\right] \tag{10}$$

Externe Phononen mit geringer Frequenz werden wie in der Marcus-Theorie weiterhin klassisch behandelt. In Abbildung 7b ist die Transferrate nach MLJ (gestrichtelte Linien) und nach Marcus (feste Linien) für verschiedene Temperaturen über $\Delta G_0 + \lambda$ aufgetragen. Besonders im inversen Marcus-Regime ist die Rate nach MLJ um Größenordnungen größer als die Rate nach Marcus und liefert eine bessere Übereinstimmung mit gemessenen Transferraten für organische Donor-Akzeptor Systeme[79] in diesem Bereich.

3.4 Nichtlineare optische Effekte

Bei hohen Laserintensitäten, wie sie kurzzeitig bei gepulsten Lasern auftreten, tragen zunehmend höhere Ordnungen der Suszeptibilität zur Polarisation in einem Medium bei. Die resultierende Polarisation ist dann nicht mehr nur proportional zur elektrischen Feldstärke sondern die nichtlineare Form der Polarisation[80]:

$$P_i = \varepsilon_0\left(\sum_j \chi_{ij}^{(1)}E_j + \sum_j\sum_k \chi_{ijk}^{(2)}E_jE_k + \sum_j\sum_k\sum_l \chi_{ijkl}^{(3)}E_jE_kE_l + \ldots\right) \tag{11}$$

muss betrachtet werden. Der Index i steht jeweils für die drei Raumrichtungen. Da die Polarisation *P* und das elektrische Feld *E* Vektorcharakter haben ist $\chi^{(1)}$ein Tensor 2. Stufe und $\chi^{(2)}$ein Tensor 3. Stufe usw. Es sei darauf hingewiesen, dass Gleichung (11) nur für Medien gilt, die verlustfrei und dispersionslos sind[81]. Damit nichtlineare Effekte sichtbar werden, also die zwei letzten Terme in Gl. (11) bedeutend werden, muss die Intensität sehr groß sein. Besonders hohe Intensitäten können nur mit sehr starken CW-Lasern wie etwa CO_2-Laser erreicht werden. Einfacher jedoch werden Spitzenintensitäten (im Bereich von einigen GW/cm^2) mit gepulsten Festkörperlasern wie Nd:YAG-Laser oder Titan-Saphir-Laser erreicht.

Ich konzentriere mich in erster Linie auf nichtlineare Effekte 2. Ordnung, da nur diese für die Messungen relevant sind. Zwei Effekte dieser Art sind die Summen- und Differenzfrequenzbildung. Beide lassen sich am einfachsten anhand virtueller Energieniveaus erklären. Eine altnernative Begründung basiert auf Störungsrechnungen am Modell des anharmonischen Oszillators[81]. Bei der Summenfrequenzbildung treffen Photonen der Frequenz $\omega_1$und ω_2 kollinear auf den nichtlinearen Kristall ohne Punktsymmetrie und es entsteht ein Photon der Frequenz $\omega_3 = \omega_1 + \omega_2$ (siehe Abb. 8a). In einem einfachen quantenmechanischen Bild werden die zwei eintretenden Photonen vernichtet und in einem einzelnen quantenmechanischen Prozess ein Photon der Frequenz ω_3 erzeugt.

3.4.1 Frequenzverdopplung (SHG)

Die Frequenzverdopplung ist ein Spezialfall der Summenfrequenzbildung bei der beide einfallenden Strahlen die gleiche Freuqenz haben. Nimmt man zwei ebene Wellen unterschiedlicher Frequenz für das komplexe elektrische Feld $\tilde{E}(t,x)$ des eintretenden Laserlichts in ein doppelbrechendes Medium ohne Punktsymmetrie an:

$$\tilde{E}(t,x) = E_1 \cdot e^{-i\omega_1 t} + E_2 \cdot e^{-i\omega_2 t} + c.c. \tag{12}$$

und setzt es in die Formel für die Polarisation (Gl 11) ein, so entstehen u.a. Terme die, die Summe und die Differenz beider Frequenzen beinhalten:

$$P(\omega_1 + \omega_2) = 2\varepsilon_0 \chi^{(2)} E_1 E_2 e^{-i(\omega_1+\omega_2)t} \tag{13}$$

$$P(\omega_1 - \omega_2) = 2\varepsilon_0 \chi^{(2)} E_1 E_2^* e^{-i(\omega_1-\omega_2)t}$$

Nehmen wir an die Frequenzen der einfallenden Wellen seien gleich, so entsteht aus dem Term mit der Summe einer mit der dopplten Frequenz 2ω, weshalb man auch von Frequenzverdopplung des Lichts (SHG) spricht. Damit es zur effizienten Konversion kommt, muss für beide Strahlen nicht nur die Energieerhaltung sondern auch die Impulserhaltung erfüllt sein. Das bedeutet, dass die Strahlen mit unterschiedlicher Frequenz aber gleicher Phase durch den Kristall propagieren. Dies ist nur für Kristalle möglich, die zwei unterschiedliche Brechungsindizes besitzen und daher doppelbrechend sind. Typischerweise läuft der Pumpstrahl entlang der Achse mit ordentlichem Brechungsindex und der Strahl mit

der dopptelten Frequenz entlang der außerordentlichen Achse. Nur für einen bestimmten Einfallswinkel des Pumpstrahls bezüglich der Kristallachse haben beide Strahlen die gleiche Phasengeschwindigkeit und die Konversionseffizienz ist maximal. Haben die Strahlen unterschiedliche Frequenzen und wählt man den Einfallswinkel entsprechend, so kann der Differenzterm verstärkt werden.

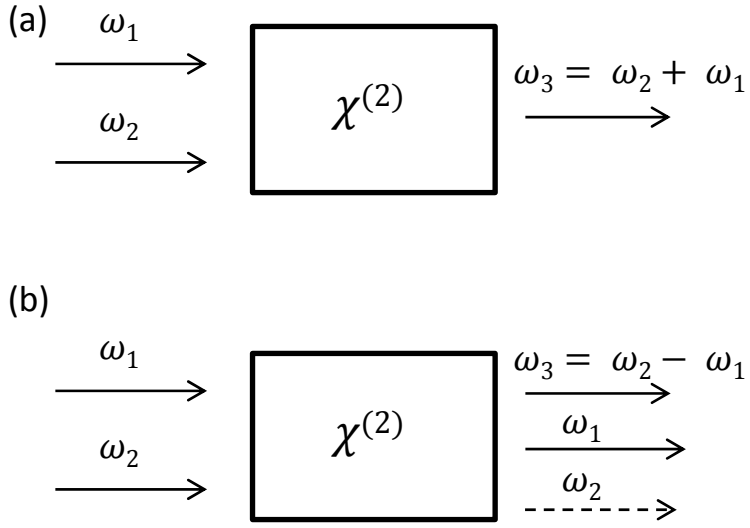

Abbildung 8: schematische Darstellung der (a) Summenfrequenzbildung und (b) Differenzfrequenzbildung.

3.4.2 Parametrische Verstärkung

Bei der Differenzfrequenzbildung wird neben dem Differenzterm der Term mit der niedrigeren Frequenz ω_1 auf Kosten des einfallenden Strahls mit der Frequenz ω_2 verstärkt. Dieser Prozess wird dann auch parametrische Verstärkung genannt und ist ebenfalls für die Messungen von Bedeutung. Da der Laserstrahl mit der höheren Frequenz eine besonders hohe Intensität haben muss, wird er typischerweise Pumpstrahl genannt ($\omega_2 = \omega_P$). Der einfallende Strahl mit der kleineren Frequenz hat dagegen zu Beginn nur eine relativ schwache Intensität und wird deshalb oft auch als „Seed"-Strahl bezeichnet ($\omega_1 = \omega_S$). Es muss dabei $\omega_P > \omega_S$ gelten. Somit lautet der Energieerhaltungssatz:

$$\omega_P = \omega_S + \omega_I. \tag{14}$$

Der ebenfalls entstandene Strahl mit der Differenzfrequenz wird auch als Hilfsstrahl, oder Idler-Strahl, mit der Frequenz $\omega_I = \omega_P - \omega_S$, bezeichnet.

Der entsprechende Impulserhaltungssatz lautet:

$$\vec{k}_p = \vec{k}_S + \vec{k}_I. \tag{15}$$

Es müssen sowohl Pump- als auch Seed-Strahl unter einem geeigneten Winkel bezüglich der optischen Achse zur Phasenanpassung auf den Kristall treffen. Im Falle eines normalen

optischen parametrischen Verstärkers fallen beide Strahlen kollinear auf den Kristall. Es gibt jedoch auch Verstärker (sogenannte NOPAs) die nicht-kollinear arbeiten.

Für dispersionslose und verlustfreie Medien (siehe *Kleinman-Symmetrie*), die in den hier betrachteten Anwendungen zum Einsatz kommen, kann der Tensor der nichtlinearen Suszeptibilität $\chi^{(2)}$ auch als 3x6-Matrix mit den Einträgen d_{il} geschrieben werden. Es gibt darüber hinaus einige weitere Symmetrien. Zwar werden in Gleichung 12 komplexe Felder betrachtet, aber die Polarisation $\vec{P}$ und das elektrische Feld $\vec{E}$ sind messbare Größen und damit rein reell. Daraus ergibt sich eine weitere Symmetrieeigenschaft für die Suszeptibilität, die die Anzahl unabhängiger Einträge d_{il} der Matrix einschränkt[80, 81].

3.4.3 Weißlichterzeugung

Um Absorptionseffekte zeitlich auflösen zu können, benötigt man Lichtpulse mit einem breiten Spektrum. Blitzlichtlampen zum Beispiel erreichen Pulsdauern im Bereich mehrerer Mikrosekunden. Für kürzere Pulsdauern nutzt man den nichtlinearen optischen Effekt der Selbstphasenmodulation. Damit dieser auftreten kann sind hohe Intensitäten nötig, die nur durch den optischen Kerr-Effekt erreicht werden. Er ist ein Effekt dritter Ordnung und basiert auf der Tatsache, dass der Brechungsindex allgemein intensitätsabhängig ist[81, 82]:

$$n(I) = n_0 + n_2 \cdot I^2 \tag{16}$$

n_0 ist der normale Brechungsindex für geringe Intensitäten und n_2 ist ein meist positiver Materialparameter, wodurch weniger intensives Licht zur optischen Achse hin gebrochen wird. Auf diese Weise kommt es zur Selbstfokussierung des eingestrahlten Laserpulses und zum weiteren Anstieg der Intensität. Es ist eine kritische Intensität P_{krit} nötig bei der Selbstfokussierung auftritt[81, 82]:

$$P_{krit} = \frac{\pi(0.61)^2\lambda_0^2}{8n_0n_2} \tag{17}$$

hierbei ist λ_0 die Zentralwellenlänge des Laserpulses. Die Phase des Laserstrahls hängt ebenfalls vom nichtlinearen Brechungsindex ab[80]:

$$\varphi = \omega\frac{l}{c}(n_0 + n_2 I) \tag{18}$$

Die zeitliche Phasenänderung $\Delta\varphi$ ist proportional zur Intensität. Somit ändert sich die momentane Frequenz ω_M innerhalb einer Zeitänderung Δt durch:

$$\omega_M = -\frac{\Delta\varphi}{\Delta t} \tag{19}$$

und es entstehen neue Wellenlängenanteile. Da der zeitliche Intensitätsverlauf sich durch den Kerr-Effekt ebenfalls ändert, ist der intensivere zentrale Teil des Pulses langsamer als der vordere und hintere Teil. Dieser Effekt wird auch „*Self-Steepening*“ genannt. Durch die

hohe normale Dispersion der meisten optischen Kristalle, die zur Weißlichterzeugung genutzt werden, läuft der blaue Anteil des erweiterten Spektrums langsamer durchs Medium als der rote Anteil. Bei zeitaufgelösten spektroskopischen Untersuchungen muss das durch eine Dispersionskorrektur berücksichtigt werden.

Durch den Effekt der Selbstfokussierung kommt es zu einem raschen Anstieg der Intensität und zum Auftreten weiterer nichtlinearer Effekte (Multiphotonenanregung, verstärkte Ramanstreuung etc.) abhängig von der Anfangsintensität des einfallenden Pulses. Es ist immer noch unklar, welche weiteren Effekte zur Weißlichterzeugung beitragen[83, 84] . Bei höheren Intensitäten werden je nach Bandlücke durch Multi-Photonen-Absorption Elektronen im Leitungsband angeregt und ein Plasma erzeugt[85], welches mit dem erzeugten Weißlicht in Wechselwirkung treten kann. Für eine genügend hohe Bandlücke sinkt die Wahrscheinlichkeit für diesen Prozess. Zu dem treten bei höheren Intensitäten mehrere Weißlichtkanäle (Multifilamente) auf, die zwar mehr Weißlichtintensität beitragen jedoch äußerst instabil sind, da sie untereinander interferieren. Das dadurch erzeugte Weißlichtspektrum ist sehr strukturiert und nur bedingt für die Spektroskopie geeignet[86]. Eine detaillierte Beschreibung des Einflusses verschiedener Effekte zur Weißlichterzeugung findet sich in der Diplomarbeit von Max Bradler[84].

3.5 Hybrides Perowskit Methylammonium-Bleiiodid

Während meiner Arbeit habe ich mich auch mit hybriden Perowskit-Materialien, insbesondere mit Methylammonium-Bleiiodid ($MAPbI_3$), beschäftigt. "Hybrid" meint dabei, dass es sich um eine Kombination aus organischen und anorganischen Komponenten handelt. Es bildet eine Perowskit-Struktur, welche in Abb. 9 gezeigt ist.

3.5.1 Eigenschaften hybrider Perowskite

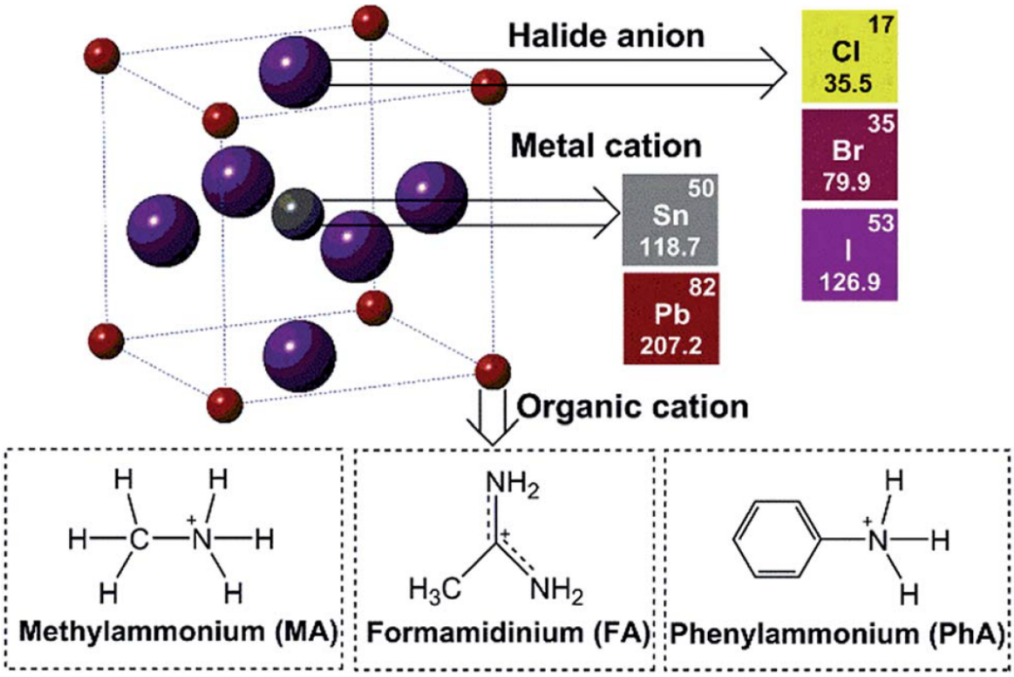

Abbildung 9: Schema der Einheitszelle einer Perowskit-Struktur. Aus [87] [Hsiao et al. J. Mater. Chem. A 2015, 3, 15372-15385] – Reprinted with permission of the Royal Society of Chemistry

Perowskite bezeichnen im allgemeinen Materialien mit einer ABX_3-Struktur und sind nach dem Mineralogen „Perovski“ benannt. In der Mitte der Einheitszelle sitzt das Blei-Kation, an den flächenzentrierten Seiten, sechs Iod-Ionen und auf den Ecken des Quaders sitzen acht Methylammonium (CH_3NH_3) Kationen. Viele Komponenten können ausgetauscht werden ohne, dass sich die prinzipielle Kristallstruktur ändert, z.B. durch Ionen mit anderen Ausdehnungen. Dadurch wird eine Variation der spektroskopischen oder optoelektronischen Eigenschaften möglich (siehe Abb. 9).

So wie viele Perowskit-Strukturen kommt auch $MAPbI_3$ für unterschiedliche Temperaturbereiche in drei Kristallstrukturen vor, die hauptsächlich durch eine Drehung des PbI_6 Oktaeders zustande kommen. Unterhalb von 160 K liegt $MAPbI_3$ in der orthorhombischen Phase vor, bei der alle Kantenlängen der Einheitszelle unterschiedlich lang sind. In der tetragonalen Phase (zwischen 160 – 330 K) ändern sich durch eine Drehung die Längen in der Ebene senkrecht auf die Drehachse. Dadurch sind sie kürzer als die

Kantenlänge entlang der Drehachse. Oberhalb von 330 K liegt $MAPbI_3$ in der kubischen Phase vor. In dieser sind alle drei Kantenlängen gleich lang[88].

$MAPbI_3$ wurde schon in den 70er Jahren von Weber u.a. untersucht[89], aber erst 2009 wurde gezeigt, dass Solarzellen aus $MAPbI_3$ Effizienzen von 9 % und mehr erreichen[6]. In den folgenden Jahren konnte durch Variation der Prozessierschritte und Änderung des Schichtaufbaus die Effizienz unter Laborbedingungen kontinuierlich weiter auf über 22 %[5] gesteigert werden. Neben der Solarzellanwenung hat sich gezeigt, dass hybride Perowskit-Strukturen sich auch für andere Anwendungen wie Leuchtdioden[90,91,92], UV- und Röntgendetektoren[93,94], Transistoren[95] oder für optisch gepumpte Laser[96] eignen. Ein wesentlicher Nachteil, der einer umfangreichen Kommerzialisierung dieses Materialtyps im Weg steht, ist der hohe Bleianteil. Da Blei als toxisch eingestuft ist, muss ein entsprechendes Recycling-Verfahren gefunden werden[97]. Ein Zweig der aktuellen Forschung in diesem Bereich versucht daher Blei durch andere Materialien wie etwa Zinn zu ersetzen[98]. Ein weiterer Aspekt ist die geringe Langzeitstabilität der Materialkomposition[99], die weiter verbessert werden muss um Marktreife zu erlangen. Ansätze können dafür im Schichtaufbau der Bauteile und der Prozessierungsschritte liegen, da diese einen hohen Einfluss auf die Stabilität haben[100,101], wie auch in Kapitel 10 verdeutlicht wird.

3.5.2 Opto-elektronische Eigenschaften von hybriden halogenen Perowskit-Strukturen

$MAPbI_3$-Perowskit lässt sich als klassischer anorganischer Halbleiter mit Valenz- und Leitungsband beschreiben, wie theoretische Berechnungen von $CH_3NH_3PbI_3$ der kubischen Phase zeigen[102] (siehe Abbildung 10). Dabei wird das Leitungsband hauptsächlich durch das 6s-Orbital des Bleis bestimmt und das Valenzband durch die 5p-Orbitale des Iods. Aufgrund des schweren Bleis muss bei der Berechnung des Leitungsbandes der Effekt der Spin-Orbit-Kopplung berücksichtigt werden, wodurch es zur Aufspaltung des Leitungsbandes kommt und die Bandlücke effektiv sinkt[88].

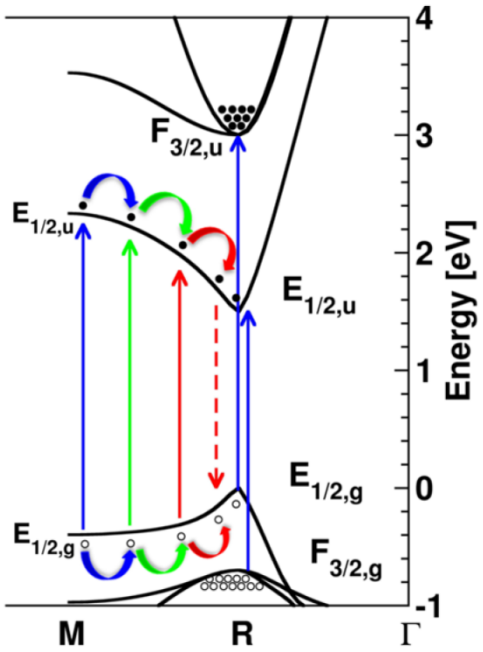

Abb. 10: Schema der Bandstruktur von $MAPbI_3$ in der kubischen Phase. Aus Referenz [102] Reprinted with permission from (Even et al. J. Phys. Chem. C 2014, 118, 11566). Copyright © (2014) American Chemical Society.

Abbildung 10 zeigt die Bandstruktur der kubischen Phase aufgetragen über die Symmetriepunkte des kubischen Gitters im k-Raum mit Γ=(0,0,0), R=(π/a, π/a, π/a) und M=(π/a, π/a,0), wobei a die Kantenlänge ist. Wie zu erkennen, ist $MAPbI_3$ eigentlich ein direkter Halbleiter, wodurch sich eine scharfe Absorptionskante bei etwa 1.6 eV (775 nm) ergibt (siehe Abb. 11a). Neuere Studien interpretieren die beobachteten Ladungsträgerdynamiken durch Eigenschaften eines indirekten Halbleiters, da zum einen eine geringe bimolekulare Rekombinationsrate sowie Absorption unterhalb der Bandkante beobachtet werden[103,104]. Durch die Verbindung der M und R-Punkte im k-Raum, relaxieren erzeugte Elektronen im Leitungsband und Löcher im Valenzband zum Minimum bzw. zum Maximum des R-Punktes im Bereich von wenigen 100 fs[102,105], wo es zur Emission kommen kann. Es ist allgemein hin akzeptiert, dass bei der Absorption direkt freie Ladungsträger erzeugt werden, da die Bindungsenergie für Exztonen im Bereich zwischen 10-50 meV[106, 107,102,108,109] liegt. Ist die thermische Energie kleiner als diese Coulombbindungsenergie zwischen dem erzeugten Elektron und Loch, kommt es zur Bildung eines Exzitons. Dies sieht man auch an einem Exzitonenpeak unterhalb der Bandlücke in Absorptionsspektren[106] bei tiefen Temperatauren. Auch mit steigender Anregungsdichte nimmt das Verhältnis von Exzitonen zu freien Ladungsträgern zu, da dann verstärkt Ladungsträger zu Exzitonen rekombinieren[106, 110].

Bei Raumtemperatur rekombinieren freie Ladungsträger radiativ oder nicht-radiativ, so dass die PL hauptsächlich dem Band-zu-Band-Übergang entspricht und daher ein bimolekularer Prozess ist[111]. Die Emission (Abb. 11a) in polykristallinen Filmen hat ihren Ursprung hauptsächlich an der Oberfläche der Kristallite. PL-Spektren aus dem inneren

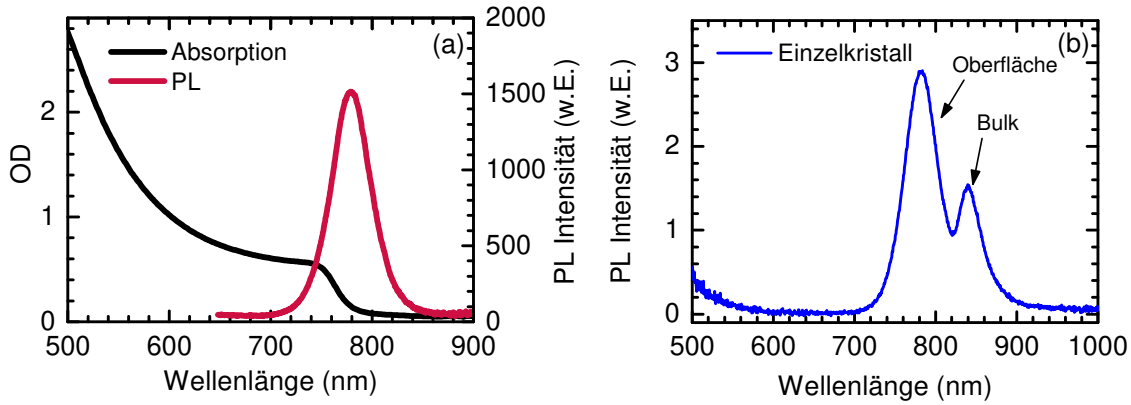

Abbildung 11: (a) Absorption- und PL-Spektrum eines $MAPbI_3$-Films bei Raumtemperatur, Anregung bei 485 nm (b) PL-Spektrum eines Einzelkristalls ($CH_3NH_3PbI_3$) angeregt mit 337 nm und etwa 80 µJ/cm². Die Messung wurde von Konstantin Schötz vom Lehrstuhl EP2 aufgenommen. Alle Spektren wurden bei Raumtemperatur aufgenommen.

Volumen der Kristallite sind im Vergleich dazu rotverschoben (siehe Abb. 11b). Dies lässt sich aus ortsaufgelösten PL-Daten sowie Messungen an Einzelkristallen ablesen[112,113].

Die Herstellungsmethode, der Filme sowie deren Qualität haben ebenfalls einen entscheidenden Einfluss auf die Anregungsdynamik, da es sich um polykristalline Systeme handelt und Größe und Reinheit der Kristallite von der Prozessierung der Filme abhängen. So zeigen Filme, die nicht mit Bleiiodid PbI_2 sondern mit Bleichlorid $PbCl_2$ als Edukt hergestellt wurden, in der Literatur oft als $CH_3NH_3PbI_xCl_{3-x}$ bezeichnet, allgemein eine deutlich höhere Quanteneffizienz ($\eta > 0.7$) der Photolumineszenz[96, 114] als Filme mit $CH_3NH_3PbI_3$ ($\eta \leq 0.2$)[115]. Jedoch zeigen Messungen zur Elementanalyse einen verschwindend geringen Chloranteil in der $MAPbI_3$-Struktur, da Chlor flüchtiger als PbI_2 ist und während der Filmbildung verdampft[116]. Ganz geklärt ist die Ursache für die unterschiedlichen Quanteneffizienzen jedoch nicht. Eine mögliche Ursache ist die beobachtete größere Dichte an nichtstrahlenden Fallenzuständen in Filmen ohne Bleichlorid[117].

Allgemein lässt sich die Dynamik der Ladungsträgerrekombination in polykristallinen Filmen durch drei Prozesse beschreiben[111], die bei jeweils unterschiedlichen Anregungsdichten dominieren. Bei geringen Anregungsdichten ($< 10^{15} cm^{-3}$) ist der Großteil der Elektronen in Fallenzuständen gefangen. Die Beschreibung gilt andersherum auch für gefangene Löcher. Die Dynamik der beobachteten PL wird bestimmt durch die nichtstrahlende Rekombination an Fallenzuständen[118] („Shockley-Read-Hall"-Mechanismus). Dann hängt die Rate in erster Ordnung von der Anregungsdichte ab und eine monoexponentielle Abklingkurve der PL wird beobachtet[110].

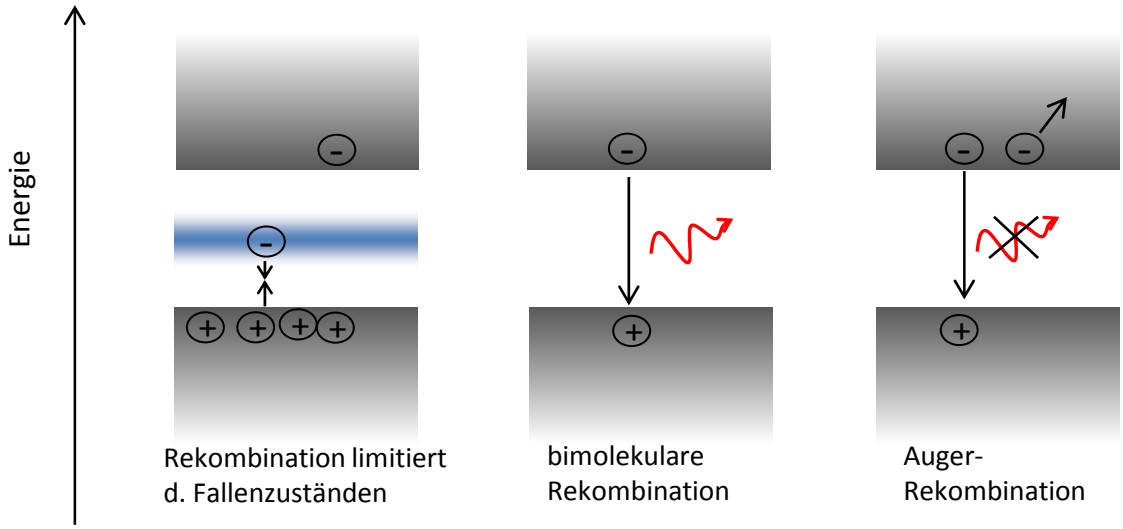

Abbildung 12: schematische Darstellung der möglichen Rekombinationsmechanismen in Perowskit-Filmen.

In Abbildung 12 ist dies schematisch dargestellt durch ein Elektron das auf einem Fallenzustand innerhalb der Bandlücke sitzt und einer größeren Anzahl freier Löcher gegenüber freien Elektronen. Allgemein ist das PL-Signal sehr langlebig im Vergleich zur typischen Exzitonenlebensdauer in organischen Halbleitern (<10ns). Dies liegt auch an der Reabsorption der emittierten Photonen innerhalb des Films. Wieder werden Ladungsträger generiert um später erneut zu rekombineren bis ein Photon die Oberfläche des Films erreicht. Dieser Effekt wird als Photonen-Recycling bezeichnet[119] und ist auch als „trivialer Transfer“ bekannt[59].

Im Anregungsbereich zwischen $10^{15} cm^{-3}$ und $10^{17} cm^{-3}$ wird die Dynamik hauptsächlich durch bimolekulare radiative Rekombination dominiert, so dass die Rate vom Quadrat der Anregungsdichte abhängt und somit der Intensitätsverlauf einem Potenzgesetz folgt. Er kann nicht mehr mit einer einfachen Exponentialfunktion beschrieben werden. Gleichzeitig steigt auch die Quanteneffizienz mit der Intensität[96, 114]. Bei höheren Anregungsdichten nimmt die Auger-Rekombination zu. Dies ist ein Prozess dritter Ordnung. Das heißt, die Rate hängt von der dritten Potenz der Anregungsdichte ab. Er beschreibt die nichtstrahlende Rekombination eines Elektrons aus dem Leitungsband und eines Lochs aus dem Valenzband, wobei die Energie und der Impuls des Elektron-Loch-Paares auf ein zweites Elektron im Leitungsband übertragen wird. In der transienten PL macht sich dies durch einen schnellen Abfall, typischerweise unterhalb von 1 ps bemerkbar. Da der Prozess ein zusätzlicher nicht-radiativer Verlustkanal ist, sinkt entsprechend auch die PL-Quanteneffizienz[114].

4 Aufbau eines Setups zur transienten Absorptionsspektroskopie

4.1 Einführung in die transiente Absorptionsspektroskopie

Pump-Probe-Spektroskopie (Transiente Absorption) basiert auf der linearen Absorptionsspektroskopie, wobei die absorbierte Lichtintensität mit dem Lambert-Beer'schen Gesetz beschreibbar ist. Der Absorptionskoeffizient α_0 hängt linear von der Anzahl absorbierender Moleküle (Chromophore) bzw. von deren beitragenden elektronischen Zuständen i und der Dichte N der absorbierenden Chromophore ab:

$$\alpha_0(v) = \sum_i \sigma_i(v) N \tag{20}$$

σ_i ist hierbei der Absorbtionsquerrschitt aus dem Grundzustand in den Zustand i. Die Transmission ergibt sich dann zu:

$$T(v) = \frac{I(v)}{I_0(v)} = e^{-\alpha_0(v)d} \tag{21}$$

dabei ist $I(v)$ die transmittierte, $I_0(v)$ die eingestrahlte Intensität und d die Dicke der Probe. Wird die Probe angeregt, ändern sich die Besetzungszahlen N_i bzw. N_j und damit auch $\alpha_0(v)$:[120]

$$\Delta\alpha(v) = \textstyle\sum_{ij} \sigma_{ij}(v)(\Delta N_i - \Delta N_j). \tag{22}$$

Im Messsignal äußert sich dies durch eine geänderte Transmission:

$$\Delta OD(v) = \frac{d}{ln10}\Delta\alpha(v) = \frac{d}{ln10}(\alpha_1(v) - \alpha_2(v)) \tag{23}$$

$$-\frac{\Delta T}{T} = \frac{e^{-\alpha_1(v)d} - e^{-\alpha_2(v)d}}{e^{-\alpha_1(v)d}} = e^{-(\alpha_1-\alpha_2)d} - 1 \tag{24}$$

Mit Hilfe der Maclaurin'schen Näherung der Exponentialserie für kleine Argumente des Exponenten, wobei höhere Terme vernachlässigt werden, ergibt sich:

$$-\frac{\Delta T(v)}{T(v)} = \Delta\alpha(v)d = ln10 \cdot \Delta OD(v) \tag{25}$$

Bei zeitaufgelöster transienter Absorption ist die Transmission aufgrund der finiten Lebensdauer der angeregten Zustände in der Probe auch zeitabhängig. Man benötigt kurze Laserpulse mit Pulsdauern im Bereich von wenigen hundert Femtosekunden sowohl für Pump- als auch Abfragepuls, um Veränderungen in diesem Zeitbereich auflösen zu können.

Ein Pumppuls verursacht eine kleine zeitabhängige Änderung der Absorption $\Delta\alpha(t)$. Diese lässt sich als Konvolution aus dem Pumppuls und der zeitabhängigen Antwortfunktion $A(t)$ der Probe auffassen: $\Delta\alpha(t) = \int_{-\infty}^{t'} I_{pump}(t')A(t-t')dt'$. Ziel des Experiments ist die Bestimmung dieser Antwortfunktion. Dazu nutzt man aus, dass sich die Transmissionsintensität eines Abfragepulses $I_{Abfrage}$, der durch die Probe läuft, ändert. Für kleine Änderungen $\Delta\alpha$ kann man durch Näherung der Exponentialfunktion zeigen[120], dass sich die Intensitätsänderung angeben lässt mit:

$$\Delta I_{Abfrage}(t) \approx -I_{Abfrage}(t)e^{-\alpha d}\Delta\alpha(t)d \qquad (26)$$

wobei *d* die Dicke der Probe ist. Das Messsignal wird häufig in der Darstellung $-\frac{\Delta T}{T}$ angegeben.

Signale in der photoinduzierten Absorptionsspektroskopie

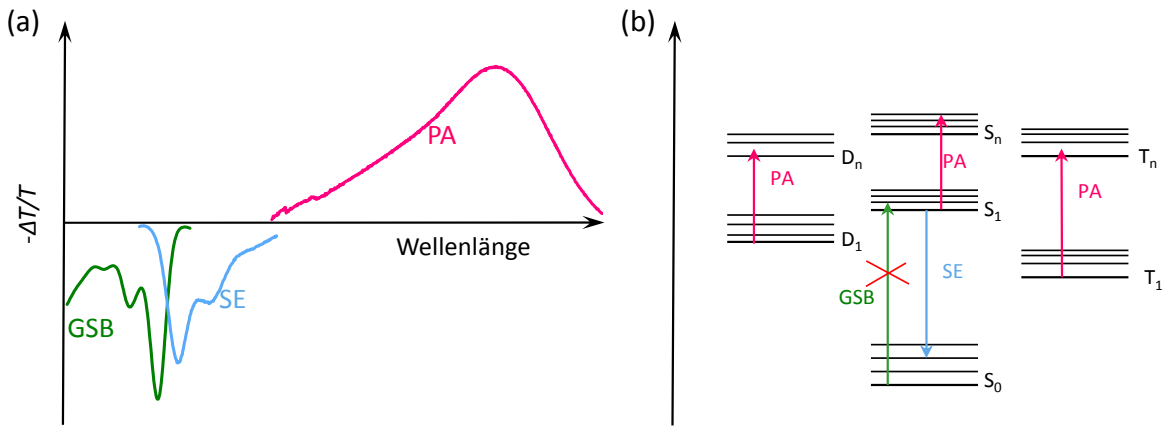

Abbildung 13: (a) schematische Darstellung eines typischen transienten Absorptionsspektrums als Funktion der Wellenlänge. Beiträge der photoinduzierten Absorption (PA), des Ground State Bleach (GSB) und der stimulierten Emission (SE) sind entsprechend gekennzeichnet, (b) Energieschema möglicher Übergänge von Singulett-, Triplett- und Dublettzuständen (Polaron) in organischen Halbleitern angedeutet durch Pfeile.

Transiente Absorptionsspektren zeigen charakteristische Merkmale (spektrale Banden). Im spektralen Bereich der Grundzustandsabsorption tritt in Transmission ein negatives Signal auf, das vom Verlauf her dem Absorptionsspektrum ähnelt aber entgegengesetztes Vorzeichen hat. Es entspricht der fehlenden Absorption von Molekülen, die nach der optischen Anregung nicht im Grundzustand sind sondern sich in einem angeregten Zustand befinden. Es wird daher auch „Ground State Bleach“ GSB genannt (grüne Linie in Abb. 13a). Im spektralen Bereich der PL erscheint in der Darstellung $-\Delta T/T$ ein negatives Signal, falls das zu untersuchende Material eine gewisse PL-Quanteneffizienz besitzt. Das Signal entpricht nahezu dem Verlauf des PL-Spektrums. Es entsteht durch Stimulation des radiativen Übergangs vom angeregten in den Grundzustand durch ein einfallendes Photon

mit der Energie, die etwa der des Übergangs entspricht. Das entsprechende Signal in transiente Absorptionsspektren wird deshalb auch stimulierte Emission (SE) (blaue Linie in Abb. 13a) genannt. Photoinduzierte Absorptionssignale (PA) haben dagegen in dieser Darstellung ein positives Vorzeichen, da sie durch den Anregepuls hervorgerufen werden und somit mehr Licht absorbieren als vor der Anregung. Dies können Übergänge von angeregten Zuständen wie z.B. Singulett-, Triplett- oder Dubletts (Polaronzuständen) zu entprechend energetisch höheren Zuständen sein (siehe schematische Abbildung 13b). Absorption von Polaronen und Singuletts liegen für viele konjugierte Polymere im NIR-Bereich bis 2 µm, weshalb entsprechende Anforderungen an das Weißlicht der Abfragepulse gestellt werden.

4.2 Aufbau zur transienten Absorptionsspektroskopie

Da in der ersten Phase meiner Promotion der Aufbau einer Messanordnung zur transienten Absorption von organischen Materialien im Vordergrund stand, wird in diesem Kapitel dieser Messaufbau näher beschrieben. Am Ende des Kapitels wird die Funktionstüchtigkeit anhand von Beispielmessungen verdeutlicht. In Abb. 14 ist der Messaufbau schematisch dargestellt.

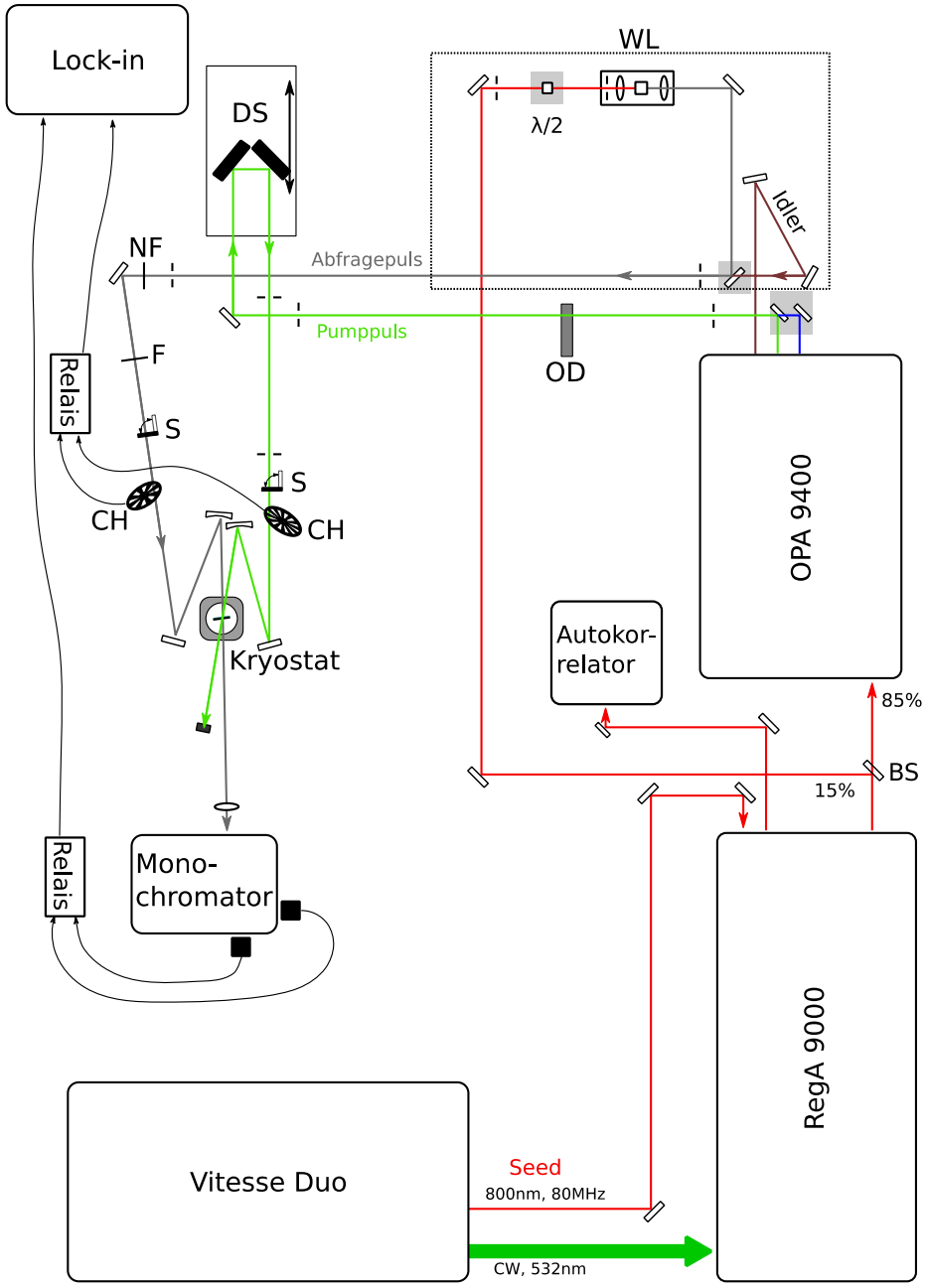

Abbildung 14: Schematische Darstellung des entwickelten Aufbaus zur Transienten Absorption mit Erweiterungen der Weißlichterzeugung durch S. Wedler (Lehrstuhl EP2), BS: Strahlteiler, $\lambda/2$: Lambda-Halbe-Platte, CH: Chopperrad, S: Schutter, F: Filter, NF: Notch-Filter 800 nm, WL: Weißlichtschiene, DS Verzögerungsschiene (Schema ist adaptiert aus der Masterarbeit von Stefan Wedler [121])

Die transiente Absorptionsspekroskopie nutzt eine Reihe verschiedener nichtlinearer Effekte aus, für die hohe Spitzenleistungen, also hohe Pulsenergien, benötigt werden. Diese werden mit einem regenerativen Laserverstärker („RegA9000“, *Coherent Inc*.) erzeugt, welcher von einem „Vitesse Duo“ Laserkopf (ebenfalls *Coherent Inc*.) gepumpt wird. Dieser beinhaltet einen Titan-Saphir Oszillator („Vitesse“) und einen frequenzverdoppelten Nd:YAG-Laser („Verdi“) im Dauerstrichmodus. Die Funktionsweise eines regenerativen Verstärkers wird in Abschnitt 5.3 erläutert. Der Oszillator erzeugt die Seed-Pulse mit einer Wellenlänge von 800 nm mit einer Repetitionsrate von 80 MHz und einer Leistung von etwa 140 mW. Der Laser emittiert bei einer Zentralwellenlänge von 532 nm eine Leistung von etwa 10 W. Im RegA9000 wird einer aus 800 Pulsen verstärkt, so dass die Repetitionsrate auf 100 KHz sinkt. Der Verstärker erzeugt Pulsenergien zwischen 6.5 und 6.8 µJ bei 100 kHz. Die Wellenlänge des Vitesse kann im Bereich zwischen ca. 700 bis 1000 nm variiert werden. Ich habe diese zu 800 nm gewählt, da hier die Leistung, des Titan:Saphir maximal ist. Eine Änderung der Wellenlänge würde eine komplette Neujustage des Verstärkersystems erfordern.

Am elektronischen Regler lässt sich die Repetitionsrate im Bereich zwischen 20-300 kHz problemlos ändern, ohne dass sich der optische Strahlengang ändert. Damit ist es im Vergleich zu gängigen 1 kHz-Verstärkersystemen hochrepetierend, wodurch kürzere Messzeiten ermöglicht werden. Das bedeutet es können auch Proben vermessen werden, die eine geringere Langzeitstabilität aufweisen, da 100 mal schneller gemittelt wird. Ich habe 100 kHz statt 300 kHz gewählt, da das Verstärkersystem bei geringerer Repetionsrate eine höhere Pulsenergie hat, die für alle nachfolgenden nichtlinearen optischen Prozesse entscheidend ist.

Etwa 15 % der Verstärkerleistung werden mit einem Strahlteiler vor dem OPA abgezweigt und über mehrere Spiegel zur externen Weißlichterzeugung genutzt (siehe Abb. 14). Die restliche Leistung wird im „OPA 9400“ (*Coherent Inc*.) für das Pumpsignal genutzt. Die externe Erzeugung des Weißlichts wurde entscheidend von Stefan Wedler im Rahmen seiner Masterarbeit verbessert. Dies betrifft u.a. die stabile Anordnung der einzelnen Komponenten der Weißlichteinheit, gekennzeichnet durch den gestrichelten Rahmen in Abbildung 14, wodurch die Reproduzierbarkeit des Strahlenganges zur Weißlichtgenerierung entscheidend verbessert wurde. Des Weiteren wurde auch der Strahlengang vom Abfragestrahl dahingehend geändert, dass der Idler-Strahl aus dem OPA alternativ zum Weißlicht als Abfragepuls verwendet werden kann. Dies ist für einige Messungen unabdingbar, da der Idler-Strahl weiter in den NIR-Bereich (bis 2000 nm) reicht. Eine detailiertere Beschreibung mit Abbildungen zum Umbau findet sich in der Masterarbeit von Stefan Wedler [121]. Der abgezweigte Teil der Verstärkerleistung für die Weißlichterzeugung muss hinsichtlich der Pulsenergie genau kontrolliert werden um ein stabiles Weißlicht zu erreichen. Vor der Weißlicht-Einheit kann ein $\lambda/2$-Plättchen für 800 nm in den Strahlengang gebracht werden um die Polarisation zwischen Pump- und Weißlicht-Abfragestrahl einzustellen. Standardmäßig wird der „magische“ Winkel von 54.7° eingestellt, um Polarisationsdynamiken bei Messungen in Lösung zu reduzieren[55, 122].

Die eigentliche Weißlichteinheit besteht aus einem undotierten YAG-Kristall, in dem das Weißlicht entsteht, und zwei Linsen nämlich eine mit 5 cm Brennweite zum Fokussieren und eine mit 3 cm Brennweite um den Laserstrahl dahinter zu kollimieren. Auf die besonderen Bedingungen der Weißlichterzeugung wird in Kapitel 4.6.3 näher eingegangen. Das erzeugte Weißlicht passiert einen 800 nm-Notchfilter, um den nicht konvertierten Anteil vom restlichen Weißlicht zu trennen. Danach wird der Abfragestrahl mit einem mechanischen Chopper moduliert (ca. 220Hz) und mit einem Fokussierspiegel der Brennweite 30 cm auf die Probe fokussiert. Wahlweise kann ein Tiefpassfilter, der nur Wellenlängen oberhalb von 850 nm durchlässt, für Messungen im NIR oder ein IR-Filter („Calflex™“, Kantenfilter bei 750 nm) für Messungen im sichtbaren Bereich eingesetzt werden. Durch die Filter wird jedoch der effektive messbare Bereich des Weißlichts eingeschränkt, so dass der Bereich zwischen 750 nm und etwa 900 nm um die zentrale Wellenlänge des regenerativen Verstärkers effektiv nicht genutzt werden kann. Der transmittierte Weißlichtstrahl hinter der Probe wird mit einer weiteren Linse in einen Gitterspektrographen (Andor SR193) eingekoppelt und so das Signal entweder mit einer Silizium-Diode für den sichtbaren (450-1000 nm) oder einer InGaAs-Diode für den nahinfraroten (1000-1500 nm) Wellenlängenbereich selektiv detektiert.

Mit dem OPA, wie in Abschnitt 4.4 detailiert beschrieben, können Wellenlängen zwischen 490 und 700 nm zum Anregen gewählt werden. Alternativ kann die zweite Harmonische des Verstärkers (400 nm) ausgekoppelt und zur Anregung genutzt werden. Spiegel auf magnetischen Halterungen erleichtern die Auswahl der gewünschten Anregungsenergie (siehe Abb. 14)

Für die Steuerung des zeitlichen Abstandes zwischen Anrege- und Abfragepuls wird der Pumpstrahl über eine steuerbare Verzögerungstrecke (DS) mit Retroreflektoren geführt. Die Strecke wird von einem Schrittmotor angetrieben und vom Messprogramm gesteuert. Die Anregungsdichte kann über ein OD-Filterrad variiert werden.

Anschließend wird der Pumpstrahl mit einem zweiten Chopperrad moduliert und ebenfalls mit einem Fokussierspiegel (30 cm) räumlich mit dem Weißlicht-Abfragestrahl zum Überlapp gebracht. Besonders kritisch ist die Justage über die Retroreflektoren entlang der Verzögerungsstrecke, da deren Position nicht die Position des Fokuspunktes auf der Probe beeinflussen darf. Durch einen portablen Spiegel, der in den Strahlengang hinter der Verzögerungsstrecke gebracht wird, kann die Positionstreue in weiter Ferne an einer Laborwand überprüft werden. Mehrere Irisblenden im Strahlengang vereinfachen die Justage des Pumpstrahls (vergleiche Abb. 14).

4.3 Funktionsweise des regenerativen Verstärkers

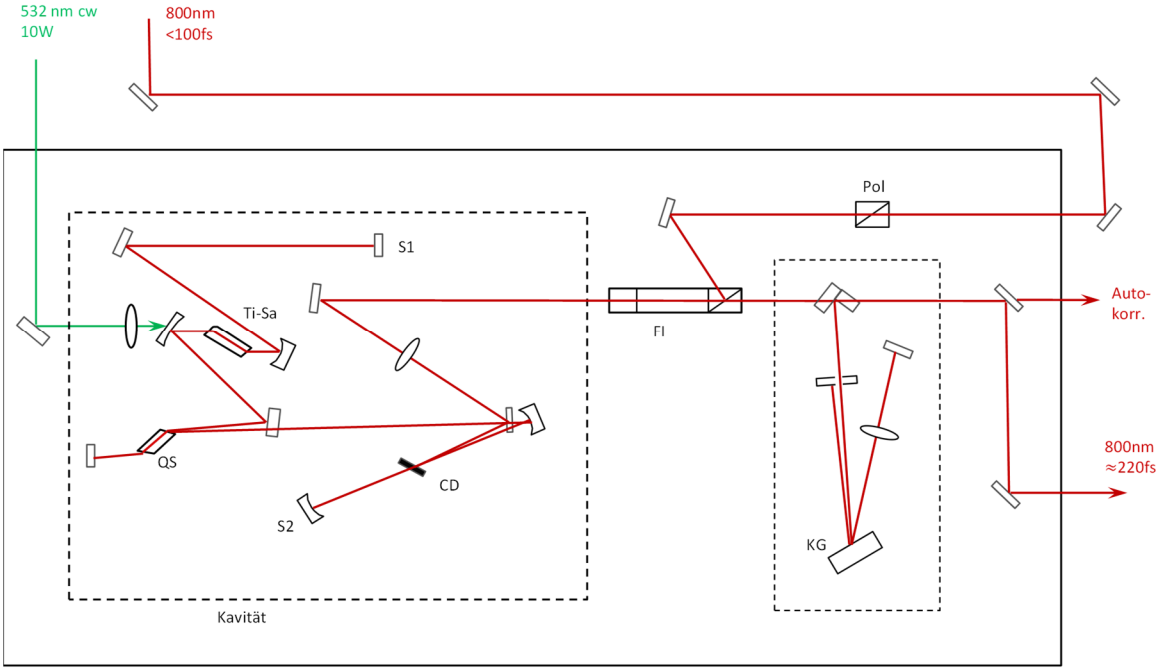

Abbildung 15: Schema des verwendeten regenerativen Verstärkers (nach Handbuch RegA9000, *Coherent Inc.*) Die verwendeten Abkürzungen werden im Text erklärt.

Der in Abbildung 15 gezeigte Verstärker arbeitet wie ein Laser. Er hat zwei Kavitätsendspiegel (S1 und S2), zwischen denen die Pulse hin und her laufen. Über Injektionsspiegel (siehe Abb. 15) werden die Seed-Pulse des Oszillators über einen Faraday-Isolator (FI) in die Verstärker-Kavität geleitet. Das aktive Medium des Verstärkers ist ein Titan:Saphir-Kristall (Ti:Sa). Der dort ablaufende Verstärkungsprozess wird durch den Nd-YAG Laserstrahl (10W) gepumpt. Ein akustooptischer Modulator (CD) selektiert einen aus 800 Seed-Pulsen und injiziert diesen in die Kavität. Ein weiterer akustooptischer Modulator (QS) verhindert Lasing, solange kein Puls in der Kavität ist. Hierducht wird die nötige Besetzungsinversion im Ti:Sa für den Verstärkungsprozess gewährleistet. Die elektronische Abstimmung beider Modulatoren wird über den Regler gesteuert. Beide Modulatoren erfüllen noch eine weitere Aufgabe während des Verstärkungsprozesses. Sie bestehen aus TeO_2, welches einen sehr hohen Dispersionskoeffizienten (868 fs^2/mm [123]) hat. Hierdurch nimmt die Pulsbreite pro Umlauf zu, so dass bei zunehmender Pulsenergie die Spitzenleistung unterhalb der Zerstörschwelle des Verstärkermediums bleibt. Nachdem die verstärkten Pulse vom „Cavity Dumper“ (CD) aus der Laserkavität ausgekoppelt werden, werden sie mit einem Gitter (KG) auf etwa 220 $fs^{(ac)}$ komprimiert. Durch Verkippen der Linse nach dem Gitter und Verfahren des Abstandes des Gitters zur Linse kann der Gangunterschied zwischen röteren und blaueren Anteilen genau eingestellt werden um die Pulsbreite zu minimieren. Die Gitterkompression kann allerdings nicht Dispersionseffekte höherer Ordnungen kompensieren. Die Pulse bleiben daher immer breiter als das mögliche Fourierlimit, wie in Kapitel 4.6 gezeigt wird. Mit einem Auskoppelspiegel nach dem

Kompressionsgitter (siehe Abb. 15), der etwa 1 % der Leistung transmittiert, kann mit einem Autokorrelator (APE) die Pulsbreite überwacht werden.

4.4 Erzeugung durchstimmbarer Anregepulse durch parametrische Verstärkung

Die Pumppulse werden im parametrischen Verstärker „OPA9000“ (Coherent) generiert. Der nicht-abgezweigte Teil der Verstärkerleistung hinter dem Strahlteiler (BS) wird mit einem weiteren Strahlteiler im OPA in 25 % und 75 % aufgeteilt. Der Hauptteil (75%) wird in einem β-Bariumborat-Kristall (BBO) auf $\lambda = 400\,nm$ frequenzverdoppelt und zum Pumpen des OPA-Prozesses verwendet. Die verbleibende Leistung (25%) erzeugt ein Weißlicht in einem Saphirkristall. Dieses dient als Seed-Strahl für den Verstärkungsprozess. Der frequenzverdoppelte Strahl (400 nm) und das Weißlicht werden für den ersten OPA-Prozess in einem weiteren BBO-Kristall räumlich zum Überlapp gebracht. Der zeitliche Überlapp wird durch einen Retroreflektor im Weißlichtstrahlengang justiert. In einem zweiten Verstärkungsschritt werden beide Strahlen erneut im BBO-Kristall zum Überlapp gebracht und der zeitliche Überlapp mit einem weiteren Retroreflektor eingestellt. Die maximal erreichbare Leistung des OPAs ist wellenlängenabhänig, da das Weißlicht spektral begrenzt ist und auch die Konversionseffizienz vom BBO-Kristall limitiert ist. Dies liegt daran, dass die Phasenanpassung, also die Impulserhaltung, nicht für alle Wellenlängen erfüllbar ist.

Der auswählbare Bereich für das Pumpsignal erstreckt sich von 480-720 nm. Typische Leistungen liegen im Bereich 5-15 mW bei 100 kHz, je nach eingestellter Wellenlänge. Der Verstärkungsprozess ist äquivalent zur Differenzfrequenzerzeugung (siehe Kapitel 3.4). Somit entsteht neben dem Signalstrahl noch ein Idler-Strahl, dessen Photonenenergie der Differenz des frequenzverdoppelten Strahls und des Signalstrahls entspricht.

4.5 Messverfahren

Das Chopperrad für den Pumpstrahl moduliert diesen mit 750 bis 850 Hz. Nach dem Fokussierspiegel treffen die Pumppulse auf die Probe und regen diese an. Der Chopper des Abfragestrahls moduliert das Weißlicht mit einer Frequenz zwischen 200 und 250 Hz. Beide Strahlen überlappen räumlich am Ort der Probe. Ein Teil der Weißlichtintensität wird von der Probe transmittiert und trifft auf den Monochromator. An dessen Ausgang misst eine Photodiode die Transmission.

Deren Photostrom wird mit einem analogen Verstärker in ein Spannungssignal gewandelt und an den Lock-in-Verstäker weitergegeben. Für die Messung der induzierten Transmissionsänderung $\Delta T(\lambda)$ wird die Referenzfrequenz des Pump-Choppers als Referenz verwendet. Diese Messung wird mehrmals wiederholt und der Mittelwert gebildet, um Rauschen des Signals zu minimieren. Die Transmissionsmessung $T(\lambda)$ für die eingestellte Wellenlänge erfolgt jeweils gleich nach der ΔT-Messung, und es wird die Referenzfrequenz des Abfrage-Choppers benutzt. Der Grund ist, dass das Weißlicht innerhalb mehrerer Sekunden schwanken kann, was hauptsächlich an der Ausgangsleistung des regenerativen

Verstärkers liegt. Daher sollte zwischen beiden Messungen nicht mehr als ein paar Sekunden liegen. Eine parallele Messung beider Signale ist aus technischen Gegebenheiten nicht möglich. Eine Relaisbox steuert, welches der Referenzsignale an den Lock-in-Verstärker gegeben wird (siehe *Relais*, in Abb. 14). Das Schwanken der Verstärkerleistung beeinflusst auch die Pumppulse des OPAs, weshalb gegebenenfalls mit einer externen Diode die Intensität des Pumpstrahls überwacht und das ΔT-Signal anschließend korrigiert werden kann. Bei der Aufnahme eines Spektrums wird die Wellenlänge geändert und der Messvorgang wiederholt sich. Stark emittierende Proben können Artefakte im Messsignal erzeugen, daher kann im Messprogramm für die momentane Wellenlänge eine PL-Korrektur durchgeführt werden, was von Stefan Wedler nachträglich eingerichtet wurde (siehe MA, Stefan Wedler[121]). Dabei wird nach der Messung für $\Delta T(\lambda)$ und der Transmission $T(\lambda)$ zusätzlich die PL beziehungsweise das Streulicht der Anregung gemessen, indem der Shutter im Weißlichtstrahlengang geschlossen wird und die Probe nur mit dem Pumpstrahl angeregt wird. Als Referenz dient entsprechend der Pump-Chopper. Das Messsignal in der häufig verwendeten Darstellung der Transmissionsänderung ergibt sich dann zu:

$$-\frac{\Delta T^{korr}(\lambda,t)}{T(\lambda)} = -\frac{\Delta T^{unkorr}(\lambda,t) - PL(\lambda,t)}{T(\lambda)}. \tag{27}$$

Wie bererits erwähnt, muss bei der Änderung der Wellenlänge noch die Verzögerungsstrecke entsprechend einer Dispersionskurve nachgezogen werden um ein Spektrum bei konstanter Zeitverzögerung aufzunehmen können. Die Dispersion, also der zeitliche Versatz von blauem und rotem Anteil des Weißlichts entsteht größtenteils während der Erzeugung des Weißlichts im YAG-Kristall. Der Einfluss der Probe und anderer optischer Komponenten ist dagegen gering. Zur Korrektur ist der genaue Verlauf einer Dispersionskurve erforderlich. Man nutzt häufig kohärente Effekte in verschiedenen Materialien, wie z.B. in Lösungsmitteln, zur Aufnahme einer solchen Dispersionskurve aus[124]. Eine spektroskopische Anforderung an diese Materialien ist, dass das Signal im gesamten spektralen Bereich instantan, also schneller als die zeitliche Auflösung des Messaufbaus, auftritt. In reinen Lösungsmitteln ist die Signalstärke nur sehr schwach, weshalb auch oft der Anstieg bekannter Signale in Farbstoffen verwendet wird. Näheres zur Aufnahme der Dispersionskurve wird im nächsten Abschnitt erläutert.

4.6 Charakterisierung des Setups

In diesem Teilkapitel sind einige Charakterisierungsmessungen aufgeführt, die teilweise während der Einrichtung des Messaufbaus gemacht wurden. Sie dienen dazu die Limitierungen des Setups aufzuzeigen. Es ist notwendig Messungen an bekannten Materialsystemen durchzuführen und mit Ergebnissen in der Literatur oder anderen Messmethoden zu vergleichen. Diese finden sich in Abschnitt 4.6.5.

4.6.1 Pulscharakterisierung nach dem regenerativen Verstärker

Die zeitliche Auflösung des Messsignals hängt hauptsächlich von der Pulsform des RegA9000 Verstärkers ab, weshalb sie regelmäßig mit einem Autokorrelator überwacht wird. Abbildung 16 zeigt einen typischen Puls des Verstärkers. Eine gängige Annahme für die Pulsform ist eine Gaußglocke. Durch einen Fit und den daraus erhaltenen Parametern kann die Zeitauflösung quantifiziert werden. Das Autokorrelationssignal ist breiter als die eigentliche Pulsform[82]:

$$\sqrt{2} \cdot \tau_{FWHM}(Gauß) = \tau_{FWHM}(ac) \tag{28}$$

Der Faktor $\sqrt{2}$ ist ein Dekonvolutionsfaktor und hängt von der Pulsform ab. $\tau_{FWHM}(Gauß)$ und $\tau_{FWHM}(ac)$ meinen die volle Breite bei halber Höhe des maximalen Intensitätswertes für die Gaußförmige Pulsform bzw. des gemessenen Autokorrelationssignals. Die Pulsform in Abbildung 16 ist nahezu gaußförmig und die zeitliche Pulsbreite kann mit $\tau_{FWHM}(ac) = 219 \pm 2fs$ angegeben werden. Üblich ist auch die Annahme einer $sech^2$-Funktion. Ein Vergleich zwischen Fits eines typischen Pulses mit Sekans-Hyperbolikus-Funktion bzw. Gaußfunktion findet sich in der Masterarbeit von Stefan Wedler[121].

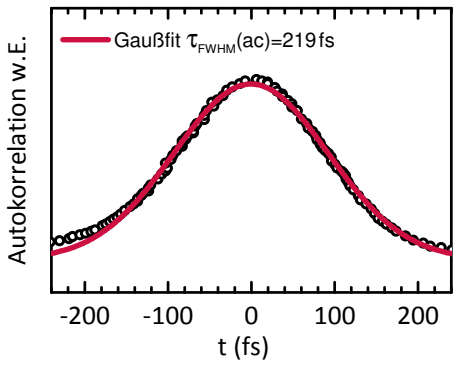

Abbildung 16: Zeitliche Pulsform des RegA9000, gemessen mit einem Autokorrelator, APE

Neben der zeitlichen Pulsbreite des Verstärkers ist die Leistung das entscheidende Kriterium für alle nachfolgenden nichtlinearen optischen Prozesse. Diese wird mit einem *FieldMate* Leistungsmessgerät der Firma *Coherent* gemessen. Es hat sich gezeigt, dass die Stabilität des Weißlichts bei Leistungen unterhalb von 620 mW schwankt. Daher muss in diesem Fall die Ausgangsleistung des Verstärkers durch Feinjustage wiederhergestellt werden. Bei der eingestellten Repetitionsrate von 100 kHz werden so 6.2 bis 6.8 μJ Pulsenergie erreicht.

4.6.2 Charakterisierung der OPA-Pulse

Die Pulsbreite des Pumpsignals nach dem OPA hängt maßgeblich von der Pulsbreite des RegA9000 Verstärkers (800 nm) ab. Die Messung des Signalstrahls des OPAs mittels Autokorrelator erfordert einen größeren Justage-Aufwand und wird daher nicht regelmäßig

durchgeführt. Der verwendete Autokorrelator (*APE*) nutzt einen BBO-Kristall zur Frequenzverdopplung. Dieser Prozess ist nur in einem bestimmten Wellenlängenbereich möglich. Um die Pulsbreite des OPA-Signals messen zu können, sollte die Wellenlänge zwischen 650-1000 nm liegen. Eine Messung der Frequenzverdoppelten (400 nm) ist mit dem BBO-Kristall daher nicht möglich. Die Pulsbreite kann aber mit dem Fourierlimit abgeschätzt werden.

Für einen angenommenen gaußförmigen Puls ist das Produkt aus Pulsdauer τ_P und Wellenlängenbandbreite $\Delta\lambda$:[80, 82]

$$\Delta\lambda \cdot \tau_P \geq 0.441 \cdot \frac{\lambda^2}{c} \tag{29}$$

Die kleinste Pulsbreite kann für fourier-limitierte Pulse erreicht werden. In Abbildung 17a ist die Autokorrelationsfunktion des OPA-Signals bei 635 nm gezeigt. Sie wurde mit Unterstützung von Stefan Wedler bei der Justage aufgenommen. Ein Fit mit einer Gaußkurve ergibt eine zeitliche Länge von $\tau_P = \frac{\tau_{FWHM}(ac)}{\sqrt{2}} = 134 \pm 4\, fs$. In Abbildung 17b sind die Spektren der Frequenzverdoppelten bei 400 nm und des Signals bei 635 nm normiert aufgetragen und um die zentrale Wellenlänge verschoben.

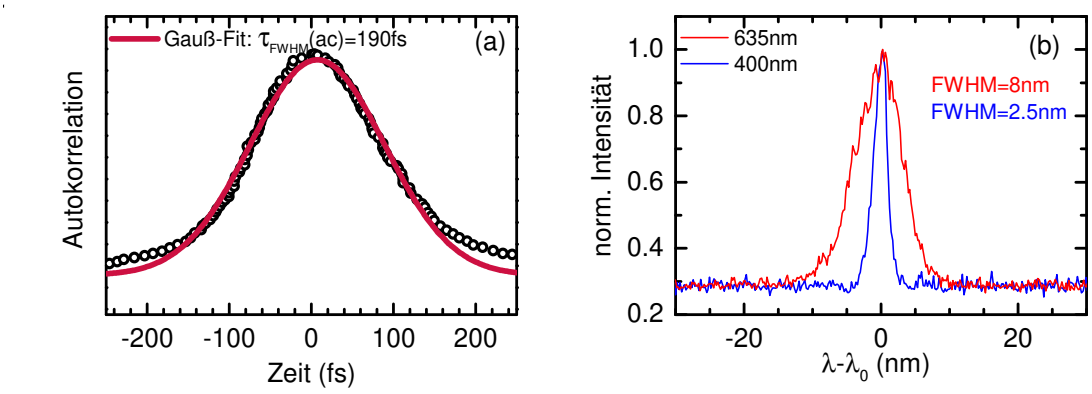

Abbildung 17: (a) Autokorrelation des OPA-Signals bei 635 nm (b) Spektren von SHG- und OPA-Signal bei 400 bzw. 635 nm aufgenommen mit USB4000-Spektrometer von OceanOptics

Es ergeben sich die nach Gleichung 29 abgeleiteten minimalen Pulsbreiten:

$$\tau_{p,Sig} \gtrsim 70\, fs$$

$$\tau_{p,SHG} \gtrsim 100\, fs$$

Beim Vergleich mit der Messung mit dem Autokorrelator fällt auf, dass im Falle des Pump-Signals die Pulsbreite deutlich größer ist als das Fourierlimit (70 fs<134 fs). Dementsprechend könnte sie durch eine Pulskompression weiter verringert werden. Das ist jedoch mit einem entsprechend hohen Justageaufwand vor jeder Messung verbunden, da bei einer Änderung der Anregungswellenlänge die Pulskompression durch Justage

nachgeregelt werden müsste. Bisher wurde darauf verzichtet, da dispersive Elemente (Kryostatfenster, Linsen etc.) die Kontrolle der Pulsform, für Pulsbreiten unterhalb von 100 fs, über den gesamten optischen Weg erschweren.

4.6.3 Weißlicht - Justage und Eigenschaften

Wie bereits in Abschnitt 4.2 erwähnt, ist bei der Weißlichterzeugung die Kontrolle einiger Parameter wichtig für hinreichende spektrale Stabilität. In einer Voruntersuchung habe ich daher die externe Weißlichterzeugung untersucht, deren Anordnung[86,125] schematisch in Abbildung 18 gezeigt ist.

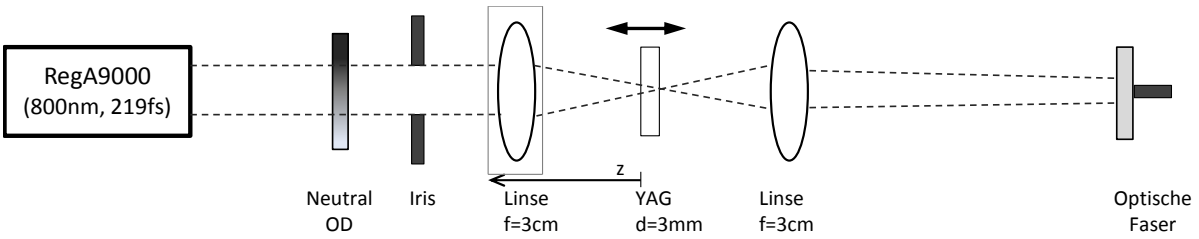

Abbildung 18: Schematische Darstellung der Anordnung zur Erzeugung und Untersuchung des Weißlichtstrahls in einem 3 mm dicken YAG-Kristall.

Etwa 15 % der Intensität des RegA-Ausgangs trifft auf ein variables OD-Filterrad und anschließend auf eine einstellbare Iris-Blende. Eine Linse mit 3 cm Brennweite fokussiert den Strahl entlang der optischen Achse auf einen 3 mm dicken YAG-Kristall, welcher mit einer Mikrometerschraube entlang der optischen Achse verstellbar aufgehängt ist. Es wird jeweils der Abstand zwischen Kristall und dem Rand der Linsenhalterung angegeben, da dieser sich als Referenzpunkt besser eignet als der Mittelpunkt der Linse. Die angegebenen Abstandswerte sind dann etwas kleiner als der Abstand zum Linsenmittelpunkt (siehe Abbildung 18). Im Abstand von etwa 7 cm zur ersten Linse ist eine weitere Linse (f=3 cm) aufgehängt, die das erzeugte Weißlicht hinter dem Kristall kollimiert und auf eine optische Faser mit angeschlossenem Spektrometer eingekoppelt. Die einfallende Leistung wurde hinter der Irisblende mit einem Strahlteiler und einem Leistungsmessgerät (*PowerMaxII, Coherent*) erfasst. Es wurde Yttrium-Aluminium-Granat (YAG) als Material für die Weißlichterzeugung gewählt, weil es einen großen nichtlinearen Koeffizienten n_2 hat. Dadurch sinkt der Schwellwert der nötigen Pulsenergie für die Weißlichterzeugung[86]. Die Pulsenergie kann mit dem variablen OD-Filter zwischen maximal 1 µJ (100 mW bei 100 kHz) und etwa 0.01 µJ (1 mW bei 100 kHz) variiert werden. Die numerische Apertur (NA) des optischen Systems, die mit Hilfe der Irisblende angepasst werden kann, hat ebenfalls Einfluss auf die Stabilität des erzeugten Weißlichts. Der Durchmesser der Irisblende wurde zwischen 2 mm und 6 mm (NA=0.05-0.15) verändert. Die Pulsenergie (0.6 µJ) und der Kristallabstand (2.8 cm) blieben dabei konstant. Die Intensität wurde mit dem verwendeten Spektrometer (USB4000,OceanOptics) gemessen und relativ verglichen. Um die zeitliche Stabilität in Abhängigkeit der Pulsenergie und der Fokusposition zu charakterisieren wurden die Spektren mit 1 s Integrationszeit über 2 min gemessen.

Für die verschiedenen Pulsenergien sind die gemessenen Spektren in Abbildung 19a dargestellt. Oberhalb von 550 nJ wird besonders die ansteigende Flanke im Spektrum für Wellenlängen kleiner als 500 nm instabil. Damit werden die Spektren für Messungen ungeeignet, obwohl die relative Intensität weiter zunimmt. Für Pulsenergien im Bereich von 400 bis 550 nJ ist der spektrale Verlauf flach und ausreichend intensiv. Zudem führen leichte Variationen der Eingangsintensität nicht zu merklichen Veränderungen des spektralen Verlaufs. Es ist damit gut geeignet für die Anwendung als Weißlicht in der Pump-Probe-Spektroskopie.

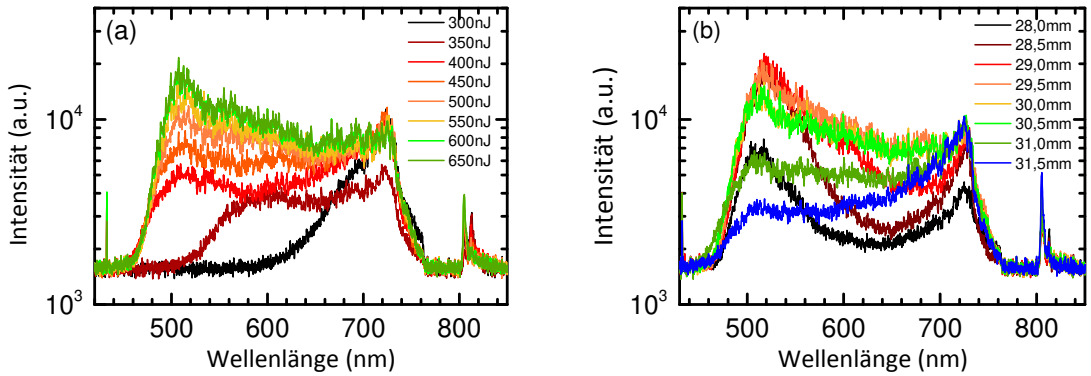

Abbildung 19: (a) Weißlichtspektren für verschiedene Pulsenergien bei einer Fokusposition von 30.5 mm und (b) für verschiedene Fokuspositionen bezüglich der Kante des YAG-Kristalls bei einer Pulsenergie von 550 nJ, Blendendurchmesser: 2 mm

Bei der Variation der numerischen Apertur (NA) hat sich gezeigt, dass ein Blendendurchmesser von etwa 3 mm ein stabiles Weißlicht mit ausreichend Intensität im sichtbaren Bereich liefert. Generell ist das Weißlicht für kleinere Irisblenden stabiler, jedoch verringert sich ebenfalls die maximal mögliche Pulsenergie. Für die Fokusposition hat sich ein Wert von 30.5 mm als am besten geeignet erwiesen, da die Intensität hoch (siehe Abb. 19b) und das Spektrum ausreichend breit ist.

4.6.4 Dispersionskorrektur

Wie schon in Abschnitt 4.5 angesprochen, weisen die Weißlichtpulse eine spektrale Dispersion auf („group velocity dispersion“, GVD). Das bedeutet für den zeitlichen Überlapp von Pump- und Probe-Puls am Ort der Probe, dass der Zeit-Nullpunkt für jede Wellenlänge bestimmt werden muss. Damit kann das Messprogramm bei der Aufnahme von Spektren zu einer festen Verzögerungszeit entsprechend die Position der Verzögerungsstrecke für jede Wellenlänge korrigieren. In Abbildung 20 ist eine typische Dispersionskurve gezeigt. Hier wurde der instantane Anstieg des GSB und der stimulierten Emission des Farbstoffs DCM in Methanol ausgenutzt um den zeitlichen Versatz zu betimmen. Die Kurve kann zum Beispiel mit einem Polynom dritten Grades gefittet werden, welches dann als Korrekturfunktion im Messprogramm bei Messung der Spektren mit fester zeitlicher Verschiebung verwendet wird. Die Disperisonskurve flacht für höhere Wellenlängen ab. Im NIR-Bereich über 900 nm sind Unterschiede in der Nullposition nicht mehr aufzulösen. Das Ausmaß der Dispersion ist

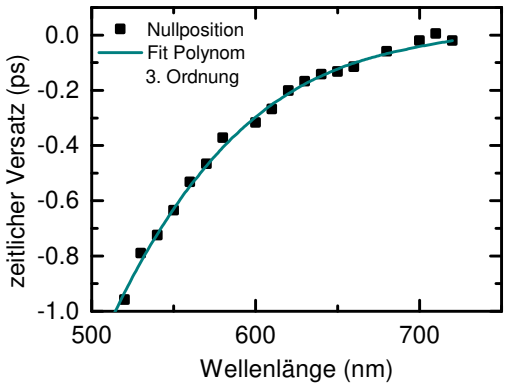

Abbildung 20: Dispersionskurve gemessen anhand des instantanen Anstiegs der fehlenden Grundzustandsabsorption (GSB) und der stimulierten Emission (SE) von DCM in Methanol (c=0.1 g/l) nach Anregung bei $\lambda = 400\ nm$.

stark von der Justage des Weißlichts abhängig. Da diese hin und wieder optimiert werden muss, sollte die Dispersionskurve daher vor jeder größeren Messreihe überprüft werden.

4.6.5 Testmessungen zur Funktionstüchtigkeit des Aufbaus

In diesem Abschnitt vergleiche ich Pump-Probe-Spektren zu verschiedenen Zeiten eines Modellsystems (Blend-Film aus P3HT:PCBM), das in der Literatur sehr gut bekannt ist. Auf diese Weise wird die Funktionsfähigkeit des Setups getestet und gleichzeitig auf die Eignung dünne organische Filme zu messen. Abbildung 21a zeigt Spektren von dünnen Filmen des Modell-Polymers P3HT:$PC_{60}BM$ für 1 ps, 10 ps und 100 ps. Die Spektren wurden zu den gleichen Verzögerungszeiten aufgenommen wie in der Literaturquelle Guo et al. [126-128].

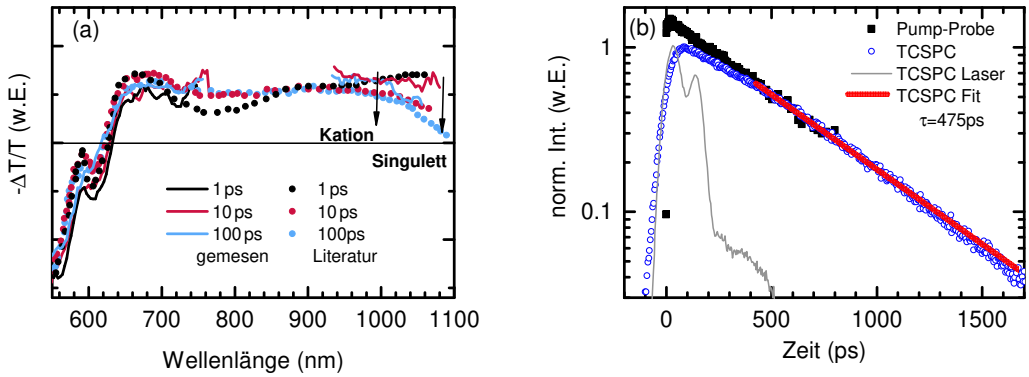

Abbildung 21: (a) transiente Absorptionsspektren von P3HT:PCBM (Film, aufgeschleudert aus Chlorbenzol Lösung c=15 g/l bei einer Rate von 1000 U/min). Die Spektren wurden zu den gleichen Zeitverschiebungen aufgenommen wie in der Literatur-Referenz [128]. adapted with permission by (Guo et al. J. Am. Chem. Soc. 2009, 132, 6154-6164). Copyright © (2009) American Chemical Society) (b) und transiente Absorptions- und TCSPC-Transiente von MEH-PPV in Chlorbenzol (c=0.2 g/l) nach Anregung bei 400 nm, gemessen bei 650 nm, mit Fit wie im Text beschrieben.

Die Filme wurden bei einer Anregungsflussdichte von $10 - 15\ \mu J/cm^2$ bei 400 nm angeregt. Die Spektren zeigen charakteristische Banden bei 550 nm und etwa 610 nm, die dem GSB, also der fehlenden Absorption in diesem Bereich, zugeordnet werden können. An der Absorptionskante um 630 nm gibt es auch Beiträge der ersten Ableitung des Absorptionsspektrum, das dem photoinduzierten Signal mit Maximum bei 650 nm zugeordnet wird[127,129]. Dieses wird in der Literatur[127] zum einen delokalisierten Polaronen in Polymeraggregaten sowie teilweise einer thermisch induzierten Absorptionsänderung zugeordnet[129]. Bei größeren Wellenlängen im NIR-Bereich zwischen 900 und 1050 nm, gibt es ein breites photoinduziertes Signal, das dem Überlapp aus Singulett- und Dublettabsorption (Kation des Polymers) zuzuordnen ist. Das Maximum des Kationsignals der amorphen Phase von P3HT liegt bei etwa 1000 nm und das Maximum der Singulettabsorption bei etwa 1250 nm[114]. Allerdings ist das Singulettsignal innerhalb von 1 ps deutlich abgeklungen, so dass für längere Zeiten nur das Kationsignal zu erkennen ist. In den gemessenen Spektren wird der Bereich um die intensive Zentralwellenlänge des regenerativen Verstärkers (800 nm) nicht gezeigt. Man sieht, dass die gemessenen Spektren mit denen aus der Literatur jeweils sehr gut übereinstimmen. Leichte Abweichungen, besonders bei etwa 1 ps im Bereich des Spektrums zwischen 500-600 nm, kommen sehr wahrscheinlich von lokalen Morphologieunterschieden zwischen den hier präparierten Filmen im Vergleich zur Probe in der Literatur. Ansonsten passen die Ergebnisse im spektralen Verlauf und in der Dynamik für Verzögerungszeiten >1ps zu denen aus der Literatur.

Des Weiteren habe ich Transienten von MEH-PPV in Chlorbenzol in einer 1 mm-Küvette vermessen und den zeitlichen Verlauf des stimulierten Emissionssignals mit Literaturwerten sowie der PL-Abklingkurve verglichen (Abb. 21b). Die PL-Abklingkurve, aufgenommen bei 650 nm, wurde mit der TCSPC-Methode mit einem kommerziellen Aufbau (*PicoHarp300*) der Firma *Picoquant* gemessen. Zur Anregung wurde ein Diodenlaser mit 405 nm verwendet. Die zeitliche Auflösung ist durch die Pulsdauer der Laserdiode auf den Bereich weniger hundert Pikoskeunden begrenzt. Zu erkennen ist dies an der Pulsform der Laserdiode in Abbildung 21b. Durch ein Rekonvolutionsverfahren und der Kenntnis der Pulsform lässt sich aus den Rohdaten eine Lebenszeit extrahieren. Man nimmt dabei an, dass die Transiente exponentiell abnimmt, was für das Singulett-Signal von MEH-PPV der Fall ist. Das Ergebnis dieser Rekonvolution, die mit dem kommerziellen Programm „Fluofit“ der Firma Picoquant durchgeführt wurde, ist in Abbildung 20b mit blauen Punkten gekennzeichnet. Der Fehler ist sicher größer als der vom Programm angegebene Wert von etwa 5 ps. Bei der gleichen Wellenlänge (650 nm) wurde auch das Pump-Probe-Signal gemessen. Dies entspricht der stimulierten Emission. Der Fit mit einem exponentiellem Abfall von $\tau_{TAS} = 480\ ps$ deckt sich im Rahmen der Messgenauigkeit mit dem TCSPC-Wert von $\tau_{TCSPC} = 475\ ps$ und entspricht auch dem Literaturwert für die Singulettlebensdauer von MEH-PPV (450 ps in Toluol[130]). Es sei noch erwähnt, dass aufgrund unterschiedlicher messtechnischer Gegebenheiten die Anregungsflussdichte bei den Messungen zur transienten Absorption etwa eine Größenordnung größer ist als bei der TCSPC-Methode.

4.7 Literaturverzeichnis

(1) C. W. Tang, *Applied Physics Letters* **48** (2), 183-185 (1986).

(2) J. J. M. Halls, K. Pichler, R. H. Friend, S. C. Moratti and A. B. Holmes, *Applied Physics Letters* **68** (22), 3120-3122 (1996).

(3) Y. Sun, G. C. Welch, W. L. Leong, C. J. Takacs, G. C. Bazan and A. J. Heeger, *Nature Materials* **11** (1), 44-48 (2011).

(4) A. Kojima, K. Teshima, Y. Shirai and T. Miyasaka, *Journal of the American Chemical Society* **131**, 6050-6051 (2009).

(5) *NREL Solar efficiency chart https://www.nrel.gov/pv/assets/images/efficiency-chart.png (Juli 2017)*.

(6) H. S. Kim, C. R. Lee, J. H. Im, K. B. Lee, T. Moehl, A. Marchioro, S. J. Moon, R. Humphry-Baker, J. H. Yum, J. E. Moser, M. Gratzel and N. G. Park, *Scientific Reports* **2**, 591 (2012).

(7) S. Ono and K. Ohno, *Physical Review B* **94** (7), 075305 (2016).

(8) H. Zhou, Y. Zhang, J. Seifter, S. D. Collins, C. Luo, G. C. Bazan, T. Q. Nguyen and A. J. Heeger, *Advanced Materials* **25** (11), 1646-1652 (2013).

(9) G. Grancini, M. Maiuri, D. Fazzi, A. Petrozza, H. J. Egelhaaf, D. Brida, G. Cerullo and G. Lanzani, *Nature Materials* **12** (1), 29-33 (2013).

(10) J. A. Bjorgaard and M. E. Köse, *The Journal of Physical Chemistry C* **118** (11), 5756-5761 (2014).

(11) C. Scharsich, F. S. U. Fischer, K. Wilma, R. Hildner, S. Ludwigs and A. Köhler, *Journal of Polymer Science Part B: Polymer Physics* **53** (20), 1416-1430 (2015).

(12) T. Xiao, H. Xu, G. Grancini, J. Mai, A. Petrozza, U. S. Jeng, Y. Wang, X. Xin, Y. Lu, N. S. Choon, H. Xiao, B. S. Ong, X. Lu and N. Zhao, *Scientific Reports* **4**, 5211 (2014).

(13) H. Bässler and A. Köhler, *Physical Chemistry Chemical Physics* **17** (43), 28451-28462 (2015).

(14) A. C. Jakowetz, M. L. Bohm, J. Zhang, A. Sadhanala, S. Huettner, A. A. Bakulin, A. Rao and R. H. Friend, *Journal of the American Chemical Society* **138** (36), 11672-11679 (2016).

(15) S. M. Falke, C. A. Rozzi, D. Brida, M. Maiuri, M. Amato, E. Sommer, A. De Sio, A. Rubio, G. Cerullo, E. Molinari and C. Lienau, *Science* **344** (6187), 1001-1005 (2014).

(16) M. Schwoerer and H. C. Wolf, *Organic Molecular Solids*. (Wiley-VCH Verlag GmbH, Weinheim, Germany, 2006).

(17) A. Köhler and H. Bässler, in *Electronic Processes in Organic Semiconductors* (Wiley-VCH Verlag GmbH & Co. KGaA, 2015), pp. 87-191.

(18) S. T. Hoffmann, H. Bässler and A. Köhler, *The Journal of Physical Chemistry B* **114**, 12 (2010).

(19) J. Gierschner, J. Cornil and H. J. Egelhaaf, *Advanced Materials* **19** (2), 173-191 (2007).

(20) W. Kuhn, *Helvetica Chimica Acta* **31** (6), 1780-1799 (1948).

(21) S. Westenhoff, W. J. D. Beenken, A. Yartsev and N. C. Greenham, *The Journal of Chemical Physics* **125** (15), 154903 (2006).

(22) M. Pope and C. E. Swenberg, *Electronic Processes in Organic Crystals and Polymers*. (Oxford University Press, 1999).

(23) A. Akande, S. Bhattacharya, T. Cathcart and S. Sanvito, *The Journal of Chemical Physics* **140** (7), 074301 (2014).

(24) B. J. Kim, H. Yu, J. H. Oh, M. S. Kang and J. H. Cho, *The Journal of Physical Chemistry C* **117** (20), 10743-10749 (2013).

(25) F. Dubin, R. Melet, T. Barisien, R. Grousson, L. Legrand, M. Schott and V. Voliotis, *Nature Physics* **2** (1), 32-35 (2005).

(26) H. Bässler, *physica status solidi (b)* **175** (1), 15-56 (1993).

(27) T. Holstein, *Annals of Physics* **8** (3), 343-389 (1959).

(28) M. Kasha, *Discussions of the Farady Society* **9** (0), 6 (1950).

(29) P. Klán and J. Wirz, *Photochemistry of organic compounds*, Repr. 2010 ed. (Wiley, Chichester, 2009).

(30) T. Elsaesser and W. Kaiser, *Annual Review of Physical Chemistry* **42** (1) (1991).

(31) A. Köhler and H. Bässler, *Materials Science and Engineering: R: Reports* **66** (4-6), 71-109 (2009).

(32) Y. Fujimura, N. Shimakura and T. Nakajima, *The Journal of Chemical Physics* **66** (8), 3530-3537 (1977).

(33) J. B. Birks, *Photophysics of Aromatic Molecules*. (Wiley-Interscience, 1970).

(34) E. Peeters, A. M. Ramos, S. C. J. Meskers and R. A. J. Janssen, *The Journal of Chemical Physics* **112** (21), 9445-9454 (2000).

(35) J.-L. Bredas, *Materials Horizons* **1** (1), 17-19 (2014).

(36) J.-L. Bredas, J. Cornil and A. J. Heeger, *Advanced Materials* **8** (5), 6 (1996).

(37) J. S. Wilson, N. Chawdhury, M. R. A. Al-Mandhary, M. Younus, M. S. Khan, P. R. Raithby, A. Köhler and R. H. Friend, *Journal of the American Chemical Society* **123** (38), 9412-9417 (2001).

(38) S. Dimitrov, B. Schroeder, C. Nielsen, H. Bronstein, Z. Fei, I. McCulloch, M. Heeney and J. Durrant, *Polymers* **8** (1), 14 (2016).

(39) G. D. Scholes, *Annu Rev Phys Chem* **54**, 57-87 (2003).

(40) L. Sudha Devi, M. K. Al-Suti, C. Dosche, M. S. Khan, R. H. Friend and A. Köhler, *Physical Review B* **78** (4) (2008).

(41) A. Damjanović, T. Ritz and K. Schulten, *Physical Review E* **59** (3), 3293-3311 (1999).

(42) H. A. M. van Mullekom, J. A. J. M. Vekemans, E. E. Havinga and E. W. Meijer, *Materials Science and Engineering: R: Reports* **32** (1), 1-40 (2001).

(43) G. Brocks and A. Tol, *The Journal of Physical Chemistry* **100** (5), 1838-1846 (1996).

(44) E. E. Havinga, W. ten Hoeve and H. Wynberg, *Polymer Bulletin* **29** (1), 119-126 (1992).

(45) D. Beljonne and J. Cornil, *Multiscale Modelling of Organic and Hybrid Photovoltaics*. (Springer Berlin Heidelberg, 2014).

(46) M. C. Scharber, D. Mühlbacher, M. Koppe, P. Denk, C. Waldauf, A. J. Heeger and C. J. Brabec, *Advanced Materials* **18** (6), 789-794 (2006).

(47) R. A. J. Janssen and J. Nelson, *Advanced Materials* **25** (13), 1847-1858 (2013).

(48) W. Li, K. H. Hendriks, A. Furlan, M. M. Wienk and R. A. Janssen, *Journal of the American Chemical Society* **137** (6), 2231-2234 (2015).

(49) J. Liu, S. Chen, D. Qian, B. Gautam, G. Yang, J. Zhao, J. Bergqvist, F. Zhang, W. Ma, H. Ade, O. Inganäs, K. Gundogdu, F. Gao and H. Yan, *Nature Energy* **1** (7), 16089 (2016).

(50) I.-W. Hwang, D. Moses and A. J. Heeger, *The Journal of Physical Chemistry C* **112** (11), 4350-4354 (2008).

(51) K. Vandewal, S. Albrecht, E. T. Hoke, K. R. Graham, J. Widmer, J. D. Douglas, M. Schubert, W. R. Mateker, J. T. Bloking, G. F. Burkhard, A. Sellinger, J. M. Frechet, A. Amassian, M. K. Riede, M. D. McGehee, D. Neher and A. Salleo, *Nature Materials* **13** (1), 63-68 (2014).

(52) R. R. Chance and C. L. Braun, *The Journal of Chemical Physics* **64** (9), 3573-3581 (1976).

(53) T. G. J. van der Hofstad, D. Di Nuzzo, M. van den Berg, R. A. J. Janssen and S. C. J. Meskers, *Advanced Energy Materials* **2** (9), 1095-1099 (2012).

(54) M. Klessinger and J. Michl, *Excited states and photochemistry of organic molecules*. (VCH, 1995).

(55) J. R. Lakowicz, *Principles of Fluorescence Spectroscopy*. (Springer, Berlin / Heidelberg, 2007).

(56) L. Stryer, *Annual Review of Biochemistry* **47** (1), 819-846 (1978).

(57) P. G. Wu and L. Brand, *Analytical Biochemistry* **218** (1), 1-13 (1994).

(58) S. C. Hovan, S. Howell and P. S. H. Park, *Journal of Biomedical Optics* **15** (6), 067001-067009 (2010).

(59) N. J. Turro, *Modern Molecular Photochemistry*. (University Science Books, Sausalito, CA, 1991).

(60) D. L. Dexter, *The Journal of Chemical Physics* **21** (5), 836-850 (1953).

(61) A. Köhler and H. Bässler, *Journal of Materials Chemistry* **21** (12), 4003-4011 (2011).

(62) A. Miller and E. Abrahams, *Physical Review* **120** (3), 745-755 (1960).

(63) I. I. Fishchuk, A. Kadashchuk, S. T. Hoffmann, S. Athanasopoulos, J. Genoe, H. Bässler and A. Köhler, *Physical Review B* **88** (12), 125202 (2013).

(64) R. A. Marcus, *The Journal of Chemical Physics* **24** (5), 966-978 (1956).

(65) I. R. Gould, D. Ege, S. L. Mattes and S. Farid, *Journal of the American Chemical Society* **109** (12), 3794-3796 (1987).

(66) A. Chakraborty, D. Chakrabarty, P. Hazra, D. Seth and N. Sarkar, *Chemical Physics Letters* **382** (5–6), 508-517 (2003).

(67) S. Fukuzumi, K. Ohkubo, H. Imahori and D. M. Guldi, *Chemistry – A European Journal* **9** (7), 1585-1593 (2003).

(68) M. R. Wasielewski, M. P. Niemczyk, W. A. Svec and E. B. Pewitt, *Journal of the American Chemical Society* **107** (4), 1080-1082 (1985).

(69) J. R. Miller, L. T. Calcaterra and G. L. Closs, *Journal of the American Chemical Society* **106** (10), 3047-3049 (1984).

(70) D. Rehm and A. Weller, *Israel Journal of Chemistry* **8** (2), 259-271 (1970).

(71) C. Leng, H. Qin, Y. Si and Y. Zhao, *The Journal of Physical Chemistry C* **118** (4), 1843-1855 (2014).

(72) K. Vandewal, K. Tvingstedt, A. Gadisa, O. Inganas and J. V. Manca, *Nature Materials* **8** (11), 904-909 (2009).

(73) K. Vandewal, K. Tvingstedt, A. Gadisa, O. Inganäs and J. V. Manca, *Physical Review B* **81** (12), 125204 (2010).

(74) T. Kubar and M. Elstner, *Physical Chemistry Chemical Physics* **15** (16), 5794-5813 (2013).

(75) A. Kubas, F. Gajdos, A. Heck, H. Oberhofer, M. Elstner and J. Blumberger, *Physical Chemistry Chemical Physics* **17** (22), 14342-14354 (2015).

(76) E. W. Castner, D. Kennedy and R. J. Cave, *The Journal of Physical Chemistry A* **104** (13), 2869-2885 (2000).

(77) N. R. Kestner, J. Logan and J. Jortner, *The Journal of Physical Chemistry* **78** (21), 2148-2166 (1974).

(78) J. Jortner, *The Journal of Chemical Physics* **64** (12), 4860-4867 (1976).

(79) M. E. Sigman and G. L. Closs, *The Journal of Physical Chemistry* **95** (13), 5012-5017 (1991).

(80) L. Bergmann, H. Niedrig and H. J. Eichler, *Optik: Wellen- und Teilchenoptik*. (de Gruyter, 2004).

(81) R. W. Boyd, in *Nonlinear Optics (Third Edition)* (Academic Press, Burlington, 2008), pp. 1-67.

(82) J.-C. Diels and W. Rudolph, in *Ultrashort Laser Pulse Phenomena (Second Edition)* (Academic Press, Burlington, 2006), pp. 1-60.

(83) D. Majus, V. Jukna, E. Pileckis, G. Valiulis and A. Dubietis, *Optics Express* **19** (17), 16317-16323 (2011).

(84) M. Bradler, Diplomarbeit, LMU München, 2009.

(85) A. Brodeur and S. L. Chin, *Journal of the Optical Society of America B* **16** (4), 637-650 (1999).

(86) M. Bradler, P. Baum and E. Riedle, *Applied Physics B* **97** (3), 561-574 (2009).

(87) Y.-C. Hsiao, T. Wu, M. Li, Q. Liu, W. Qin and B. Hu, *Journal of Materials Chemistry A* **3** (30), 15372-15385 (2015).

(88) L. M. Herz, *Annual Review of Physical Chemistry* **67**, 65-89 (2016).

(89) A. Poglitsch and D. Weber, *The Journal of Chemical Physics* **87** (11), 6373-6378 (1987).

(90) Z.-K. Tan, R. S. Moghaddam, M. L. Lai, P. Docampo, R. Higler, F. Deschler, M. Price, A. Sadhanala, L. M. Pazos, D. Credgington, F. Hanusch, T. Bein, H. J. Snaith and R. H. Friend, *Nature Nanotechnology* **9** (9), 687-692 (2014).

(91) G. Li, Z. K. Tan, D. Di, M. L. Lai, L. Jiang, J. H. Lim, R. H. Friend and N. C. Greenham, *Nano Letters* **15** (4), 2640-2644 (2015).

(92) H. Cho, S.-H. Jeong, M.-H. Park, Y.-H. Kim, C. Wolf, C.-L. Lee, J. H. Heo, A. Sadhanala, N. Myoung, S. Yoo, S. H. Im, R. H. Friend and T.-W. Lee, *Science* **350** (6265), 1222-1225 (2015).

(93) G. Maculan, A. D. Sheikh, A. L. Abdelhady, M. I. Saidaminov, M. A. Haque, B. Murali, E. Alarousu, O. F. Mohammed, T. Wu and O. M. Bakr, *The Journal of Physical Chemistry Letters* **6** (19), 3781-3786 (2015).

(94) B. Náfrádi, G. Náfrádi, L. Forró and E. Horváth, *The Journal of Physical Chemistry C* **119** (45), 25204-25208 (2015).

(95) X. Y. Chin, D. Cortecchia, J. Yin, A. Bruno and C. Soci, *Nature Communications* **6**, 7383 (2015).

(96) F. Deschler, M. Price, S. Pathak, L. E. Klintberg, D. D. Jarausch, R. Higler, S. Huttner, T. Leijtens, S. D. Stranks, H. J. Snaith, M. Atature, R. T. Phillips and R. H. Friend, *The Journal of Physical Chemistry Letters* **5** (8), 1421-1426 (2014).

(97) A. Binek, M. L. Petrus, N. Huber, H. Bristow, Y. Hu, T. Bein and P. Docampo, *ACS Applied Materials & Interfaces* **8** (20), 12881-12886 (2016).

(98) F. Hao, C. C. Stoumpos, D. H. Cao, R. P. H. Chang and M. G. Kanatzidis, *Nature Photonics* **8** (6), 489-494 (2014).

(99) Z. Song, A. Abate, S. C. Watthage, G. K. Liyanage, A. B. Phillips, U. Steiner, M. Graetzel and M. J. Heben, *Advanced Energy Materials* **6** (19), 1600846 (2016).

(100) M. Anaya, J. P. Correa-Baena, G. Lozano, M. Saliba, P. Anguita, B. Roose, A. Abate, U. Steiner, M. Gratzel, M. E. Calvo, A. Hagfeldt and H. Miguez, *Journal of Materials Chemistry A* **4** (29), 11214-11221 (2016).

(101) J. Yang and T. L. Kelly, *Inorganic Chemistry* **56** (1), 92-101 (2017).

(102) J. Even, L. Pedesseau and C. Katan, *The Journal of Physical Chemistry C* **118** (22), 11566-11572 (2014).

(103) E. M. Hutter, M. C. Gelvez-Rueda, A. Osherov, V. Bulovic, F. C. Grozema, S. D. Stranks and T. J. Savenije, *Nature Materials* **16** (1), 115-120 (2017).

(104) T. Kirchartz and U. Rau, *The Journal of Physical Chemistry Letters* **8** (6), 1265-1271 (2017).

(105) M. B. Price, J. Butkus, T. C. Jellicoe, A. Sadhanala, A. Briane, J. E. Halpert, K. Broch, J. M. Hodgkiss, R. H. Friend and F. Deschler, *Nature Communications* **6**, 8420 (2015).

(106) V. D'Innocenzo, G. Grancini, M. J. Alcocer, A. R. Kandada, S. D. Stranks, M. M. Lee, G. Lanzani, H. J. Snaith and A. Petrozza, *Nat Commun* **5**, 3586 (2014).

(107) K. Galkowski, A. Mitioglu, A. Miyata, P. Plochocka, O. Portugall, G. E. Eperon, J. T.-W. Wang, T. Stergiopoulos, S. D. Stranks, H. J. Snaith and R. J. Nicholas, *Energy & Environmental Science* **9** (3), 962-970 (2016).

(108) K. Tanaka, T. Takahashi, T. Ban, T. Kondo, K. Uchida and N. Miura, *Solid State Communications* **127** (9-10), 619-623 (2003).

(109) A. Miyata, A. Mitioglu, P. Plochocka, O. Portugall, J. T.-W. Wang, S. D. Stranks, H. J. Snaith and R. J. Nicholas, *Nature Physics* **11** (7), 582-587 (2015).

(110) S. D. Stranks, V. M. Burlakov, T. Leijtens, J. M. Ball, A. Goriely and H. J. Snaith, *Physical Review Applied* **2** (3), 034007 (2014).

(111) C. Wehrenfennig, M. Liu, H. J. Snaith, M. B. Johnston and L. M. Herz, *Energy & Environmental Science* **7** (7), 2269 (2014).

(112) D. W. de Quilettes, S. M. Vorpahl, S. D. Stranks, H. Nagaoka, G. E. Eperon, M. E. Ziffer, H. J. Snaith and D. S. Ginger, *Science* **348** (6235), 683-686 (2015).

(113) B. Murali, E. Yengel, C. Yang, W. Peng, E. Alarousu, O. M. Bakr and O. F. Mohammed, *ACS Energy Letters*, 846-856 (2017).

(114) F. Staub, H. Hempel, J.-C. Hebig, J. Mock, U. W. Paetzold, U. Rau, T. Unold and T. Kirchartz, *Physical Review Applied* **6** (4) (2016).

(115) G. Xing, N. Mathews, S. S. Lim, N. Yantara, X. Liu, D. Sabba, M. Gratzel, S. Mhaisalkar and T. C. Sum, *Nature Materials* **13** (5), 476-480 (2014).

(116) B. Philippe, B.-W. Park, R. Lindblad, J. Oscarsson, S. Ahmadi, E. M. J. Johansson and H. Rensmo, *Chemistry of Materials* **27** (5), 1720-1731 (2015).

(117) X. Wu, M. T. Trinh, D. Niesner, H. Zhu, Z. Norman, J. S. Owen, O. Yaffe, B. J. Kudisch and X. Y. Zhu, *Journal of the American Chemical Society* **137** (5), 2089-2096 (2015).

(118) W. Tress, *Advanced Energy Materials* **7** (14), 1602358 (2017).

(119) L. M. Pazos-Outón, M. Szumilo, R. Lamboll, J. M. Richter, M. Crespo-Quesada, M. Abdi-Jalebi, H. J. Beeson, M. Vrućinić, M. Alsari, H. J. Snaith, B. Ehrler, R. H. Friend and F. Deschler, *Science* **351** (6280), 1430-1433 (2016).

(120) G. Cerullo, C. Manzoni, L. Luer and D. Polli, *Photochemical & Photobiological Sciences* **6** (2), 135-144 (2007).

(121) S. Wedler, Masterarbeit, Universität Bayreuth, 2016.

(122) H. E. Lessing and A. Von Jena, *Chemical Physics Letters* **42** (2), 213-217 (1976).

(123) N. Uchida, *Physical Review B* **4** (10), 3736-3745 (1971).

(124) M. Rasmusson, A. N. Tarnovsky, E. Åkesson and V. Sundström, *Chemical Physics Letters* **335** (3-4), 201-208 (2001).

(125) C. Romero, R. Borrego-Varillas, A. Camino, G. Mínguez-Vega, O. Mendoza-Yero, J. Hernández-Toro and J. R. Vázquez de Aldana, *Optics Express* **19** (6), 4977-4984 (2011).

(126) J. O. Guo, H; Benten, H; Ito, S, *Journal of the American Chemical Society* **131**, 11 (2009).

(127) H. Ohkita and S. Ito, *Polymer* **52** (20), 4397-4417 (2011).

(128) J. Guo, H. Ohkita, H. Benten and S. Ito, *Journal of the American Chemical Society* **132** (17), 6154-6164 (2010).

(129) S. Albert-Seifried and R. H. Friend, *Applied Physics Letters* **98** (22), 223304 (2011).

(130) L. Rothberg, in *Semiconducting Polymers*, edited by G. Hadziioannou and G. Malliaras (Wiley, Weinheim, 2006), pp. 179-204.

5 Überblick der Publikationen

In der Arbeit wird der Einfluss der Konformation organischer Materialien in Lösung sowie der Morphologie von dünnen Filmen organischer und hybrider Materialien auf die Dynamik opitscher Anregungen untersucht. Dies ist ein Schlüssel zum Verständnis zum einen der effizienten Ladungsträgertrennung und zum anderen der Limitierung der Effizienz durch Rekombination der erzeugten Ladungsträger. Die Arbeit, und die zugehörigen veröffentlichten Publikationen, lassen sich in zwei Teilbereiche gliedern. Der erste Teilbereich behandelt die einzelnen Schritte der Exzitonendissoziation (Diffusion, Transfer und Trennung) an Grenzflächen in organischen Materialsystemen. Im zweiten Teil liegt der Fokus auf der Untersuchung der Vorgänge an Grenzflächen in hybriden Systemen (Methylammonium-Blei-Iodid $CH_3NH_3PbI_3$ und $CH_3NH_3PbI_xCl_{3-x}$).

Zu Beginn meiner Promotion habe ich einen Messaufbau zur transienten Absorption auf ultraschneller Zeitskala eingerichtet um die Dynamik der Exzitonen sowie die Schritte ihrer Trennung zeitlich auflösen zu können. Damit lassen sich Relaxationsdynamiken von geladenen und ungeladenen Zuständen in dünnen Filmen oder Lösungen verfolgen. Außerdem ist es möglich dunkle Zustände, als mögliche Verlustkanäle für Ladungsträger oder Exzitonen, aufzuspüren.

Um die Dynamik in einem komplexen Blend-System, zum Beispiel für organische Solarzellen, zu verstehen, ist es sinnvoll die Betrachtung zuerst auf einzelne Prozesse zu beschränken. Daher beschäftigt sich der erste Teil dieser Arbeit mit der Untersuchung der Anregungsdynamik an Grenzflächen, die zum einen zwischen unterschiedlichen Phasen des Polymerdonors und zum anderen zwischen Donor und Akzeptor gebildet werden.

Viele Polymere, die in Solarzellen als Elektronendonor agieren, zeigen abhängig von den Prozessierungsbedingungen unterschiedliche Konformationen. Dabei kommt es auch zur Bildung von Grenzflächen zwischen den unterschiedlichen Phasen. Dies wird zum Beispiel beobachtet in Materialien wie P3HT, PCPDTBT oder PFO. Des Weiteren hängt die Morphologie in Blend-Filmen aus Polymer und Fulleren auch vom Aggregationsverhalten der Polymer-Ketten und deren Anordnung ab, was sich wiederum auf die Dynamik der angeregten Zustände auswirkt. Insbesondere die Löslichkeit des Polymers im verwendeten Lösungsmittel spielt eine wichtige Rolle.

Am Beispiel des Polymers MEH-PPV wird in Abschnitt 6 daher untersucht, wie sich die Dynamik der Anregungen verhält, wenn es zur kontrollierten Bildung einer aggregierten, geordneten Phase durch Veränderung der Löslichkeit kommt. Dieses erreicht man durch Absenken der Temperatur der Lösung. Zum ersten Mal konnten bekannte Methoden zur Analyse optischer Spektren, die am Lehrstuhl etabliert sind, auf zeitabhängige Absorptionsspektren angwendet werden. Auf diese Weise ist es möglich die Dynamik den einzelnen Phasen zuzuordnen und Übergänge zwischen aggregierter und ungeordneter Phase zu charakterisieren. Aufbauend auf diesem Wissen wird in Abschnitt 7 etwas genauer

die Dynamik in der aggregierten Phase betrachtet. Um allein diese Phase anzuregen, wird das Wissen über die spektrale Trennung aus Abschnitt 6 ausgenutzt. Mit Hilfe transienter Absorptionsspektroskopie und kohärenter 2D-Spektroskopie kann dann der Relaxationsprozess und die zugehörigen einzelnen Energietransferschritte innerhalb der aggregierten Phase aufgedeckt werden. Dabei wird die Entwicklung der Spektren bei verschiedenen Anregungsenergien der Laserpulse verglichen um unterschiedliche Zustandsniveaus innerhalb der Zustandsdichte der geordneten Phase anzuregen. So konnte der komplexe Relaxationsprozess innerhalb der aggregierten Polymerphase aufgedeckt werden.

Im weiteren schließt sich die Betrachtung von Elektronen- und Energietransferprozessen in Systemen an, die sowohl eine Donor- als auch eine Akzeptor-Einheit enthalten. Um separat die Transferschritte zwischen beiden Komponenten zu betrachten, muss sichergestellt werden, dass der räumliche Abstand zwischen beiden Einheiten nicht zu groß ist, um den Beitrag der Diffusion der Anregungen zu minimieren. Am besten eignet sich daher eine chemische Bindung zwischen beiden Einheiten. Dies ist ebenfalls ein möglicher Ansatz zur Morphologiekontrolle der Grenzfläche in dünnen Filmen. In Abschnitt 8 wird deshalb Energie- und Ladungstransfer am Beispiel einer chemischen Dyade in Lösung untersucht. Die Dyade besteht aus einem Elektrondonor (Perylenbisimid, PBI) und einem Elektonakzeptor (Kupferphthalocyanin, CuPc), die kovalent über eine flexible aliphatische Brücke verbunden sind. Durch Simulationen der Moleküldynamik und verschiedenen zeitaufgelösten spektroskopischen Methoden konnte geklärt werden, wie unterschiedliche räumliche Konformationszustände die Bildung weiterer energetischer Zustände beeinflusst. So begünstigt die lange flexible Verbindung eine Faltung der Dyade, also ein Aufeinanderklappen der beiden Komponenten, wobei sich CuPc- und PBI-Einheiten parallel zueinader anordnen. Die Bildung eines erwünschten langlebigen ladungsgetrennten Zustands wird verhindert. Die Arbeit zeigt also die Bedeutung der lokalen Konformation an der Donor-Akzeptor-Grenzfläche und deren Einfluss auf Ladungsträgertrennung beziehungsweise Energietransfer.

Nachdem in den vorgien Abschnitten in speziellen Systemen auf die einzelnen Vorgänge Diffusion oder Exzitonentrennung eingegangen wurde, wird nun beides in Blend-Filmen zugelassen. Dabei wird systematisch der Donorkomponente variiert um die freie Enthalpieänderung des Elektronentransfers zu ändern und dessen Einfluss auf die Transferrate zu analysieren. Der Elektronakzeptor PCBM wird dabei gleich gelassen. Ziel ist es die Anwendbarkeit unterschiedlicher Modelle, die Ladungstransfer beschreiben, zu überprüfen um auf die zugrundeliegenden physikalischen Prozesse zu schließen. Dazu wird unter anderem auch die Temperaturabhängigkeit der Transferrate untersucht. In Abschnitt 9 kann ich zeigen, dass die allgemeine Beschreibung des Elektronentransfers in Filmen für organische Solarzellen mit dem Marcus-Modell nicht möglich ist. Anhand der Pump-Probe-Messungen kann die vorhergesagte starke Temperaturabhängigkeit der Rate nicht bestätigt werden. Es müssen eher Modelle in Betracht gezogen werden, die stärker

quantenmechanisches Tunneln der Ladungsträger mit einbeziehen und auch die genaue Morphologie der Grenzfläche berücksichtigen.

Im zweiten Teil der Arbeit steht das Modellsystem Methylammonium-Bleiiodid im Fokus. Aufgrund der geringen optischen Bandlücke und der geringeren Exzitonenbindungsenergie zeigen Perowskit-Solarzellen höhere Effizienzen als organische Materialien, dennoch gibt es zahlreiche „dunkle“ nichtstrahlende Rekombinationskanäle. Analog zum ersten Teil ist es Ziel diese Verlustkanäle mit Hilfe verschiedener spektroskopischer und morphologischer Messmethoden aufzudecken.

Ähnlich wie bei den untersuchten organischen Systemen wird die Filmmorphologie durch die Art der Prozessierung beeinflusst. Da es sich um polykristalline Materialien handelt, spielen hier die Grenzflächen an Korngrenzen eine besondere Bedeutung. Die Morphologie dieser Grenzflächen hat nicht nur Auswirkungen auf die elektronischen Solarzelleigenschaften sondern auch auf die Stabilität der polykristallinen Perowskit-Struktur. Perowskit-Filme weisen eine geringere Stabilität als etwa organische Solarzellen auf. Sie zeigen Zersetzung der Kristallstruktur unter Einfluss von Sauerstoff und Wasser aus der Luft. Um dies zu untersuchen haben meine Koautoren nach der Filmbildung kontrolliert das Verhältnis der Ausgangsstoffe Methylammoniumiodid (MAI) und Bleiiodid (PbI_2) durch Aufheizen des fertigen Films variiert. Neben morphologischen Charakterisierungen werden ebenfalls PL- und Absorptionsspektroskopie genutzt um spektrale Eigenschaften des Films mit Solarzellparametern des fertigen Bauteils zu korrelieren. Die Ergebnisse aus Kapitel 10 belegen zwar, dass die Filme mit wenigen Prozent Bleiiodid-Gehalt eine höhere Solarzelleffizienz und höhere PL-Intensität zeigen, jedoch führt dies auch zu einer kürzeren Lebensdauer der entsprechenden Solarzellen. Aus SEM-Aufnahmen und Ergebnissen der Röntgenbeugung geht hervor, dass es zur Bildung kristallinen Bleiiodids an den Korngrenzen kommt. Dies spricht auch für eine besondere Bedeutung der polykristallinen Struktur für die strahlende und nichtstrahlende Rekombination freier Ladungsträger in Perowskit-Filmen.

In Kapitel 11 wurde die Ursache solcher nichtstrahlender Rekombinationsprozesse mittels makroskopischer und ortsaufgelöster PL untersucht. Mikroskopieaufnahmen polykristalliner Perowskit-Filme zeigen ein zeitliches Blinkverhalten einzelner Kristallite bei optischer Anregung. Ein Vergleich des PL-Verhaltens zwischen Perowskit-Filmen mit und ohne zusätzlich aufgetragener Akzeptorschicht deutet auf einen Rekombinationsmechanismus beruhend auf dem Auger-Effekt als Ursache des Blinkverhaltens hin. Dieser ist ein Verlustkanal für freie Ladungsträger in Perowskit-Filmen und limitiert die Effizienz von Solarzellen.

Eigene Beiträge

Kapitel 6

Diese Veröffentlichung wurde in *ACS Macro Letters* (2015, 4, 412-416) publiziert und trägt den Titel:

„Ultrafast Energy Transfer between Disordered and Highly Planarized Chains of Poly[2-methoxy-5-(2-ethylhexyloxy)-1,4-phenylenevinylene] (MEH-PPV)“

Von Thomas Unger, Fabian Panzer, Cristina Consani, Federico Koch, Tobias Brixner, Heinz Bässler, Anna Köhler

Ich habe den Messaufbau zur transienten Absorption eingerichtet und das Messprogramm dazu geschrieben. Damit konnte ich die transienten Absorptionsspektren bei 120 K messen. Ich habe die Probenlösung für die zeitabhängigen Messungen präpariert und die transienten Spektren zu verschiedenen Verzögerungszeiten gemessen. Außerdem habe ich die spektrale Zerlegung (zeitabhängige Spektren) in aggregierte und amorphe Phase vorgenommen und ausgewertet, sowie Teile des Manuskripts geschrieben.

Kapitel 7

Die hier vorgestellte Publikation ist in *Journal of Chemical Physics* (2015, 142, 212429) veröffentlicht mit dem Titel:

„Relaxation dynamics and exciton energy transfer in the low-temperature phase of MEH-PPV“

Von Cristina Consani, Federico Koch, Fabian Panzer, Thomas Unger, Anna Köhler, Tobias Brixner

Ich habe ein transientes Absorptionsspektrum bei 120 K gemessen, bei der Interpretation der Daten geholfen und das Manuskript überprüft.

Kapitel 8

Diese Publikation ist veröffentlicht in *Physical Chmistry Chemical Physics* (2017, 19, 22169) und trägt den Titel:

„Excited State Dynamics and Conformations of a Cu(II)-Phthalocyanine-Perylenebisimide Dyad“

Von Kevin Wilma, Thomas Unger, Christoph Hunger, Manuel Hollfelder, Sinem Tuncel Kostakoğlu, Aişe Gül Gürek , Mukundan Thelakkat, Jürgen Köhler, Anna Köhler, Stephan Gekle, Richard Hildner

Ich habe alle Messungen zur transienten Absorption im fs bis ps-Bereich durchgeführt und bei den Messungen im ns-Bereich geholfen sowie alle zugehörigen Daten ausgewertet (Kurzzeit-Spektren und Transienten im Hauptmanuskript und in der SI). Zusammen mit Kevin Wilma habe ich die PL-Quanteneffizienz für die Dyade und die PBI-Komponente gemessen. Darüber hinaus habe ich einen Teil des Textes geschrieben und bei der Interpretation der Daten geholfen. Kevin Wilma und ich haben zu gleichen Teilen zur vorliegenden Arbeit beigetragen.

Kapitel 9

Diese Publikation ist veröffentlicht in *The Journal of Physical Chemistry C* (2017, 121, 22739) mit dem Titel:

„The Impact of Driving Force and Temperature on the Electron Transfer in Donor-Acceptor Blend Systems”

Von Thomas Unger, Stefan Wedler, Julian Kahle, Ullrich Scherf, Heinz Bässler, Anna Köhler

Ich habe die transienten Absorptionsmessungen am Polymer-Film des MeLPPP-Systems durchgeführt. Zusammen mit Stefan Wedler habe ich die temperaturabhängigen Transienten am Blend-Film des MeLPPP-Systems gemessen. Darüber hinaus habe ich die Transienten und Spektren der Polymer-Filme für PCPDTBT und PTB7 gemessen. Stefan Wedler hat Messungen zu den zugehörigen Blend-Filmen durchgeführt. Wir haben die Ergebnisse gemeinsam diskutiert. Des Weiteren habe ich das PL-Spektrum des reinen MeLPPP-Films sowie die UV-Vis-Spektren in Abbildung 1c gemessen. Darüber hinaus habe ich Teile des Manuskripts geschrieben. Stefan Wedler und ich haben zu gleichen Teilen zur Arbeit beigetragen.

Kapitel 10

Diese Publikation ist veröffentlicht bei *Physical Chemistry Chemical Physics* (2018) und trägt den Titel:

"The Role of PbI_2 on $CH_3NH_3PbI_3$ Perovskite Stability, Device Parameters and Degradation"

Von Tanaji P. Gujar, Thomas Unger, Fabian Panzer, Martina Fried, Andreas Schönleber, Sander van Smaalen, Anna Köhler, Mukundan Thelakkat

Ich habe alle steady state PL-Spektren gemessen und ausgewertet sowie die Absorptionsspektren ausgewert und die entsprechenden Graphen erstellt. Zudem habe ich auch die Graphen in Abbildung 6 erstellt. Außerdem habe ich Teile des Manuskripts geschrieben und überarbeitet.

Kapitel 11

Diese Publikation ist in *Molecules* (2016, 21, 1081) veröffentlicht mit dem Titel:

„Emission Enhancement and Intermittency in Polycrystalline Organolead Halide Perovskite Films"

Von Cheng LI, Yu Zhong, Carlos A. M. Luna, Thomas Unger, Konstantin Deichsel, Anna Gräser, Jürgen Köhler, Anna Köhler, Richard Hildner, Sven Hüttner

Ich habe die PL-Spektren, die Quanteneffizienzen für verschiedene Anregungsdichten und die zeitaufgelöste PL mit der TCSPC-Methode gemessen. Des Weiteren war ich bei der Diskussion und Interpretation der Ergebnisse beteiligt und habe einen Teil des Manuskripts geschrieben.

Ultrafast Energy Transfer between Disordered and Highly Planarized Chains of Poly[2-methoxy-5-(2-ethylhexyloxy)-1,4-phenylenevinylene] (MEH-PPV)

In dieser Veröffentlichung sind zeitaufgelöste spektroskopische Untersuchungen an unterschiedlichen Konformationen des Polymers MEH-PPV gelöst in MTHF bei verschiedenen Temperaturen zusammengefasst. Mit Verminderung der Temperatur von 300 – 180 K planarisiert das Polymergrundgerüst. Daraus resultiert eine Rotverschiebung und eine Strukturierung des Absorptionsspektrums (Abb. 22a). Im Bereich zwischen 180 – 120 K bildet sich ein geordneter Zustand der Polymerketten. Die Ketten richten sich mit weiterem Abkühlen weiter aus und treten miteinander in schwache Wechselwirkung. Zu erkennen ist dies im Absorptionsspektrum an einer neuen Absorptionsbande, die bei niedrigen Energien um 2.1 eV erscheint (Abb. 22a). Diese wächst mit sinkender Temperatur, dafür sinkt der Beitrag bei höheren Energien von 2.3-2.8 eV, der der amorphen Phase ungeordneter Polymerketten zugeordnet wird. Die unterschiedlichen Beiträge der geordneten und der ungeordneten Phase lassen sich für verschiedene Temperaturschritte trennen (Abb.22b). Dies ist nur möglich, da ein isosbestischer Punkt bei etwa 2.24eV (siehe Abb. 22a) vorliegt. Es ist das Verhältnis der unterschiedlichen Oszillatorenstärken beider Phasen zu berücksichtigen. In diesem Fall beträgt es etwa eins. Der relative Anteil planarisierter Chromophore, bestimmt aus der Absorption, sättigt bei etwa 30 % für tiefe Temperaturen. Anhand der PL-Spektren wird bei tiefen Temperaturen ein Verhältnis von 100 % ermittelt, weil nach einem Energietransfer die gesamte PL für Temperaturen unterhalb von 160 K ausschließlich von der aggregierten Phase stammt. Mit dem Wissen der Spektren beider Phasen in PL und Absorption lässt sich auf einen sehr effizienten Energietransfer schließen, der mit Hilfe transienter Absorption zeitlich aufgelöst werden kann. Bei einer Pumpenergie von 2.12 eV (585 nm) wird ausschließlich die geordnete Phase angeregt und das transiente Absorptionsspektrum zeigt daher nur den Anteil des *„Ground State Bleach“* (GSB) und der stimulierten Emission (SE) dieser Phase. Durch entsprechendes Skalieren des PL-Spektrums für die entsprechende Temperatur an die transienten Absorptionsspektren lassen sich die Anteile von stimulierter Emission und GSB für verschiedene Verzögerungszeiten trennen. Dies wurde für eine höhere Anregungsenergie (2.48 eV), bei der fast ausschließlich die amorphe Phase absorbiert, wiederholt. Der GSB besteht dann aufgrund des Energietransfers aus Anteilen beider Phasen. Diese lassen sich jedoch mit Hilfe der vorigen Messung ebenfalls separieren (siehe Abb. 23a). Die zugehörigen Spektren wurden integriert und die erhaltenen Anteile bei 120 K sind in Abbildung 23b über die Zeit aufgetragen. Der Anteil zum Zeitpunkt t=0 ist durch die Absorption bei der Anregungswellenlänge gegeben. Nach etwa 1 ps sind nur noch etwa 30% der Anregungen in der amorphen Phase. Für längere Zeiten sättigt der Anteil bei 20%. Der zeitliche Verlauf ist in Übereinstimmung mit dem gängigen Bild eines Transfers, der in mehreren Schritten abläuft und passt zu einer Verteilung von Abständen zwischen Chromophoren der ungeordneten amorphen Phase und der geordneten Phase.

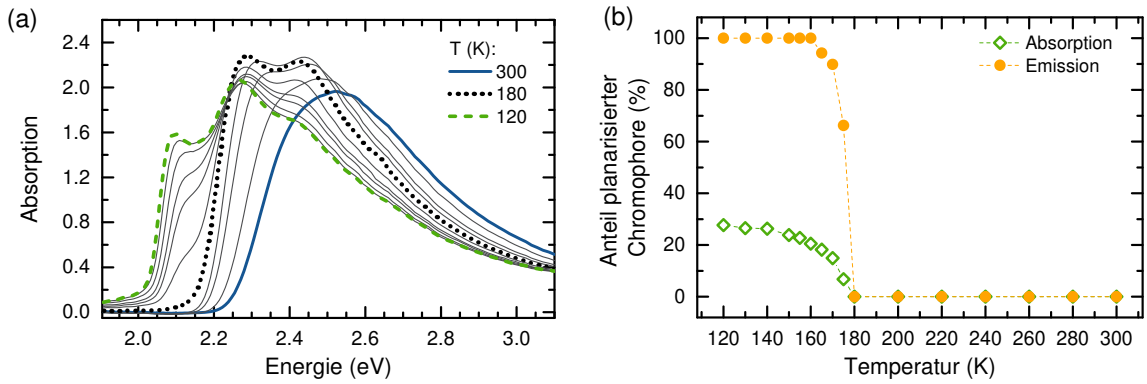

Abbildung 22: (a) Absorption für MEH-PPV in MTHF-Lösung, c=0.2 g/l (b) Anteil der geordneten Phase, abgelesen aus Absorptionsspektren (grün offene Diamanten) sowie aus Fluoreszenzspektren (gefüllte orange Kreise)

Es lässt sich erkennen, dass kurz nach der Anregung der Transfer zu benachbarten Chromophoren der aggregierten Phase überwiegt, der sich im Rahmen der Messgenauigkeit mit einer Zeitkonstante von <500 fs beschreiben lässt. Der Verlauf bei langen Zeiten lässt sich nicht monoexponentiell fitten, sondern hat die Form einer gestreckten Exponentialfunktion. Dies lässt sich durch unterschiedliche Abstände zwischen emittierenden Bereichen der amorphen Phase und dem aggregierten Bereich begründen. Der Parameter ß im Kohlrausch-Williams-Watt Gesetz, das eine gestreckte Exponentialfunktion beschreibt:

$$I(t) = I_0 exp\left[-\left(\frac{t}{t_0}\right)^{\beta}\right]$$

gibt den Grad der Abweichung vom monoexponentiellen Zerfall an und nimmt für einen Förster-Energie-Transfer in drei Dimensionen den Wert 0.5 an. Damit lässt sich der Transferprozess für längere Zeiten mit einer charkteristischen Zeitkonstanten von $t_0 = 1\,ps$ fitten. Aufrund der geringen Transferzeit können man darauf schließen, dass beide Phasen in unmittelbarer Nähe zueinander vorliegen müssen, zum Beispiel, indem Polymerketten an Aggregationskeimen planarisieren aber noch von ungeordnetem Material umgeben sind.

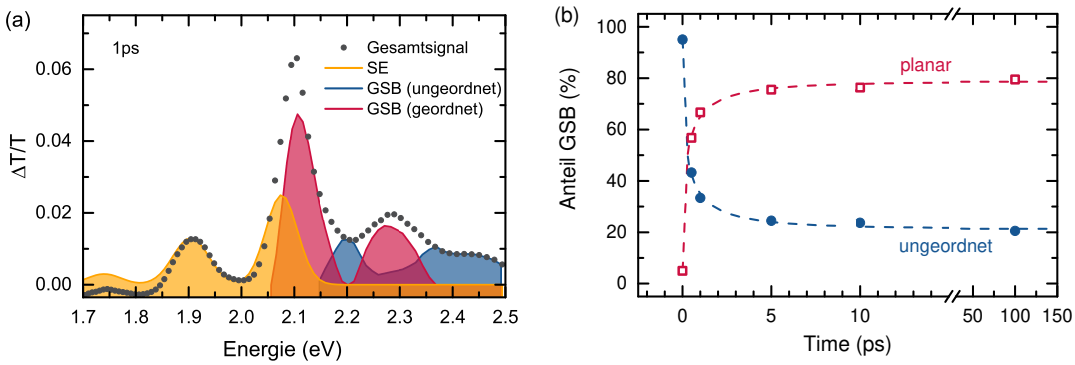

Abbildung 23: (a) Pump-Probe-Spektren für MEH-PPV in MTHF-Lösung, c=0.2 g/l für 1 ps nach Anregung mit 2.48 eV bei 120 K. Die unterschiedlichen Anteile der stimulierten Emission, des GSB der planarisierten und der ungeordneten Phasenanteile sind entsprechend farblich gekennzeichnet. (b) Anteil des GSB der geordneten Chromophore (rote offene Quadrate) oder der ungeordneten (gefüllte blau Kreise) über die Zeit nach der Anregung. Die gestrichelten Linien dienen der Veranschaulichung des Verlaufs.

Relaxation dynamics and exciton energy transfer in the low-temperature phase of MEH-PPV

Nachdem ich in Kapitel 6 die Dynamik zwischen amorphen und aggregierten Phasen am Beispiel des konjugierten Polymers MEH-PPV untersucht habe, soll hier die Anregungsdynamik in der aggregierten geordneten Phase näher untersucht werden. Dazu wurde die Lösung bei 140 K mit Laserpulsen der Energie <2.2 eV, bei der ausschließlich die energetisch niedrigere geordnete Phase absorbiert, angeregt. Dadurch wird die Anregung der amorphen Phase ausgeschlossen. Bei den Untersuchungen kommen sowohl transiente Absorption als auch kohärente 2D-Spektroskopie zum Einsatz um die beitragenden Einzelprozesse zur Dynamik zu trennen. Bei Energien um 2.1 eV werden Zustände im Zentrum der gaußverbreiterten Zustandsdichte angeregt, von wo aus Relaxationsprozesse zu niederen Zustände auftreten können. Um den Beitrag dieser Relaxation zu quantifizieren wurden die Chromophore am unteren Ende der Zustandsdichte bei 2.03 eV angeregt. Die transienten Absorptionsspektren zeigen bei diesen Anregungsenergien strukturierte Banden, die sich analog zu den Spektren in Kapitel 6 den vibronischen Übergängen des GSB (B_{01} und B_{00}) beziehungsweise der stimulierten Emission (SE_{01}) zuordnen lassen (siehe Abb. 24). Um eine genaue Analyse der Dynamik vornehmen zu können, wurde für jedes Spektrum jeweils das erste M_1 und nullte M_0 spektrale Moment ermittelt, die zum einen die Verschiebung der Banden und zum anderen die Besetzungszahl der angeregten Zustände beschreiben. Die Momente sind wie folgt definiert:

$$M_0 = \sum_{\nu_2}^{\nu_2} I(\nu)\Delta\nu$$

$$M_1 = \frac{1}{M_0}\sum_{\nu_1}^{\nu_2} I(\nu)\nu\Delta\nu$$

Dabei sind $\Delta\nu$ das Frequenzintervall, $I(\nu)$ die Intensität des Spektrums und ν_1 und ν_2 die Grenzen der Banden. Die Dyanmik der Besetzungszahl der einzelnen Banden, also des nullten Moments, kann entweder mit einer gestreckten Exponentialfunktion oder einer Multi-Exponentialfunktion mit vier Zerfallszeiten gefittet werden. Letztere entspricht der Beschreibung mit vier unabhängigen Zerfallsprozessen deren Zuordnung zu physikalisch möglichen Ursachen ohne weitere Kenntnisse über das System schwierig ist. Eine gestreckte Exponentialfunktion hingegen würde einer Verteilung von Zerfallsraten entsprechen. Diese wird wahrscheinlich hervorgerufen durch die Varianz an Kettenlängen (PDI=4) und Abständen zwischen den Chromophoren. Betrachtet man das nullte Moment der Bande B_{00} im Überlappbereich von GSB und SE in einer Darstellung nach Kohlrausch-Williams-Watt (siehe Abb. 24b) so fällt auf, dass für Zeiten kleiner als 1 ps ein Anstieg von 1 vorliegt. Dies entspricht einem monoexponentiellen Zerfall und es gibt nur eine charakteristische Zerfallsrate von etwa 220 fs.

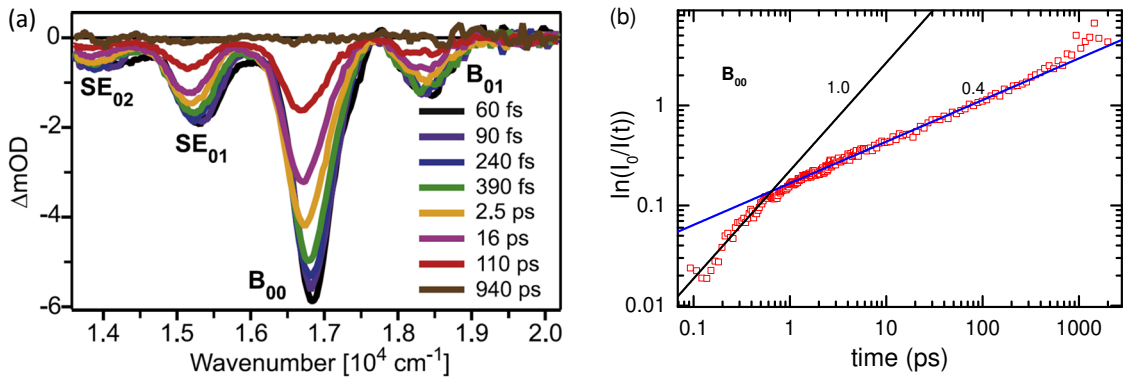

Abbildung 24: (a) transiente Absorptionsspektren bei 140 K nach Anregung bei 2.12 eV für verschiedene Zeiten nach der Anregung (siehe Legende) (b) KWW-Darstellung des nullten Moments des Überlapps von GSB und SE nach Anregung der geordneten Phase (2.12 eV)

Dies kann durch Sprünge zwischen benachbarten Zuständen höherer Energie zu Fallenzuständen wie zum Beispiel Oxidationsprodukten erklärt werden. Bei längeren Zeiten überwiegen Sprünge zu weiter entfernten Zuständen und Fallen und es ergibt sich einer Verteilung von Lebensdauern. Für größere Zeiten beträgt der Anstieg in der KWW-Darstellung etwa 0.4. Er liegt zwischen 1/3 und 0.5, die den zu erwartenden Werten für einen Förster-Energietransfer in zwei bzw. drei Dimensionen entsprechen. Ähnliche Werte für die Anstiege ergeben sich auch für die anderen Banden des Spektrums. Eine Analyse mit 4 verschiedenen Exponentialfunktionen fittet die Daten gleichermaßen und gibt somit gemittelte Lebensdauerwerte der unterschiedlichen Zeitbereiche.

Der Populationsdynamik ist zusätzlich eine spektrale Verschiebung der Banden überlagert, was anhand der ersten spektralen Momente abgelesen werden kann. Die Banden der stimulierten Emission (SE) verschieben nach Anregung mit 2.1 eV auf einer schnelleren Zeitskala von etwa 200-250 fs und einer längeren Zeitskala von etwa 4 ps zu kleineren Energien um etwa 11 meV. Bei Anregung am unteren Ende der Zustandsdicht mit 2.03 eV wird keine weitere Verschiebung der Bänder und damit auch keine Relaxation beobachtet.

Nicht nur in den transienten Absorptionsdaten auch in den 2D-Spektren erkennt man, dass die Bänder der stimulierten Emission auf einer Zeitskala von ca. 4 ps eine Rotverschiebung zu kleineren Energien zeigen. Dies entspricht der Relaxation lokalisierter Exzitonen zum unteren Ende der Zustandsdichte. Zusätzlich geht aus den 2D-Spektren hervor, dass es innerhalb von 30 fs zur Lokalisierung der Anregung kommt, da nach Anregung bei 2.1 eV nur die Banden der stimulierten Emission rotverschieben nicht jedoch die Bande des GSB. Die Ergebnisse aus transienter Absorption und der Analyse der 2D-Spektren für die Dynamik der aggregierten Phase von MEH-PPV bei 140 K sind in Abbildung 25 schematisch zusammengefasst.

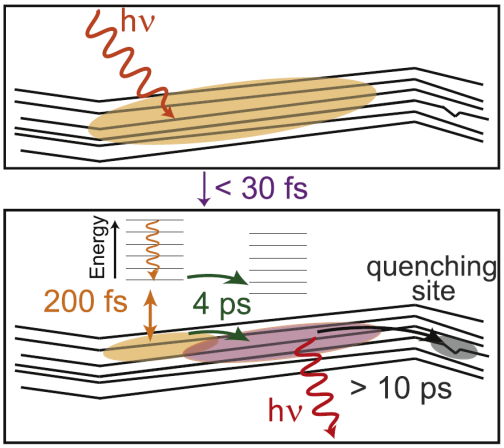

Abbildung 25: Schema der Anregungsdynamik innerhalb der aggregierten Phase von MEH-PPV in Lösung unterhalb der Übergangstemperatur.

Excited State Dynamics and Conformations of a Cu(II)-Phthalocyanine-Perylenebisimide Dyad

Nachdem wir in den vorhergehenden Abschnitten die Photophysik eines einzelnen Materialsystems näher betrachtet haben, wenden wir uns nun gemischten Systemen zu. Diese bestehen aus Komponenten, die nach einer Photoanregung dazu neigen Elektronen abzugeben (Elektrondonor) und anderen, die diese Elektronen aufnehmen (Elektronakzeptor). Eine Möglichkeit besteht darin beide Einheiten chemisch zu koppeln, zum Beispiel in einer sogenannten Dyade. In dem hier vorliegenden Fall besteht der eine Teil aus einem Cu(II)-Phthalocyanin (CuPc) und der andere aus dem Derivat eines Perylenebisimides (PBI). Beide sind über eine etwa 3 nm lange flexible aliphatische Kette kovalent gebunden. CuPc und PBI-Derivate sind bekannt dafür als Donor- und Akzeptoreinheit in einer organischen Solarzelle zu fungieren und wurden zum Beispiel von Tang in der ersten Veröffentlichung zu diesem Thema verwendet (C. W. Tang, *Two-layer organic photovoltaic cell*, Appl. Phys. Lett. 1986, 48, 2, 183-185). Gemeinsam mit K. Wilma und Koautoren untersuchte ich, wie sich die Konformation und die Photophysik im Vergleich zu den einzelnen Komponenten verändern. Rechnungen zur Moleküldynamik (MD), die auch die Lösungsmittelumgebung berücksichtigen, deuten auf drei mögliche Konformationszustände hin, in der die Dyade im Lösungsmittel Toluol vorliegen kann. Die freie Energie als Funktion des Abstands der Schwerpunkte beider Einheiten hat drei Minima und damit drei mögliche Konformationszustände (siehe Abb. 26a). Der Zustand mit der geringsten Wahrscheinlichkeit ist der offene Zustand (OPEN), bei der beide Einheiten einen Abstand von etwa 2.6 nm haben. Beim zweithäufigsten Zustand beträgt der Abstand 1 nm. In diesem Fall stehen die Einheiten mit den Molekülebenen senkrecht aufeinander und die aliphatische Verbindung ist gebogen. Mit einer sehr hohen Wahrscheinlichkeit (etwa 99 %) befindet sich die Dyade jedoch im gefalteten Zustand (FOLDED),

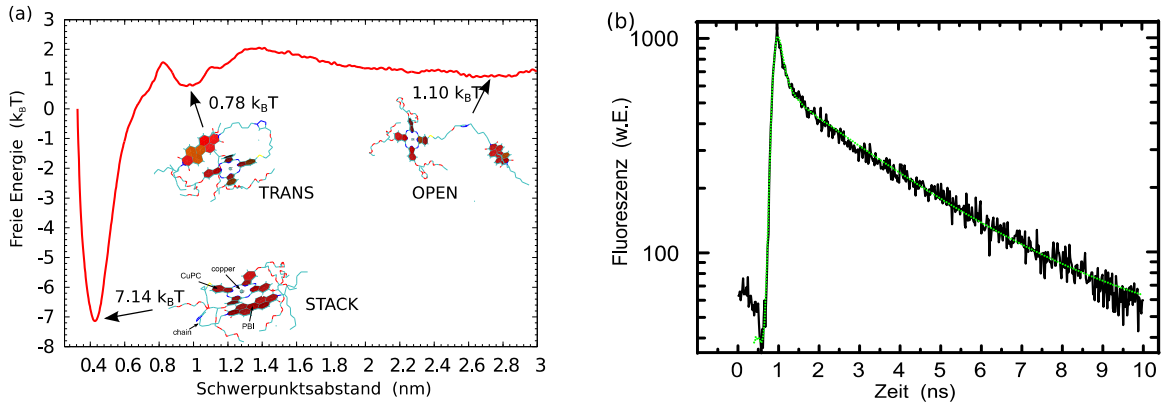

Abbildung 26: (a) MD-Simulation der Freien Energie als Funktion des Schwerpunktabstandes beider Moleküleinheiten in Lösung (Toluol). Die Simulationen wurden von Manuel Hollfelder am Lehrstuhl von Prof. Stefan Gekle durchgeführt. (b) Transiente Fluoreszenzmessung des integrierten Dyade-Spektrums nach Anregung mit 450 nm (2.76 eV) (parallele Polarisation). Die Messungen wurden von Kevin Wilma am Lehrstuhl EP4 mit einer Streak-Kamera durchgeführt.

wobei der Abstand nur etwa 0.5 nm beträgt und beide Molekülebenen parallel ausgerichtet sind. Anhand der transienten Fluoreszenz des PBIs lässt sich schließen, dass es einen dunklen, nicht emittierenden Zustand im System gibt, da das Signal einen klaren bi-exponentiellen Zerfall mit zwei Zerfallszeiten zeigt (siehe Abb. 26b). Die kürzere von beiden liegt unterhalb der zeitlichen Auflösungsgrenze des Messsystems (<100 ps). Die größere beträgt etwa 3.5 ns und entspricht der Zerfallsdauer der PBI-Komponente. Der Wert deckt sich ebenfalls mit Literaturwerten und entspricht der intrinsischen Singulettlebensdauer vom PBI. Um den Ursprung der schnellen Zerfallskomponente aufzudecken habe ich Pump-Probe Spektren gemessen, um eventuelle dunkle Zustände aufzudecken. Nach Anregung des PBI-Teils der Dyade (aus technischen Gründen bei 510 nm, 2.43 eV) erscheint im Bereich von 500-600 nm ein induziertes Signal („excited state absorption“, ESA) sowie der GSB des CuPc zwischen 650 und 700 nm. Beide steigen innerhalb von 2-3 ps nach dem Anregungspuls an (siehe Abbildung 27a und b).

Wir schließen daraus, dass die Anregungsenergie vom PBI auf das CuPc innerhalb der Dyade übertragen wird, andernfalls wäre der GSB von CuPc nicht zu erkennen. Da er auftritt, sobald das CuPc angeregt ist, entspricht der Anstieg des Signals der Rate des Energietransfers.

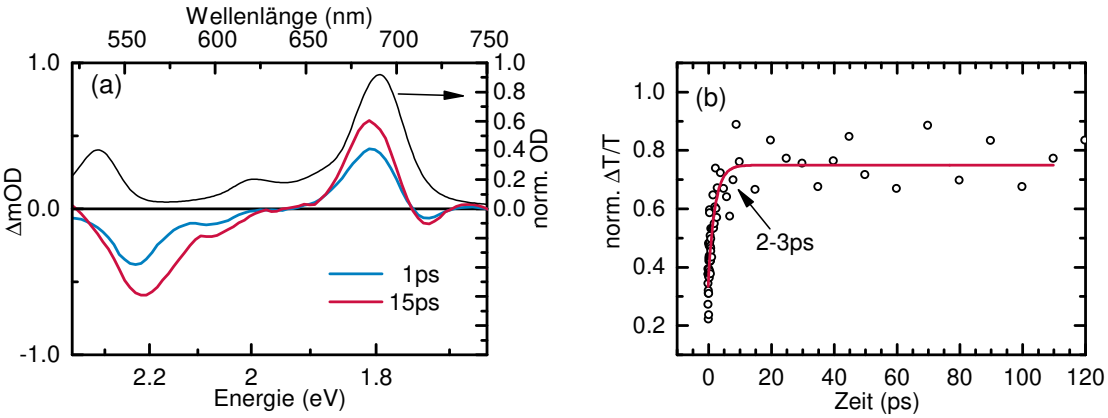

Abbildung 27: (a) Pump-Probe-Spektren der Dyade in Lösung (Toluol) nach Anregung bei 510 nm für 1 ps (blau) und 15 ps (rot), Absorptionsspektrum der Dyade (schwarz) (b) Transiente der Absorption der Dyade nach Anregung mit 510 nm (2.76 eV) (parallele Polarisation) gemessen bei 680 nm (GSB der CuPc-Komponente) mit exponentiellem Fit (rote Linie).

Durch den Vergleich der gemessenen Spektren der Dyade mit Pump-Probe-Spektren von CuPc und PBI in älteren Publikationen können wir die induzierte Bande (ESA) der Triplett-Absorption, also dem Übergang T_1->T_n, der CuPc-Komponente zuordnen. Wie viele andere Metallkomplexe besitzt auch CuPc eine hohe Intersystem-Crossing-Rate. Das heißt, nach dem Energietransfer geht CuPc vom Singulett- in den angeregten Triplett-Zustand über. Dies geschieht unterhalb der Zeitauflösung des Systems, so dass ESA und GSB des CuPc mit der gleichen Rate ansteigen.

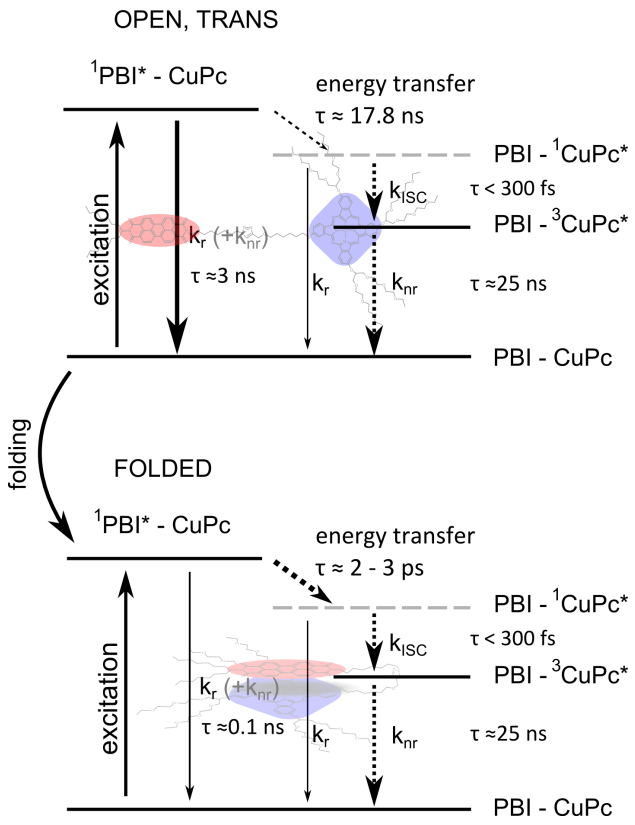

Abbildung 28 Energie-Diagramm der Dyade in Lösung (Toluol) nach Anregung der PBI-Komponente bei 510 nm, Übergänge zwischen den einzelnen Zuständen sind durch Pfeile gekennzeichnet.

Die Lebensdauer der induzierten Bande habe ich in Zusammenarbeit mit einem Koautor an einem Aufbau für transiente Absorption im Nanosekunden-Bereich zu 25 ns bestimmt. Dies entspricht laut Literatur der Triplettlebensdauer von CuPc. Die Spektren sind konsistent mit den Messungen im Pikosekunden-Bereich. Die gleichen Messungen wurden an der reinen CuPc-Komponente wiederholt. Spektren und gemessene Lebenszeiten stimmen für den Nanosekundenbereich mit den Daten der Dyade überein. Da die Dyade mit einer sehr hohen Wahrscheinlichkeit von über 99 % im gefalteten Zustand vorliegt, ordnen wir diesem auch den beobachteten Energietransfer zu. In Abbildung 28 ist die Dynamik des geöffneten und des gefalteten Zustands der Dyade durch Übergangsraten in einem Energie-Diagramm schematisch dargestellt. Im geöffneten Fall relaxiert das System hauptsächlich über den strahlenden Zerfall des PBI in den Grundzustand und nur ein kleiner Teil der Anregung geht über einen Förster-Transfer auf den CuPc-Teil über. Der Großteil der Moleküle liegt jedoch im gefalteten Zustand vor (99 %) in der die Anregungsenergie innerhalb weniger Pikosekunden auf das CuPc übertragen wird und dort einen Triplettzustand bildet, welcher nicht-radiativ zerfällt.

The Impact of Driving Force and Temperature on the Electron Transfer in Donor-Acceptor Blend Systems

Nachdem in den vorigen Abschnitten einzelne Schritte der Ladungsträgertrennung näher untersucht wurden, also Diffusion zur Grenzfläche oder konkurrierende Prozesse wie Triplettbildung, betrachte ich in dieser Veröffentlichung die Exzitonendissoziation in einem Blend-Film. Hierbei sind Donor- und Akzeptoreinheiten nicht chemisch miteinander verbunden sondern bilden Mischsysteme (Blend-Filme), welche die aktive Schicht in organischen Solarzellen darstellen.

In dieser Veröffentlichung wird untersucht inwieweit, die Änderung der freien Enthalpie ΔG_0 als Triebkraft des Elektronentransfers und die Temperatur eine Rolle beim ersten Schritt der Exzitonendissoziation, also der Bildung eines ladungsgetrennten Zustands (CT-Zustand), spielen. In der Fachgemeinschaft werden die Einflüsse quantenmechanischer Effekte, der treibenden Kraft und der Temperatur kontrovers diskutiert. Um mehr Klarheit zu bekommen habe ich verschiedene Donor-Polymere (PCPDTBT, PTB7 und MeLPPP) mit dem häufig verwendenten Akzeptor $PC_{60}BM$ gemischt und mittels transienter Absorption den Anstieg des Kations nach Anregung des Donorpolymers temperaturabhängig gemessen. Zuvor wurde durch chemisches Dotieren der Polymerfilme mit einer Eisenchlorid-Lösung das Absorptionsspektrum des auftretenden Kations identifiziert. Für die Systeme PTB7 und PCPDTBT liegt das Maximum der Kationabsorption entsprechend bei etwa 1200 und 1100 nm. Die Absorptionsbanden sind jeweils sehr breit, so dass für beide Systeme 1120 nm als Abfrage-Wellenlänge benutzt wurde. Das Absorptionsmaximum des MeLPPP-Kations wird bei 650 nm detektiert (siehe Abb. 29). Die freie Enthalpie ΔG_0, die die treibende Kraft des Elektronentransfers darstellt, variiert für die hier betrachteten Systeme zwischen -0.2 und -1.1 eV. Die Werte für ΔG_0 wurden aus den Literaturwerten der Singulettenergie des jeweiligen Donorpolymers und der CT-Zustandsenergie im Blend ermittelt. Es wurde darauf geachtet, dass die Werte für die CT-Zustandsenergie sowie für die Reorganisationsenergie aus den Spektren der externen Quanteneffizienz (EQE) und CT-Emissionsspektren ermittelt wurden. Für MeLPPP:PCBM wurden sie aus EQE-Spektren und CT-Emissionsspektren experimentell bestimmt. Im Blendsystem PCPDTBT:PCBM ist die gemessene Transferrate jeweils für Raumtemperatur und für tiefe Temperaturen (12 K) durch die Auflösung des Messaufbaus begrenzt und liegt bei $\geq 3\times10^{12}s^{-1}$. Für Blend-Filme des Systems PTB7:$PC_{60}BM$ haben Ward und andere (Ward et al Adv. Mater. 2015, 27, 2496) mittels PL-Quenching eine Rate gemessen, die bei $k=7\times10^{11}\ s^{-1}$ liegt.

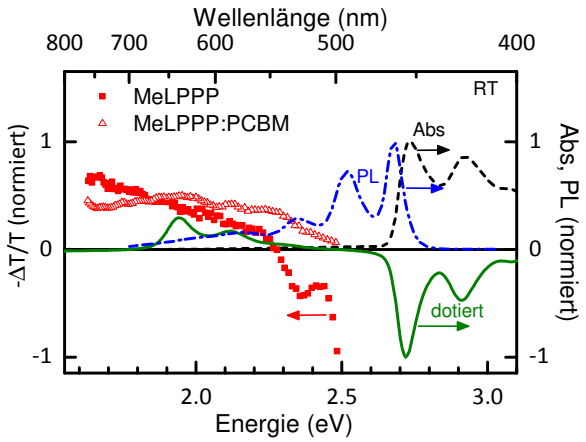

Abbildung 29: Pump-Probe Spektren für MeLPPP Blend-Film und für Polymerfilm von MeLPPP nach Anregung bei 400 nm, sowie Absorptions- und Emissionsspektrum von MeLPPP und Differenzspektrum eines MeLPPP-Films nach Dotierung in $FeCl_3$.

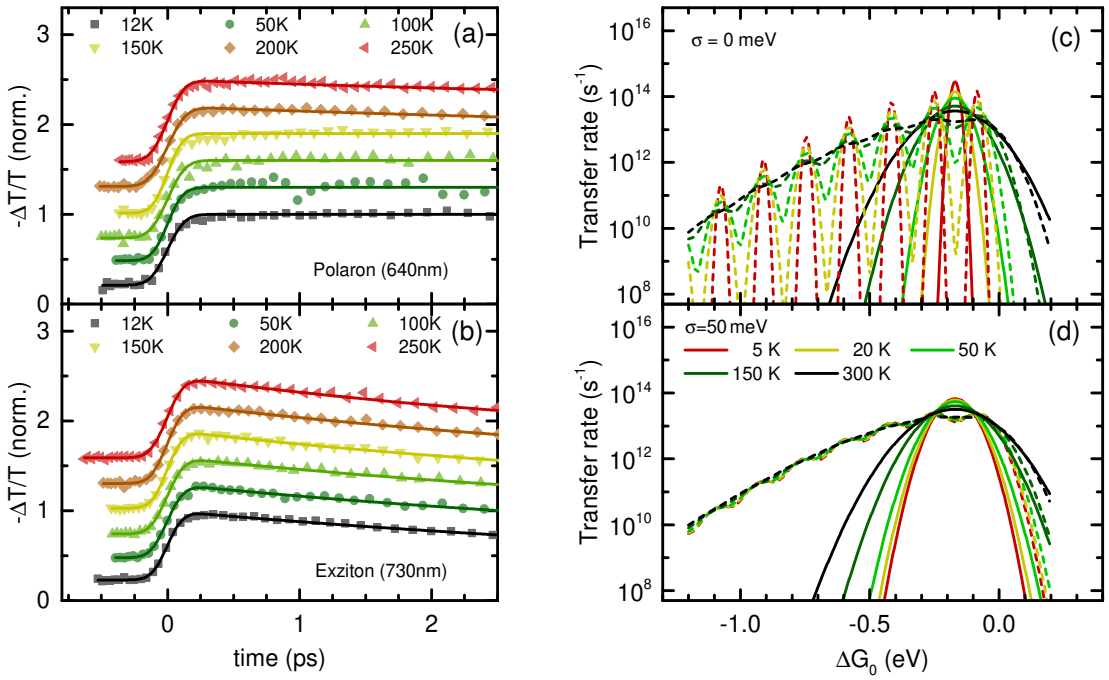

Abbildung 30: (a) Anstieg des Polaronsignals und (b) des Exzitons für MeLPPP:PC_{60}BM Blend-Film für verschiedene Temperaturen nach Anregung bei 400 nm mit etwa 15 µJ/cm² und (c) die theoretische Transferrate aufgetragen über ΔG_0 nach dem Markus-Modell (durchgezogene Linien) und dem Modell nach Levich-Jortner (gestrichtelte Linien) ohne Einfluss der statischen Unordnung für eine effektive vibronische Mode von 165 meV und zugehörigem Huang-Rhys-Parameter S=1 und (d) für beide Modelle mit einer gaußverbreiterten Zustandsdichte der Breite $\sigma = 50\ meV$.

Dies konnte durch unsere Messungen mit transienter Absorption nicht bestätigt werden. Wir messen sowohl bei Raumtemperatur als auch bei 12 K eine durch unseren Aufbau begrenzte Rate von $\geq 3\times10^{12}s^{-1}$. Bei beiden Blend-Systemen liegen Reorganisationsenergie λ und negative freie Enthalpieänderung $-\Delta G_0$ nur um wenige meV auseinander, dadurch wird nach der Theorie von Marcus die Rate des Transfers maximal. Zusätzlich ist die Rate nur

schwach temperaturabhängig und steigt sogar leicht mit sinkender Temperatur. Im Rahmen des Wertebereichs der Parameter aus der Literatur für PCPDTBT und PTB7 lässt sich also nicht entscheiden, ob die Theorie nach Marcus zur prinzipiellen Beschreibung des Elektronentranfers geeignet ist, da ΔG_0 und λ von gleicher Größe aber unterschiedlichem Vorzeichen sind. Für das MeLPPP:PCBM-System liegt die treibende Kraft ΔG_0 bei ca. -1.1 eV und gleichzeitig ist die Reorganisationsenergie relativ klein (<0.2 eV). Aus diesem Grund sollte die Rate nach der Theorie von Marcus bei Raumtemperatur verschwindend klein (etwa 10^{-30} s^{-1}) sein. Wir beobachten jedoch ebenfalls eine Transferrate, die durch die Auflösung begrenzt ist, was auch konsistent mit beobachteten Solarzelleffizienzen in der Literatur ist. Ebenso zeigt auch die Transferrate im MeLPPP:PCBM-System keine Temperaturabhängigkeit. Innerhalb der Auflösungsgrenze des Messsystems sieht man im Bereich von 300 bis 12 K keine Verlangsamung im Anstieg des Polaron-Signals (siehe Abb. 30a). Die Reorganisationsenergie λ ist viel kleiner als der negative Wert der freien Enthalpieänderung - ΔG_0, daher liegt hier das „inverse Marcus-Regime“ vor. Das Marcus-Modell verliert hier seine Gültigkeit, da zunehmend vibronische Schwingungen quantenmechanisch an den Transfer koppeln. In der Erweiterung zum Marcus-Modell von Marcus-Levich-Jortner (MLJ) werden diese mit einem entsprechenden Huang-Rhys-Parameter berücksichtigt (vgl. Kapitel 2.3). In Abbildung 30c sind die theoretischen Raten für verschiedene Temperaturen sowohl für das Marcus-Modell (volle Linie) als auch nach MLJ (gestrichelte Linien) dargestellt. Allgemein wird die Temperaturabhängigkeit im MLJ-Modell reduziert und auch für größere Abstände zwischen der Reorganisationsenergie und ΔG_0 nimmt die Rate im inversen Regime um Größenordnungen zu. Allerdings ist sie für Temperaturen kleiner 50 K entscheidend von den genauen Parameterwerten für λ bzw. ΔG_0 abhängig. Dies ist an der starken Modulation der Transferrate bei tieferen Temperaturen zu erkennen. Berücksichtigt man zusätzlich eine gewisse gaußsche Verteilung, was einer für organische Halbleiter typischen statischen Unordnung entspricht, ergeben sich entsprechend veränderte Raten, wie in Abbildung 30d gezeigt ist. Dies erreicht man durch eine Faltung der Raten von MLJ und Marcus mit einer gaußschen Verteilung der Breite σ. Ein Wert von $\sigma = 50\,meV$ wurde hier als typischer Mittelwert gewählt. Man erkennt, dass besonders bei tiefen Temperaturen die Transferrate im Marcus-Modell für einen größeren Bereich der treibenden Kraft größer geworden ist. Beim Modell von MLJ ist die Temperaturabhängigkeit im Bereich des „inversen“ Regimes praktisch verschwunden. Diese Erweiterung erklärt zumindest die fehlende Temperaturabhängigkeit in den gemessenen Raten beim MeLPPP:PCBM-System. Betrachtet man allgemein Donor-Akzeptor-Systeme, von denen die meisten Werte für ΔG_0 zwischen -0.1 und 0.5 eV haben und die Reorganisationsenergie λ typischerweise um 0.3 eV liegt, so fällt auf, dass sowohl beim Marcus-Modell als auch bei MLJ immer Raten über 10^{13} s^{-1} erreicht werden und die Abhängigkeit des Transfers von der treibenden Kraft vernachlässigbar ist. Nicht-adiabatische Modelle wie Marcus-Modell oder MLJ verlieren für die meisten Solarzellsysteme, mit typischerweise großen Transferraten, an Gültigkeit und sind nicht mehr geeignet die grundlegenden Prozesse der Exzitonentrennung zu beschreiben.

The Role of PbI_2 on Perovskite Stability, Device Parameters and Degradation

Nicht nur in rein organischen Solarzellsystemen, sondern auch in hybriden Perowskit-Strukturen beeinflusst die Morphologie die Erzeugung und Rekombination von Ladungsträgern. In nur wenigen Jahren konnte eine erhebliche Steigerung der Effizienz in Solarzellen allein durch Variation der Prozessierungsbedingungen erreicht werden. So ist zum Beispiel bekannt, dass Änderungen im stöchiometrischen Verhältnis von Methylammoniumiodid (MAI) und PbI_2 einen positiven Einfluss auf die Effizienz haben kann. Insbesondere ein leichter Überschuss an PbI_2 von wenigen Prozent in der Ausgangslösung, aus dem die Filme prozessiert werden, steigert den Wirkungsgrad. Die Ursache dafür ist bisher unklar. Ebenso wenig ist geklärt, wie sich der Überschuss auf andere Solarzellparameter wie Stabilität, Hysterese und die optischen Eigenschaften auswirkt. Um einen höheren PbI_2-Gehalt in Filmen aus dem Perowskit $CH_3NH_3PbI_3$ zu erhalten, wurden die verwendeten Filme in einer sogenannten „dampfgestützten Umwandlungsmethode“ hergestellt, bei der ein Bleiiodid-Film in einer MAI-Atmosphäre umgewandelt wird. Die fertigen Filme wurden dann für längere Zeit bei 165°C erhitzt. Die Dauer des Erhitzens bestimmt den unterschiedlichen Anteil an zusätzlichem PbI_2 im Film. Es wurden fünf unterschiedliche Zeitintervalle verwendet, nämlich 0, 15, 30, 45 und 60 Minuten, um entsprechend 0, 21, 34, 44 und 48 % zusätzlichen Anteil PbI_2 zu erhalten. Diese Anteile wurden aus XRD-Messungen durch Vergleich des jeweiligen PbI_2-Signals und dem Perowskit-Signal bestimmt. Es ist bekannt, dass bei dieser Herstellungsmethode der Filme die Filmstruktur kompakt ist. Das heißt es existieren fast keine Hohlräume zwischen den Kristalliten. In SEM-Aufnahmen der verschiedenen Filme sieht man, dass mit zunehmender Heizdauer die Abstände zwischen den Korngrenzen größer werden. Zusätzlich deuten Röntgenbeugungsdaten darauf hin, dass an den Rändern die Perowskit-Struktur zersetzt wird und kristallines PbI_2 entsteht.

Anhand von Absorptionsmessungen mit einer Ulbrichtkugel und Berücksichtigung der Tauc-Relation für direkte Halbleiter lässt sich die optische Bandlücke aus dem Schnittpunkt einer Fitgeraden mit der y-Achse ablesen (Abb. 31a). Die optische Bandlücke ist für alle Filme konstant bei etwa 1.6 eV. Des Weiteren zeigen die Absorptionsspektren der Substrate mit längeren Heizdauern eine Schulter bei etwa 500 nm, die ebenfalls ein Indiz für die Absorption von kristallinem PbI_2 ist. In den PL-Spektren ist die für polykristalline $MAPbI_3$-Filme typische Emission mit Maximum bei 780 nm zu erkennen. Sie resultiert aus der Rekombination freier Ladungsträger. Die PL-Intensität ist umso größer, je länger die Heizdauer der Filme war (Abb. 31b). Um den Einfluss von Luftfeuchtigkeit und Sauerstoff auf die Stabilität der Filme und Solarzellen zu untersuchen, haben wir sie über einen Monat lang bei etwa 50 % Luftfeuchtigkeit unter normalen Atmosphärenbedingungen gelagert und PL-Spektren und Quanteneffizienzen in regelmäßigen Abständen gemessen.

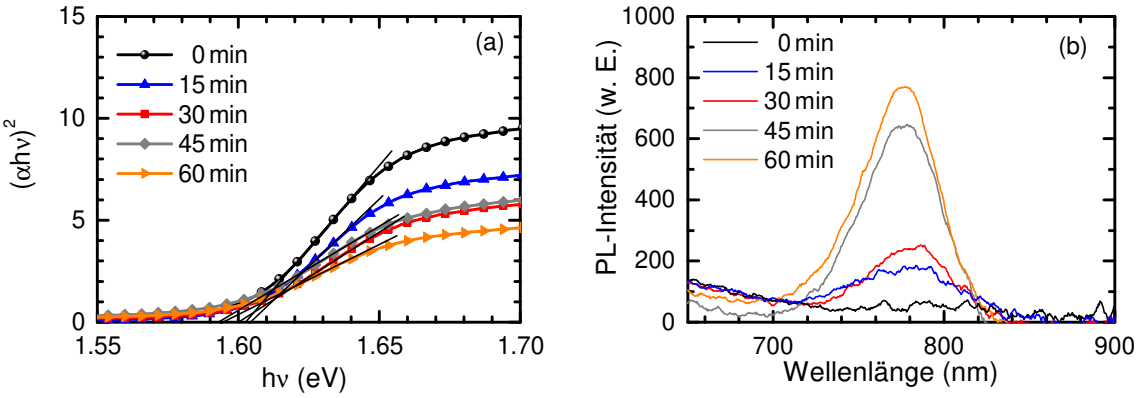

Abbildung 31: (a) Tauc-Darstellung der Absorptionskante für Perowskit-Filme mit unterschiedlichem Anteil an zusätzlichem PbI_2 (siehe Legende). Gerade Linien sind Fitgeraden entsprechend der Tauc-Relation (b) Photolumineszenz-Spektren für die Filme mit 0-60 min Erhitzungsdauer für Anregung bei 485 nm.

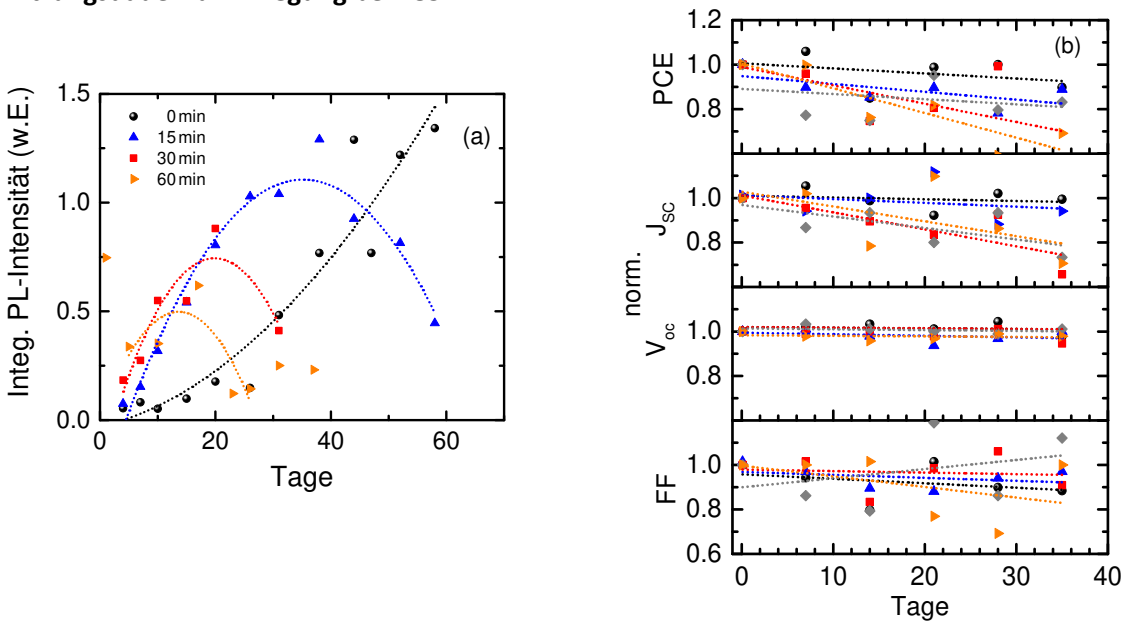

Abbildung 32: (a) PL Intensität über Lagerungszeit und (b) Solarzellparameter (PCE, Jsc, Voc and FF) über Lagerungszeit für 0 min (schwarze Punkte), 15 min (blaue Dreiecke), 30 min (rote Quadrate) and 60 min (orange Dreiecke).

Mit zunehmender Lagerungszeit, nimmt die Intensität der PL für den Referenzfilm mit 0 min stetig zu. Bei den Filmen mit höherem Anteil an PbI_2 steigt die Anfgangsintensität mit steigendem PbI_2-Anteil, jedoch erreichen sie ihre maximale Intensität bei immer kürzerer Lagerungszeit und der maximale Intensitätswert nimmt mit zunehmender Lagerungszeit ab (Abb. 32a). Der erhöhte PbI_2-Anteil führt nur bei frisch hergestellten Filmen zu einer verbesserten PL-Quanteneffizienz. In der Literatur ist bekannt, dass neben der Solarzelleffizienz (PCE) auch die PL-Quanteneffizienz für einen gewissen Überschussanteil an PbI_2 ein Maximum annimmt. Dies passt zu unseren Ergebnissen, dass die PL-Intensität mit

zunehmender Lagerungszeit ebenfalls ansteigt. Der relative Verlauf der PL-Intensität ist daher eng mit dem Grad der Degradation verbunden.

Aufgrund des Zellaufbaus mit luftempfindlichen Elektroden wurden die Solarzellen unter Stickstoffatmosphäre gelagert. Die Degradationsdynamik läuft daher langsamer ab, als an Luft. Degradationseffekte sind jedoch auch hier zu erkennen. Während Leerlaufspannung (V_{OC}) und Füllfaktor (FF) für alle Filme (0 min-60 min) über einen Monat hinweg stabil sind, bleiben Effizienz (PCE) und Kurzschlussstrom (J_{SC}) nur für die Filme mit 0 und 15 min Erhitzungsdauer in etwa konstant. Trotz relativ großer Streuung von ≈10 % lässt sich durch Anlegen von Fitgeraden in Abbildung 32b erkennen, dass Effizienz und Kurzschlussstrom mit zunehmendem PbI_2-Gehalt teilweise um über 30 % abnehmen, trotz Lagerung in Stickstoff-Atmosphäre. Nicht nur die Solarzellen-Parameter zeigen, dass Filme ohne zusätzliches PbI_2 am stabilisten sind. Auch UV-Vis Absorptionsmessungen an Luft gelagerter Filmen belegen, dass auch nach 30 Tagen keine Degradation an Luft zu erkennen ist. Wir haben zudem festgestellt, dass die relative PL-Intensität auf den Grad der Degradation sensitiv reagiert, da leichte die veränderte Kristallitoberfläche großen Einfluss auf die strahlende bzw. nichtstrahlende Rekombinationsrate der Elektronen und Löcher hat.

Emission Enhancement and Intermittency in Polycrystalline Organolead Halide Perovskite Films

Es ist weitestgehend akzeptiert, dass die Ladungsträgerdissoziation in Perowskit-Filmen analog zu anorganischen Halbleitern aufgrund der geringen Exzitonbindungsenergie sehr effizient ist. Dies wird dem hohen Grad an Kristallinität und der hohen Dielektrizitätskonstante zugeordnet. Die Effizienz der Solarzellen aus polykristallinen Filmen ist jedoch durch nichtstrahlende Verlustkanäle begrenzt. Im vorigen Abschnitt wurde deutlich, dass die Qualität der Filme, abhängig von der Prozessierung, einen starken Einfluss auf die Rekombination der Ladungsträger und damit auf die Photolumineszenz hat. Mittels konfokaler Mikroskopie lässt sich die Morphologie der polykristallinen Filme mit der Dynamik der Photoanregungen verbinden um so mögliche nichtstrahlende Prozesse aufzudecken und zu identifizieren.

Die hier untersuchten Perowskit-Filme wurden von Cheng Li mit einer „ein-Schritt-Methode“ hergestellt, d.h. Bleichlorid ($PbCl_2$) und Methylammonium-Iodid (MAI) wurden beide in Lösung gemischt und auf ein Substrat aufgebracht. Durch Aufheizen bei 180°C für eine Stunde bildet sich dann die polykristalline Perowskit-Struktur. Zur Charakterisierung der Filme habe ich PL-Quanteneffizienzen und transiente PL an Filmen auf Quarzglas gemessen. Die Daten zeigen, dass die Quanteneffizienz bei niedrigen Anregungsintensitäten (<20 mW/cm^2) klein ist, mit steigender Intensität rasch zunimmt und ab etwa 60 mW/cm^2 bei 30% sättigt. In diesem Bereich ist die PL durch die bimolekulare Rekombination von Elektronen aus dem Leitungsband und Löchern aus dem Valenzband in der Nähe der Oberfläche der Kristallite dominiert, was an der für polykristalline Filme typischen Emission mit Maximum bei 785 nm zu erkennen ist (siehe Abb. 33a). Die bimolekulare Rekombination lässt sich an der PL-Abklingkurve erkennen, die mit einem bimolekularen Fit der Form $I(t) = I_0/(1 + \beta I_0 t)$ beschrieben werden kann (Abb. 33b).

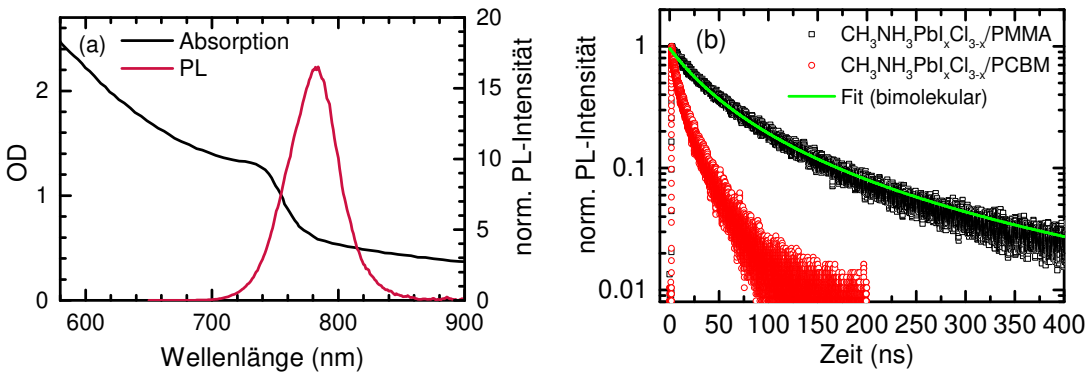

Abbildung 33: (a) Absorptions- und PL-Spektrum eines Zweischichtfilms aus $MAPbI_xCL_{3-x}$ und PMMA (b) normierte transiente PL für Zweischichtfilm aus $MAPbI_xCL_{3-x}$+PMMA (schwarze Linie) und Zweischichtfilm aus Perowskit+PCBM (rote Linie)

Schaut man sich die PL mit einem Mikroskop an, erkannt man, dass einige einzelne Kristallite für mehrere Sekunden völlig dunkel bleiben. Dieses Phänomen ist bisher nur bei Messungen an Einzelkristallen bekannt. Ein Problem bei der Identifizierung dieser An- und Auszustände der einzelnen Kristallite ist die teilweise Überstrahlung durch die PL benachbarter Kristallite, da diese ebenfalls von der Sammellinse eingefangen wird. Zur Hintergrundkorrektur muss man den über einen ausreichend großen Bereich über den gleichen Zeitraum vermessen um den zeitlichen Verlauf der Hintergrundemission zu erhalten, denn durch einen Effekt, der im englischen „light Soaking“ genannt wird, steigt mit zunehmender Belichtungszeit die Intensität biexponentiell an. Integriert man nun über einzelne Kristallite wie zum Beispiel der orange markierte Kreis in Abbildung 34a, und zieht die Hintergrundemission ab, so ergibt sich ein PL-Intensitätsverlauf wie in Abbildung 34b. Es zeigen sich Intensitätsunterschiede zwischen hellen und dunklen Zuständen. Die Identifizierung solcher "An"- und "Aus"-Zustände ist in Abbildung 34b an längeren Zeitintervallen von bis zu 10-20 s zu erkennen. Dieses "Blinken" wird durch einen nichtstrahlenden Rekombinationsmechanismus verursacht. Um diesen aufzuklären und festzustellen, welchen Einfluss Ladungsträger dabei spielen, wird eine Schicht eines Elektronen-Akzeptors (PCBM) aufgebracht. Nach der Erzeugung freier Ladungsträger durch die Laseranregung gehen Elektronen an der Grenzfläche auf den Akzeptor über, so dass die Elektronendichte in der Perowskitschicht sinkt. Dies konnte ich auch an Messungen der transienten PL mit Pikosekunden Auflösung, erkennen, da die PL-Intenisität mit Akzeptorschicht deutlich schneller abfällt (siehe Abb. 33b). Deren Verlauf lässt sich mit einem Diffusionsmodell der Ladungsträger zur Grenzfläche sehr gut beschreiben. Des Weiteren konnte ich eine deutlich reduzierte PL-Quanteneffizienz feststellen. In Filmen mit Akzeptorschicht lassen sich kaum Kristallite finden, deren Intensitätsverlauf oberhalb der Auflösungsgrenze, nach Abzug der Hintergrund-PL, liegt. Das Löschen der PL durch den Elektronenakzeptor und Hinweise in der Literatur legen nahe, dass gefangene Elektronen in einem Auger-Mechanismus strahlende Rekombination benachbarter Ladungsträger verhindern und so die PL einzelner Kristallite "ausschalten".

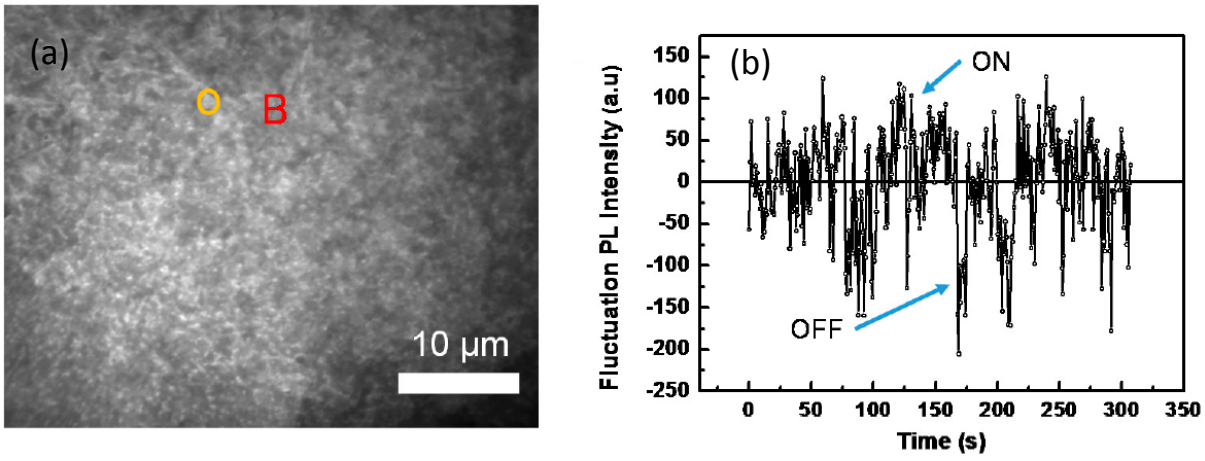

Abbildung 34: (a) Mikroskopaufnahme eines $CH_3NH_3PbI_xCl_{3-x}$ dünnen Films mit PMMA als Versiegelung (b) räumlich integriertes PL-Signal bei 780 nm aus dem markierten runden Bereich in Abbildung a) in Abhängigkeit der Belichtungszeit.

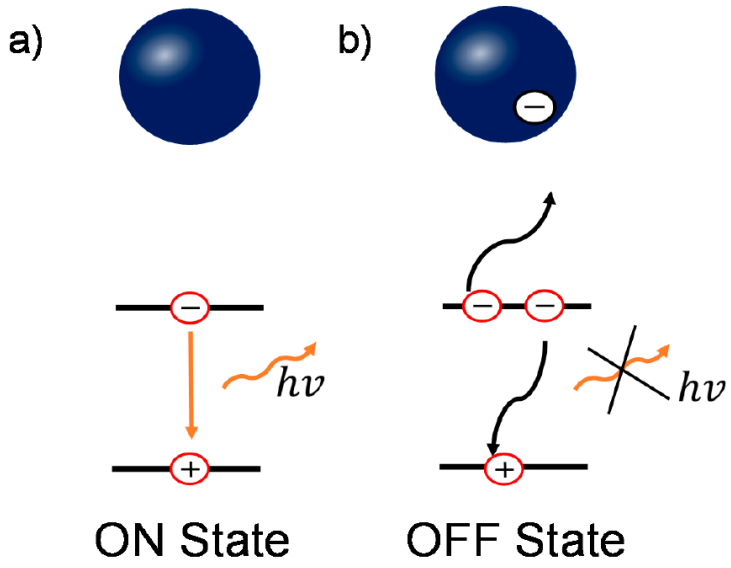

Abbildung 35: (a) im ungeladenen Zustand des Kristallits ist die radiative Rekombination freier Ladungsträger dominant, dagegen (b) im geladenen Zustand die nichtstrahlende Auger-Rekombination wobei ein weiteres Elektron die Energie aufnimmt.

Obwohl die PL-Transienten bimolekulare Rekombination freier Ladungsträger zeigen, findet man in den Mikroskopieaufnahmen Hinweise für einzelne lokale Auger-Rekombinationsprozesse. Diese machen sich jedoch in den Transienten, die über einen großen Bereich integrieren, erst bei höheren Anregungsdichten von $> 10^{17} cm^{-3}$ bemerkbar. Der beschriebene Mechanismus, der zum Ausschalten der PL des Kristalliten führt, ist in Abbildung 35 schematisch dargestellt.

6 Ultrafast Energy Transfer between Disordered and Highly Planarized Chains of Poly[2-methoxy-5-(2-ethylhexyloxy)-1,4-phenylenevinylene] (MEH-PPV)

Thomas Unger, Fabian Panzer, Cristina Consani, Federico Koch, Tobias Brixner, Heinz Bässler und Anna Köhler

Veröffentlicht in
ACS Macro Letters 4 (2015), 412-416

(DOI: 10.1021/acsmacrolett.5b00133)

ACS Macro Letters

Letter

pubs.acs.org/macroletters

Ultrafast Energy Transfer between Disordered and Highly Planarized Chains of Poly[2-methoxy-5-(2-ethylhexyloxy)-1,4-phenylenevinylene] (MEH-PPV)

Thomas Unger,[†,‡] Fabian Panzer,[†,‡] Cristina Consani,[§] Federico Koch,[§] Tobias Brixner,[§,∥] Heinz Bässler,[‡] and Anna Köhler*[,†,‡]

[†]Experimental Physics II, University of Bayreuth, 95540 Bayreuth, Germany

[‡]Bayreuth Institute of Macromolecular Research (BIMF), University of Bayreuth, 95440 Bayreuth, Germany

[§]Institut für Physikalische und Theoretische Chemie and [∥]Center for Nanosystems Chemistry (CNC), Universität Würzburg, Am Hubland, 97074 Würzburg, Germany

Supporting Information

ABSTRACT: Upon cooling a solution of poly[2-methoxy-5-(2-ethylhexyloxy)-1,4-phenylenevinylene] (MEH-PPV), a phase transition occurs, leading to the formation of aggregates. We have studied the dynamics of singlet excitons in MEH-PPV solution below the critical temperature of the phase transition using steady-state photoluminescence measurements and pump−probe fs-spectroscopy at different temperatures. Spectral analysis indicates the coexistence of disordered chromophores with highly planarized chromophores. The high planarity is evidenced by a remarkably high 0−0/0−1 peak ratio in the spectra. By spectrally separating the contributions of either type of chromophore to the pump−probe signal we find that energy transfer takes place within less than 1 ps from disordered, unaggregated chain segments to highly planarized, aggregated chain segments. The short time scale of the energy transfer indicates intimate intermixing of the planarized and disordered polymeric chromophores.

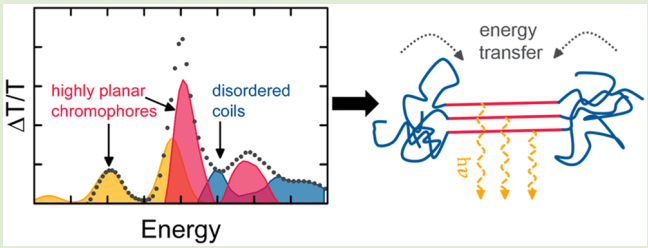

Conjugated polymers are prone to aggregation in solution.[1−3] Below a critical transition temperature that depends on the chain length,[4] isolated and more or less coiled chains tend to aggregate with a concomitant increase of their effective conjugation length. A manifestation of this phenomenon is the appearance of lower-energy absorption and fluorescence bands so that the spectra exhibit an isosbestic point. Absorption spectra demonstrate, nevertheless, that both phases coexist well below the phase transition temperature with the fractional contribution of the ordered phase increasing upon further cooling. On the other hand, the fluorescence comes almost exclusively from the ordered phase. This is a signature of efficient energy transfer between both phases.

The purpose of the current work was to unravel the interplay between the disordered and ordered phases, identify the nature of both phases and measure of rate of energy transfer between them. As a test material, we chose MEH-PPV in solution as a prototypical π-conjugated polymer for which a wealth of information is already existing, employing steady-state absorption and fluorescence spectroscopy, as well as time-resolved pump−probe spectroscopy within a broad temperature range. Based on spectral decomposition techniques and adopting Spano et al.'s H/J-aggregate model,[5] we are able to associate the room temperature phase with disordered chains or chain segments, while, in the aggregated phase, chains or chain segments prevail that are extended with predominant J-type character. From the observation that energy transfer from the disordered to the planarized chromophores occurs on a subps time scale we will conclude that both types of chromophores are intimately connected, for example, by forming an array of extended chains surrounded with a "hairy" surface of coiled chains.

For the investigation, we used MEH-PPV that was purchased from American Dye Source Ltd. (ADS). It was dissolved in methyltetrahydrofuran (MTHF) at a concentration of 0.2 mg/mL. To ensure that all of the polymer chains are completely dissolved, the solution was heated to 50−60 °C and stirred for about 10 h until no macroscopic particles could be observed. The experiments were performed in a temperature range between 300 and 120 K where MTHF is liquid.[6] Steady-state absorption and emission spectra at different temperatures were recorded with a home-built setup. The solutions were filled into a 1 mm fused silica cuvette and put in a temperature-controlled continuous flow cryostat (Oxford Instruments). In order to minimize the light intensity impinging on the sample, we used two correlated monochromators for incident as well as transmitted light. The latter was recorded by a silicon diode and a lock-in-amplifier.

Received: February 19, 2015
Accepted: March 26, 2015

DOI: 10.1021/acsmacrolett.5b00133
ACS Macro Lett. 2015, 4, 412−416

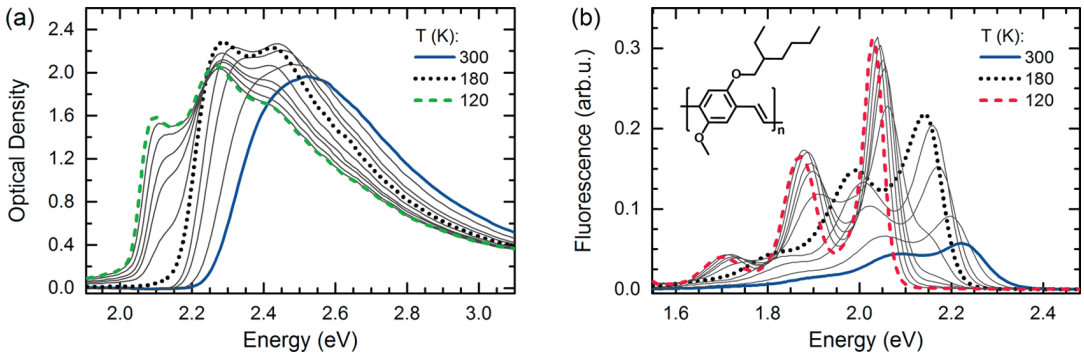

Figure 1. Steady-state (a) absorption and (b) fluorescence spectra of MEH-PPV in MTHF for different temperatures, that is, at 300, 260, 220, 200, 180, 175, 170, 170, 165, 155, 140, and 120 K. Fluorescence spectra were corrected for the relative changes in absorption at the excitation energy (3.06 eV).

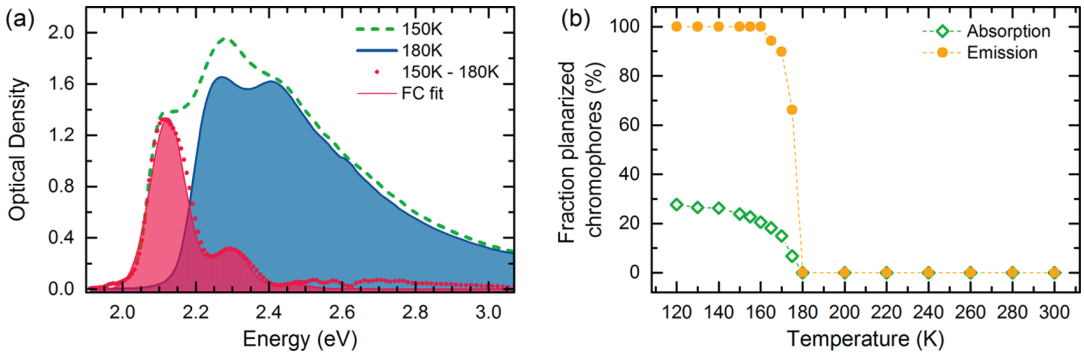

Figure 2. (a) Absorption spectrum at 150 K (green dashed line) together with the absorption spectrum of the disordered phase (filled blue curve) that was measured at 180 K and subsequently normalized to match the high energy tail of the 150 K absorption spectrum. The difference between the 150 and 180 K spectra is shown by the red dots. This difference spectrum can be reproduced by a Franck–Condon progression (filled red curve). (b) Fraction of planarized chromophores as a function of temperature obtained from the absorption spectra (open green diamonds) and from the emission spectra (orange dots), as described in the Supporting Information.

For steady-state emission measurements, the xenon lamp and the first monochromator were replaced via a shutter by a diode laser with an excitation wavelength at 405 nm (3.06 eV), exciting the sample at a shallow angle. Emission was recorded by the same detection unit. This ensured recording absorption and fluorescence spectra at the same sample spot and temperature immediately after one another. All spectra were corrected for the transmission of the setup, using an Oriel calibration lamp. Sample heating or cooling was done in a stepwise fashion with a heating or cooling rate of 2 K per min and waiting 30 min before taking the measurement at a given temperature to ensure thermal equilibrium within the sample.

The transient absorption data with excitation at 2.48 eV (pulse length 190 fs) were obtained using a 100 kHz setup from Coherent Ltd., as described in more detail in the Supporting Information (SI). In brief, the pump-pulse fluence was set to about 10 μJ/cm^2 to keep the pump–probe signal linear with fluence (see Figure S1). The spectra were recorded using a lock-in amplifier and a monochromator with a silicon diode. To obtain transient absorption data with excitation at 2.12 eV (pulse length 42 fs), a 1 kHz setup from Spectra Physics was employed. Here also excitation pulse energies were low enough to keep the signal in the linear regime.

Figure 1 shows the absorption and photoluminescence (PL) spectra of MEH-PPV in MTHF solution in the temperature range between 300 and 120 K. In absorption, the 300 K spectrum is vibrationally unresolved with a maximum at 2.5 eV (Figure 1a). It is associated with disordered coil-like polymer chains.[7−9] Upon cooling to 180 K, the spectra shift to the red by about 80 meV. They continuously acquire vibrational structure and a 0−0 feature near 2.3 eV develops. In contrast, the emission spectrum at 300 K shows vibrational structure with $S_1 \rightarrow S_0$ 0−0, 0−1, 0−2 peaks at 2.23, 2.07, and 1.89 eV, respectively (Figure 1b). When lowering the temperature from 300 to 180 K, the spectra shift to the red by about 80 meV similar to the behavior in absorption. This is accompanied by a continuous increase in overall intensity, where the area beneath the spectrum at 180 K more than triples compared to the area at 300 K (see Figure S2 in SI for energetic shifts of the S_1−S_0 0−0 peak and area under the spectra as a function of temperature). Thus, upon cooling until 180 K, absorption and emission spectra shift to the red and become more intense. This indicates that the conjugated segments of the chain become more extended, although their overall chain conformation still corresponds to that of a disordered coil conformation.[4,10,11] This is similar to the behavior that was recently observed when cooling solutions of P3HT,[2,4] as well as PCPDTBT.[12]

When further cooling below 180 K, a new absorption (emission) peak near 2.1 eV (2.05 eV) appears and grows in intensity at the expense of absorption (emission) from coiled chains. It is assigned to the absorption (emission) of planarized MEH-PPV chain segments in aggregates.[7] Below 170 K, emission from the coiled chains vanishes and the fluorescence spectrum is dominated by the planarized chromophores. This is consistent with earlier work,[7] and has been attributed to the

DOI: 10.1021/acsmacrolett.5b00133
ACS Macro Lett. 2015, 4, 412−416

occurrence of a disorder−order transition. The PL spectra of the planarized chromophores bear out a bathochromic shift from 2.053 to 2.026 eV upon further cooling from 170 to 120 K and the associated absorption spectra shift by the same amount (Figure S2).

To gain detailed information about the absorption from the planarized chains or chain segments requires decomposition of the measured spectra below 180 K. Here we followed a scaling approach, similar to that in Reference 13, which we already used for decomposing absorption spectra of aggregated P3HT in solution.[2,4] This approach is applicable to MEH-PPV because the spectra bear out an isosbestic point at 2.24 eV in the temperature range of 180 to 140 K (Figure 1a), which is an unambiguous evidence that a transition from a coiled to an ordered phase is occurring.[14,15] Figure 2a illustrates the decomposition approach and shows the measured absorption spectrum at 150 K (green dashed line) together with the normalized absorption spectrum of the disordered phase measured at 180 K (filled blue curve). The difference between these spectra (red dots) is attributed to absorption from planarized chromophores with peaks at 2.1 and 2.3 eV. A Franck−Condon analysis of this absorption spectrum (filled red curve) from the planarized chromophores yields a Huang−Rhys parameter of $S = 0.25$, an I_{0-0}/I_{0-1} ratio = 4, an effective vibrational mode of $E_d = 170$ meV and a Gaussian line width of $\sigma = 48$ meV. In the framework of the H/J-aggregate model developed by Spano and co-workers,[5] such a high I_{0-0}/I_{0-1} ratio is a signature of strong coupling along the polymer chain (intrachain) in the aggregated phase and correspondingly weak coupling between different polymer chains (interchain). The same high ratio applies to coupling along a linear arrangement of chromophores and to coupling between chromophores in an adjacent, face-to-face arrangement, respectively. Similar remarkably high I_{0-0}/I_{0-1} ratios have been observed for fully planarized single crystals of P3HT.[16] This appears to be a signature of ordered domains of π-conjugated chains in general, tractable in terms of Spano et al.'s theory.[5] The fraction of planarized chromophores as a function of temperature is displayed in Figure 2b. It was obtained from the absorption fraction of planarized chain segments, taking into account the relative change in oscillator strength between disordered and planarized chain segments, as detailed in the SI.

From the absorption data we infer that below the critical transition temperature, the percentage of planarized chromophores increases continuously, saturating at a maximum value of about 30% at 120 K. In contrast, the percentage of fluorescence from planarized chromophores increases steeply below the transition temperature, until below 160 K, emission results entirely from the planarized chromophores. The fact that emission results entirely from planarized chromophores though they make up only 30% of the total composition implies efficient energy transfer from disordered to planarized chromophores.

Figure 3 shows the transient absorption spectrum of MEH-PPV in solution at 120 K, excited at 2.12 eV and probed between 2.5 and 1.7 eV with a delay time of 75 fs. As the disordered chains do not absorb for excitation at 2.12 eV, we assign the peak observed near 2.3 eV to the ground-state bleach (GSB) of the $S_1 \rightarrow S_0$ 0−1 transition of the planarized chromophores. The feature near 2.1 eV is the superposition of the ground-state bleach of the 0−0 transition of the planarized chromophores (as evident from Figure 1a) and the associated stimulated emission (SE). Accordingly, the feature centered

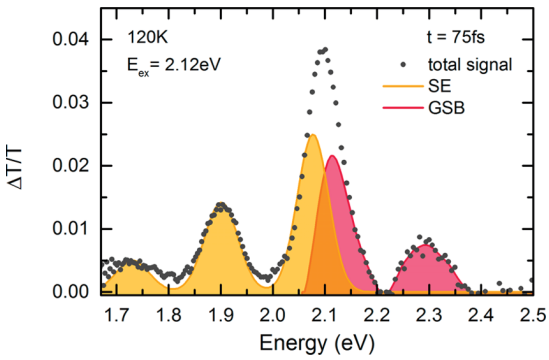

Figure 3. Pump−probe spectrum (gray dots) taken at 120 K, 75 fs after excitation at 2.12 eV, where only the planarized chains absorb. The spectrum is decomposed into the contributions from stimulated emission (SE, filled orange curve) and ground-state bleach (GSB, filled red curve). The SE contribution was obtained by normalizing the 120 K PL spectrum to match the 1.9 eV SE peak. The GSB contribution was obtained by subtracting the normalized 120 K PL spectrum from the total $\Delta T/T$ signal.

near 1.9 eV is assigned to the 0−1 feature of the stimulated emission transition (SE 0−1). Since the fluorescence spectrum of the planarized chromophores is evident in Figure 1b, it is possible to spectrally decompose the 0−0 feature of the pump−probe spectrum into the contributions from GSB and SE. To this end, we take the 120 K photoluminescence (PL) spectrum and normalize it in such a way that the 0−1 peak of the PL spectrum matches the 1.9 eV $\Delta T/T$ signal in intensity, taking into account a slight spectral shift of about 10 meV between the steady-state and the time-resolved spectra. Subtraction of the 120 K PL spectrum from the $\Delta T/T$ signal yields the spectrum associated with the ground-state bleach.

From this spectral decomposition we find a 0−0/0−1 ratio of the GSB that significantly exceeds unity, similar to that of the absorption spectra obtained for the planarized chromophores from steady-state data (Figure 2a). In a recent publication,[17] absorption spectra of aggregated MEH-PPV were simulated theoretically resulting in a significantly smaller 0−0/0−1 ratio compared to this work, mainly due to an underestimated contribution of the coiled phase to the overall absorption spectrum.

When exciting a sample held at 120 K with 2.48 eV, Figure 2a tells us that 95% of the absorbing chromophores are in a disordered conformation. Yet already at 1 ps after excitation, the GSB signal shows signatures of both disordered and planarized chromophores. This is documented by Figure 4 in which pump−probe spectra are shown that are detected after a delay time of 1 and 5 ps.

Spectra at further delay times are listed in the SI. Based on the same decomposition routine as above, the total GSB signal, due to disordered chromophores and to planarized chromophores, was obtained. We then used the GSB signal from the planarized chains derived in Figure 3, normalized it appropriately, and subtracted it from the total GSB signal to derive the GSB contribution of the disordered chain, analogous to the spectral decomposition approach described above. The relative contribution of planarized and of disordered chromophores obtained by this procedure is displayed in Figure 5 as a function of time. In both, Figures 4 and 5, we see that the contribution due to the lower-energy, planarized chromophores grows at the expense of the higher-energy, disordered chromophores.

DOI: 10.1021/acsmacrolett.5b00133
ACS Macro Lett. 2015, 4, 412−416

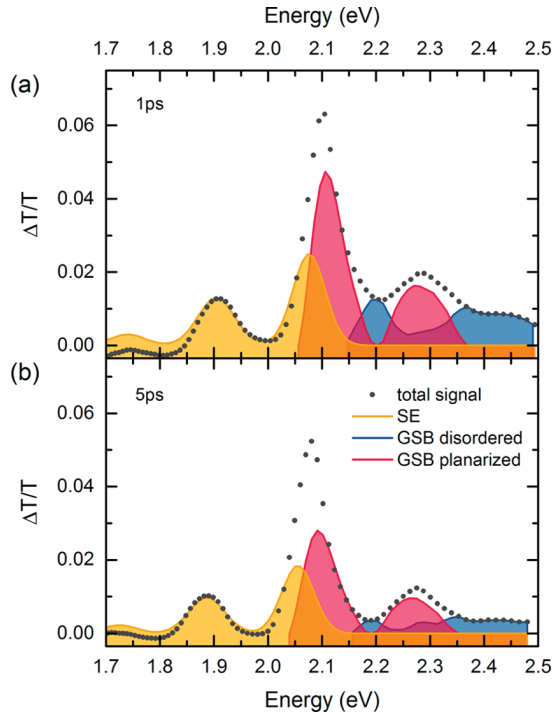

Figure 4. Pump–probe spectra for excitation at 2.48 eV (where coiled chains absorb) at 120 K for different time delays after excitation, that is, (a) 1 and (b) 5 ps. In addition to the total $\Delta T/T$ signal (dots), the contributions of SE, GSB from disordered chromophores, and the GSB from the planarized chromophores are indicated by orange, blue, and red solid lines, respectively.

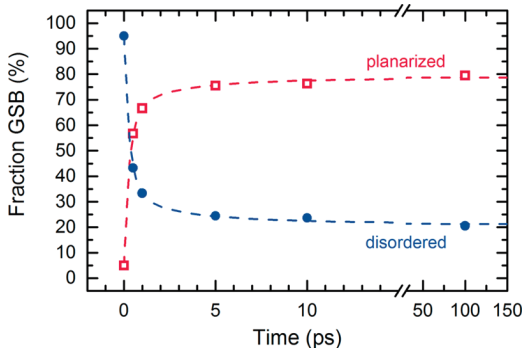

Figure 5. Percentage of the ground-state bleach signal that is due to planarized chromophores (open square symbols) or to disordered chromophores (filled round symbols) as a function of time. The dashed line is a guide to the eye, indicating a decay/growth pattern with an initial exponential decay/growth, followed by a stretched-exponential decay/growth.

We interpret the rising contribution from the planarized chromophores to result from energy transfer from the higher-energy disordered chromophores that is completed within a few ps. A similarly rapid energy transfer from disordered to ordered chain segments has been observed also in polyfluorene (PFO) thin films.[18] Such a fast transfer is incompatible with long-range energy transfer from isolated coiled chains to planarized chains (see SI). It rather suggests that planarized and coiled chromophores are in close proximity, for example, by planarized chain segments forming an ordered cluster surrounded by more disordered coiled chains or chain segments, which was also proposed recently.[19,20] Since experimental and theoretical previous work suggests that MEH-PPV forms planarized segments above a certain concentration,[7,21] the planarized segments are more likely to arise from coalescing chains than by self-folding.

In structures where acceptor chromophores are embedded in a matrix of donor chromophores, energy transfer is characterized by a kinetics comprising several components.[22−24] Initially, fast monoexponential decay of the donor emission prevails due to energy transfer to immediately adjacent acceptor sites. In a second step, the decay becomes dispersive since energy transfer takes place over a range of distances and in a multistep fashion. Both transfer types, that is, (parallel) transfer over a range of distances and (sequential) multistep transfer, have been shown to result in a stretched-exponential decay law,[25−31] also referred to as Kohlrausch–Williams–Watts (KWW) decay law[32]

$$I(t) = I_0 \exp\left[-\left(\frac{t}{t_0}\right)^{\beta}\right]$$

where β is a parameter that accounts for the deviation from nonexponentiality. β takes the value of 0.5 in the case of Förster-type energy transfer. In the long-time limit, finally, the donor decay is dominated by those donor chromophores that decay naturally before energy transfer to distant acceptor sites can occur. The donor emission thus asymptotically approaches the natural donor decay lifetime. Figure 5 indicates that the temporal evolution of the GSB contributions of disordered chromophores and of planarized chromophores is consistent with such a picture. The dashed lines indicate such a decay/growth pattern with an initial exponential decay/growth with about 300 fs lifetime, followed by a stretched-exponential with β = 0.5 and a characteristic time in the range of 1 ps. Similar values and quality of fit result when using a multiexponential approach.

In passing we mention that, in Figure 4, we consider that the slight difference between the measured $\Delta T/T$ signal at 1.75 eV and the SE (derived from the normalized PL spectra) indicates some excited-state absorption from disordered chromophores.

We now consider the decay of the pump–probe signal near 2.1 eV. This is interpreted as the decay of the excitations on the planarized segments. Figure 6 reveals a decay that is not exactly exponential yet approaches an exponential decay with a lifetime of about 350 ps. Such deviation from monoexponentiality is an ubiquitous phenomenon not only in energy-transfer studies but also in time-resolved fluorescence studies on conjugated polymers.[24] It is usually associated with residual trapping at unidentified traps such as oxidation products with a time-dependent trapping rate that translates into a dispersive decay law, described in terms of the Kohlrausch–Williams–Watts (KWW) decay law,[32] mentioned above. An exponent of 0.8 indicates that a small fraction of aggregate excitations are lost via a weakly dispersive exciton motion toward unidentified scavengers such as electron traps that are ubiquitous in π-conjugated polymers.[33−35]

In conclusion, in addition to the observed ultrafast energy transfer and implied core–shell structure of the aggregates, an intriguing aspect of the present work relates to the decomposition of the absorption spectra of MEH-PPV in MTHF solution near and below the transition temperature. At first glance, the overall spectra shown in Figure 2 resemble the absorption spectra of weakly interacting H-aggregates in P3HT, bearing out an apparent ratio of the 0–0 and 0–1 features of

DOI: 10.1021/acsmacrolett.5b00133
ACS Macro Lett. 2015, 4, 412−416

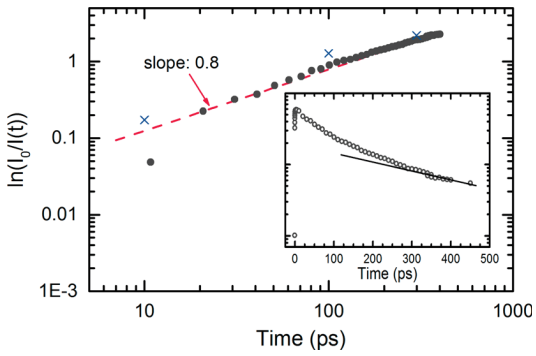

Figure 6. Decay of $\Delta T/T$ at 2.07 eV (dots) for E_{Ex} = 2.48 eV at 120 K, presented in a Kohlrausch–Williams–Watts (KWW) plot for times >10 ps. The red dashed line indicates a slope of 0.8, as discussed in the text. For comparison, the blue crosses indicate the values obtained for the area below the GSB + SE 0–0 band centered at 2.1 eV (=zeroth spectral moment). Slight deviation at early time scales originate from a spectral band shift. The inset shows $\Delta T/T$ at 2.07 eV plotted in a semilogarithmic fashion, with the solid line indicating a mono-exponential decay function with a lifetime of 350 ps.

less than unity. Separating those spectra disproves this conjecture. It turns out that the isolated spectrum of the planarized chromophores is mirror-symmetric with the fluorescence spectrum, thus, implying a high planarity of the aggregated chains. In fact, comparison of the emission spectra indicates the planarized chromophores in MEH-PPV to be as planar as ladder-type poly(*p*-phenylene) (MeLPPP), where covalent bridges enforce a rigid, flat structure and which recently has shown room temperature Bose–Einstein condensation of cavity exciton-polaritons.[36]

■ ASSOCIATED CONTENT

Supporting Information

Details on transient absorption setup. Relative change of area under emission spectra and spectral shift of emission and absorption as a function of temperature. Details on the calculation of the fraction of planarized chains, relative change of oscillator strength as a function of temperature. Transient absorption spectra for further times after excitation. Estimation of energy transfer range. This material is available free of charge via the Internet at http://pubs.acs.org.

■ AUTHOR INFORMATION

Corresponding Author

*E-mail: anna.koehler@uni-bayreuth.de.

Notes

The authors declare no competing financial interest.

■ ACKNOWLEDGMENTS

We acknowledge financial support by the Bavarian State Ministry of Science, Research, and the Arts through the Collaborative Research Network "Solar Technologies go Hybrid", by the German Science Foundation DFG through the doctoral training center GRK1640 and by the Federal Ministry of Education and Research (BMBF) through the Project "OLYMP".

■ REFERENCES

(1) Yamagata, H.; Hestand, N. J.; Spano, F. C.; Köhler, A.; Scharsich, C.; Hoffmann, S. T.; Bässler, H. *J. Chem. Phys.* **2013**, *139*, 114903.
(2) Scharsich, C.; Lohwasser, R. H.; Sommer, M.; Asawapirom, U.; Scherf, U.; Thelakkat, M.; Neher, D.; Köhler, A. *J. Polym. Sci., Part B: Polym. Phys.* **2012**, *50*, 442–453.
(3) Cone, C. W.; Cheng, R. R.; Makarov, D. E.; Vanden Bout, D. A. *J. Phys. Chem. B* **2011**, *115*, 12380–12385.
(4) Panzer, F.; Bässler, H.; Lohwasser, R.; Thelakkat, M.; Köhler, A. *J. Phys. Chem. Lett.* **2014**, *5*, 2742–2747.
(5) Yamagata, H.; Spano, F. C. *J. Chem. Phys.* **2012**, *136*, 184901.
(6) Aycock, D. F. *Org. Process Res. Dev* **2007**, *11*, 156–159.
(7) Köhler, A.; Hoffmann, S. T.; Bässler, H. *J. Am. Chem. Soc.* **2012**, *134*, 11594–11601.
(8) Mirzov, O.; Scheblykin, I. G. *Phys. Chem. Chem. Phys.* **2006**, *8*, 5569–5576.
(9) Schwartz, B. J. *Annu. Rev. Phys. Chem.* **2003**, *54*, 141–172.
(10) Hsu, J.-H.; Fann, W.; Tsao, P.-H.; Chuang, K.-R.; Chen, S.-A. *J. Phys. Chem. A* **1999**, *103*, 2375–2380.
(11) Wood, P.; Samuel, I. D. W.; Schrock, R.; Christensen, R. L. *J. Chem. Phys.* **2001**, *115*, 10955–10963.
(12) Scharsich, C.; Fischer, F. S. U.; Wilma, K.; Hildner, R.; Ludwigs, S.; Köhler, A. Manuscript in preparation, 2015.
(13) Collison, C. J.; Rothberg, L. J.; Treemaneekarn, V.; Li, Y. *Macromolecules* **2001**, *34*, 2346–2352.
(14) Scheibe, G. *Angew. Chem.* **1937**, *50*, 212–219.
(15) Cohen, M. D.; Fischer, E. *J. Chem. Soc.* **1962**, 3044–3052.
(16) Rahimi, K.; Botiz, I.; Agumba, J. O.; Motamen, S.; Stingelin, N.; Reiter, G. *RSC Adv.* **2014**, *4*, 11121–11123.
(17) Yamagata, H.; Hestand, N. J.; Spano, F. C.; Köhler, A.; Scharsich, C.; Hoffmann, S. T.; Bässler, H. *J. Chem. Phys.* **2013**, *139*, 114903.
(18) Khan, A. L. T.; Sreearunothai, P.; Herz, L. M.; Banach, M. J.; Köhler, A. *Phys. Rev. B* **2004**, *69*, 085201.
(19) Lee, C. K.; Hua, C. C.; Chen, S. A. *Macromolecules* **2013**, *46*, 1932–1938.
(20) Peteanu, L. A.; Sherwood, G. A.; Werner, J. H.; Shreve, A. P.; Smith, T. M.; Wildeman, J. *J. Phys. Chem. C* **2011**, *115*, 15607–15616.
(21) De Leener, C.; Hennebicq, E.; Sancho-Garcia, J.-C.; Beljonne, D. *J. Phys. Chem. B* **2009**, *113*, 1311–1322.
(22) Brunner, K.; Tortschanoff, A.; Warmuth, C.; Bässler, H.; Kauffmann, H. F. *J. Phys. Chem. B* **2000**, *104*, 3781–3790.
(23) Mollay, B.; Lemmer, U.; Kersting, R.; Mahrt, R. F.; Kurz, H.; Kauffmann, H. F.; Bässler, H. *Phys. Rev. B* **1994**, *50*, 10769–10779.
(24) Herz, L. M.; Silva, C.; Grimsdale, A. C.; Müllen, K.; Phillips, R. T. *Phys. Rev. B* **2004**, *70*, 165207.
(25) Klafter, J.; Shlesinger, M. F. *Proc. Natl. Acad. Sci. U.S.A.* **1986**, *83*, 848–851.
(26) Klafter, J.; Blumen, A. *Chem. Phys. Lett.* **1985**, *119*, 377–382.
(27) Palmer, R. G.; Stein, D. L.; Abrahams, E.; Anderson, P. W. *Phys. Rev. Lett.* **1984**, *53*, 958–961.
(28) Budimir, J.; Skinner, J. L. *J. Chem. Phys.* **1985**, *82*, 5232–5241.
(29) Blumen, A.; Zumofen, G.; Klafter, J. *Phys. Rev. B* **1984**, *30*, 5379–5382.
(30) Klafter, J.; Blumen, A. *J. Chem. Phys.* **1984**, *80*, 875–877.
(31) Mollay, B.; Kauffmann, H. F. *J. Chem. Phys.* **1992**, *97*, 4380–4397.
(32) Williams, G. Molecular aspects of multiple dielectric relaxation processes in solid polymers. *Electric Phenomena in Polymer Science*; Springer: Berlin Heidelberg, 1979; Vol. 33, pp 59–92.
(33) Nicolai, H. T.; Kuik, M.; Wetzelaer, G. A. H.; de Boer, B.; Campbell, C.; Risko, C.; Brédas, J. L.; Blom, P. W. M. *Nat. Mater.* **2012**, *11*, 882–887.
(34) Köhler, A. *Nat. Mater.* **2012**, *11*, 836–837.
(35) Mikhnenko, O. V.; Kuik, M.; Lin, J.; van der Kaap, N.; Nguyen, T.-Q.; Blom, P. W. M. *Adv. Mater.* **2014**, *26*, 1912–1917.
(36) Plumhof, J. D.; Stöferle, T.; Mai, L.; Scherf, U.; Mahrt, R. F. *Nat. Mater.* **2014**, *13*, 247–252.

DOI: 10.1021/acsmacrolett.5b00133
ACS Macro Lett. 2015, 4, 412–416

Supporting information to:

Ultrafast energy transfer between disordered and highly planarized chains of Poly[2-methoxy-5-(2-ethylhexyloxy)-1,4-phenylenevinylene] (MEH-PPV)

Thomas Unger[†,‡], Fabian Panzer[†,‡], Cristina Consani[#], Federico Koch[#], Tobias Brixner[#,‖], Heinz Bässler[‡], Anna Köhler[†,‡,*]

[†]Experimental Physics II

University of Bayreuth, 95540 Bayreuth, Germany

[‡]Bayreuth Institute of Macromolecular Research (BIMF)

University of Bayreuth, 95440 Bayreuth, Germany

[#]Institut für Physikalische und Theoretische Chemie, Universität Würzburg,

Am Hubland, 97074 Würzburg, Germany

[‖] Center for Nanosystems Chemistry (CNC), Universität Würzburg, Am Hubland,

97074 Würzburg, Germany

1. Description of the transient absorption setup with excitation at 2.1eV

Transient absorption measurements with excitation at 2.48 eV were performed with a 100 kHz setup, consisting of a RegA9000 regenerative amplifier system from Coherent that delivered pulses, centered at 800 nm with a pulse width of about 190 fs as confirmed by an autocorrelator. 12% of the intensity was used to create the probe light externally in a YAG-crystal in the range from 480 to 1300 nm. The remaining intensity pumped a dual-pass optical parametric amplifier to produce the excitation pulses in the range from 2.48 eV to 2.0 eV. The pump beam diameter was about 200 µm to ensure homogeneous excitation. For the measurements, the pump pulse fluence was set to about 10 µJ/cm^2, at which the pump-probe signal was linear with fluence (see Figure S1). Spectra were recorded using a lock-in amplifier and a monochromator with a silicon diode.

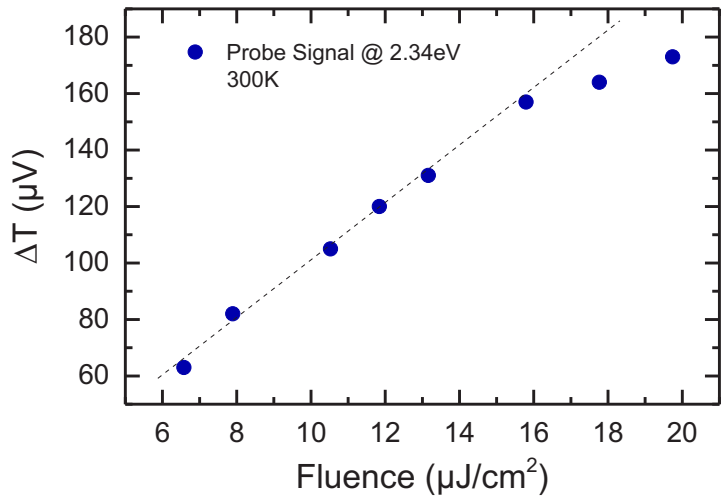

Figure S1: Pump-probe signal as a function of fluence, probed at an energy of 2.34 eV.

For the transient absorption measurements exciting at 2.1 eV, the sample was filled in a 0.3 mm thick cell and placed in a continuous-flow cryostat (Oxford Instruments) operated with liquid nitrogen. The 42 fs excitation pulses at 2.1 eV were generated by a commercial parametric amplifier (TOPAS, Light Conversion), pumped by the output of a 1 kHz regenerative amplifier (Spitfire Pro, Spectra Physics) delivering 120 fs, 2.5 mJ pulses at 800 nm. The white-light continuum used as a probe beam was generated by focusing a small fraction of the 800 nm pulses in a CaF2 window. Pump and probe diameters at the sample position were 50 µm and

30 µm, respectively. Also in this case, we used excitation-pulse energies (1.8 nJ) within the linear regime of excitation, where exciton-exciton annihilation processes are negligible.

2. Changes of steady-state absorption and emission spectra as a function of temperature

The relative change of area under the measured emission spectrum was normalized to the area under the measured spectrum at a temperature of 300 K. Upon cooling down to 180 K, the area continuously increases and finally triples at 180 K (Figure S2a). Spectral shifts of emission and absorption spectra were determined by considering the energetic position of the S_1-S_0 0-0 peaks. In emission this was easily possible within the whole measured temperature range. In contrast to that, simple determination of the S_1-S_0 0-0 peak from the spectrally unresolved absorption spectra of the disordered phase was not possible (Figure S2b).

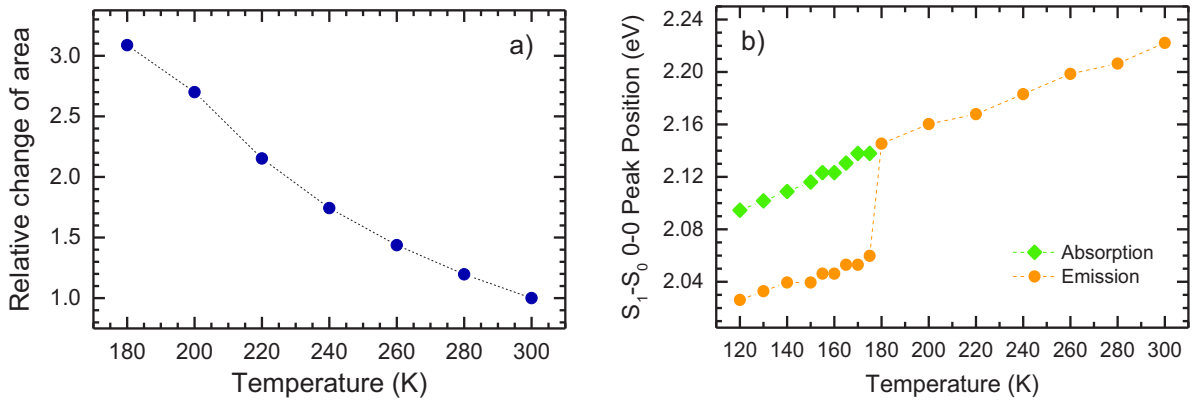

Figure S2: (a) Relative change in area under emission spectra, normalised to the area at 300 K. (b) Energetic position of the S_1-S_0 0-0 peaks of the aggregated phase (< 180 K) and disordered phase (>180 K).

3. Calculating the fraction of aggregates from absorption spectra

The fraction of aggregated chains f_{agg} as a function of temperature is calculated by

$$f_{agg} = F * f_{absaggr}$$

where $f_{absaggr}$ is the fraction of aggregate absorption from the measured absorption spectrum and F is the relative change of oscillator strength between disordered and aggregated chain conformation. We derived the relative change in oscillator strength between the aggregated and disordered phase, $\varepsilon_{aggregate}/\varepsilon_{disordered}$, similar to the approach which is described in detail in the supporting informations of previous works by Clark et al.[1] and Scharsich et al.[2], using

$$\frac{A_{aggregate}}{A_{disordered}} = -\frac{\varepsilon_{aggregate}}{\varepsilon_{disordered}} = F$$

with the areas taken from the shaded regions as illustrated in Figure S3.

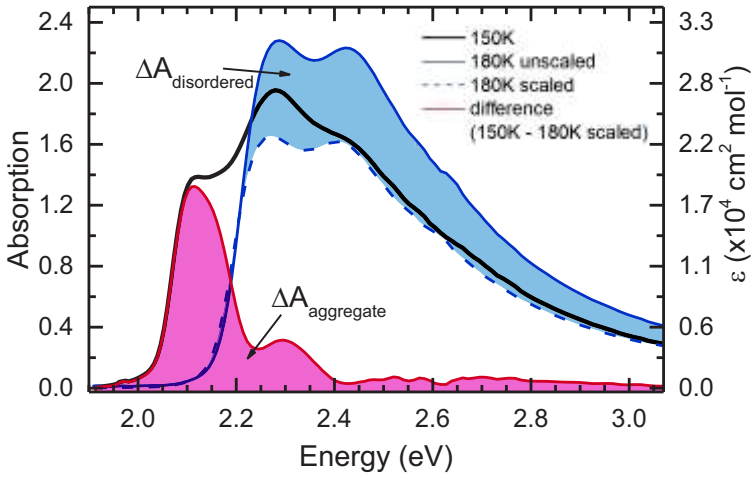

Figure S3: Exemplary illustration of the procedure to determine the change in oscillator strength between coiled and aggregated phase of MEH-PPV. The required areas $A_{disordered}$ and $A_{aggregate}$ are highlighted.

From this approach, the relative change in oscillator strength between disordered and aggregated phase can be obtained within the temperature range between 180 K and 140 K, which is found to be near unity (Figure S4).

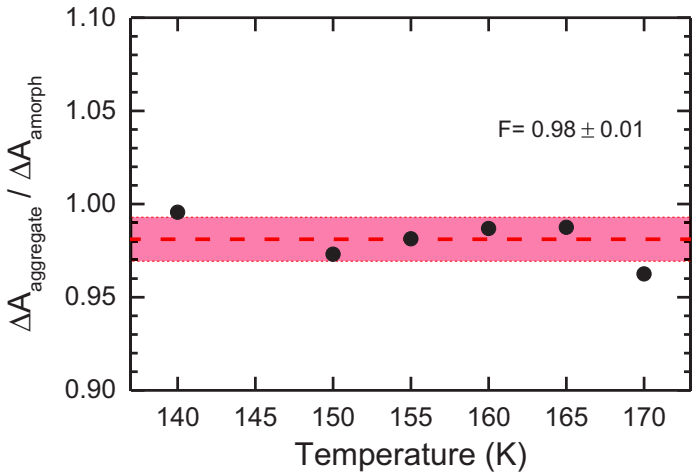

Figure S4: Relative change of oscillator strength between disordered and aggregated phase as a function of temperature.

4. Transient absorption spectra

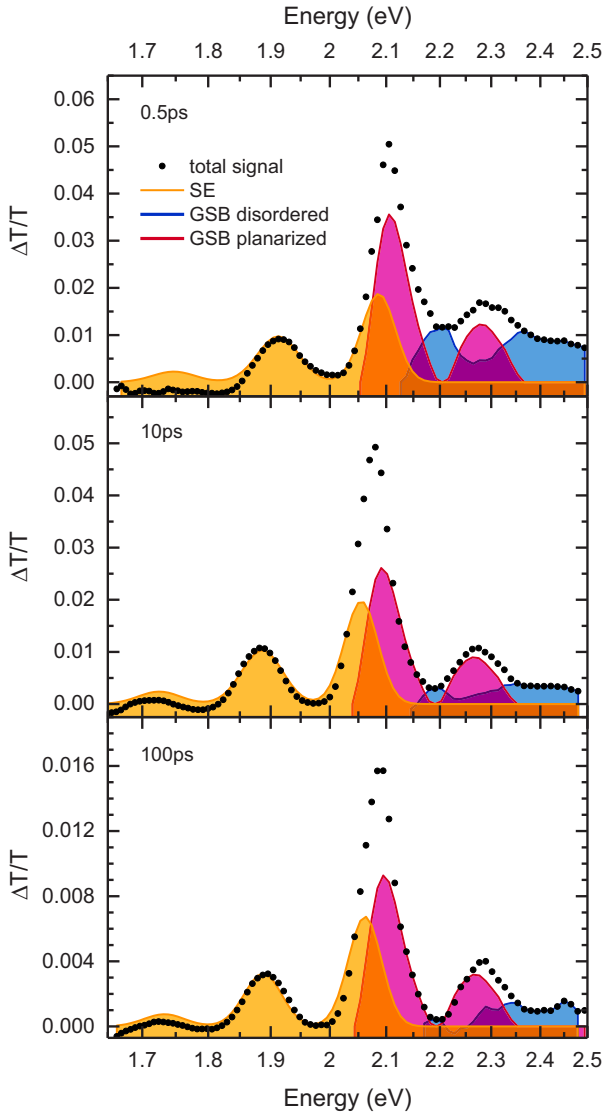

Figure S5: Pump-probe spectra for excitation at 2.48 eV (where coiled chains absorb) at 120 K for different time delays after excitation, i.e. (a) 0.5 ps, (b) 10 ps and (c) 100 ps. In addition to the total ΔT/T signal (dots), the contributions of SE, GSB from disordered chromophores and the GSB from the planarized chromophores are indicated by orange, blue and red solid lines, respectively.

5. Estimate of energy transfer range

We will argue that the short timescale of energy transfer (< 1 ps) is not compatible with long-range energy transfer from coiled to planarized chains. Transfer from coiled to planarized chains is completed within 1 ps. Thus, a generous upper limit for the transfer rate k is 1×10^{12} s^{-1}.

Suppose the transfer takes place from a coiled chromophore to a planarized chromophore that are separated by a long distance R. "Long", in this context, in particular implies that the distance separating the centres of mass of the two chromophores is larger than their size. Thus, the point-dipole approximation applies. Let us suppose further that coupling between these chromophores is weak and that relaxation within S_1 has occurred prior to energy transfer, so that the energy transfer can be presumed to be of a Förster-type nature.

In the case of Förster-type energy transfer, the energy transfer rate k from one chromophore to another at a distance R is given by

$$k = \frac{1}{\tau_0}\left(\frac{R_0}{R}\right)^6, \qquad (1)$$

where τ_0 is the lifetime of the donor chromophore in the absence of the acceptor chromophore and R_0 is the Förster radius. The Förster radius depends on the mutual orientation of the two chromophores, the refractive index of the surrounding medium, the fluorescence quantum yield of the donor chromophore and the spectral overlap between the donor emission and the acceptor absorption. Solving eq. (1) for R yields

$$R = \frac{R_0}{\sqrt[6]{\tau_0 k}}. \qquad (2)$$

For the lifetime of the donor chromophore we take a lifetime of 500 ps, which is typical for π-conjugated polymers[3] and which is consistent with the data shown in Figure 5 in the manuscript. Typical Förster radii are in the range of a few nanometers, with 5 nm being a generous upper limit for R_0 when all parameters are maximized.[4]

Thus, an upper limit for the distance between the two chromophores is $\boldsymbol{R} \leq$ 1.8 nm. This estimate demonstrates that energy transfer occurring on a picosecond timescale implies proximity between donor and acceptor chromophores.

Addendum – Estimate of the maximum Förster radius of 5 nm:

R_0 is given by:[4]

$$\frac{R_0}{nm} = 2.108 * 10^{-2} \left\{ \kappa^2 \Phi_D^0 n^{-4} \int_{\lambda}^{0} I_\lambda^D(\lambda) \left[\frac{\varepsilon_A(\lambda)}{dm^3 mol^{-1} cm^{-1}} \right] \left(\frac{\lambda}{nm} \right)^4 d\lambda \right\}^{1/6}$$

with κ^2 being the dipole orientation factor, Φ_D^0 the fluorescence quantum yield of the donor in the absence of the acceptor, *n* the refractive index of the solvent medium, ε_A the molar extinction coefficient of the donor and I_λ^D the donor emission spectrum normalized to an area value of unity. Φ_D^0 can at most be unity, and the refractive index cannot be lower than 1. For the extinction coefficient of the donor we take a maximum constant value of 10^5 cm^2 mol^{-1},[5] i.e. we assume a step function. So far, all values have been assumed to take the maximum value that is allowed by theory.

Let us presume that the overlap of donor and acceptor extends over a range of 100 nm, say, from 500 to 600 nm. Note that this is again a generous estimate and that typical values are smaller. Inserting these values into the above equation and carrying out the integral leads to R_0=3.7 nm as maximum possible Förster radius.

Thus, allowing for some margin, presuming a value of R_0=5 nm is a generous upper limit.

References:

1. Clark, J.; Chang, J.-F.; Spano, F. C.; Friend, R. H.; Silva, C. *Applied Physics Letters* **2009,** 94, (16), 163306.
2. Scharsich, C.; Lohwasser, R. H.; Sommer, M.; Asawapirom, U.; Scherf, U.; Thelakkat, M.; Neher, D.; Köhler, A. *J Polym Sci Pol Phys* **2012,** 50, (6), 442-453.
3. Ariu, M.; Lidzey, D. G.; Sims, M.; Cadby, A. J.; Lane, P. A.; Bradley, D. D. C. *Journal of Physics: Condensed Matter* **2002,** 14, (42), 9975.
4. Lakowicz, J. R., *Principles of fluorescence spectroscopy*. Springer US: 2006.
5. See, e.g. Chapter 5 in Turro, N. J., Modern Molecular Photochemistry, University Science Books,1991

7 Relaxation dynamics and exciton energy transfer in the low-temperature phase of MEH-PPV

Cristina Consani, Federico Koch, Fabian Panzer, Thomas Unger, Anna Köhler und Tobias Brixner

Veröffentlicht in
The Journal of Chemical Physics 142 (2016), 2212429

(DOI: 10.1063/1.4918645)

Relaxation dynamics and exciton energy transfer in the low-temperature phase of MEH-PPV

Cristina Consani,[1] Federico Koch,[1] Fabian Panzer,[2] Thomas Unger,[2] Anna Köhler,[2] and Tobias Brixner[1,3,a)]

[1]*Institut für Physikalische und Theoretische Chemie, Universität Würzburg, Am Hubland, 97074 Würzburg, Germany*

[2]*Lehrstuhl Experimentalphysik II, Universität Bayreuth, Universitätsstraße 30, 95440 Bayreuth, Germany*

[3]*Center for Nanosystems Chemistry (CNC), Universität Würzburg, Am Hubland, 97074 Würzburg, Germany*

(Received 2 February 2015; accepted 8 April 2015; published online 21 April 2015)

Understanding the effects of aggregation on exciton relaxation and energy transfer is relevant to control photoinduced function in organic electronics and photovoltaics. Here, we explore the photoinduced dynamics in the low-temperature aggregated phase of a conjugated polymer by transient absorption and coherent electronic two-dimensional (2D) spectroscopy. Coherent 2D spectroscopy allows observing couplings among photoexcited states and discriminating band shifts from homogeneous broadening, additionally accessing the ultrafast dynamics at various excitation energies simultaneously with high spectral resolution. By combining the results of the two techniques, we differentiate between an initial exciton relaxation, which is not characterized by significant exciton mobility, and energy transport between different chromophores in the aggregate. © *2015 AIP Publishing LLC.* [http://dx.doi.org/10.1063/1.4918645]

I. INTRODUCTION

Molecular functional materials are currently subject to extensive studies because of their applications in organic electronics and photovoltaics. Among these materials, conjugated polymers are particularly attractive as they combine high absorption cross sections with low-cost production and deposition over flexible substrates.[1–3] However, typical efficiencies of solar cells based on conjugated polymers are currently limited to <11%.[4]

The key parameters to understand photoinduced function in these devices are the interactions of polymer structural units (monomers), both within a single polymer chain and between neighboring polymer chains in aggregates. Indeed, such interactions affect the relaxation time scale of the excited states, the population yield of mobile excitons versus nonmobile species (e.g., excimers), the capability to transport the absorbed energy over long distances, the formation of charge-transfer states, and their dissociation into free charges in proximity of the donor-acceptor interface. Particularly, the efficiency of energy transport from the bulk of the donor material towards the interface with the acceptor is among the factors that have a significant influence on the performance of organic photovoltaic devices.

Conformational disorder, which is among the distinctive characteristics of conjugated polymers, has profound effects on the dynamics of excitons and energy transfer. Together with spatial variations in the polarization of the environment, conformational disorder breaks the conjugation along the polymer chains and forms short conjugated segments called "conformational subunits."[5,6] Absorption of a photon populates exciton states which are initially delocalized over several conformational subunits but localize on sub-100 fs time scales on smaller domains due to dynamic coupling between electronic and nuclear degrees of freedom.[7] On a longer time scale, electronic energy transfer is typically described in terms of a sequence of Förster energy transfer steps between localized excitons,[8,9] although intermediate regimes characterized by coherent intrachain energy transfer have been reported for Poly[2-methoxy-5-(2-ethylhexyloxy)-1,4-phenylenevinylene] (MEH-PPV) in chloroform.[10] The dynamics of energy transfer differs significantly along the polymer chain (intrachain) and between different polymer chains (interchain). The latter is typically one to two orders of magnitude faster than intrachain energy transfer,[11–14] explaining the more efficient energy transport observed in films as compared to isolated polymer chains in solution.[12,15,16]

The picture of exciton dynamics described above applies in general for conjugated polymers. However, the dynamics of the photoexcited species, as well as the rate, the efficiency, and the length scale of energy transport, can differ strongly for different systems. Additionally, the photophysics of conjugated polymers and their aggregates depends not only on the chemical nature of the compound but also on its structure and morphology.[12,17–21] Hence, understanding the key factors controlling exciton dynamics requires the capability to control the structure of the aggregate. A possibility in this respect is to use systems where both aggregation and the morphology of the self-aggregated state can be controlled by external parameters.

In this paper, we investigate the low-temperature self-aggregated phase of the polymer MEH-PPV in solution. In MEH-PPV, two classes of chromophores have been observed, one emitting at higher energy ("blue sites") than the other ("red sites").[22–25] The picture emerging from single-molecule spectroscopy suggests that MEH-PPV can be found in two distinct conformational classes, and that the relative amount

a)Electronic mail: brixner@phys-chemie.uni-wuerzburg.de

of blue and red sites in a single chain is controlled by the presence of interactions between segments of the polymer chain that are brought into contact by chain folding. The red sites have been repeatedly ascribed to planarized segments characterized by an increased conjugation length compared to the blue sites.[25,26] It was also suggested that the formation of the red sites might be related to aggregation.[22,27] Recent studies showed that concentrated solutions of MEH-PPV in 2-methyltetrahydrofuran (MeTHF) undergo a phase transition from a coiled conformation ("blue phase"), characteristic of room temperature, to an aggregated and planarized phase at low temperatures ("red phase"), characterized by very long conjugation length.[28] The phase transition is accompanied by the appearance of a low-energy band in both the absorption and emission spectra.[28,29] In the following, we will refer to the blue (red) phase as coiled (aggregated) phase.

Although the ultrafast dynamics of the room-temperature coiled phase of MEH-PPV has been extensively studied both in solution and films,[14,18,24,30,31] knowledge on the ultrafast dynamics of the aggregated red phase is still sparse. In the following, we use broadband transient absorption spectroscopy and coherent electronic two-dimensional (2D) spectroscopy to observe the exciton relaxation and energy transfer dynamics in the planarized aggregated phase of MEH-PPV. Combining the results from these experiments allows us to individuate two regimes of energy relaxation in the aggregated phase of MEH-PPV. In particular, we separate the initial exciton relaxation within a manifold of excitons sharing a common ground state (relaxation without significant energy transport) from the energy hopping between excitonic states located on different polymer segments. Furthermore, we show that the average time scale for energy hopping in the aggregated phase is comparable with the typical values reported for the red-emitting sites in single molecules.

II. EXPERIMENTAL METHODS

MEH-PPV was purchased from Sigma Aldrich (CAS 138184-36-8). Gel permeation chromatography measurements were performed (PSS Polymer Standards Service Gmbh in Mainz) using polystyrene as the calibration standard and solving the MEH-PPV in 1,2,4-trichlorbenzol at a temperature of 150 °C to make sure that it was completely dissolved. This measurement provided the weight-average molecular weight of the batch of sample used for our experiments (M_w = 218.8 kDa) and the number-average molecular weight (M_n = 58.12 kDa), resulting in a dispersity of $D = M_w/M_n$ = 3.76. The sample was dissolved in distilled MeTHF (Sigma Aldrich) at a concentration of 0.2 mg/ml. The solution was stirred and heated at ≈40–45 °C for 24 h, until no macroscopic particles could be observed anymore. Absorption and emission spectra at different temperatures were recorded with a home-built setup which is described in detail elsewhere.[32]

For the time-resolved measurements, the 0.3 mm thick sample cell was placed in a continuous-flow cryostat (Oxford Instruments) operated with liquid nitrogen. Upon cooling the sample from room temperature to 140 K, an optical density of ≈0.4 OD at 2.11 eV was achieved.

The light source for the ultrafast spectroscopy experiments was a commercial Spitfire Pro-regenerative amplifier (Spectra Physics) providing 120 fs, 2.5 mJ pulses at 800 nm with a repetition rate of 1 kHz. A small portion (<1 μJ) of the 800 nm pulses beam was focused onto a CaF_2 window to generate the white-light continuum probe. About one quarter of the laser intensity was used to pump a commercial non-collinear parametric amplifier (TOPAS White, Light Conversion) to generate the tunable excitation pulses. For the experiments described here, the excitation pulses were centered at 2.10 eV and 2.03 eV and pulse lengths were 42 fs and 60 fs, respectively. Beam diameters at the sample position were ≈50 μm and ≈30 μm for the excitation and probe beams, respectively. For all the experiments, we made sure that excitation-pulse energies were within the linear regime of excitation, where exciton-exciton annihilation processes are negligible (see also Fig. S1 in the supplementary material).[33,80] For the transient absorption experiments, photon flux of 9.4×10^{13} photons/cm^2 and 4.9×10^{14} photons/cm^2 were used upon 2.10 eV and 2.03 eV excitation, respectively.

The setup for 2D spectroscopy was described extensively elsewhere.[34] Briefly, 35 fs excitation pulses centered at 2.10 eV were generated by the TOPAS White and split into four replicas, which served as three excitation pulses and local oscillator in an inherently phase-stabilized fully noncollinear four-wave mixing setup with heterodyne detection. The time delay between the local oscillator and the third pulse was set to 2.8 ps. The coherence time τ was sampled in steps of $\Delta\tau$ = 5.5 fs, covering a range of ±143 fs. Scattering contributions may lead to distortions of the 2D signals and possible errors in the phasing procedure, since they add up to the projection of the signal on the detection axis. This might lead to errors in the phasing procedure or misinterpretation of cross-peaks and oscillating contributions. Therefore, it is important to efficiently subtract these undesired scattering contributions. Working with samples in the liquid phase often requires circulation of the sample to reduce photodamage, but this might lead to dynamic scattering. This dynamic scattering can be effectively reduced by double-modulation lock-in detection.[35] In our experiment, where the sample is still above the glass temperature but is not circulated inside the cryostat, we can perform scattering correction by acquiring certain scattering contributions at each delay point and subtracting them from the spectral interferograms before Fourier evaluation of the data.[36] In addition to our scattering correction routine, we added a polarizer in the signal beam to reduce remaining unpolarized scattered light. Data sets were phased to spectrally resolved pump-probe data acquired in the same setup (see also Fig. S2 in the supplementary material[80]). Optical signals were recorded with a CCD-array spectrometer (Acton SpectraPro 2500i equipped with PIXIS 2K CCD camera).

III. RESULTS AND ANALYSIS

A. Transient absorption

Figure 1(a) shows the normalized steady-state $S_1 \leftarrow S_0$ absorption (red solid) and $S_1 \rightarrow S_0$ emission spectra (red

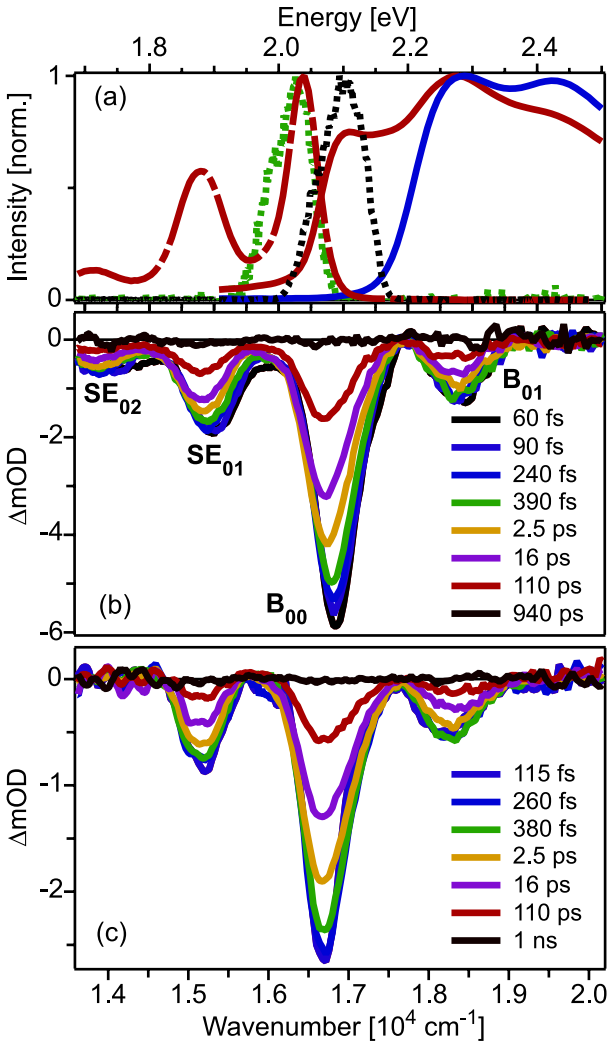

FIG. 1. (a) Static absorption (solid) and emission (dashed dotted) of the aggregated phase (red) and coiled phase (blue) of MEH-PPV at 140 K and 180 K, respectively. The laser spectra used in the experiments are also shown (black and green dotted). Selection of transient absorption spectra at 140 K and different population times upon excitation at (b) 2.10 eV (1.69×10^4 cm^{-1}) and (c) 2.03 eV (1.64×10^4 cm^{-1}).

dashed-dotted) of MEH-PPV at 140 K, together with the spectra of the laser pulses used for the experiments (black and green dotted lines). The low-energy absorption feature at 2.1 eV only appears below a critical temperature (here 180 K, see also the steady-state absorption at temperatures immediately above the phase transition, plotted in blue in Fig. 1(a)) and is attributed to the 0–0 transition of the aggregated phase.[28] The emission at 140 K is characterized by three major bands at 2.04 eV, 1.88 eV, and 1.71 eV, which are ascribed to the 0–0, 0–1, and 0–2 transitions, respectively.

Selections of transient absorption spectra of the aggregated phase of MEH-PPV at 140 K and different population times T are shown for excitation at 2.10 eV (Fig. 1(b)) and 2.03 eV (Fig. 1(c)). No significant difference in the dynamics is observed by lowering the temperature to 120 K (Fig. S3 in the supplementary material[80]). As it is the purpose of this study to selectively investigate the dynamics in the aggregated phase, we did not excite the sample at energies higher than 2.1 eV, where absorption from a fraction of the sample in the coiled phase may still be present. For both excitation energies, the transient signals are dominated by three major negative bands at ≈2.27 eV, ≈2.08 eV, and ≈1.88 eV. A fourth small negative band at ≈1.72 eV is evident upon 2.10 eV excitation; upon 2.03 eV excitation, the noise in this spectral region is comparable with the expected magnitude of such a feature. By comparing the shape and energy position of the observed bands with the inverted static absorption and emission (see Fig. 1(a)), we can ascribe the negative feature at 2.27 eV to the ground-state bleach of the vibronic 0–1 transition and we will refer to this band as B_{01} in the following. The band at 2.08 eV (B_{00} in the following) contains contributions from both the ground-state bleach and the stimulated emission (SE) of the 0–0 transition, while the negative bands at ≈1.88 eV (SE_{01}) and ≈1.72 eV (SE_{02}) arise from SE from the 0–1 and 0–2 vibronic transitions, respectively. No clear signatures of excited-state absorption (positive ΔOD signals) are observed in the entire investigated spectral range.

Interestingly, the ground-state bleach signal in the 2.10–2.50 eV region does not resemble the steady-state absorption, but it appears as the mirror image of the stimulated emission. Since no signatures of excited-state absorption are detected in this spectral region, the discrepancy between bleach and steady-state absorption must be ascribed to the fact that only a fraction of the steady-state absorption stems from the states absorbing at 2.10 eV, i.e., from the aggregated phase. Although a precise determination of the fraction of MEH-PPV in the planarized conformation is still pending, the formation of the planarized chromophores is expected to affect only a fraction of the sample. In fact, in conjugated polymers typically between 40% and 60% of the polymer chains can form planarized chromophores.[32,37] Thus, we assign the steady-state absorption above 2.10 eV that is not reflected in a transient bleach signal to the contribution from the coiled phase.

For both excitation energies, the transient absorption signal decays non-exponentially and completely recovers in less than 1 ns (Fig. S4 in the supplementary material[80]). The most pronounced difference between the evolution of the transient signals at the two excitation energies is observed in the sub-10 ps dynamics. Upon excitation at 2.10 eV, all the bands show a shift to lower energies, most pronounced in the SE (Fig. 1(b)). The amplitude of this shift is almost completely suppressed when the excitation is tuned to the lowest edge of the aggregated-phase absorption at 2.03 eV (Fig. 1(c)).

In general, broadband transient absorption data can be described globally by assuming kinetic models with rates that are independent from the detection wavenumber. Such global description allows identifying the spectral features associated with different processes through their time evolution. However, when the transient spectra show pronounced spectral shifts on time scales comparable with the population relaxation (such as in Fig. 1(b)), the results from such a global analysis can be difficult to interpret.

Here, we follow a different approach. Since the transient absorption signals are dominated by well-separated bleach and SE bands, an analysis of the spectral moments of these bands can be performed to disentangle different molecular processes. We define the spectral moments $M_0^{(i)}$ and $M_1^{(i)}$ of

the three major bands i (i = B_{01}, B_{00} and SE_{01}) according to

$$M_0^{(i)}(T) = \sum_{\nu=\nu_1^{(i)}}^{\nu_2^{(i)}} I(\nu,T) \cdot \Delta\nu, \tag{1a}$$

$$M_1^{(i)}(T) = \frac{1}{M_0^{(i)}(T)} \sum_{\nu=\nu_1^{(i)}}^{\nu_2^{(i)}} \nu \cdot I(\nu,T) \cdot \Delta\nu, \tag{1b}$$

where $I(\nu,T)$ is the absorbance change at frequency ν and population time T, $\nu_1^{(i)}$ and $\nu_2^{(i)}$ are the frequency summation limits for each band i, and $\Delta\nu$ is the frequency interval between data points. As long as bands are not overlapping, the band integrals $M_0^{(i)}$ (zero-order moments) are not sensitive to variations in the shape or position of the bands, but probe exclusively the population dynamics. The first spectral moments $M_1^{(i)}(T)$ correspond to the average spectral positions of the bands and allow us to directly monitor band shifts.

Figures 2(a) and 2(b) depict $M_0^{(i)}(T)$ for 2.10 eV and 2.03 eV excitation, respectively (symbols). At both excitation energies, the temporal evolution of the band integrals appears as a non-exponential decay. *A priori*, due to the wide distribution of polymer lengths and possible conformations in our sample, the measured temporal evolution could arise either (I) from a broad distribution of rates or (II) from several distinct kinetic processes. We will now proceed to analyze the observed population dynamics both via model I and model II and provide arguments for both of them. However, we stress that the main conclusion of our work, i.e., the characterization of the dynamics of exciton relaxation and transport within the aggregated phase, will be based on the band-shift analysis that is completely independent from the choice of the population-kinetics model.

Kinetics in case I can be modelled with a stretched exponential function according to $M_0^{(i)}(T) = A \cdot e^{-(\frac{T}{\tau})^{\beta}}$ with amplitude A, characteristic time τ, and distribution width β. This stretched exponential form is also known as Kohlrausch-Williams-Watts (KWW) function.[38] A number of theoretical treatments have shown that the stretched exponential is recovered when modelling independent, parallel single-step processes on one hand yet, on the other hand, also for sequential, multistep processes on disordered structures.[38–45] In particular, energy-dispersive hopping in disordered organic semiconductors is characterized by a KWW-like behaviour.[8,46,47] In that case, the double logarithmic plot $\ln(I(T=0)/I(T))$ of the signal intensity I versus the time T typically shows two regimes (see Fig. S5 in the supplementary material[80]). For short times, a slope β of unity—equivalent to an exponential decay—indicates vanishing dispersion. This is commonly interpreted

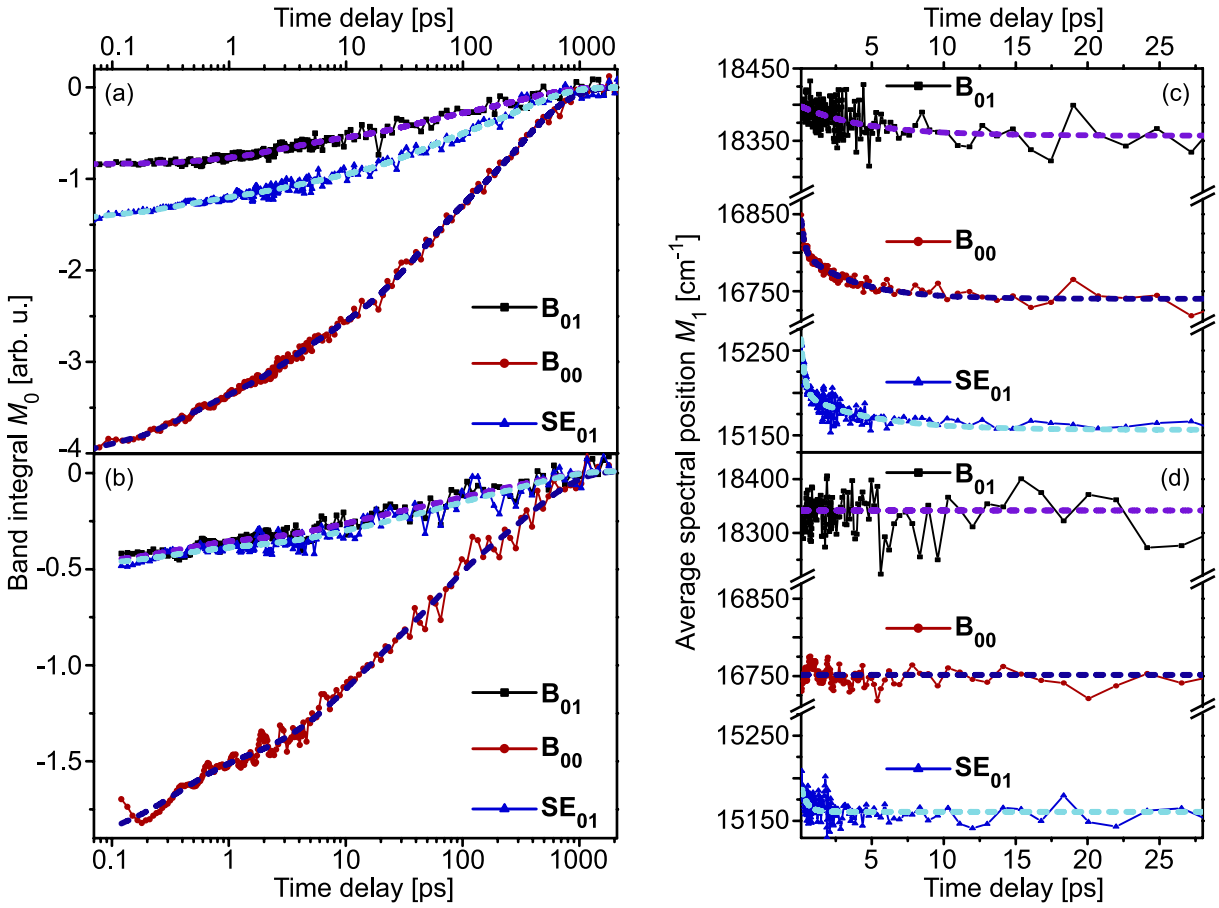

FIG. 2. Spectral moments of the three major bands observed in the transient absorption experiments as a function of the population time T: integrated intensity $M_0^{(i)}$ (Eq. (1a)) of the three major bands for excitation at (a) 2.10 eV and (b) 2.03 eV and their average spectral position $M_1^{(i)}$ (Eq. (1b)) upon excitation at (c) 2.10 eV and (d) 2.03 eV. Consistent with the results of the maximum entropy method analysis, the temporal dependence of the spectral moments is fitted by a multi-exponential kinetics (dashed lines).

to designate energetic relaxation by jumps to lower energy nearest neighbors. Subsequently, lower energy sites immediately adjacent to an excitation are no further available. Thus, at longer times, jumps to non-nearest neighbours prevail and the slope β acquires a value near 0.5. Note that values of $\beta = 1/2$ and $\beta = 1/3$ are expected for Förster transfer from a random ensemble of donors to a dilute array of acceptors in a 3D and 2D case, respectively.

In case II, a multiexponential fit function $M_0^{(i)}(T) = \sum_{j=1}^{4} A_j \cdot e^{-\frac{T}{\tau_j}}$, with amplitudes A_j and characteristic times τ_j, is suitable. Both models are approximately consistent with our experimental data (Fig. S6 in the supplementary material[80]). In order to attempt a discrimination without initial bias, the maximum entropy method (MEM) is employed, via the open-source program MemExp,[48,49] to simulated data for models I and II and to the experimental data (Fig. S7 in the supplementary material[80] shows exemplary results for $M_0^{(B_{00})}$). The MEM analysis of the experimental data contains four distinct time scale peaks (Figs. S4, S7, and S8[80]) and thus more clearly resembles model II rather than model I. Thus, we further discuss our results in terms of a multi-exponential fit. Fit constants are listed in Table I. Note that despite the use of a multi-exponential model, the retrieved time constants may be distributed; thus for the following discussion, the values reported in Table I must be interpreted as the average time constants of different rate distributions. The fit results for model I are listed in Table S1 of the supplementary material.[80]

The temporal evolution of the average spectral position $M_1^{(i)}(T)$ of the three major bands is plotted in Figs. 2(c) and 2(d) for excitation at 2.10 eV and 2.03 eV, respectively, and fit results are again reported in Table I. Upon excitation at 2.10 eV, all bands show a red-shift which is completed within the first 15 ps. The bleach band (B_{01}) shifts mono-exponentially towards lower wavenumbers on a ≈4 ps time scale (see also the τ_2^s values in Table I). A red-shift with similar time constants is observed also in the average spectral position of bands B_{00} and SE_{01}, preceded by an additional fast ($\tau_1^s \approx 200 - 250$ fs) red-shift. Noteworthy, the amplitude of the ≈4 ps red-shift is virtually identical (42 ± 3 cm^{-1}) for the B_{01} and SE_{01} bands.

The sub-300 fs shift appears exclusively in bands containing contributions from SE, thus we ascribe it to processes occurring in the excited state. The lack of such contribution in the B_{01} band is a further indication that no significant excited-state absorption is contributing to the signal in this spectral region.

Upon excitation at 2.03 eV (Fig. 2(d)), no spectral evolution is observed in the three bands, except for a very small initial red-shift on a sub-500 fs time scale in the SE_{01} band.

B. Coherent 2D spectroscopy

Coherent electronic 2D spectroscopy can be seen as an extension of transient absorption spectroscopy, where the time-dependent molecular signal is measured as a function of both the excitation and detection frequency. In coherent 2D spectroscopy, the molecular response to the interaction with three electromagnetic fields is measured as a function of three time delays. For each fixed population time T (between the second and third pulse), Fourier transformation of the emitted signal with respect to the time delay τ between the first two pulses, and t between the third pulse and the signal, yields the excitation and detection axes, respectively. Since the 2D signal and its time evolution allow mapping of electronic couplings and correlations between initial and final electronic states during molecular relaxation, respectively, coherent 2D spectroscopy is particularly suitable to characterize processes of energy transfer in complex systems.[50–52] In the following, we apply coherent 2D spectroscopy to discriminate between band shifts and homogeneous broadening in the temporal evolution of the aggregated-phase signal of MEH-PPV, as well as to observe exciton dynamics and energy transfer at several excitation energies with high frequency resolution.

Figures 3(a)-3(d) show a selection of 2D spectra of MEH-PPV in the aggregated phase for four different population times T. Data are acquired at 140 K with the excitation pulses shown in Fig. 1(a) (black dotted), thus the lowest transition band of the aggregated phase is selectively investigated. At all population times, the 2D spectra are dominated by a single feature, containing contributions from the bleach and SE of the $0 \rightarrow 0$ transition (see also Fig. 1(b)). No clear signatures of excited-state absorption are detected.

TABLE I. Characteristic time constants obtained from a multi-exponential global fit of the integrated signals $M_0^{(i)}(T)$ and from the independent fits of the average spectral position $M_1^{(i)}(T)$ of the three major bands ($i = B_{01}$, B_{00}, and SE_{01}) of the transient absorption data described in Sec. III A.

	Excitation energy Temperature	2.10 eV 120 K	2.10 eV 140 K	2.03 eV 140 K
Population decay $M_0(T)$ $M_0(T) = \sum_{j=1}^{4} A_j e^{-\frac{T}{\tau_j}}$	τ_1 (fs)	220 ± 50	290 ± 40	240 ± 60
	τ_2 (ps)	2.6 ± 0.2	2.5 ± 0.3	5 ± 2
	τ_3 (ps)	41 ± 4	32 ± 3	41 ± 8
	τ_4 (ps)	320 ± 20	312 ± 11	380 ± 50
Band shift $M_1^{B_{01}}(T)$	τ_1^s (fs)	…	…	…
	τ_2^s (ps)	3.9 ± 0.8	4.8 ± 0.8	…
Band shift $M_1^{B_{00}}(T)$	τ_1^s (fs)	200 ± 80	230 ± 70	<100
	τ_2^s (ps)	2.9 ± 0.5	3.6 ± 0.6	…
Band shift $M_1^{SE_{01}}(T)$	τ_1^s (fs)	170 ± 40	250 ± 50	400 ± 200
	τ_2^s (ps)	2.8 ± 0.6	4.7 ± 1.1	…

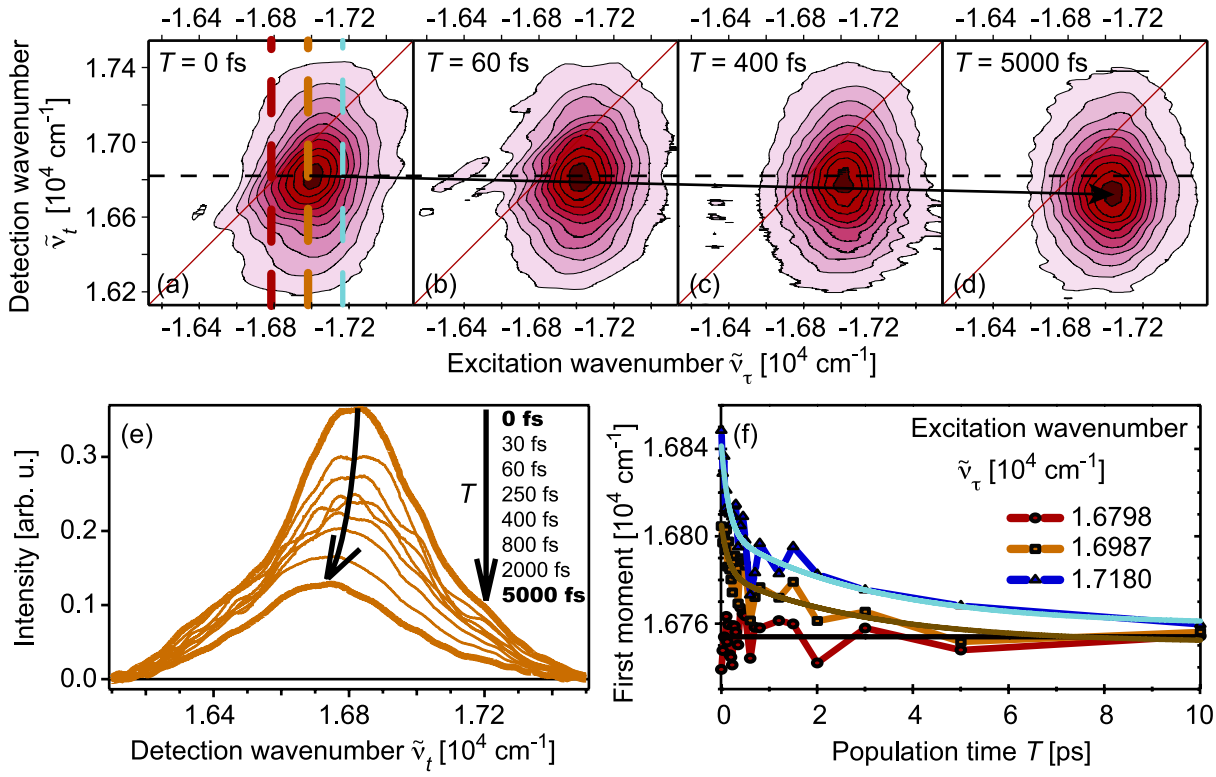

FIG. 3. Selection of experimentally retrieved (normalized) 2D spectra of MEH-PPV at different population times T: (a) 0 fs, (b) 60 fs, (c) 400 fs, and (d) 5000 fs. Contour lines display signal levels from 5% (light pink) to 95% (dark red) in steps of 10%. The dashed horizontal line marks the $T = 0$ average spectral position of the 2D signal at $\widetilde{\nu}_\tau = 1.6987 \times 10^4$ cm^{-1}, while the black arrow indicates the shift of the 2D signal towards lower detection wavenumbers as a function of the population time T. (e) Spectral evolution of the signal along the detection axis for excitation at $\widetilde{\nu}_\tau = 1.6987 \times 10^4$ cm^{-1} (orange vertical dashed line in panel (a)). (f) Temporal evolution of the first moment (i.e., average spectral position) of the signal along the detection axis (symbols) for the different excitation wavenumbers shown by the vertical lines in panel (a). Overlayed solid lines show the best individual bi-exponential fit of each trace.

The most prominent features in these spectra are the initial elongation of the signal along the ($-\widetilde{\nu}_\tau = \widetilde{\nu}_t$) diagonal, which disappears on a time scale of <100 fs, and the continuous red-shift of the 2D signal along the detection axis $\widetilde{\nu}_t$ (see the horizontal dashed line and solid arrow in Figs. 3(a)-3(d)).

The temporal evolution of the 2D signal can be inspected by performing a global analysis and constructing two-dimensional decay-associated spectra (2D-DAS).[53–55] The 2D-DAS are not required for further analysis but are reported in Fig. S9 and discussed in Sec. S3 of the supplementary material[80] for completeness. In the following, we focus on the spectral evolution of the 2D signal along $\widetilde{\nu}_t$ for different (fixed) values of $\widetilde{\nu}_\tau$. One exemplary spectral evolution is plotted in Fig. 3(e) for $\widetilde{\nu}_\tau = 1.6987 \times 10^4$ cm^{-1} (i.e., along the dashed orange cut in Fig. 3(a)). Similar to the analysis of the transient absorption data, at each $\widetilde{\nu}_\tau$, we quantify the temporal evolution of the average spectral position of the signal by calculating the first spectral moment $M_1(\widetilde{\nu}_\tau, T)$ (see Eq. (1b)). The $M_1(\widetilde{\nu}_\tau, T)$ at three different $\widetilde{\nu}_\tau$ values are plotted in Fig. 3(f) and show that the red-shift is absent (within our signal-to-noise ratio) when exciting at the lowest edge of the MEH-PPV absorption band (red) and increases in amplitude upon increasing $\widetilde{\nu}_\tau$ (orange and blue). Independent of $\widetilde{\nu}_\tau$, the band shift is almost complete within 10 ps and the average position of the 2D signal reaches an asymptotic value of $\approx 1.6750 \times 10^4$ cm^{-1}.

In analogy with the analysis of the transient absorption data, we fit the temporal evolution of the $M_1(\widetilde{\nu}_\tau, T)$ at all $\widetilde{\nu}_\tau$ (not just the exemplary ones shown in Fig. 3(f)) with bi-exponential kinetics. The first time constant is allowed to be different for $\widetilde{\nu}_\tau < 1.679 \times 10^4$ cm^{-1}, where an ultrafast (<40 fs) blue-shift is observed. An independent fit of the $M_1(\widetilde{\nu}_\tau, T)$ for different frequencies suggests a small increase of both time constants with increasing $\widetilde{\nu}_\tau$. Such a trend would be expected if the shift originates from the transfer of energy from high- to low-energy exciton states, as relaxation from higher-energy states can proceed through more intermediate steps than from the lower-energy states. However, the signal-to-noise ratio of the data did not allow for an accurate analysis of the $\widetilde{\nu}_\tau$ dependence of the shift rates. Thus, we preferred to describe the evolution of the $M_1(\widetilde{\nu}_\tau, T)$ with the same time constants for all $\widetilde{\nu}_\tau$. The time constants retrieved from this global analysis are 180 ± 30 fs and 4.5 ± 1.1 ps and should be seen as average values over the observed spectral range. These time constants also agree well with the time scales of the band shifts observed in the transient absorption data (Table I).

IV. DISCUSSION

A. Population dynamics

The analysis of the transient absorption data at different excitation energies revealed complex population dynamics. The 2D experiment identified an additional ultrafast (sub-30 fs) component, shorter than our instrumental response function

(see Fig. S9a in the supplementary material[80]). This component accounts for an ultrafast loss of memory in the system, visible as the disappearance of the diagonal elongation in the 2D spectra within the first 100 fs; the non-resonant response of the solvent is also expected to contribute to this signal. An ultrafast (≤25 fs) component was observed with three-pulse photon echo peak shift (3PEPS)[31,56,57] on MEH-PPV at room temperature and ascribed to ultrafast exciton localization. The ultrafast depolarization of the anisotropy, proceeding on a similar time scale, has been explained in terms of several competing molecular processes, including exciton relaxation within a manifold of delocalized states and exciton localization.[14,58] As such processes lead to a loss of the initial memory in the system, we tentatively ascribe the <30 fs component observed in the 2D experiment to the initial exciton relaxation and localization.

Non-exponential kinetics have been repeatedly observed in solutions, films, and isolated molecules of MEH-PPV.[22,24,26,27,30,59,60] It was suggested that photoluminescence decay in isolated chains is mono-exponential with characteristic time scales between 0.4 and 1.2 ns, while non-exponential relaxation was observed in presence of aggregation,[24,27] in films,[17,61,62] and in collapsed MEH-PPV chains.[23,63] All the aforementioned configurations are characterized by a strong reduction in the photoluminescence quantum yield, which is ascribed to the formation of non-emissive interchain species.[16,24,64–66] These species, absorbing above 600 nm, were assigned alternately to excimers, aggregates, polarons, or polaron pairs, which are formed either via direct photoexcitation or via quenching of the singlet excitons.[16,18,58,59,63,67,68]

In none of our experiments on the aggregated phase of MEH-PPV do we detect clear signatures of excited-state absorption signals, neither in the transient spectra nor in the temporal evolution of the signals (Figs. 1(b)-1(c) and Fig. S3 in the supplementary material[80]). This is somewhat surprising, because excited-state absorption to the two-exciton state should appear at energies close to the one-exciton absorption. Deviations from this behavior can be expected in presence of strong electron correlations such as in polyenes. We cannot exclude that some excited-state absorption from the one-exciton states overlaps with the signal at certain wavenumbers (but not with the band B_{01}, see Sec. III A); however, if present, these contributions are not dominant. The 2D signal at $T = 0$ peaks below the diagonal, and this feature could arise from excited-state absorption contributions above the diagonal or from an instantaneous Stokes shift or relaxation process occurring within our time resolution. Although we cannot unambiguously discriminate between the two interpretations, we note that some instantaneous relaxation is expected because of the ultrafast exciton localization process. Two-dimensional double-quantum coherence spectroscopy[69] could provide a direct way to measure the energy position of the two-exciton states in this system, as well as their correlations with the one-exciton states. Instead, we can exclude the presence of long-lived (>1 ns) excited species formed upon direct photoexcitation, which are suggested to relax by re-population of the emissive singlet exciton state in MEH-PPV films. To the best of our knowledge, such excited species were observed exclusively when the excitation energy was tuned above 2.14 eV,[16,17,24,59,63,67,68] where the coiled phase absorbs. Thus, we suggest that these long-lived species are not generated in significant amounts at the excitation energies of our pulses.

In Sec. III A, we have reported the results of a multi-exponential analysis of the $M_0^{(i)}(T)$ for the three major bands observed in the transient absorption experiments. An alternative model which describes the data as a linear combination of a single exponential and a stretched exponential decay is additionally presented in the supplementary material (Table S1).[80] While our data cannot distinguish unambiguously between the two models, both models result in a similar interpretation for the population dynamics in the aggregated phase of MEH-PPV.

For the following discussion, we distinguish between two kinetic regimes: a "slow regime" comprising processes occurring with characteristic time scales of tens to hundreds of ps and a "fast regime" describing processes faster than 10 ps. The processes occurring in the "slow regime" result in a complete recovery of the transient absorption signal at all detection wavenumbers (i.e., a recovery of the thermalized electronic ground state). As energy transfer between excitonic states occurs on sub-10 ps time scales (see also the detailed discussion in Sec. IV B), we ascribe the population decay in the "slow regime" to the $S_1 \rightarrow S_0$ relaxation of the exciton states at the bottom of the density of states. According to the multi-exponential model, two distributed kinetics account for exciton relaxation in the "slow regime," with average time scales of ≈40 ps and ≈320 ps. Upon 2.10 eV excitation and at 140 K, the ≈40 ps and ≈320 ps components account for a 25% and 43% decay of the excited population, respectively. By lowering the temperature to 120 K, about 38% of the total population decay takes place on 40 ps, while the percentage of excitons relaxing on the long time scale decreases to 32%. The presence of two relaxation processes, with virtually the same time scales as observed here, was previously reported for MEH-PPV aggregates in solution, where interchain interactions are likely to play a role in the photophysics.[70] Motivated by the simultaneous decay of an excited-state absorption and the bleach signal, Rothberg and co-workers[70] ascribed the faster process to the non-radiative decay of polaron pairs, and this interpretation additionally explained the low photoluminescence quantum yield of their sample. In our experiment, the ≈40 ps component appears as a simultaneous decay of the bleach and SE signals. Thus, it cannot be explained by the (non-radiative) decay of non-emissive states like polaron pairs, which would not cause a decay of the SE. It has been suggested that the geminate recombination of polaron pairs may result in a delayed population of the emissive singlet exciton states.[24,61] Such a process has been invoked to explain the long-lived emission tail in MEH-PPV films; however, it can also not explain our experimental observations as it would result in an increase (and not a decrease) of the SE signal and it would not affect the bleach. Instead, we suggest that the 40 ps component might be related to energy transfer proceeding from the lowest-energy exciton states of the aggregated phase to defect sites, while the 320 ps kinetics could map the (radiative and intrinsic non-radiative) relaxation of chromophores that are not in proximity of defect sites, and thus are not quenched by such energy transfer process.

In the same way as when interpreting the data in a multi-exponential way, when describing the dynamics in the "slow regime" as a single stretched exponential, i.e., by assuming that the exciton relaxation has a very broad ($\beta \approx 0.48$) distribution of rates, the slow (>10 ps) kinetics is considered to describe the $S_1 \rightarrow S_0$ relaxation. However, in contrast to the multi-exponential decay, the approximate $\exp\left(-\left(\frac{T}{\tau}\right)^{0.5}\right)$ dependence can be interpreted to indicate dispersive energy transfer, e.g., by dipole-dipole coupling, to lower-energy sites where the excitation is immediately quenched.[8,46,47] The spatial distribution of such defect sites would lead to a concomitant distribution of transfer rates and thus to the stretched-exponential decay observed in the signals from stimulated emission and ground-state bleach. In the structurally closely related alkoxy-PPV-derivative OC1C10-PPV, a density of electron traps with depth 0.7 eV on the order of 1023 m^{-3} was determined. These electron traps have been shown to be omnipresent at about the same density in π-conjugated polymers as they are likely to arise from some kind of water-oxygen complex.[71,72] It has been suggested that they also function as exciton traps and in this way limit the exciton diffusion length.[73]

A significant fraction of the excited population relaxes to the ground electronic state on time scales faster than 10 ps, as shown by the simultaneous decrease of both SE and bleach signals. As shown in Figs. 2(c)-2(d) and Table I, the band-shift evolution, which probes exciton relaxation and transfer (see also the discussion in Sec. IV B), is also limited to the "fast regime." We tentatively ascribe the population decay in the "fast regime" to non-radiative internal conversion processes mediated by the presence of defects in the aggregated phase. According to this interpretation, exciton relaxation and transfer can result in the population of defect states that efficiently quench the excited population.[23] Such interpretation is consistent with the decrease of emission quantum yield reported for MEH-PPV films and aggregates as compared to single solvated chains.[16,24,65,66]

B. Energy transport and relaxation

Turning now to the temporal evolution of the spectral average position of the transient bleach and stimulated emission bands, the analysis of the transient absorption data allowed us to distinguish two processes occurring on ≈200 fs and ≈4 ps time scales. The former appears as a red-shift of only the SE signals, while the latter can be detected in both the ground-state bleach and the SE bands and is absent when exciting at the onset of the absorption (2.03 eV).

Let us consider the slow (≈4 ps) shift first. A spectral shift of the ground-state bleach can arise from spectral diffusion in the electronic ground state or from Förster energy transfer from higher-energy to lower-energy excitons located at different sites in the aggregate (exciton hopping). We now discuss both putative explanations before illustrating how to differentiate them.

Spectral diffusion in the ground state is observed in presence of an inhomogeneous distribution of transition energies. Photoexcitation with spectra narrower than the inhomogeneous spectral width selects a sub-ensemble of chromophores with their electronic transition matching the energy of the excitation pulse. The hole generated in the ground-state distribution by such photoselection is refilled prior to the excited-state relaxation due to environment-induced fluctuations in the transition energy of non-photoexcited chromophores. Depending on whether the excitation pulse selects a sub-ensemble of chromophores in the center of the transition energy distribution (i.e., in the middle of the absorption band) or at one edge of it, this process will appear as a broadening or as a shift of the bleach band, respectively.

As the second possible explanation, (Förster) energy transfer within the exciton density of states also results in a shift of both absorption and emission towards lower energies as the energy flows from higher-energy to lower-energy exciton states located on different segments of the polymer. Förster energy transfer occurs between excitonic states with little or no orbital overlap by dipole-dipole coupling. Since the donor and acceptor excitons do not share a common ground state, relaxation of the excitons absorbing at higher energies results in the recovery of the high-energy tail of the ground-state bleach, while the simultaneous excitation of lower-energy exciton states causes an increase of the low-energy side of the bleach signal.

Coherent 2D spectroscopy can discriminate very clearly between the aforementioned two processes as follows. Spectral diffusion by homogeneous broadening in the ground state appears as a loss of the memory of the initial excitation (i.e., loss of the diagonal elongation), while the 2D signal broadens symmetrically and becomes round. In our data, none of these features is observed on time scales longer than 100 fs. Instead, on a 4 ps time scale, the signal intensity shifts asymmetrically towards the cross-peak below the diagonal, and this signifies excitonic energy transfer. Indeed, a 2D spectrum correlates the initially photoexcited states (along $\tilde{\nu}_\tau$) with the signal arising from the states populated after waiting time T. Thus in 2D spectroscopy, energy transfer appears as a rise of the cross peaks between the initial high-energy states (along $\tilde{\nu}_\tau$) and the final lower-energy states (along $\tilde{\nu}_t$). When, as in the case of MEH-PPV, the high exciton density prevents us to distinguish the single exciton states (and thus the single cross peaks), the energy flow through these states appears as a red-shift of the 2D signal along the detection axis. Consistent with our interpretation, the amplitude of red-shift increases when moving the excitation to higher wavenumbers, because higher-energy excitonic states are accessed (see also Fig. 3(f)).

Two-dimensional spectroscopy further allows us to observe the dynamics of energy transfer as a function of the excitation wavenumber $\tilde{\nu}_\tau$. The amplitude of the ≈4.5 ps red-shift observed in the 2D experiment is obtained from the global analysis of $M_1(\tilde{\nu}_\tau, T)$ and is plotted in Fig. 4 as a function of $\tilde{\nu}_\tau$. Since the bleach and SE components of the signal shift simultaneously and with the same amplitude (as it is well resolved by the analysis of the first moments of the transient absorption bands B_{01} and SE_{01} upon 2.10 eV excitation), the amplitude of the shift at each $\tilde{\nu}_\tau$ reflects the amount of energy relaxation. No shift of the signal is observed, within our signal-to-noise ratio, for $\tilde{\nu}_\tau < 1.6750 \times 10^4$ cm^{-1}, except for a small ultrafast component (<40 fs blue-shift) ascribed to the initial loss of the diagonal elongation. Accordingly,

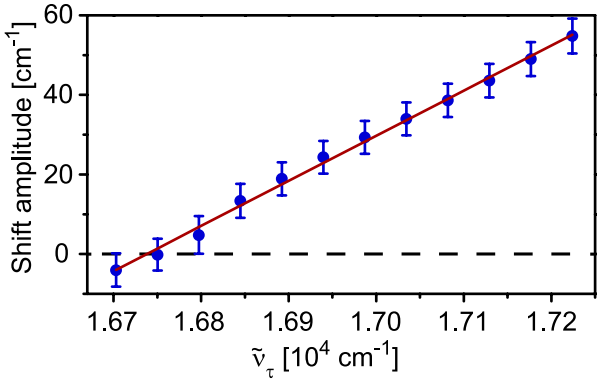

FIG. 4. Amplitude of the ≈4.5 ps red-shift along the detection axis observed in the 2D experiment as a function of the excitation wavenumber $\widetilde{\nu}_\tau$, obtained from the bi-exponential global fit of the $M_1(\widetilde{\nu}_\tau, T)$. Error bars are $\pm\sigma$. The data are phenomenologically described by a linear fit (red line) with slope of 0.113 ± 0.002.

we conclude that the position of the 0–0 transition for the lowest exciton states in the aggregated phase of MEH-PPV is $\widetilde{\nu} = (16750 \pm 50)\,\mathrm{cm}^{-1}$, where the confidence value of 50 cm^{-1} is given by the wavenumber separation between consecutive $\widetilde{\nu}_\tau$ points in Fig. 4.

Noteworthy, despite the fact that $M_1(\widetilde{\nu}_\tau, T)$ reaches the same asymptotic value for each $\widetilde{\nu}_\tau$ (Fig. 3(f)), the ≈4.5 ps red-shift (Fig. 4) accounts only for a small fraction of the energy relaxation (≈55 cm^{-1} at $\widetilde{\nu}_\tau = 1.7224 \times 10^4\ \mathrm{cm}^{-1}$ instead of the expected ≈400 cm^{-1}). This indicates that most of the energy relaxation occurs on time scales much faster than 4.5 ps and populates the low-energy exciton states, at most ≈55 cm^{-1} higher in energy than the lowest energy states of the aggregated phase. Thus, Förster energy transfer occurs between states at the bottom of the density of states.

The typical intrachain energy transport in the blue phase of MEH-PPV is on the order of ≈250 ps, while much faster energy transport is observed in films and ascribed to interchain exciton hopping.[12,15,16,74] The short average time scale observed in our work indicates strongly, by comparison, that energy transfer in the aggregated phase has mostly an interchain character. The dominant interchain character of energy hopping in the aggregated phase is not surprising, due to the higher percentage of chromophores with interchain neighbors in the ordered aggregated structure as compared to the solvated molecules at room temperature. Additionally, the average value of ≈4 ps for energy transfer in the aggregated phase of MEH-PPV compares well with the observation by Basché and coworkers,[26] who reported a 3.9 ps average energy transfer time between red-emitting chromophores in packed chain regions of single MEH-PPV molecules. Thus, it is likely that the molecular organization of MEH-PPV in packed chain regions is locally ordered and resembles that of the low-temperature aggregate.

It would be meaningful to compare the average time scale for Förster-like energy transfer in the aggregated phase and in the coiled phase. However, we are not aware of a precise estimation of either the excitation-dependent or the average time constants for interchain exciton energy transfer in the coiled phase of MEH-PPV. Energy transport in both room-temperature and low-temperature films of MEH-PPV is found to occur on a few-ps time scale with a rate that increases with increasing excitation energy;[16,75] however, it is not clear how these value relate with the energy migration between blue and red sites of MEH-PPV, which are believed to co-exist in films.

We noted before that both our transient absorption and 2D experiments show an additional ultrafast (≈200 fs) red-shift of the transient signal, which is observed exclusively in the SE bands and whose amplitude increases at higher excitation energies. The ≈200 fs shift amplitude is plotted in Fig. S10 of the supplementary material[80] as a function of the excitation wavenumber; however, the interpretation of these data is complicated by the presence of overlapping contributions. Several processes can cause a red-shift of the SE, and in general, it is not trivial to distinguish whether such a red-shift arises from exciton relaxation, vibrational relaxation, or conformational dynamics in the excited state. As the ≈200 fs shift is observed exclusively in the SE signal, we can exclude that it originates from Förster electronic energy transfer between states located on different segments of the polymer, which would result also in a red-shift of the bleach signal.

A decay in the transient grating and 3PEPS signals of the room-temperature phase of MEH-PPV on similar time scales (≈200 – 400 fs) was reported[31,56] and ascribed to exciton relaxation. The sub-ps red-shift of the emission observed in several PPV-based polymers at room temperature was also ascribed to exciton relaxation. Indeed, being absent in small oligomers, this red-shift cannot be accounted for exclusively by vibrational relaxation or solvation dynamics.[76,77] A similar argument has also been used to exclude that the aforementioned red-shift is primarily due to conformational dynamics and planarization in the excited state. Conformational dynamics in the excited state are believed to play an important role in the relaxation of photoexcited polymers. In particular, ultrafast structural relaxation on a time scale comparable with the period of high-frequency vibrational modes is believed to

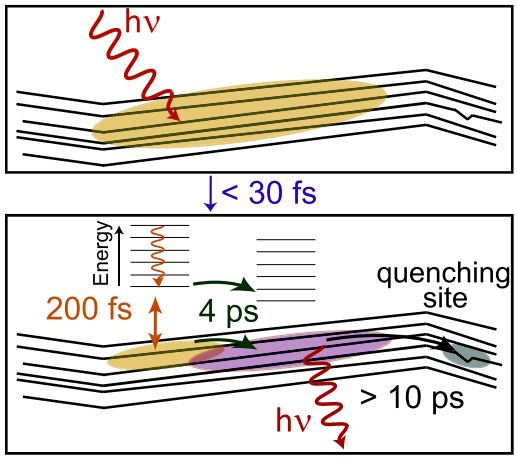

FIG. 5. Schematic view of the photophysics of the aggregated phase of MEH-PPV. The delocalized exciton states initially photoexcited (upper frame) localize on an ultrafast (<30 fs) time scale on smaller domains on the aggregate chains (lower frame). Within the following ≈200 – 250 fs, exciton relaxation within these smaller domains occurs and leads to the population of the exciton states at the bottom of the density of states. On a ≈4 ps time scale, Förster energy transfer leads to migration of the exciton towards the lowest energy states of the aggregated phase, from which energy transfer to defect states and radiative relaxation take place.

be responsible for the ultrafast exciton localization in MEH-PPV.[7,31,57,58] In contrast, torsional relaxation and excited-state planarization are expected to take place on a time scale of a few ps or longer in MEH-PPV at room temperature and in solution.[60,78,79] In an aggregated state and at low temperature, we expect such conformational changes to be even slower.

In agreement with all these observations, we argue that the ≈200 fs shift arises mostly from exciton relaxation within a manifold of electronic states sharing the same ground state (otherwise the bleach would shift as well). This assignment is further supported by the fact that, as discussed above, on a ps time scale, the exciton population is already relaxed to exciton states at the bottom of the density of states, from which Förster energy transfer takes place.

V. SUMMARY AND CONCLUSIONS

Summarizing, the combination of broadband transient absorption and coherent 2D spectroscopy experiments allows us to propose the relaxation pathways shown in Fig. 5 for the aggregated phase of MEH-PPV at low temperatures.

The initially delocalized photoexcited exciton states localize on a sub-30 fs time scale on smaller conjugated domains of the polymer chains (spectroscopic units in the following).[7] Depending on the excitation frequency and owing to the energetic disorder within the aggregate, different spectroscopic units can be accessed. Exciton relaxation within the manifold of states sharing the same ground state occurs on a time scale of ≈200 fs, simultaneous with cooling. This mechanism can be regarded as a relaxation process occurring within each spectroscopic unit and leads to the ultrafast population of the lowest excitonic states belonging to that spectroscopic unit. Our 2D measurements reveal that in the frequency range accessed by our pulses, the average energy of the exciton states populated after the ≈200 fs relaxation is at most ≈55 cm^{-1} higher than the lowest exciton states of the aggregate. It would be interesting to compare this value with the theoretical inhomogeneous width of the lowest-exciton density of states in the aggregated phase that can be accessed by our excitation pulses, as a function of the energetic disorder and the excitonic density of states within the single spectroscopic units.

Diffusion of the relaxed excitons occurs on a longer (≈4 ps) time scale via interchain Förster energy transfer. As no further signatures of energy transfer within the aggregated-phase are detected on longer time scales, we conclude that the ≈4 ps exciton diffusion localizes efficiently the excitons in the energetic states at the bottom of the aggregated-phase density of states. From these states, further exciton transfer towards defect sites, as well as poplation relaxation, occurs with a broad distribution of rates on time scales >10 ps.

Noteworthy, despite chain planarization in the excited state is expected in polymers, we do not see clear signatures of such a process in our data. The MEH-PPV aggregated phase compares better to a bulk polymer than to solvated chains, thus conformational effects are expected on time scales longer than 10 ps. It is possible that due to the already highly planar structure of the aggregated phase, the effects of conformational changes on the emission spectra are too small to be detected in our experiments. Experiments monitoring the aggregated-phase emission with a higher spectral resolution could give an answer to this question.

Coherent 2D spectroscopy is a particularly suited technique to observe the energetic relaxation as a function of the excitation energy in complex systems. By combining coherent 2D spectroscopy and transient absorption, we have characterized the energy relaxation in the aggregated low-temperature phase of MEH-PPV. In particular, we showed that most exciton relaxation is ultrafast with little spatial energy displacement, and that 95% of excitons are localized in the low-energy exciton states within the first ≈12 ps after excitation.

ACKNOWLEDGMENTS

We acknowledge the Free State of Bavaria for financial support through the "Solar Technologies Go Hybrid (Soltech)" program and T.B. acknowledges the European Cooperation in Science and Technology (COST) Action "PERSPECT-H2O" (CM1202). We also thank Professor Patrick Nuernberger, Professor Heinz Bässler, and Dr. Jakub Dostál for helpful discussions.

[1]K. M. Coakley and M. D. McGehee, Chem. Mater. **16**, 4533 (2004).
[2]B. Zhao, Z. He, X. Cheng, D. Qin, M. Yun, M. Wang, X. Huang, J. Wu, H. Wu, and Y. Cao, J. Mater. Chem. C **2**, 5077 (2014).
[3]B. Muhsin, R. Roesch, G. Gobsch, and H. Hoppe, Sol. Energy Mater. Sol. Cells **130**, 551 (2014).
[4]J. You, L. Dou, K. Yoshimura, T. Kato, K. Ohya, T. Moriarty, K. Emery, C.-C. Chen, J. Gao, G. Li, and Y. Yang, Nat. Commun. **4**, 1446 (2013).
[5]I. Hwang and G. D. Scholes, Chem. Mater. **23**, 610 (2011).
[6]S. T. Hoffmann, H. Bässler, and A. Köhler, J. Phys. Chem. B **114**, 17037 (2010).
[7]W. J. D. Beenken and T. Pullerits, J. Phys. Chem. B **108**, 6164 (2004).
[8]L. M. Herz, C. Silva, A. C. Grimsdale, K. Müllen, and R. T. Phillips, Phys. Rev. B **70**, 165207 (2004).
[9]R. Q. Albuquerque, C. C. Hofmann, J. Köhler, and A. Köhler, J. Phys. Chem. B **115**, 8063 (2011).
[10]E. Collini and G. D. Scholes, Science **323**, 369 (2009).
[11]G. Padmanaban and S. Ramakrishnan, J. Am. Chem. Soc. **122**, 2244 (2000).
[12]B. J. Schwartz, T.-Q. Nguyen, J. Wu, and S. H. Tolbert, Synth. Met. **116**, 35 (2001).
[13]E. Hennebicq, G. Pourtois, G. D. Scholes, L. M. Herz, D. M. Russell, C. Silva, S. Setayesh, A. C. Grimsdale, K. Müllen, J. L. Brédas, and D. Beljonne, J. Am. Chem. Soc. **127**, 4744 (2005).
[14]T. E. Dykstra, E. Hennebicq, D. Beljonne, J. Gierschner, G. Claudio, E. R. Bittner, J. Knoester, and G. D. Scholes, J. Phys. Chem. B **113**, 656 (2009).
[15]T.-Q. Nguyen, J. Wu, V. Doan, B. J. Schwartz, and S. H. Tolbert, Science **288**, 652 (2000).
[16]I. Martini, A. Smith, and B. Schwartz, Phys. Rev. B **69**, 035204 (2004).
[17]T.-Q. Nguyen, I. B. Martini, J. Liu, and B. J. Schwartz, J. Phys. Chem. B **104**, 237 (2000).
[18]B. J. Schwartz, Annu. Rev. Phys. Chem. **54**, 141 (2003).
[19]R. J. Kline and M. D. McGehee, J. Macromol. Sci., Part C: Polym. Rev. **46**, 27 (2006).
[20]J. Clark, C. Silva, R. H. Friend, and F. C. Spano, Phys. Rev. Lett. **98**, 206406 (2007).
[21]H. Yamagata, C. M. Pochas, and F. C. Spano, J. Phys. Chem. B **116**, 14494 (2012).
[22]T.-Q. Nguyen, V. Doan, and B. J. Schwartz, J. Chem. Phys. **110**, 4068 (1999).
[23]J. Yu, D. Hu, and P. F. Barbara, Science **289**, 1327 (2000).
[24]C. J. Collison, L. J. Rothberg, V. Treemaneekarn, and Y. Li, Macromolecules **34**, 2346 (2001).
[25]D. Y. Kim, J. K. Grey, and P. F. Barbara, Synth. Met. **156**, 336 (2006).
[26]F. A. Feist, M. F. Zickler, and T. Basché, ChemPhysChem **12**, 1499 (2011).
[27]H. Lin, R. P. Hania, R. Bloem, O. Mirzov, D. Thomsson, and I. G. Scheblykin, Phys. Chem. Chem. Phys. **12**, 11770 (2010).

[28]A. Köhler, S. T. Hoffmann, and H. Bässler, J. Am. Chem. Soc. **134**, 11594 (2012).
[29]P. Wood, I. D. W. Samuel, G. R. Webster, and P. L. Burn, Synth. Met. **119**, 571 (2001).
[30]A. Dogariu, D. Vacar, and A. J. Heeger, Phys. Rev. B **58**, 10218 (1998).
[31]J. Sperling, A. Nemeth, P. Baum, F. Šanda, E. Riedle, H. Kauffmann, S. Mukamel, and F. Milota, Chem. Phys. **349**, 244 (2008).
[32]F. Panzer, H. Bässler, R. Lohwasser, M. Thelakkat, and A. Köhler, J. Phys. Chem. Lett. **5**, 2742 (2014).
[33]J.-L. Brédas, D. Beljonne, V. Coropceanu, and J. Cornil, Chem. Rev. **104**, 4971 (2004).
[34]U. Selig, F. Langhojer, F. Dimler, T. Löhrig, C. Schwarz, B. Gieseking, and T. Brixner, Opt. Lett. **33**, 2851 (2008).
[35]R. Augulis and D. Zigmantas, Opt. Express **19**, 13126 (2011).
[36]T. Brixner, T. Mančal, I. V. Stiopkin, and G. R. Fleming, J. Chem. Phys. **121**, 4221 (2004).
[37]C. Scharsich, R. H. Lohwasser, M. Sommer, U. Asawapirom, U. Scherf, M. Thelakkat, D. Neher, and A. Köhler, J. Polym. Sci., Part B: Polym. Phys. **50**, 442 (2012).
[38]G. Williams, *Electric Phenomena in Polymer Science*, Advances in Polymer Science Vol. 33 (Springer, Berlin, Heidelberg, 1979), pp. 59–92.
[39]J. Klafter and A. Blumen, J. Chem. Phys. **80**, 875 (1984).
[40]R. G. Palmer, D. L. Stein, E. Abrahams, and P. W. Anderson, Phys. Rev. Lett. **53**, 958 (1984).
[41]A. Blumen, G. Zumofen, and J. Klafter, Phys. Rev. B **30**, 5379 (1984).
[42]J. Budimir and J. L. Skinner, J. Chem. Phys. **82**, 5232 (1985).
[43]J. Klafter and A. Blumen, Chem. Phys. Lett. **119**, 377 (1985).
[44]J. Klafter and M. F. Shlesinger, PNAS **83**, 848 (1986).
[45]B. Mollay and H. F. Kauffmann, J. Chem. Phys. **97**, 4380 (1992).
[46]B. Mollay, U. Lemmer, R. Kersting, R. F. Mahrt, H. Kurz, H. F. Kauffmann, and H. Bässler, Phys. Rev. B **50**, 10769 (1994).
[47]K. Brunner, A. Tortschanoff, C. Warmuth, H. Bässler, and H. F. Kauffmann, J. Phys. Chem. B **104**, 3781 (2000).
[48]P. J. Steinbach, R. Ionescu, and C. R. Matthews, Biophys. J. **82**, 2244 (2002).
[49]P. J. Steinbach, Anal. Biochem. **427**, 102 (2012).
[50]S. Mukamel, Annu. Rev. Phys. Chem. **51**, 691 (2000).
[51]T. Brixner, J. Stenger, H. M. Vaswani, M. Cho, R. E. Blankenship, and G. R. Fleming, Nature **434**, 625 (2005).
[52]C. Y.-C. Ginsberg, S. Naomi, and G. R. Fleming, Acc. Chem. Res. **42**, 1352 (2009).
[53]C. Consani, G. Auböck, F. v. Mourik, and M. Chergui, Science **339**, 1586 (2013).
[54]V. I. Prokhorenko, EPA Newsl., issue June 2012, pp. 21–23.
[55]F. Milota, V. I. Prokhorenko, T. Mancal, H. von Berlepsch, O. Bixner, H. F. Kauffmann, and J. Hauer, J. Phys. Chem. A **117**, 6007 (2013).
[56]G. D. Scholes, D. S. Larsen, G. R. Fleming, G. Rumbles, and P. L. Burn, Phys. Rev. B **61**, 13670 (2000).
[57]T. E. Dykstra, V. Kovalevskij, X. Yang, and G. D. Scholes, Chem. Phys. **318**, 21 (2005).
[58]A. Ruseckas, P. Wood, I. Samuel, G. Webster, W. Mitchell, P. Burn, and V. Sundström, Phys. Rev. B **72**, 115214 (2005).
[59]L. J. Rothberg, M. Yan, F. Papadimitrakopoulos, M. E. Galvin, E. W. Kwock, and T. M. Miller, Synth. Met. **80**, 41 (1996).
[60]R. E. Di Paolo, J. Seixas de Melo, J. Pina, H. D. Burrows, J. Morgado, and A. L. Maçanita, ChemPhysChem **8**, 2657 (2007).
[61]M. Yan, L. J. Rothberg, E. W. Kwock, and T. M. Miller, Phys. Rev. Lett. **75**, 1992 (1995).
[62]L. Rothberg, in *Semiconducting Polymers: Chemistry, Physics and Engineering*, 2nd ed. (Wiley, 2006), Chap. Photophysics of Conjugated Polymers, p. 179.
[63]H. Lin, S. R. Tabaei, D. Thomsson, O. Mirzov, P.-O. Larsson, and I. G. Scheblykin, J. Am. Chem. Soc. **130**, 7042 (2008).
[64]H. A. Mizes and E. M. Conwell, Phys. Rev. B **50**, 11243 (1994).
[65]J. W. Blatchford, S. W. Jessen, L.-B. Lin, T. L. Gustafson, D.-K. Fu, H.-L. Wang, T. M. Swager, A. G. MacDiarmid, and A. J. Epstein, Phys. Rev. B **54**, 9180 (1996).
[66]H. Lin, Y. Tian, K. Zapadka, G. Persson, D. Thomsson, O. Mirzov, P.-O. Larsson, J. Widengren, and I. G. Scheblykin, Nano Lett. **9**, 4456 (2009).
[67]R. Jakubiak, C. J. Collison, W. C. Wan, L. J. Rothberg, and B. R. Hsieh, J. Phys. Chem. A **103**, 2394 (1999).
[68]C.-X. Sheng, M. Tong, S. Singh, and Z. Vardeny, Phys. Rev. B **75**, 085206 (2007).
[69]J. Kim, S. Mukamel, and G. D. Scholes, Acc. Chem. Res. **42**, 1375 (2009).
[70]P. Wang, C. J. Collison, and L. J. Rothberg, J. Photochem. Photobiol., A **144**, 63 (2001).
[71]H. T. Nicolai, M. Kuik, G. a. H. Wetzelaer, B. de Boer, C. Campbell, C. Risko, J. L. Brédas, and P. W. M. Blom, Nat. Mater. **11**, 882 (2012).
[72]A. Köhler, Nat. Mater. **11**, 836 (2012).
[73]O. V. Mikhnenko, M. Kuik, J. Lin, N. van der Kaap, T.-Q. Nguyen, and P. W. M. Blom, Adv. Mater. **26**, 1912 (2014).
[74]K. M. Gaab and C. J. Bardeen, J. Phys. Chem. B **108**, 4619 (2004).
[75]J. Sperling, F. Milota, A. Tortschanoff, C. Warmuth, B. Mollay, H. Bässler, and H. F. Kauffmann, J. Chem. Phys. **117**, 10877 (2002).
[76]R. Kresting, U. Lemmer, R. F. Mahrt, K. Leo, H. Kurz, H. Bässler, and E. O. Göbel, Phys. Rev. Lett. **70**, 3820 (1993).
[77]K. S. Wong, H. Wang, and G. Lanzani, Chem. Phys. Lett. **288**, 59 (1998).
[78]S. Westenhoff, W. J. D. Beenken, R. H. Friend, N. C. Greenham, A. Yartsev, and V. Sundström, Phys. Rev. Lett. **97**, 166804 (2006).
[79]P. Parkinson, C. Müller, N. Stingelin, M. B. Johnston, and L. M. Herz, J. Phys. Chem. Lett. **1**, 2788 (2010).
[80]See supplementary material at http://dx.doi.org/10.1063/1.4918645 for information on the linearity of the signal with the photon flux, supplementary figures, two-dimensional decay-associated spectra, and the excitation-dependent amplitude of the fast band-shift.

Supporting Information for:

Relaxation dynamics and exciton energy transfer in the low-temperature phase of MEH-PPV

Cristina Consani,[1] Federico Koch,[1] Fabian Panzer,[2] Thomas Unger,[2] Anna Köhler,[2] and Tobias Brixner[1, 3, a)]

[1)] *Institut für Physikalische und Theoretische Chemie, Universität Würzburg, Am Hubland, 97074 Würzburg, Germany*

[2)] *Lehrstuhl Experimentalphysik II, Universität Bayreuth, Universitätsstraße 30, 95440 Bayreuth, Germany*

[3)] *Center for Nanosystems Chemistry (CNC), Universität Würzburg, Am Hubland, 97074 Würzburg, Germany*

(Dated: 22 June 2015)

[a)] Electronic mail: brixner@phys-chemie.uni-wuerzburg.de

S1. LINEARITY OF THE SIGNAL WITH THE PHOTON FLUX

For all our experiments, we made sure to work in experimental conditions where our signal was linear with the excitation power. As an example, in Fig. S1 we show time-dependent traces at different photon flux upon excitation at 2.10 eV.

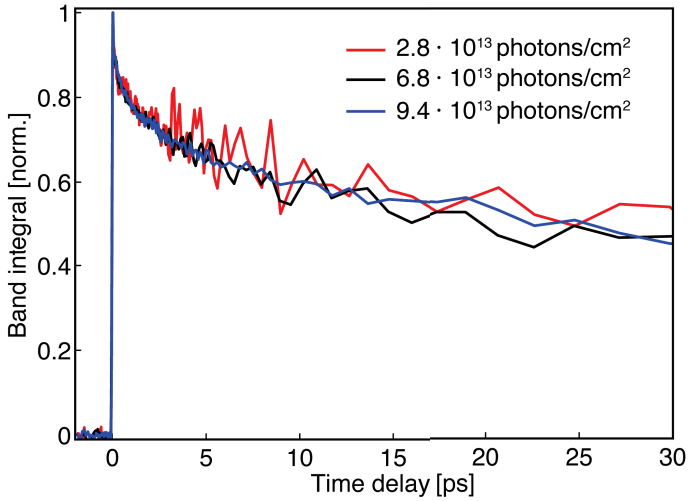

FIG. S1. Normalized band integral M_0 for the band B_{00} (see also eq. 1a of the main paper) for different photon fluxes upon excitation at 2.10 eV. Within our signal-to-noise ratio, no differences are observed in these conditions, thus we conclude that, if exciton-exciton annihilation effects are present in our data, they are too small to be visible in our measurements. The photon flux is determined as the total number number of photons per pulse and per unit area. The latter is calculated with a radius of 2σ of the beam size.

S2. SUPPLEMENTARY FIGURES AND TABLES

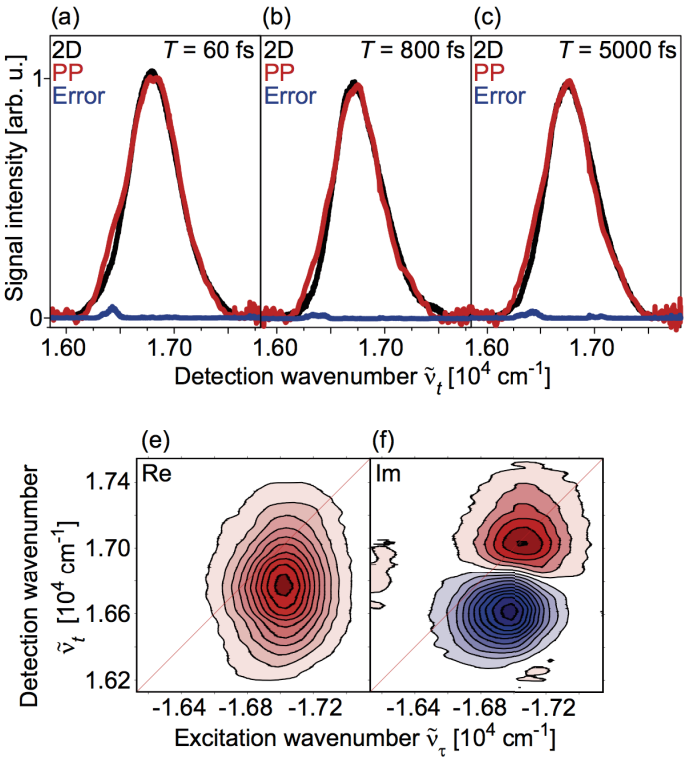

FIG. S2. Optimal projection of the 2D data along the detection axis after phasing (black) and pump-probe data acquired in the same setup of the 2D experiment and with the same excitation pulses (PP, red) for different population times: (a) 60 fs, (b) 800 fs and (c) 5000 fs. The blue line shows the difference of the 2D projection and the pump-probe data. The (d) real and (e) imaginary of the signal at 800 fs is also shown for completeness.

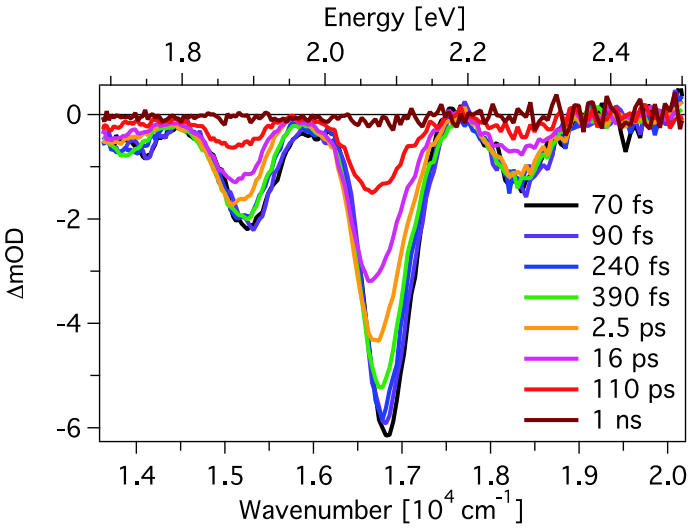

FIG. S3. Selection of transient absorption spectra at different population times for the aggregated phase of MEH-PPV at 120 K and upon excitation at 2.10 eV (1.69×10^4 cm^{-1}).

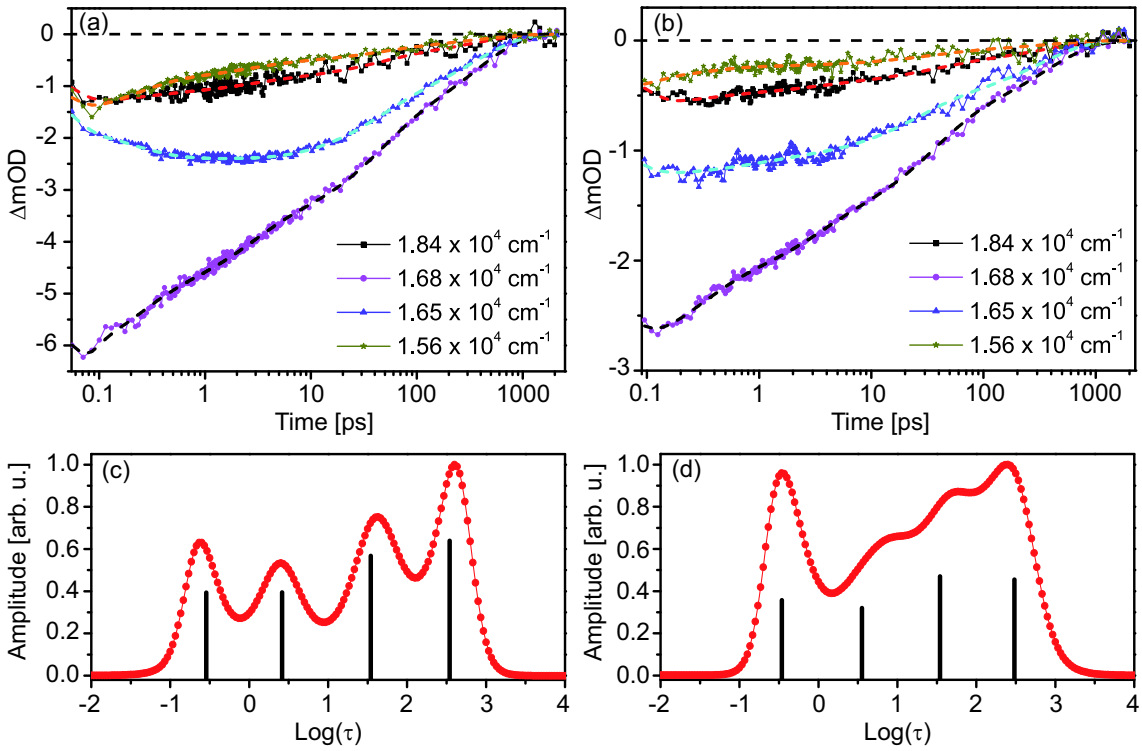

FIG. S4. Temporal evolution of the transient absorption signal at four different probe wavenumbers (symbols) upon (a) 2.10 eV excitation and (b) 2.03 eV excitation. Dashed lines are the best multi-exponential fits to the observed kinetics. The best rate distributions describing the temporal evolution of the signal at 1.68×10^4 cm^{-1} eV are retrieved via the maximum entropy method via the program MemExp and are shown (red) for (c) 2.10 eV excitation and (d) 2.03 eV excitation. Vertical bars (black) indicate the time constants that best describe the data when a multi-exponential model is assumed.

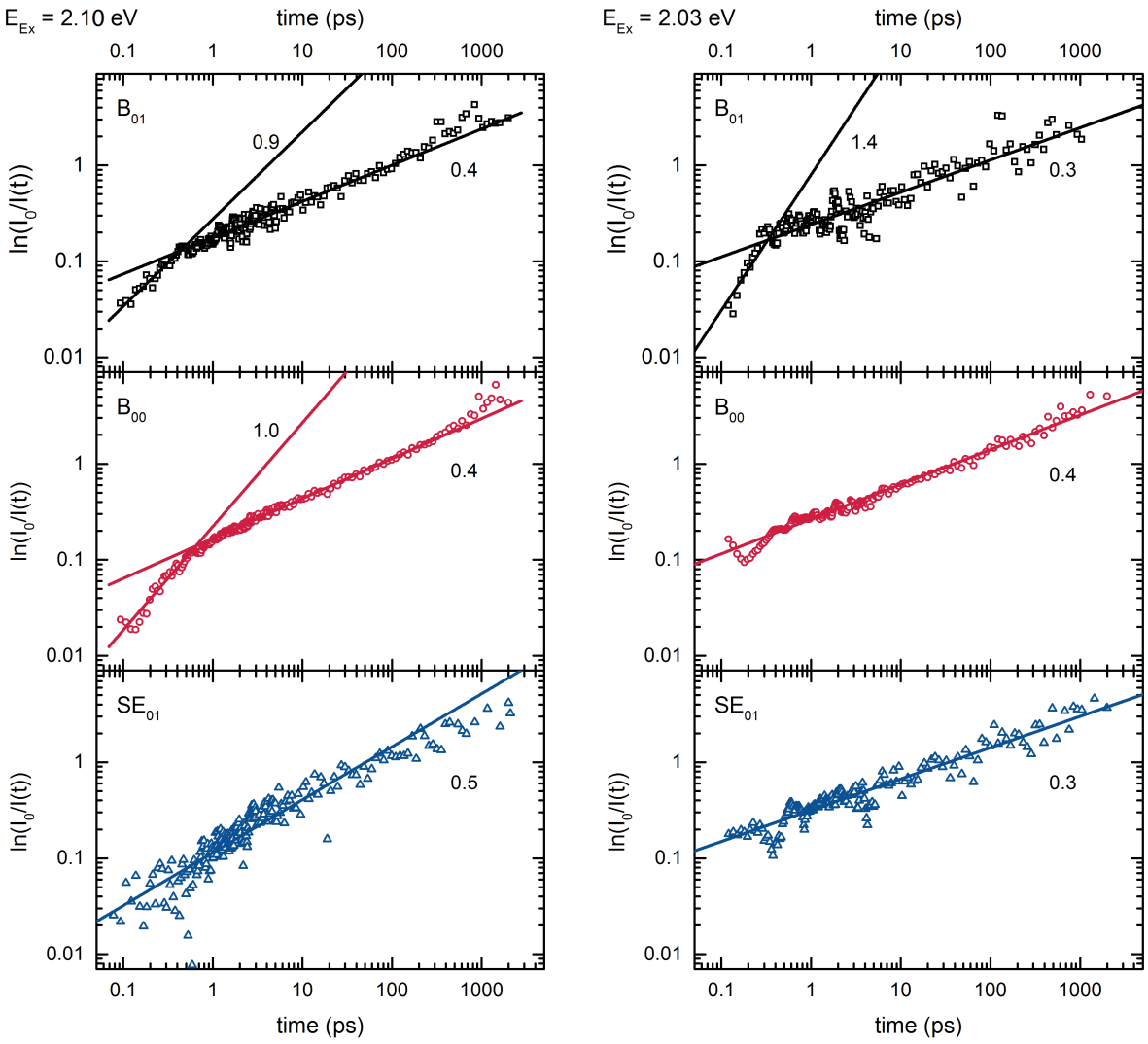

FIG. S5. Kohlrausch-Williams-Watt representation of the $M_0^{(i)}(T)$ decays (symbols) for $i = \mathrm{B}_{01}$, B_{00} and SE_{01} at 140 K upon excitation at 2.10 eV (left panel) and 2.03 eV (right panel). The solid lines indicate different slopes for ease of comparison.

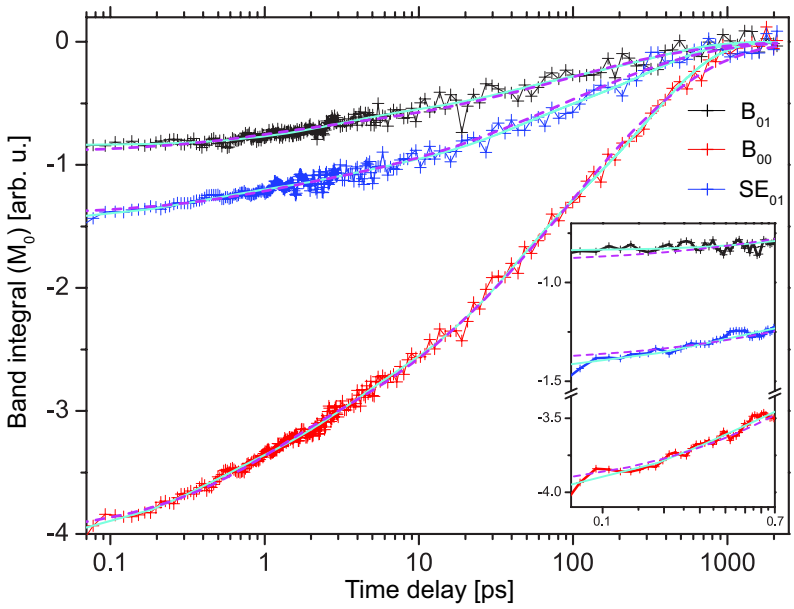

FIG. S6. Comparison between the fit of the $M_0^{(i)}(T)$ with a multi-exponential model (dashed) and with a linear combination of an exponential and stretched exponential decay (solid) upon excitation at 2.10 eV, 140 K.

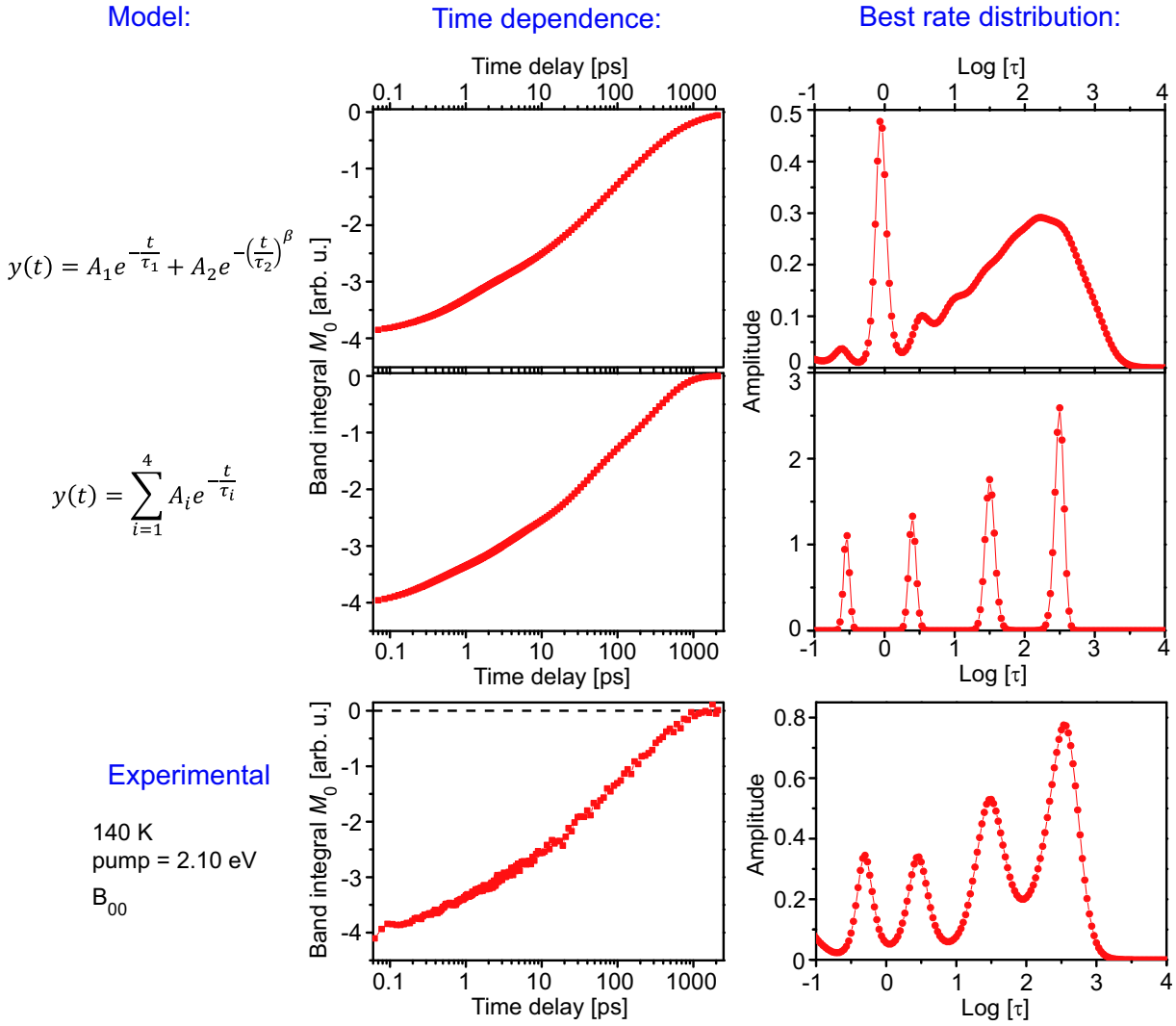

FIG. S7. Comparison between different kinetic models and experimental data. Time dependence and best rate distribution retrieved by the MEM analysis via the program MemExp for the linear combination of an exponential and a stretched exponential decay (first line), a multi-exponential decay with four time constants (second line) and the experimentally measured band integral M_0^{B00} upon excitation at 2.10 eV of the 140 K sample (third line).

TABLE S1. Characteristic time constants obtained from a fit of the integrated signals $M_0^{(i)}(T)$ (i = B_{01}, B_{00} and SE_{01}) of the transient absorption data described in Section III.A of the main paper, with the fit function $M_0(T) = A_1 e^{-\frac{T}{\tau_1}} + A_2 e^{-(\frac{T}{\tau_2})^\beta}$

	Excitation energy	2.10 eV	2.10 eV	2.03 eV
	Temperature	120 K	140 K	140 K
Population decay $M_0(T)$	τ_1 [ps]	1.18 ± 0.12	0.88 ± 0.07	0.26 ± 0.17
	τ_2 [ps]	74 ± 3	94 ± 3	63 ± 3
	β [ps]	0.48 ± 0.01	0.49 ± 0.01	0.45 ± 0.02

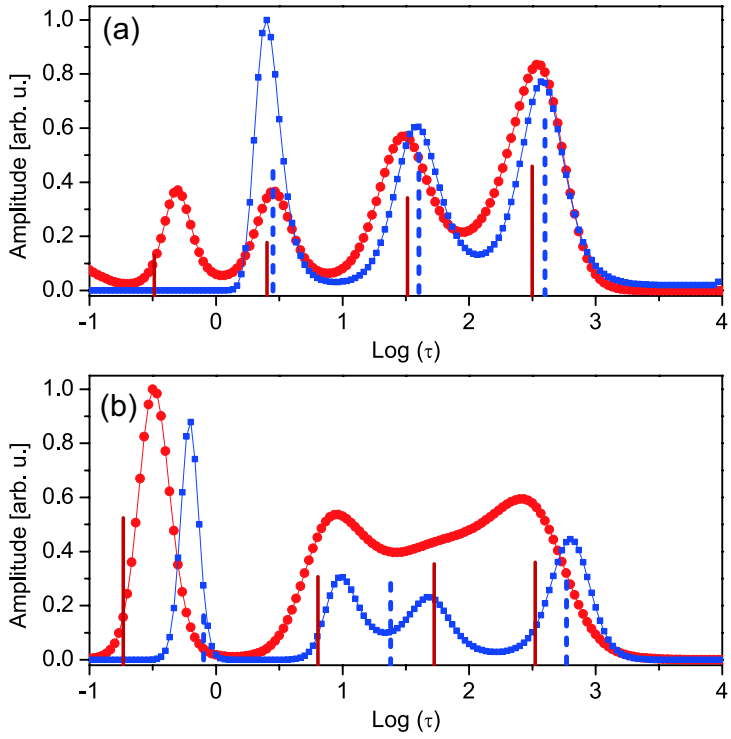

FIG. S8. Best rate distributions describing the temporal evolution of M_0 for the bleach bands B_{01} (blue squares) and B_{00} (red circles), upon excitation at (a) 2.10 eV and (b) 2.03 eV, as retrieved via the maximum entropy method analysis. Vertical blue dashed (red solid) lines show the best rate constants for the multi-exponential fit of the B_{01} (B_{00}) population dynamics.

S3. TWO-DIMENSIONAL DECAY-ASSOCIATED SPECTRA

We can describe the temporal dependence of the 2D signal by global analysis with a multi-exponential model. We note here that, similar to the analysis of the transient absorption data in Section III A of the main paper, discussing results with a multi-exponential fit does not necessarily imply that the observed kinetics must arise from four different processes with sharp timescales. However, this approach allows separating different features in the temporal evolution of the signal.

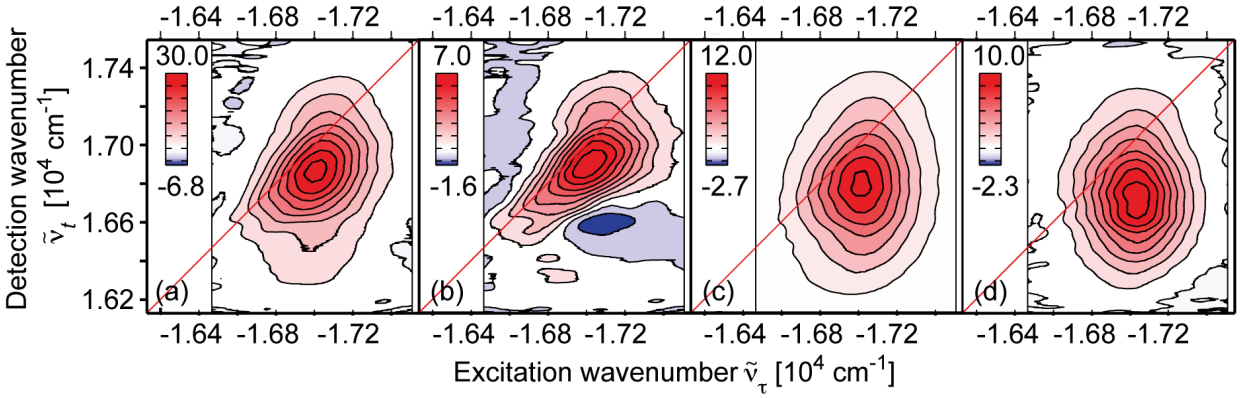

FIG. S9. Two-dimensional decay-associated spectra (2D-DAS) obtained from global analysis of the 2D data and associated with (a) sub-30 fs, (b) 290 fs, (c) 2.9 ps, and (d) $\gg$ 10 ps kinetics. The data at lowest excitation wavenumbers, where no signal was detected, were removed from the analysis. Contour lines are drawn from 0 to the maximum (minimum) value in steps of 12.5%.

The two-dimensional decay-associated spectra are constructed as described in [Consani, *et al.*, Science **339**, 1586 (2013)]. We first performed a two-dimensional singular-value decomposition. When the relevant kinetic components are described by a multi-exponential model, four time constants (global parameters) are necessary to reproduce the measured kinetics. The time constants retrieved from the analysis are $\tau_1^{2D} < 30$ fs, $\tau_2^{2D} = 290 \pm 60$ fs, $\tau_3^{2D} = 2.9 \pm 0.5$ ps, and an offset $\tau_4^{2D} \gg 10$ ps, in good agreement with the multi-exponential global description of the transient absorption data (see Table 1 in the main paper). The two-dimensional decay-associated spectra (2D-DAS) are the pre-exponential coefficients associated to each characteristic times τ_i^{2D}, for each couple of ($\widetilde{\nu}_\tau$, $\widetilde{\nu}_t$) values. The 2D-DAS are plotted in Figs. S9a-d. The ultrafast (τ_1^{2D}) component (Fig. S9a) shows the initial decay of the diagonal feature. The 290 fs DAS (Fig. S9b) contains a positive (decay)

contribution along the diagonal and a negative (rise) contribution below the diagonal, thus it corresponds to a process where the signal intensity shifts from higher to lower wavenumbers along the detection axis $\widetilde{\nu}_t$. The time constant τ_2^{2D} compares well with the red-shift of the SE bands observed in the transient absorption measurements (compare with Fig. 2c and Table 1 in the main paper). Accordingly, we ascribe the spectral evolution on this timescale to a red-shift of the SE contribution to the 2D signal. However, at all $\widetilde{\nu}_\tau$ the amplitude of the signal decay is larger than the amplitude of the rise. Hence a decay of the 2D signal intensity occurs simultaneously with the red-shift of the SE. The DAS associated with the later kinetics are round and structureless, however the 2D-DAS associated with the τ_4^{2D} component (Fig. S9d) peaks at a lower $\widetilde{\nu}_t$ than the τ_3^{2D} 2D-DAS (Fig. S9c).

S4. EXCITATION-DEPENDENT AMPLITUDE OF THE FAST BAND-SHIFT

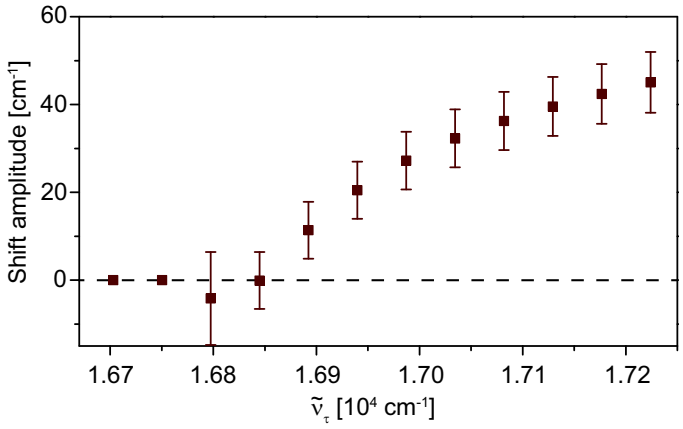

FIG. S10. Amplitude of the $\approx$ 200 fs red-shift along the detection axis observed in the 2D experiment on the B_{00} band as a function of the excitation wavenumber $\widetilde{\nu}_\tau$, obtained from the bi-exponential global fit of $M_1(\widetilde{\nu}_\tau, T)$. Error bars are $\pm\sigma$. Note that, in the fit, the amplitude of the $\approx$ 200 fs component was fixed to 0 for $\widetilde{\nu}_\tau < 1.679 \times 10^4$ cm^{-1}, where no shift on this time constant was observed within our signal-to-noise ratio. The B_{00} band contains contributions from both bleach and SE. Differently from the $\approx$ 4 ps dynamics, where both the bleach and SE contributions to the signal shift simultaneously towards lower wavenumbers, on a $\approx$ 200 fs timescale only the SE band red-shifts. Since $M_1(\widetilde{\nu}_\tau, T)$ measures center of mass frequency of a signal composed by overlapping (0-0) bleach and SE bands, the amplitude of the $\approx$ 200 fs shift is not a direct quantitative measure of the shift of the SE band. We also observe that the $\approx$ 200 fs shift is small with respect to the amount of excess energy originally input in the system via the excitation pulses. This is consistent with the absence of a bleach shift on this short timescale.

8 Excited State Dynamics and Conformations of a Cu(II)-Phthalocyanine-Perylenebisimide Dyad

Kevin Wilma*, Thomas Unger*, Christoph Hunger, Manuel Hollfelder, S. Tuncel Kostakoğlu, A. G. Gürek, Mukundan Thelakkat, Jürgen Köhler, Anna Köhler, Stefan Gekle und Richard Hildner

**Diese Autoren haben gleichermaßen beigetragen*

Veröffentlicht in

Physical Chemistry Chemical Physics 19 (2017), 22169-22176

(DOI: 10.1039/C7CP04026A)

PCCP

PAPER

Cite this: *Phys. Chem. Chem. Phys.*, 2017, **19**, 22169

Excited state dynamics and conformations of a Cu(II)-phthalocyanine-perylenebisimide dyad†

K. Wilma,‡[a] T. Unger,‡[b] S. Tuncel Kostakoğlu,[cd] M. Hollfelder,[e] C. Hunger,[c] A. Lang,[c] A. G. Gürek,[d] M. Thelakkat,[cf] J. Köhler,[af] A. Köhler,[bf] S. Gekle[e] and R. Hildner*[a]

Received 15th June 2017,
Accepted 4th August 2017

DOI: 10.1039/c7cp04026a

rsc.li/pccp

We investigate the excited state dynamics and the conformations of a new molecular donor-bridge-acceptor system, a Cu(II)-phthalocyanine (CuPc) covalently linked *via* a flexible aliphatic spacer to a perylenebisimide (PBI). We performed time-resolved polarization anisotropy and pump–probe measurements in combination with molecular dynamics simulations. Our data suggest the existence of three conformations of the dyad: two more extended, metastable conformations with centre-of-mass distances >1 nm between the PBI and CuPc units of the dyad, and a highly stable folded structure, in which the PBI and CuPc units are stacked on top of each other with a centre-of-mass distance of 0.4 nm. In the extended conformations the dyad shows emission predominantly from the PBI unit with a very weak contribution from the CuPc unit. In contrast, for the folded conformation the PBI emission of the dyad is strongly quenched due to fast energy transfer from the PBI to the CuPc unit (3 ps) and subsequent intersystem-crossing (300 fs) from the first excited singlet state of CuPc unit into its triplet state. Finally, the CuPc triplet state is deactivated non-radiatively with a time constant of 25 ns.

Introduction

The design of new organic molecular systems for efficient light-energy conversion has become one of the greatest challenges in physical chemistry in recent years. To this end, several multi-chromophoric architectures, such as dyads, triads and even more complex structures have been synthesised and characterised.[1–4] Such structures are usually designed as donor–acceptor systems to allow for efficient energy and/or charge transfer between the building blocks upon photoexcitation.[5] Although a huge variety of organic dye molecules exists,[6–10] particularly perylene bisimide (PBI) and phthalocyanine (Pc) (and their derivatives) have emerged as promising building blocks for these purposes.[6,9] PBIs are known for their outstanding photophysical properties, such as broad and tunable absorption in the visible range and photoluminescence quantum yields close to unity, as well as for their high photochemical stability.[10–15] Furthermore, they exhibit high electron affinity[16] and are therefore well suited as electron accepting material. Pcs also feature a high thermal and chemical stability, as well as a strong absorption in the red/near infrared spectral region. Moreover, Pcs are known for their ability to act as an electron donor.[17,18] Their absorption range and performance in solar cell architectures can be improved using metallo-Pcs with a central metal ion.[19] Particularly devices employing CuPc and ZnPc exhibit a high performance which was attributed to a decreasing number of intermediate states (zero for ZnPc, one for CuPc) leading to decreased rates for non-radiative relaxation. In fact, the very first two-layer organic solar cell reported by Tang consisted of CuPc and a perylene tetracarboxylic derivative.[6] Later, a hybrid planar-mixed molecular heterojunction solar cell consisting of CuPc as donor and fullerene as acceptor has been fabricated with a power conversion efficiency of 5%.[20]

Combining the favourable properties of PBI and metallo-Pc is therefore a promising approach for creating efficient donor–acceptor compounds for photovoltaic applications.[1,21–29] The absorptions of these molecules are complementary and cover a broad spectral region, which allows to harvest a large fraction of the visible solar spectrum. Moreover, specifically CuPc possesses favourable energy levels for charge transfer towards PBI. A crucial factor for device fabrication is the miscibility and co-crystallisation of Pcs and PBIs. Their substitution patterns allow them to be

[a] *Experimentalphysik IV, University of Bayreuth, Bayreuth 95440, Germany. E-mail: richard.hildner@uni-bayreuth.de; Fax: +49 921 554002; Tel: +49 921 554040*
[b] *Experimentalphysik II, University of Bayreuth, Bayreuth 95440, Germany*
[c] *Applied Functional Polymers, Macromolecular Chemistry I, University of Bayreuth, Bayreuth 95440, Germany*
[d] *Department of Chemistry, Gebze Technical University, Gebze 41400, Turkey*
[e] *Physics Department, University of Bayreuth, Bayreuth 95440, Germany*
[f] *Bayreuth Institute of Macromolecular Research (BIMF), University of Bayreuth, Bayreuth 95440, Germany*
† Electronic supplementary information (ESI) available. See DOI: 10.1039/c7cp04026a
‡ These authors contributed equally to this work.

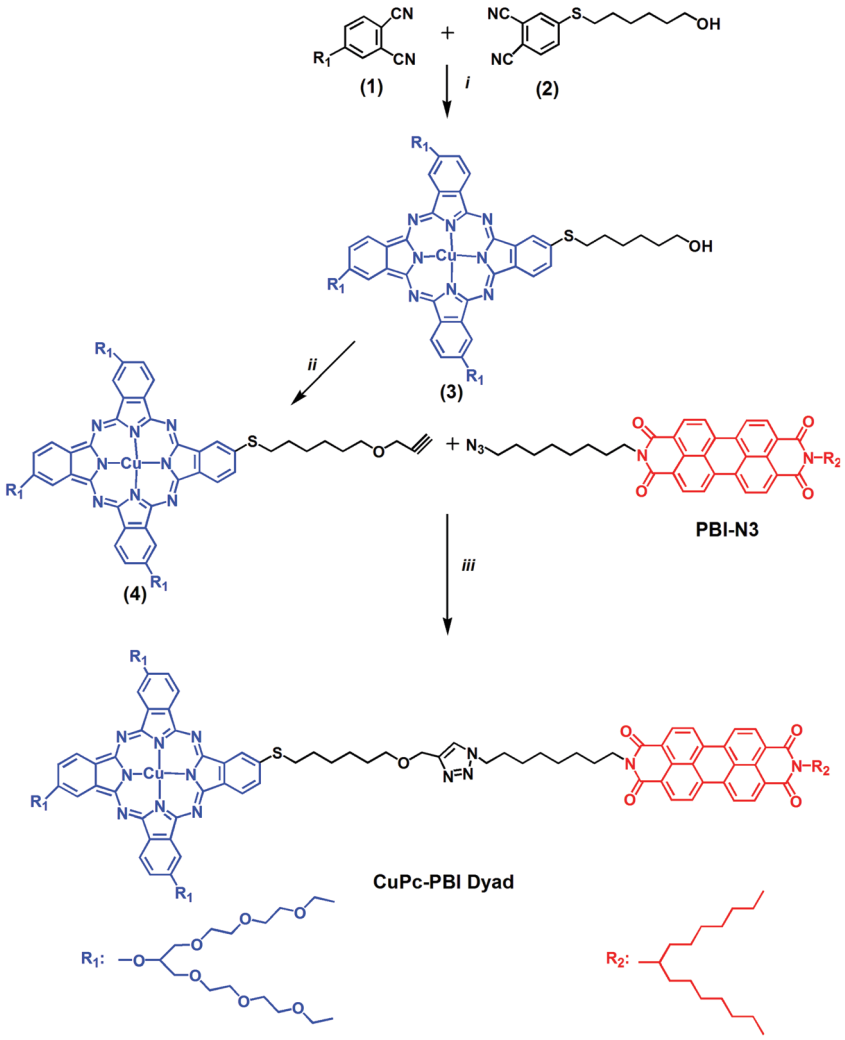

Scheme 1 Synthesis of the CuPc-PBI-dyad *via* click chemistry. (i) Anhydrous *N*,*N*-dimethylaminoethanol, anhydrous $CuCl_2$; (ii) anhydrous NaH, THF, propargyl bromide; (iii) CH_2Cl_2 CuBr, *N*,*N*,*N*′,*N*″,*N*″ pentamethyldiethylenetriamine.

crystalline or liquid crystalline in nature, and consequently the stacking of these molecules into homocolumns or heterocolumns can be controlled. In this respect, we synthesised differently substituted CuPcs and PBIs with alkyl, alkyloxy or ethylene glycol side chains and studied their miscibility and co-crystallisation.[30] These studies demonstrate that a definite degree of immiscibility in bulk is a prerequisite for a phase separated columnar arrangement of each moiety. Accordingly, incompatible substituents should be favoured, *i.e.* ethylene glycol for CuPc and alkyl substituents for PBI. Since these substitution patterns, however, do not allow to control the domain size of each moiety in the blend, we designed a dyad containing a Cu(II)-Pc (CuPc) and a PBI unit which are covalently linked *via* a non-conjugated, aliphatic bridge (Scheme 1). This bridge ideally ensures a small distance, and thus effective interactions between PBI and Pc to allow for photoinduced energy transfer and/or charge separation.[31] Yet, too short bridges often prevent self-assembly and phase-separation of these units during processing, which is required for efficient device operation.[32] Hence, we used a rather long and flexible aliphatic linker. Here, we fully characterise the photophysics of this dyad using picosecond time-resolved as well as femtosecond and nanosecond pump–probe spectroscopy in combination with molecular dynamics simulations. We find that the vast majority of the dyads exists in a highly stable folded conformation, with the CuPc unit stacked on top of the PBI unit. Although this conformation favours highly efficient energy transfer from the PBI to CuPc unit, a photo-induced charge separated state is not formed. The excitation energy is rather deactivated rapidly *via* intersystem-crossing to the triplet state of CuPc and ultimately back to the ground state.

Results and discussion

Synthesis

To covalently link CuPc and PBI, copper-catalyzed azide–alkyne cycloaddition reaction was used which has emerged as the most prominent example of "click" chemistry, one of the simplest and most efficient methods.[33] In Scheme 1 the synthetic route is illustrated (see ESI,† Experimental section). All compounds

were characterized by Fourier-transform infrared spectroscopy, time-of-flight mass spectroscopy as well as by elemental analysis. All synthesized CuPc compounds (**3**, **4** and CuPc-PBI-dyad, Scheme 1) are highly soluble in polar and nonpolar solvents such as chloroform, benzene, carbon tetrachloride, tetrahydrofuran, toluene, acetone, and ethanol.

Steady-state UV/vis and PL spectroscopy

Fig. 1a (solid line) shows the normalized steady-state absorption spectrum of the CuPc-PBI-dyad dissolved in toluene, which features three main bands around 350 nm, 540 nm and 700 nm. Comparing this absorption of the dyad with that of an isolated CuPc moiety (Fig. 1a dashed line, see also ESI,† Fig. S1), the bands around 350 nm and 700 nm can be attributed to the B- and Q-bands of CuPc, respectively.[17] The band around 540 nm in the dyad's absorption is characteristic of the PBI absorption (ESI,† Fig. S2). The photoluminescence (PL) spectrum of the dyad upon excitation of the PBI unit at 450 nm is displayed in Fig. 1b, which reflects the PL of PBI with its maximum at 540 nm and the characteristic vibronic progression (ESI,† Fig. S2). Nevertheless, a weak signal around 720 nm is present (Fig. 1b, inset), that can be ascribed to the Q-band emission of the CuPc unit of the dyad (ESI,† Fig. S1). Because at a wavelength of 450 nm nearly exclusively PBI is excited (see Fig. 1a) and because the PL of PBI is significantly quenched (see ESI,† Section 4), the appearance of CuPc emission indicates some energy transfer from PBI to CuPc within the dyads. In contrast, emission at 720 nm is not observed from the isolated PBI moiety, see ESI,† Fig. S2.

Picosecond time-resolved spectroscopy

To study the excited state dynamics of the dyads in toluene solution, we performed picosecond time-resolved experiments using pulsed excitation at 450 nm and a Streak-camera as detector. This setup allows us to record simultaneously PL decays with the emission polarisation parallel ($I_{\parallel}$) and perpendicular ($I_{\perp}$) with respect to the polarisation of the excitation light (see ESI,† Experimental section and Fig. S3). Both decays are spectrally integrated from 467 nm to 800 nm, *i.e.* over the PBI and the CuPc emission. From these data we construct the magic angle decay curve according to $(I_{\parallel} + 2I_{\perp})/3$, which eliminates contributions of rotational diffusion of the dyads to the decay curve. This magic angle trace is displayed in Fig. 1c, and features two clearly distinct decay components. A bi-exponential fit to the data yields a short time constant of τ_1 = 0.1 ns and a longer one with τ_2 = 3.2 ns. Note that τ_1 is determined by the instrument response function (time resolution) of our setup and thus reflects a much faster decay process (*vide infra*). The ratio of the corresponding amplitudes of the exponentials is $A_1/A_2 \sim 3$, *i.e.* the short component dominates the decay.

Because the PL signal of the CuPc unit of the dyad is extremely weak in comparison with the PBI emission (see Fig. 1b), it is reasonable to assume that the PL decay of the dyad is exclusively determined by the PBI unit. Given the lifetime of 3.9 ns of isolated PBI in toluene solution (ESI,† Fig. S2), the bi-exponential decay of the dyad's PBI emission therefore suggests the presence of two quenching mechanisms for the PBI unit: an efficient one gives rise to the short (0.1 ns) component and a weaker quenching process yields the longer (3.2 ns) component. The fast and efficient quenching process may be caused by (i) stacking of two or more PBIs from different dyads on top of each other or by (ii) charge and/or energy transfer from the photoexcited PBI unit to the CuPc unit within the same dyad. Although PBI molecules are highly prone to stacking,[10,14] we can rule out option (i). In this situation weakly emissive H-type PBI aggregates would form that feature a substantially red-shifted PL spectrum with a strongly distorted vibronic progression.[34] Yet, the PL of the PBI unit does not show this behavior (Fig. 1b). Thus, charge and/or energy transfer (option (ii)) takes place with a transfer efficiency exceeding 99%, as estimated from the measured time constants (ESI,† Section 4). For both transfer processes to be that efficient, a small centre-of-mass distance (sub-nm) between the PBI and the CuPc unit is required. This can be realised owing to the flexible bridge between these units, *e.g.* in a folded conformation with the CuPc unit stacked on top of the PBI unit.

The long decay time (τ_2 = 3.2 ns) of the dyad is slightly smaller than the excited state lifetime of 3.9 ns of isolated PBI moieties (ESI,† Fig. S2). These numbers indicate a weaker quenching of the dyad's PBI emission with an efficiency of about 0.18 (ESI,† Section 4), and thus imply the presence of dyads with a more open conformation. Distances of some nm between PBI and CuPc can easily be achieved (up to ~4 nm when fully extended, see Scheme 1), which would still allow for energy transfer with a reasonable efficiency.

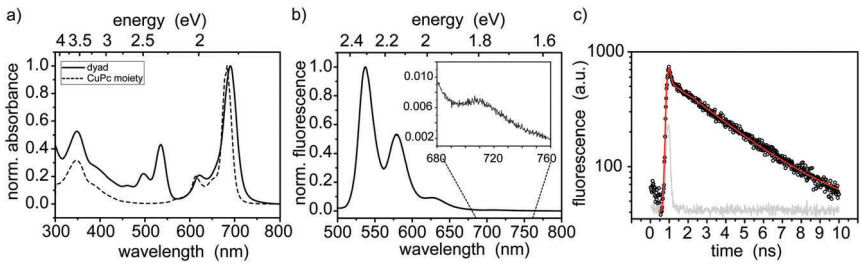

Fig. 1 (a) Absorption spectrum of the CuPc-PBI dyads (solid) and of the symmetric CuPc moiety (dashed). (b) Photoluminescence spectrum of the CuPc-PBI dyad using an excitation wavelength of 450 nm. The inset shows an enlarged view of the region with non-vanishing PL of the Q-band of the CuPc unit. (c) Magic angle PL decay curve of the dyad using an excitation wavelength of 450 nm (black dots) together with a biexponential fit (red line; time constants: 0.1 ns and 3.2 ns, amplitudes: 2800 a.u. and 820 a.u.). The grey line represents the instrument response function. For all measurements toluene was used as solvent.

Hence, our picosecond data suggest that the dyads exist in (at least) two distinct conformations in solution, *i.e.* a folded and a more open one. In the following we study possible conformations of the dyad, and we further investigate the nature and time scales of the rapid quenching process by femto- and nanosecond pump–probe spectroscopy.

Molecular dynamics simulations

Molecular dynamics (MD) simulations were performed with one dyad solvated in 1800 toluene molecules at normal conditions (temperature: T = 300 K; pressure: 1000 mbar). To obtain free energy profiles, we employed the umbrella sampling implemented in Gromacs. The force fields were obtained as detailed in the Experimental section in the ESI.† In Fig. 2a the free energy surface along the center-of-mass (COM) distance between PBI and CuPc is shown. It features three distinct minima at distances of *ca.* 0.4 nm, 1 nm, and 2.8 nm. Corresponding snapshots of the dyad's conformation at those COM distances are displayed in Fig. 2b. The lowest free energy of $-7.14\ k_BT$, and thus the most stable conformation, is found for the closest COM distance of 0.4 nm. Here, the PBI and CuPc units are stacked on top of each other by back-folding of the aliphatic spacer between these units (FOLDED conformation). This conformation appears to be further stabilised by the substituents of CuPc, that are wrapped around the PBI unit. A local minimum with a free energy of $0.78\ k_BT$ is found at a larger COM distance, where the PBI and CuPc units are separated by ~1 nm. This represents a transition (TRANS) conformation between a completely folded and completely unfolded configuration. The spacer is still back-folded to a large extent, but the stabilising wrapping of the CuPc-substituents is not present. Finally, at a COM distance of 2.8 nm a very shallow local minimum is observed, corresponding to a conformation with an extended spacer (OPEN conformation). Beyond 2.8 nm the free energy rises again due to the entropically unfavourable stretching of the aliphatic chain.

The conformational changes TRANS → OPEN and TRANS → FOLDED are separated by an energy barrier of 1.3 k_BT and 0.8 k_BT, respectively, indicating that the TRANS conformation is metastable and tends to change into the OPEN or FOLDED conformation due to the thermal energy available in the system (the same holds true for the transition OPEN → TRANS). Once the dyad assumes the FOLDED conformation, it is trapped due to the high barrier of ~8 k_BT for the FOLDED → TRANS transition. This free energy profile therefore illustrates that the vast majority of the dyads can be expected in the FOLDED state.

These findings allow us to connect the conformations of the dyads obtained from MD simulations with the picosecond lifetime measurements presented above (Fig. 1c): for the FOLDED conformation the COM distance is very small (0.4 nm). Hence, both charge and energy transfer from the photoexcited PBI to the CuPc unit can be expected to be very fast and efficient (efficiency > 0.99), which results in the short resolution-limited time constant of τ_1 = 100 ps. In the OPEN and TRANS conformations the COM distances are too large (1 to 2.8 nm) to allow for efficient charge transfer. However, energy transfer is still possible with reasonable efficiency (here ~0.18) at such inter-molecular distances, which gives rise to weakly quenched PBI emission with the longer time constant of τ_2 = 3.2 ns. From these measured time constants and the corresponding amplitudes of the dyad's PBI emission (Fig. 1c), we estimate that more than 99.9% of the dyads exist in the FOLDED conformation (ESI,† Section 4), as also indicated by the molecular dynamics simulations.

Although the probability to find the dyad in the OPEN & TRANS conformations is accordingly very small, the contribution

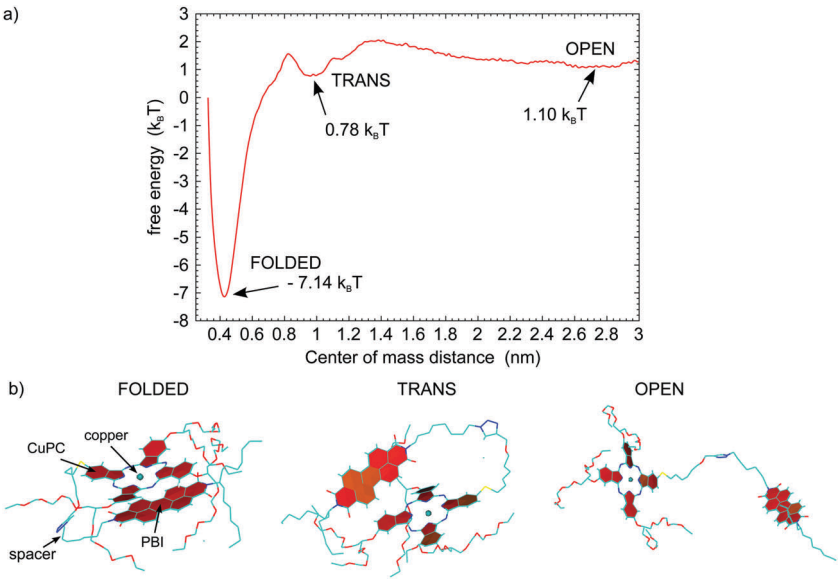

Fig. 2 (a) Free energy profile of the dyad as a function of the center-of-mass distance between the PBI and the CuPc unit of the dyad, determined by molecular dynamics simulations. (b) Snapshots from molecular dynamics simulations of the three different conformations FOLDED, TRANS and OPEN of the dyad taken along the free energy profile. Nitrogen atoms: dark blue, carbon atoms: light blue, oxygen atoms: red, sulfur atom: yellow; aromatic rings are filled with red color, and the copper atom is displayed as sphere.

of weakly quenched PBI emission with the long time constant (3.2 ns) is clearly visible in the lifetime data. This observation can be related to the high PL quantum yield of PBI (0.88 in isolated PBI; 0.70 in OPEN/TRANS dyads), whereas in the FOLDED dyad conformation the measured PL quantum yield of the PBI unit is below 0.005, which is in good agreement with the calculated number of smaller than 0.001 (ESI,† Section 4).

Femtosecond pump–probe spectroscopy

Owing to the limited temporal resolution of our picosecond measurements, we performed femtosecond pump–probe spectroscopy on the dyads dissolved in toluene to further investigate the nature and time scales of the rapid quenching mechanism for the PBI emission. Note that the response in femtosecond pump–probe spectra is entirely determined by FOLDED dyads, because of the very high probability of $>$ 99.9% to find this conformation in solution. The home-built pump–probe setup comprises an OPA pumped by a regenerative amplifier; the temporal resolution is 210 fs (see Experimental section in the ESI† for details). Fig. 3a shows two examples for pump–probe $\Delta T/T$ spectra of the dyad at 1 ps (blue curve) and 15 ps (green curve) after pumping of the PBI unit at 510 nm. Here, T represents the transmission of the sample without preceding pump pulse, and ΔT denotes the difference in transmission with and without preceding pump pulse. The spectra show a positive $\Delta T/T$ signal between 640 and 710 nm, which is attributed to the ground state bleach (GSB) of the CuPc unit by comparison with the UV/vis absorption spectrum of the dyad (grey shaded area in Fig. 3a). The negative $\Delta T/T$ signal between 520 and 630 nm is assigned to photoinduced triplet absorption of the CuPc unit based on nanosecond pump–probe experiments (see below) and literature data.[35–38] The magnitudes of both $\Delta T/T$ signatures rise within the first few ps after the pump pulse. As an example we show the transient signal probed at the GSB of CuPc at 680 nm (Fig. 3b), which features an initial rise with a time constant of 3 ps as indicated by the exponential fit to the transient.

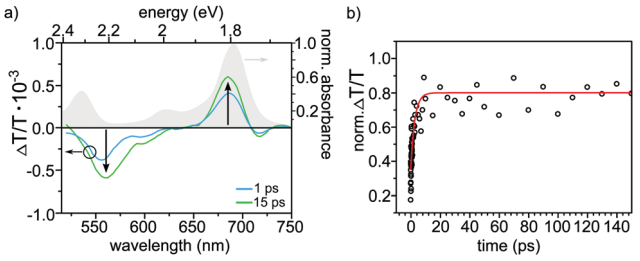

Fig. 3 Femtosecond pump–probe measurements of the CuPc-PBI dyad in toluene solution. (a) Transient absorption spectra of the dyad at 1 ps (blue solid line) and 15 ps (green solid line) after pumping the PBI unit at 510 nm. The grey filled area is the steady-state absorption spectrum of the dyad. (b) Transient of the dyad (black dots) at a probe wavelength of 680 nm (Q-band of the CuPc unit). The red solid curve displays an exponential fit with a time constant of 3 ps. The vertical axes $\Delta T/T$ in both panels display the transmission difference ΔT between the transmission of the sample with and without preceding pump pulse divided by the transmission T of the sample without preceding pump pulse.

The rapid GSB of the CuPc unit demonstrates a fast population of its lowest excited singlet state (Q-band) after photoexcitation of PBI at 510 nm, which indicates energy transfer from the PBI to the CuPc unit in the FOLDED dyads, in agreement with other dyad systems containing PBI derivatives.[21] This interpretation is further corroborated by the absence of the stimulated emission (SE) band of PBI (positive $\Delta T/T$ signal), which is observed for the isolated PBI moiety in the range between 540 and 600 nm, as well as by the absence of the GSB of PBI (positive $\Delta T/T$ signal) around 530 nm (see ESI,† Fig. S5, for the corresponding transient absorption spectrum of the isolated PBI moiety). We note, however, that the complete absence of the SE and GSB bands of PBI is partially due to their spectral overlap with the triplet absorption band of CuPc (see the nanosecond pump–probe spectra below). The magnitude of the photoinduced triplet absorption of CuPc around 580 nm rises with about the same time constant as the GSB signal of the CuPc unit around 680 nm. This observation shows that the energy transfer from PBI to CuPc is immediately followed (on time scales of the temporal resolution of our setup) by fast intersystem crossing (ISC) from the first excited singlet state of CuPc to its lowest energy triplet state. For isolated CuPc moieties it is indeed known that after photoexcitation of the CuPc singlet Q-band rapid ISC into its triplet state takes place within about 300 fs.[17] Although this ultrafast ISC may be related to a significant spin–orbit coupling induced by the heavy copper atom, an alternative mechanism has been proposed to promote ISC, which involves a "spin-exchanging" short-lived intermediate charge-transfer state with the copper atom.[39] This efficient quenching of the CuPc singlet state by ISC also explains the very small PL signal from its Q-band observed in the steady-state spectra of the dyad (Fig. 1b, inset).

Based on these femtosecond pump–probe data charge transfer within FOLDED dyads can be ruled out, because neither a negative band due to the anion absorption of the PBI nor the cation of the CuPc is observed (see ref. 40 and 41). Moreover, in the case of electron transfer a GSB signal would arise as a positive band at the spectral position of the absorption of PBI between 450 and 560 nm, which is not found. The absence of charge transfer in our dyad, in contrast to similar other dyad-systems, is probably due to the rapid competing processes, *i.e.*, energy transfer from PBI to CuPc and ISC in CuPc.

Nanosecond pump–probe spectroscopy

The maximum temporal window of the femtosecond pump–probe setup is limited to about 1.5 ns. Within this window the decay of *e.g.* the GSB of the CuPc unit (recovery of its ground state population) around 680 nm could not be observed. To resolve such slower processes we measured transient absorption spectra on nanosecond time scales using a flash-photolysis setup with a time resolution of 5–6 ns. The resulting $\Delta T/T$ spectra of the dyad after pumping the PBI unit at 540 nm are shown in Fig. 4a. Generally, these nanosecond $\Delta T/T$ spectra are very similar to those measured with femtosecond pump–probe spectroscopy; yet, here both the negative photoinduced triplet absorption (around 500 nm) as well as the GSB (around 680 nm) of the CuPc unit appear immediately within the temporal

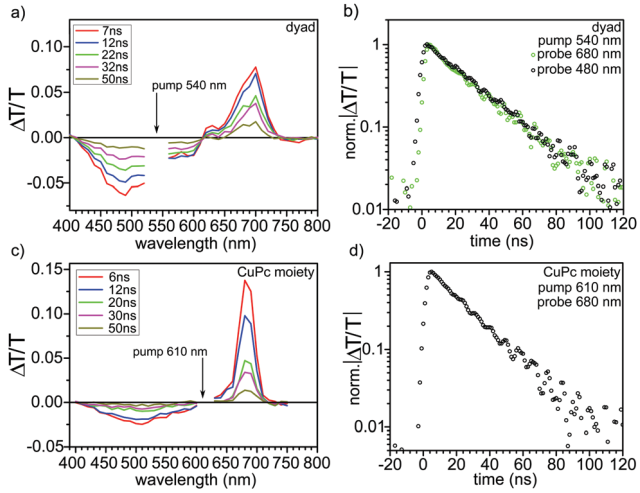

Fig. 4 (a) Nanosecond pump–probe spectra of the dyad dissolved in toluene upon pumping at 540 nm. (b) Transients of the dyad at probe wavelengths of 480 nm (black circles) and 680 nm (green circles) after pumping at 540 nm. (c) Nanosecond pump–probe spectra of the isolated CuPc moiety upon pumping at 610 nm. (d) Transients (magnitudes) of the dyad at probe wavelengths of 680 nm (black circles) after pumping at 650 nm. For all transient spectra in (a) and (c) the laser line was clipped.

resolution of the flash-photolysis setup. Fig. 4b shows the magnitudes of two transients at probe wavelengths of 480 nm and 680 nm, which both decay with the same time constant of ~25 ns. To verify that both the negative and positive $\Delta T/T$ signals can indeed be related to processes exclusively in the CuPc unit of the dyad, we also performed measurements on an isolated CuPc moiety dissolved in toluene using a pump wavelength of 610 nm (Fig. 4c). These spectra exhibit the same broad and negative photoinduced triplet absorption band around 500 nm together with the positive GSB signal around 680 nm. The transients retrieved at probe wavelengths of 480 nm and 680 nm (Fig. 4d) reveal a ~25 ns decay.

The magnitudes of the $\Delta T/T$ transients of the GSB and of the photoinduced triplet absorption from both the dyad and isolated CuPc decay with very similar time constants around 25 ns independent of pump and probe wavelengths. This observation shows that deactivation of the CuPc triplet state repopulates its singlet ground state within 25 ns. This triplet lifetime is very short and be related to enhanced ISC due to the presence of the Cu atom as discussed above and in agreement with literature data.[37,38] Finally, we comment on the difference between the femtosecond and nanosecond pump–probe spectra, because in the former the photoinduced triplet absorption band (around 500 nm) is more red shifted and significantly narrower. In femtosecond pump–probe spectra the negative $\Delta T/T$ triplet signal of CuPc is partially cancelled and thus narrowed by two positive $\Delta T/T$ signals from the PBI unit, its GSB between 500 and 550 nm and its stimulated emission between 540 and 600 nm (see the transient absorption spectrum of the isolated PBI moiety in Fig. S5, ESI†). Because these positive $\Delta T/T$ signals contribute only on sub-nanosecond time scales, they do not play a role in the nanosecond pump–probe spectra anymore and thus broaden the nanosecond triplet signal.

Concluding remarks

Our experiments allow us to deduce an energy level scheme for both the OPEN (TRANS) and FOLDED conformations (Fig. 5). For the OPEN conformation (left panel), we excite the PBI unit of the dyad with a wavelength of 450 nm into its lowest excited singlet state, while the CuPc unit is in its ground state, which is denoted by ^{1}PBI*-CuPc. The dominating subsequent relaxation channel is radiative and non-radiative decay of PBI with a time constant of 3.2 ns back to its electronic ground state. There is, however, also energy transfer taking place from PBI to the singlet excited state of CuPc with a transfer time of 17.8 ns (or an efficiency of ~0.18), *i.e.* PBI-^{1}CuPc* is formed, which then rapidly decays *via* two channels to its ground state: (i) direct (non-)radiative decay to the CuPc ground state with a very small probability, and (ii) ISC into the CuPc triplet state (PBI-^{3}CuPc*) within less than 300 fs and then to the ground state within 25 ns. For the FOLDED conformation the PBI unit of the dyad is again excited into its first excited singlet state (^{1}PBI*-CuPc). Within 3 ps the energy is transferred to the CuPc excited singlet state (PBI-^{1}CuPc*) with an efficiency of >0.99, from where again two deactivation channels exist: (i) the dominating process is ISC within 300 fs to the triplet state of CuPc (PBI-^{3}CuPc*), with

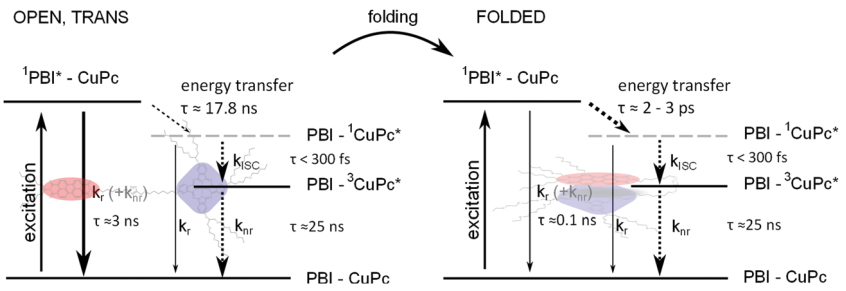

Fig. 5 Energy level schemes of the dyad in the OPEN/TRANS (left) and the FOLDED conformation (right). The CuPc (PBI) units are marked with blue (red). k_r, k_{nr}, and k_{ISC} are radiative (solid arrows), non-radiative, and intersystem crossing rates (dotted arrows) for the indicated transitions between energy levels; the symbols τ denote the corresponding lifetimes as determined in this work. The thickness of the arrows displays the magnitude of the transition rates in each of the conformations.

subsequent non-radiative deactivation into the electronic ground state with a time constant of 25 ns; (ii) radiative decay from PBI-^{1}CuPc* to the ground state PBI-CuPc is also possible with a very small probability, as supported by the very weak fluorescence of the CuPc unit observed at 720 nm in the steady-state data in Fig. 1b. In FOLDED dyads the close distance of 0.4 nm between the PBI and CuPc units should favour charge separation. However, the deactivation of excitation energy due to energy transfer and ISC seems to be too rapid and efficient to allow for the formation of a stable charge-separated state.

It is interesting to note that a superposition of UV/vis spectra of PBI and CuPc is a very good approximation to the dyad's absorption. In other words, the energy levels (singlets and also triplets) of the building blocks of the dyad are not substantially shifted when linked together covalently *via* a spacer group. This observation appears to be even more surprising given that the dyad exists nearly exclusively in the FOLDED conformation with a very short center-of-mass distance of only 0.4 nm, for which the Coulomb-interactions between the transition dipole moments of PBI and CuPc units are expected to be rather strong. For similarly densely packed molecules we recently determined Coulomb-interactions to be >44 meV (>350 cm^{-1}).[42] However, the site energy mismatch between the PBI and the CuPc unit can be estimated to be about 525 meV (4200 cm^{-1}) from the maxima of the corresponding absorptions at 540 nm (2.31 eV or 18 500 cm^{-1}) for PBI and 700 nm (1.79 eV or 14300 cm^{-1}) for CuPc. From those numbers we obtain a ratio between Coulomb-coupling and site energy mismatch of <0.1, which clearly places the FOLDED dyad system into the weak coupling regime in Kasha's exciton theory.[43] Consequently, exciton states do not form, electronic excitations are localised on the building blocks, and the absorption spectra of the dyad can be constructed by a simple superposition of the PBI and CuPc units.

Acknowledgements

We gratefully acknowledge funding from the German Research Foundation DFG within projects HI1508/3 (KW, RH) and GRK1640 (KW, TU, MT, JK, AK, SG, RH), from Elitenetzwerk Bayern (ENB, elite study programme *Macromolecular Science*, RH), the Bavarian State Ministry of Science, Research, and the Arts for the Collaborative Research Network *Solar Technologies go Hybrid* (MT, JK, AK), and from TUBITAK-BIDEB (2219-International Postdoctoral Research Fellowship Programme, STK). We also thank Inga Elvers for her assistance with the Streak-camera measurements.

References

1 Y. Chen, Y. Lin, M. E. Ei-khouly, X. Zhuang and Y. Araki, *J. Phys. Chem. Lett.*, 2007, **111**, 16096–16099.
2 S. E. Webber, *Chem. Rev.*, 1990, **90**, 1469–1482.
3 A. J. Jimenez, F. Spänig, M. Salome Rodriguez-Morgade, K. Ohkubo, S. Fukuzumi, D. M. Guldi and T. Torres, *Org. Lett.*, 2007, **9**, 2481–2484.
4 A. Petrella, J. Cremer, L. De Cola, P. Bäuerle and R. M. Williams, *J. Phys. Chem. A*, 2005, **109**, 11687–11695.
5 M. R. Wasielewski, *Chem. Rev.*, 1992, **92**, 435–461.
6 C. W. Tang, *Appl. Phys. Lett.*, 1986, **48**, 183–185.
7 N. Cai, S.-J. Moon, L. Cevey-Ha, T. Moehl, R. Hymphry-Baker, P. Wang, S. M. Zakeeruddin and M. Grätzel, *Nano Lett.*, 2011, **11**, 1452–1456.
8 K. Hara, Y. Tachibana, Y. Ohga, A. Shinpo, S. Suga, K. Sayama, H. Sugihara and H. Arakawa, *Sol. Energy Mater. Sol. Cells*, 2003, **77**, 89–103.
9 P. Peumans and S. R. Forrest, *Appl. Phys. Lett.*, 2001, **79**, 126.
10 F. Würthner, T. E. Kaiser and C. R. Saha-Möller, *Angew. Chem., Int. Ed.*, 2011, **50**, 3376–3410.
11 C. C. Hofmann, S. M. Lindner, M. Ruppert, A. Hirsch, S. A. Haque, M. Thelakkat and J. Köhler, *J. Phys. Chem. B*, 2010, **114**, 9148–9156.
12 E. Lang, R. Hildner, H. Engelke, P. Osswald, F. Würthner and J. Köhler, *ChemPhysChem*, 2007, **8**, 1487–1496.
13 E. Lang, F. Wüthner and J. Köler, *ChemPhysChem*, 2005, **6**, 935–941.
14 F. Würthner, *Chem. Commun.*, 2004, 1564–1579.
15 H. Yoo, J. Yang, A. Yousef, M. R. Wasielewski and D. Kim, *J. Am. Chem. Soc.*, 2010, **132**, 3939–3944.
16 K. Wilma, A. Issac, Z. Chen, F. Würthner, R. Hildner and J. Köhler, *J. Phys. Chem. Lett.*, 2016, **7**, 1478–1483.
17 K. Kadish, K. M. Smith and R. Guilard, *Porphyr. Handb.*, Academic Press, 1999.
18 F. D'Souza and O. Ito, *Chem. Commun.*, 2009, 4913–4928.
19 I. Bruder, J. Schöneboom, R. Dinnebier, A. Ojala, S. Schäfer, R. Sens, P. Erk and J. Weis, *Org. Electron.*, 2010, **11**, 377–387.
20 B. J. Xue, B. P. Rand, S. Uchida and S. R. Forrest, *Adv. Mater.*, 2005, **17**, 71–73.
21 F. Javier Céspedes-Guirao, K. Ohkubo, S. Fukuzumi, Á. Sastre-Santos and F. Fernández-Lázaro, *J. Org. Chem.*, 2009, **74**, 5871–5880.
22 M. A. Miller, R. K. Lammi, S. Prathapan, D. Holten and J. S. Lindsey, *J. Org. Chem.*, 2000, **65**, 6634–6649.
23 V. M. Blas-Ferrando, J. Ortiz, L. Bouissane, K. Ohkubo, S. Fukuzumi, F. Fernández-Lázaro and Á. Sastre-Santos, *Chem. Commun.*, 2012, **48**, 6241.
24 V. M. Blas-Ferrando, J. Ortiz, K. Ohkubo, S. Fukuzumi, F. Fernández-Lázaro and Á. Sastre-Santos, *Chem. Sci.*, 2014, **5**, 4785–4793.
25 S. Fukuzumi, K. Ohkubo, J. Ortiz, A. M. Gutiérrez, F. Fernández-Lázaro and A. Sastre-Santos, *J. Phys. Chem. A*, 2008, **112**, 10744–10752.
26 D. M. Guldi, T. Da Ros, P. Braiuca and M. Prato, *Photochem. Photobiol. Sci.*, 2003, **2**, 1067–1073.
27 H. Zhou, X. Li, T. Fan, F. E. Osterloh, J. Ding, E. M. Sabio, D. Zhang and Q. Guo, *Adv. Mater.*, 2010, **22**, 951–956.
28 D. I. Schuster, P. Cheng, P. D. Jarowski, D. M. Guldi, C. Luo, L. Echegoyen, S. Pyo, A. R. Holzwarth, S. E. Braslavsky, R. M. Williams and G. Klihm, *J. Am. Chem. Soc.*, 2004, **126**, 7257–7270.
29 A. Mateo-Alonso, C. Sooambar and M. Prato, *C. R. Chim.*, 2006, **9**, 944–951.

30 A. Wicklein, *Self-Organizing n-type Perylene Derivatives for Organic Photovoltaics – Synthesis, Characterization and Application*, Dissertation University of Bayreuth, 2010, retrieved from urn:nbn:de:bvb:703-opus-7208.
31 D. Gosztola, B. Wang and M. R. Wasielewski, *J. Photochem. Photobiol., A*, 1996, **102**, 71–80.
32 S.-S. Sun, *US Pat.*, 20040099307 A1, 2004.
33 J. E. Hein and V. V. Fokin, *Chem. Soc. Rev.*, 2010, **39**, 1302–1315.
34 J. M. Lim, P. Kim, M.-C. Yoon, J. Sung, V. Dehm, Z. Chen, F. Würthner and D. Kim, *Chem. Sci.*, 2013, **4**, 388.
35 J. McVie, R. S. Sinclair and T. G. Truscott, *J. Chem. Soc., Faraday Trans. 2*, 1978, **74**, 1870.
36 G. J. Dutton, W. Jin, J. E. Reutt-Robey and S. W. Robey, *Phys. Rev. B: Condens. Matter Mater. Phys.*, 2010, **82**, 073407.
37 A. V. Nikolaitchik, O. Korth and M. A. J. Rodgers, *J. Phys. Chem. A*, 1999, **103**, 7587–7596.
38 B. W. Caplins, T. K. Mullenbach, R. J. Holmes and D. A. Blank, *Phys. Chem. Chem. Phys.*, 2016, **18**, 11454–11459.
39 M. H. Ha-Thi, N. Shafizadeh, L. Poisson and B. Soep, *J. Phys. Chem. A*, 2013, **117**, 8111–8118.
40 D. Schmidt, M. Son, J. M. Lim, M. J. Lin, I. Krummenacher, H. Braunschweig, D. Kim and F. Würthner, *Angew. Chem., Int. Ed.*, 2015, **54**, 13980–13984.
41 F. Spreitler, M. Sommer, M. Thelakkat and J. Köhler, *Phys. Chem. Chem. Phys.*, 2012, **14**, 7971–7980.
42 A. T. Haedler, K. Kreger, A. Issac, B. Wittmann, M. Kivala, N. Hammer, J. Köhler, H.-W. Schmidt and R. Hildner, *Nature*, 2015, **523**, 196–199.
43 M. Kasha, H. R. Rawls and M. Ashraf El-Bayoumi, *Pure Appl. Chem.*, 1965, **11**, 371–392.

Supporting Information for

Excited State Dynamics and Conformations of a Cu(II)-Phthalocyanine-Perylenebisimide Dyad

K. Wilma[1,†], T. Unger[2,†], S. Tuncel Kostakoğlu[3,4], M. Hollfelder[5], C. Hunger[3], A. Lang[3], A. G. Gürek[4], M. Thelakkat[3,6], J. Köhler[1,6], A. Köhler[2,6], S. Gekle[5], and R. Hildner[1,*]

[1] *Experimentalphysik IV, University of Bayreuth, 95440 Bayreuth, Germany*
[2] *Experimentalphysik II, University of Bayreuth, 95440 Bayreuth, Germany*
[3] *Applied Functional Polymers, Macromolecular Chemistry I, University of Bayreuth, 95440 Bayreuth, Germany*
[4] *Department of Chemistry, Gebze Technical University, 41400 Gebze, Turkey*
[5] *Physics Department, University of Bayreuth, 95440 Bayreuth, Germany*
[6] *Bayreuth Institute of Macromolecular Research (BIMF), University of Bayreuth, 95440 Bayreuth, Germany*

† these authors contributed equally to this work

* Corresponding author:
E-Mail: richard.hildner@uni-bayreuth.de
Phone: +49 921 554040
Fax: +49 921 554002

Contents

1. Absorption and PL spectra of Copper-Phthalocyanine (CuPc) in solution

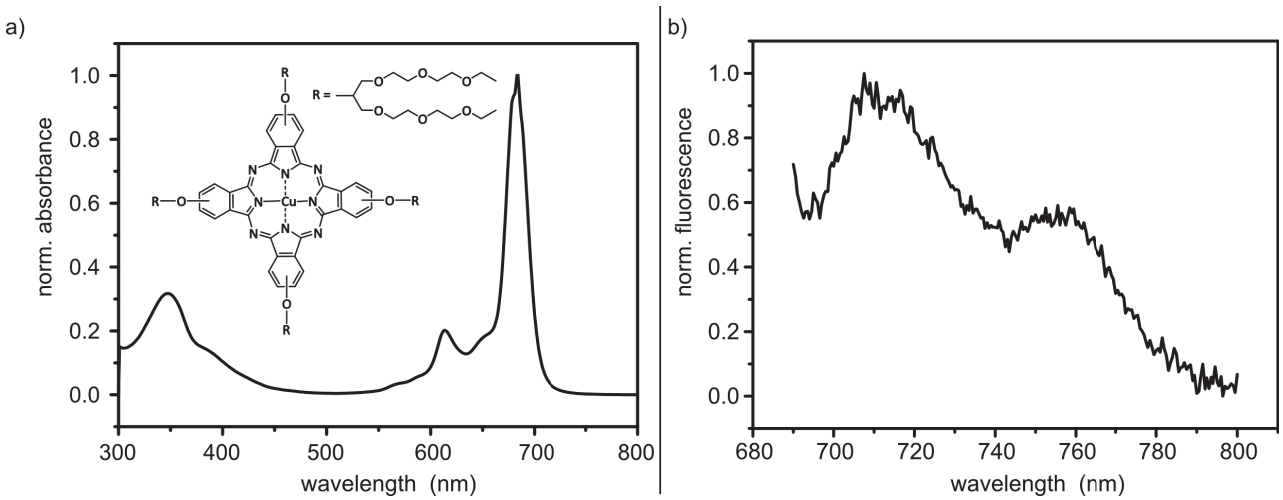

Fig. S1. Spectroscopy of the symmetric CuPc moiety dissolved in toluene. **a)** Absorption spectrum and the chemical structure. **b)** Photoluminescence of the Q-band of the CuPc moiety using an excitation wavelength of 683 nm.

2. Photophysics of Perylene Bisimide (PBI) in solution

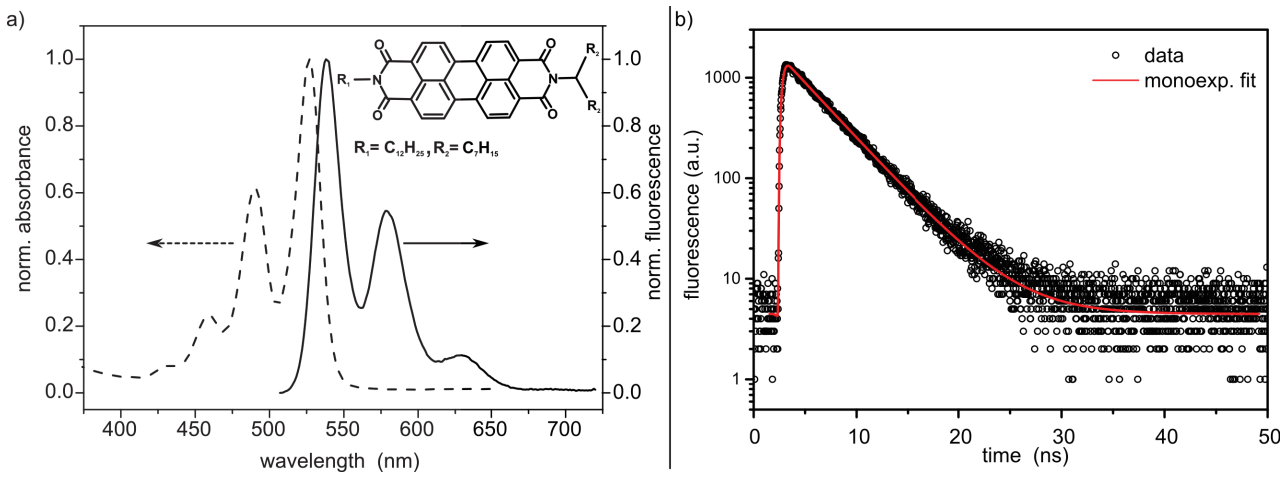

Fig. S2. a) Normalised absorption (dashed line) and PL spectrum (solid, excitation at 491 nm) of the PBI moiety. The chemical structure is shown in the inset. **b)** PL lifetime decay (black circles, excitation at 485 nm) of the PBI moiety with an exponential fit (red solid line) yielding a lifetime of 3.9 ns. Using the measured PL quantum yield of 0.88, we obtain a radiative lifetime of 4.43 ns. For all measurements PBI was dissolved in toluene.

3. Polarisation resolved picosecond lifetime measurements

Magic angle picosecond PL measurements allow to eliminate contributions due to rotational diffusion of the CuPc-PBI-dyads in solution; thus only the excited state decay is resolved. The magic angle intensity I_{ma} shown in Fig. 1c in the main text was calculated according to: [1]

$$I_{ma} = \frac{I_{\perp} + 2 \cdot I_{\parallel}}{3} . \qquad (1)$$

The corresponding decay curves measured with parallel $I_{\parallel}$ and perpendicular $I_{\perp}$ polarisation with respect to the excitation polarisation using the Streak setup are shown in Fig. S3. The $I_{\parallel}$ curve can be fitted well with a bi-exponential function with lifetimes of 0.1 ns and 3.2 ns. For the $I_{\perp}$ curve three exponentials are required: two decaying components with time constants of 0.1 ns and 3.6 ns, respectively, as well as a rising component with a time constant of 0.1 ns (see table S1). This rising component is caused by rotational diffusion of the dyads.

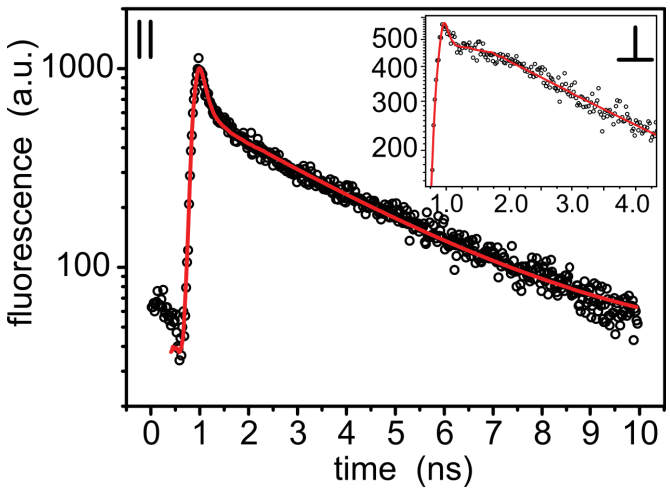

Fig. S3. Fluorescence decay curves (black circles) with polarisations parallel || and perpendicular ⊥ (inset) to the polarisation of the excitation light. The red lines are multi-exponential fits to the data, see table S1.

		decay		rise
		short	long	
∥	τ (ns)	0.1 ± 0.05	3.2 ± 0.05	-
	A (a.u.)	341 ± 20	127 ± 2	-
⊥	τ (ns)	0.1 ± 0.05	3.6 ± 0.05	0.1 ± 0.05
	A (a.u.)	1015 ± 44	171 ± 2	-518 ± 33

Table S1. Table with the fitted time constants τ and amplitudes *A* from the fits to the decay curves in Figure S3. Temporal errors represent the resolution of the setup.

4. Estimation of the fraction of FOLDED dyads

Based on the measured time constants for isolated PBI as well as for the dyads in the OPEN and FOLDED conformation, we can estimate the fraction of FOLDED dyads. To simplify the discussion we neglect the dyad's CuPc emission and consider only its PBI emission, which is justified by the data presented in Fig. 1 in the main text.

a) Isolated PBI:

For isolated PBI we measured a total decay rate of $k_{PBI} = k_{r,PBI} + k_{nr,PBI} = 1/(3.9\ ns)$, with $k_{r,PBI}$ and $k_{nr,PBI}$ being the radiative and non-radiative decay rates for PBI (Fig. S2). Together with the PL quantum yield $\Phi_{PBI} = 0.88$, measured with an integrating sphere, we obtain a radiative rate of $k_{r,PBI} = 1/(4.43\ ns)$.

b) OPEN dyad:

The measured decay rate of the PBI emission of the dyads in OPEN (or TRANS) conformation was $k_{OPEN} = 1/(3.2\ ns)$, see Fig. 1. Since in OPEN dyads energy transfer from the PBI to the CuPc unit with a rate constant $k_{T,O}$ also contributes, it follows $k_{OPEN} = k_{r,PBI} + k_{nr,PBI} + k_{T,O}$. Hence, $k_{T,O} = 1/(17.8\ ns)$, which translates into a transfer efficiency of $E_{T,O} = k_{T,O} / k_{OPEN} = 0.18$. The PL quantum yield of PBI in an OPEN dyad then is $\Phi_{OPEN} = k_{r,PBI} / k_{OPEN} = \Phi_{PBI} – E_{T,O} = 0.7$.

c) FOLDED dyad:

The picosecond data revealed a decay rate faster than $1/(0.1\ ns)$ for the dyads in FOLDED conformation. As this rate is limited by the resolution of the Streak-setup, we start here with the transfer rate of $k_{T,F} = 1/(3\ ps)$ for the transfer from the PBI to the CuPc unit of the FOLDED dyads determined from the femtosecond pump-probe data (see Fig. 3b). Hence, the decay rate for PBI in a FOLDED dyad is $k_{FOLD} = k_{r,PBI} + k_{nr,PBI} + k_{T,F} = 1/(2.99\ ps)$. These numbers yield a transfer efficiency from PBI to

CuPc of $E_{T,F}$ = 0.997 and a calculated PL quantum yield of PBI of Φ_F = 0.0007 in a FOLDED dyad. The latter number is in good agreement with the measured PL quantum yield of ≤ 0.005.

From our picosecond data we obtained an amplitude for the short (FOLDED) component that is three times larger than that of the long (OPEN) component, or in other words, we measure three times more photons from FOLDED dyads than from OPEN ones. Based on the PL quantum yields of PBI in both conformations, as derived above, it is straightforward to show that more than 99.9 % of all dyads must exist in the FOLDED conformation to yield such amplitudes.

5. Additional nanosecond pump-probe data on the dyads

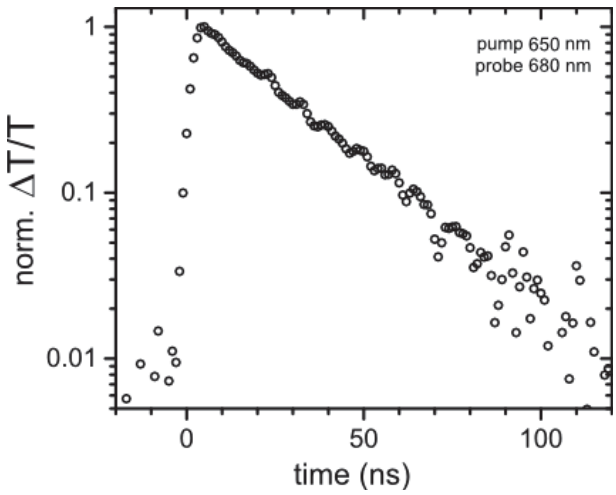

Fig. S4. Nanosecond pump-probe transient of the dyad dissolved in toluene using pump at 650 nm and probe at 680 nm.

6. Additional femtosecond pump-probe data on PBI

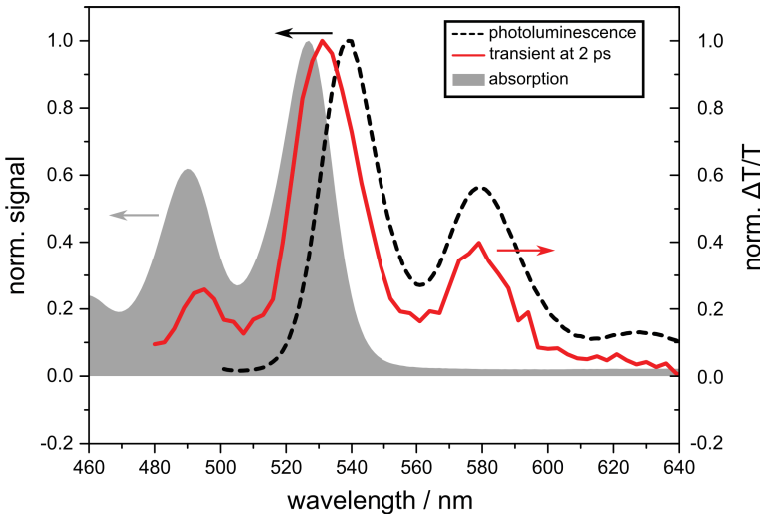

Fig. S5. Femtosecond pump-probe transient spectrum of the isolated PBI moiety at 2 ps delay with pump at 520 nm (solid red line). Comparing this transient with the absorption spectrum (grey filled area) and the PL spectrum of PBI (dashed line), the positive $\Delta T/T$ signals can be clearly attributed to ground state bleach (around 520 nm) and to stimulated emission (around 550 nm) of the PBI moiety.

7. Experimental section

A. Materials and Methods

4-{2-[2-(2-ethoxyethoxy)ethoxy]-1-[2-((2-ethoxyethoxy)-ethoxy)ethoxymethyl] ethyloxy}-1,2-dicyanobenzene (1) [2], 4-(6-hydroxyhexylsulfanyl)-1,2-dicyanobenzene (2) [3] and N-(1-Heptyloctyl),N'-(octyl-8'-azido)-perylene-3,4,9,10-tetracaboxylic acid bisimide (PBI-N3) [4] were synthesized and purified according to literature procedures. All reaction solvents were dried and purified as described by Perrin and Armarego [5]. The commercially available reagents were used without further purification. Silica gel (E. Merck) was used for column chromatography. Fourier transform infrared (FT-IR) spectra were recorded between 4000 and 650 cm^{-1} using a Perkin Elmer Spectrum 100 FT-IR spectrometer with an attenuated total reflection (ATR) accessory featuring a zinc selenide (ZnSe) crystal. The mass spectra were recorded on MALDI (matrix assisted laser desorption ionization) BRUKER Microflex LT using 2,5-dihydroxybenzoic acid as matrix.

For the spectroscopic measurements the molecules were dissolved in spectroscopic grade toluene (Sigma Aldrich, 99.8 %). The resulting concentration of all samples was 10^{-6} M. The steady-state absorption and emission spectra were recorded using commercial spectrometers (absorption: Perkin-Elmer Lambda-750, emission: Varian Cary Eclipse). The photoluminescence quantum yield was measured with a spectrofluorometer (JASCO, FP 8600) with an integrating sphere. The accuracy of these measurements is ± 0.005.

The fluorescence lifetime curves were measured using a Streak-camera setup. The solution was excited with a power of P = 0.58 mW at 450 nm using the frequency doubled and linearly polarized output of a pulsed titan:sapphire laser (Tsunami, Model 3980, both Spectra Physics; pulse width: 5 ps; repetition rate: 81 MHz). The emission of the dyad was collected under an angle of 90° to reduce scattered laser light and was directed to two

broadband polarising beam splitters. To detect simultaneously the emission with parallel and perpendicular polarisation with respect to that of the excitation light, we slightly displaced the second beam splitter to combine both signals again with a spatial offset [6]. These two parallel beams are directed onto a spectrograph that is equipped with a mirror, and detected by a Streak-camera in photon counting mode (C5680, Hamamatsu). By reconvolution of the recorded picosecond transients with the instrument response function a time resolution of 100 ps is achieved. The instrument response function was measured using a scattering solution.

For the femtosecond pump-probe measurements we employed a RegA9000 regenerative amplifier system (pulse length 210 fs) at 100 kHz repetition rate from Coherent. 88 % of its output intensity was used to pump an OPA (Coherent), which provides the pump beam at a wavelength of 510 nm. The pump beam diameter was set to about 300 µm and the pump fluence was 10 – 30 µJ/cm². The remaining 12 % of the output intensity of the regenerative amplifier was used to create the probe light between 480 and 750 nm by means of a YAG-crystal. The DT/T spectra were recorded using a lock-in amplifier (SR830, Stanford Research) and a monochromator (spectral resolution 3 nm, $\lambda/\Delta\lambda = 200$) with a silicon diode.

Nanosecond pump-probe spectra were measured using a flash photolysis setup (Applied Photophysics). The sample solution was excited at 540 nm, 610 nm or 650 nm, respectively, by an optical parametric oscillator (Rainbow-Quantel) which was pumped with the 3rd harmonic output of a Nd:YAG laser (Brilliant-Quantel). The excitation energy flux was fixed to 360 µJ / cm². The probe was provided by a Xenon white light source. The $\Delta T/T$ spectra were recorded using a monochromator and a photomultiplier. The data were collected using a Keysight DSOS104A oscilloscope.

B. Synthesis

2(3),9(10),16(17)-Tri-({2-[2-(2-ethoxyethoxy)ethoxy]-1-[2-(2- ethoxyethoxy)) ethoxymethyl] ethoxy}- 23- (6-hydroxyhexylsulfanyl) phthalocyaninato copper(II)(3)

A mixture of 4-{2-[2-(2-ethoxyethoxy)ethoxy]-1-[2-((2-ethoxyethoxy)-ethoxy) ethoxymethyl] ethyloxy}-1,2-dicyanobenzene (**1**) (783 mg, 1.740 mmol, 9 equiv.), 4-(6-hydroxyhexylsulfanyl)-1,2-dicyanobenzene (**2**) (51 mg, 0.194 mmol) and anhydrous $CuCl_2$ (174 mg, 1.305 mmol) were refluxed in anhydrous N,N-dimethylaminoethanol (1.8 ml) for 24 h under argon atmosphere. N,N-dimethylaminoethanol was removed by adding hexane to the reaction mixture, the crude product was precipitated. The solid was dissolved in dichloromethane, filtered to remove inorganic impurities, and then concentrated. The crude product was purified by column chromatography over silica gel using CH_2Cl_2:EtOH/25:1 as eluent to collect asymmetric **3** and symmetric Pc derivatives. Furthermore, the phthalocyanine **3** was purified by using preparative silica gel thin layer chromatography using CH_2Cl_2:EtOH/25:2 as eluent. Yield: 12% (40 mg). R_f 0.62 (CH_2Cl_2:EtOH/25:2). IR n_{max}/cm^{-1} (ATR): 3400 (OH), 3040 (ArCH), 2985-2860 (CH_2, CH_3), 1654 (C=N), 1608 (ArC=C), 1507, 1472, 1400, 1345, 1278, 1233, 1120-1085 (C–O–C). Calcd. for $C_{83}H_{118}N_8O_{22}SCu$: %C, 59.44; %H, 7.09; %N, 6.68. Found: %C, 59.25; %H, 7.05; %N, 6.70. MS (MALDI-TOF) *m*/*z*: Calc.: 1675.5; Found: 1676.9 $[M+H]^+$, 1838.4 $[M+7Na]^+$.

2(3),9(10),16(17)-Tri-({2-[2-(2-ethoxyethoxy)ethoxy]-1-[2-(2- ethoxyethoxy)) ethoxymethyl] ethoxy} -23-[(prop-2-ynyloxy)hexylsulfanyl] phthalocyaninato copper(II) **(4)**

NaH (20 mg, 0.85 mmol) was added to solution of **3** (143 mg, 0.085 mmol) in anhydrous THF (6 ml) under argon atmosphere. After stirring for 10 min, propargyl bromide (1 ml, 7.2 mmol) was added. The reaction mixture was stirred under argon atmosphere at room temperature for 24 h. The greenish-blue mixture was filtered off and solvent was evaporated under reduced pressure. The oily crude product was purified by using preparative silica gel thin layer chromatography using CH_2Cl_2:EtOH/25:2 as eluent. Yield 85 mg (58 %). R_f 0.76 (CH_2Cl_2:EtOH/25:2). IR n_{max}/cm^{-1} (ATR): 3241 (CºC-H), 3040 (ArCH), 2972-2860 (CH_2, CH_3), 2105(CºC), 1605 (ArC=C), 1508, 1472, 1400, 1344, 1232, 1120-1080 (C–O–C). Calcd. for $C_{86}H_{120}N_8O_{22}SCu$: %C, 60.26; %H, 7.06; %N, 6.53. Found: %C, 60.12; %H, 7.05; %N, 6.45. MS (MALDI-TOF) *m*/*z*: Calc.: 1714.05; Found: 1789.6 $[M+2K]^+$, 1876.7$[M+7Na]^+$.

***2(3),9(10),16(17)-Tri-({2-[2-(2-ethoxyethoxy)ethoxy]-1-[2-(2-ethoxyethoxy)) ethoxymethyl] ethoxy}- 23- [({N-(1-heptyloctyl), perylene-3,4,9,10-tetracaboxylic acid bisimide- N'-(octyl-)8'-1H-1,2,3-triazole-4-yl)}-methoxy) hexylsulfanyl)] phthalocyaninato copper(II)*(CuPc-PBI Dyad)**

Alkynylphthalocyanine **4** (75 mg, 0.044 mmol) and N-(1-heptyloctyl), N'-(octyl-8'-azido)-perylene-3,4,9,10-tetracaboxylic acid bisimide (**PBI-N3**) (54 mg, 0.072 mmol) were dissolved in degassed CH_2Cl_2 (10 mL) under argon atmosphere. N,N,N',N'',N'' pentamethyldiethylenetriamine (14 mg, 0.071 mmol) was added and the solution was purged 5 min with argon. Then copper (I) bromide (11 mg, 0.077 mmol) was added and the mixture was purged with argon 5 min more. The reaction mixture was stirred at room

temperature for 24 h, then diluted with CH_2Cl_2 and washed with water (10 mL). The organic phase was dried on Na_2SO_4 and concentrated. CuPc-PBI Dyad was purified by silica gel column chromatography. Elution with ethylacetate removed most of the impurities, then the column was equilibrated with CH_2Cl_2 and eluted by a gradient ending with CH_2Cl_2: EtOH/25:2. CuPc-PBI Dyad was obtained pure in after a last purification by preparative silica gel thin layer chromatography using CH_2Cl_2: EtOH/100:9 as eluent. Yield: 63% (68 mg). R_f 0.62 (CH_2Cl_2: EtOH/100:9). IR n_{max}/cm^{-1} (ATR): 3040 (ArCH), 2922-2859 (CH_2, CH_3), 1692(C=N), 1654 (C=N), 1606 (ArC=C), 1508, 1466, 1403, 1341, 1233, 1120-1085 (C–O–C). Calcd. for $C_{133}H_{175}N_{13}O_{26}SCu$: %C, 64.72; %H, 7.16; %N, 7.37. Found: %C, 64.65; %H, 7.09; %N, 7.45. MS (MALDI-TOF) *m*/*z*: Calc.: 2468.02; Found: 2469.12 $[M+H]^+$, 2545.34$[M+2K]^+$, 2633.55$[M+7Na]^+$.

C. Molecular Dynamics, Forcefield Generation

MD simulations were carried out using Gromacs 5 1. [7]) In principle, an exact MD simulation would require the determination of force fields including partial charges from first-principles quantum-mechanical calculations, which would be a formidable task (for such a large molecule). We therefore take a more approximate route by using GROMOS 54A7 [8] compatible forcefield topologies which were created using automated topology builder (ATB)[9].

Copper atoms cannot be handled by the ATB server directly and the forcefield topology of the dyad thus had to be built in three steps. As a first step, a forcefield template (bonds, angles, dihedrals, etc.) without charges was calculated with ATB for the entire

phthalocyanine-perylene dyad (Pc-PBI). The copper was omitted and replaced by two hydrogen atoms.

In the second step, the charge distribution was calculated. Here, the Pc-PBI dyad was split up along the aliphatic chain in two separate parts. Each part was submitted separately to the ATB server. From the two parts, the charge distribution was obtained and inserted into the Pc-PBI dyad template from the first step.

In the third step, the two hydrogen atoms were replaced by the copper atom (parameters from GROMOS 54A7 forcefield set) by hand and it was connected to the two nitrogen atoms by a metallic GROMOS bond manually. The partial charge of a copper atom in a similar CuPc molecule without the oxygen-substituted side-groups and the sulphur atom was calculated by Liao and Schreiner [10, 11]. Assuming that the side-groups do not change the main charge distribution significantly, we used their partial charges and modified them in order to be compatible with the additional side-groups of the dyad.

The toluene force field was taken directly from the ATB database [9].

Umbrella sampling was carried out using Gromacs and free energy curves were reconstructed using the WHAM algorithm as implemented by the Gromacs tool g_wham similar as in [12]). We pulled the PBI and CuPc units away from each other along two different paths: the umbrella sampling of the first path contains 19 simulation windows of 10 ns simulation time, and that of the second path comprises 23 windows of 10 ns simulation time. The curve shown in the main text is an average over both.

8. References

1 J. R. Lakowicz, *Principles of Fluorescence Spectroscopy Principles of Fluorescence Spectroscopy*, 2006.

2 M. Menaf Ayhan, G. Altinbas Özpinar, M. Durmus and A. G. Gürek, *Dalt. Trans.*, 2013, **42**, 14892–14904.

3 M. N. Yarasir, M. Kandaz, A. Koca and B. Salih, *Polyhedron*, 2007, **26**, 1139–1147.

4 A. S. Lang and M. Thelakkat, *Polym. Chem.*, 2011, **2**, 2213.

5 D. D. Perrin and W. L. F. Armarego, *Elsevier*, 2001, **4th Edt.**

6 F. Spreitler, M. Sommer, M. Hollfelder, M. Thelakkat, S. Gekle and J. Köhler, *Phys. Chem. Chem. Phys.*, 2014, **16**, 25959–25968.

7 M. J. Abraham, T. Murtola, R. Schulz, S. Pall, J. C. Smith, B. Hess and E. Lindahl, *SoftwareX*, 2015, **1-2**, 19–25.

8 N. Schmid, A. P. Eichenberger, A. Choutko, S. Riniker, M. Winger, A. E. Mark and W. F. Van Gunsteren, *Eur. Biophys. J.*, 2011, **40**, 843–856.

9 A. K. Malde, L. Zuo, M. Breeze, M. Stroet, D. Poger, P. C. Nair, C. Oostenbrink and A. E. Mark, *J. Chem. Theory Comput.*, 2011, **7**, 4026–4037.

10 S. Bode, C. C. Quentmeier, P.-N. Liao, N. Hafi, T. Barros, L. Wilk, F. Bittner and P. J. Walla, *Proc. Natl. Acad. Sci. U. S. A.*, 2009, **106**, 12311–12316.

11 M. S. Liao and S. Scheiner, *J. Chem. Phys.*, 2001, **114**, 9780–9791.

12 M. Hollfelder and S. Gekle, *J. Phys. Chem. B*, 2015, **119**, 10216–10223.

9 The Impact of Driving Force and Temperature on the Electron Transfer in Donor-Acceptor Blend Systems

Thomas Unger*, Stefan Wedler*, Julian Kahle, Ullrich Scherf, Heinz Bässler und Anna Köhler

**Diese Autoren haben gleichermaßen beigetragen*

Veröffentlicht in

The Journal of Physical Chemistry C 121 (2017), 22739-22752

(DOI: 10.1021/acs.jpcc.7b09213)

THE JOURNAL OF PHYSICAL CHEMISTRY C

Article

Cite This: J. Phys. Chem. C 2017, 121, 22739-22752

pubs.acs.org/JPCC

The Impact of Driving Force and Temperature on the Electron Transfer in Donor−Acceptor Blend Systems

Thomas Unger,[†,∥] Stefan Wedler,[†,∥] Frank-Julian Kahle,[†] Ullrich Scherf,[§] Heinz Bässler,[‡] and Anna Köhler*[,†,‡]

[†]Experimental Physics II, University of Bayreuth, 95447 Bayreuth, Germany

[‡]Bayreuth Institut of Macromolecular Research (BIMF), University of Bayreuth, 95447 Bayreuth, Germany

[§]Makromolekulare Chemie, Bergische Universität Wuppertal, 42119 Wuppertal, Germany

Supporting Information

ABSTRACT: We discuss whether electron transfer from a photoexcited polymer donor to a fullerene acceptor in an organic solar cell is tractable in terms of Marcus theory, and whether the driving force ΔG_0 is crucial in this process. Considering that Marcus rates are presumed to be thermally activated, we measured the appearance time of the polaron (i.e., the radical-cation) signal between 12 and 295 K for the representative donor polymers PTB7, PCPDTBT, and Me-LPPP in a blend with PCBM as acceptor. In all cases, the dissociation process was completed within the temporal resolution of our experimental setup (220−400 fs), suggesting that the charge transfer is independent of ΔG_0. We find that for the PCPDTBT:PCBM ($\Delta G_0 \approx -0.2$ eV) and PTB7:PCBM ($\Delta G_0 \approx -0.3$ eV) the data is mathematically consistent with Marcus theory, yet the condition of thermal equilibrium is not satisfied. For MeLPPP:PCBM, for which electron transfer occurs in the inverted regime ($\Delta G_0 \approx -1.1$ eV), the dissociation rate is inconsistent with Marcus theory but formally tractable using the Marcus−Levich−Jortner tunneling formalism which also requires thermal equilibrium. This is inconsistent with the short transfer times we observed and implies that coherent effects need to be considered. Our results imply that any dependence of the total yield of the photogeneration process must be ascribed to the secondary escape of the initially generated charge transfer state from its Coulomb potential.

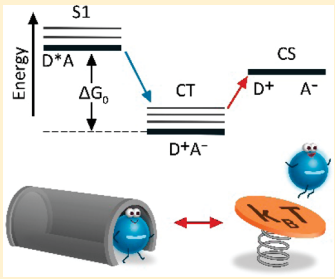

1. INTRODUCTION

The conversion of optical energy into electrical energy in organic solar cells is meanwhile established to occur as a two-step process.[1] The initial step is the transfer of an electron from a photoexited donor chromophore to an acceptor chromophore. This leads to the formation of a charge-transfer state, or, more generally, a Coulomb-bound electron−hole (eh) pair, that separates into free charges in a subsequent step.[2,3] The initial electron transfer step is exothermic, while the subsequent charge separation step is endothermic. A key parameter here is the "driving force ΔG_0" of the process, commonly considered to be the difference in the energies of the initial and final states of the system. More precisely, the driving force is the difference in Gibbs free energy (also known as free enthalpy) between the initial and final states, $\Delta G_0 = \Delta H - T\Delta S$, with H being the enthalpy, T the temperature, and S the entropy.[4] It is an intuitively attractive idea that the overall process may be more efficient when more energy is released during the initial electron transfer from the excited donor to the acceptor. Furthermore, when ΔG_0 becomes more negative, then the excess energy might be used to facilitate overcoming the Coulomb barrier of the initially created electron−hole pair.[5,6] On the other hand, there is growing evidence that this subsequent dissociation process starts from a "cold" eh pair.[2] If so, would a high driving force still be of advantage for the cell efficiency irrespective of the fact that a high driving force implies a lower open circuit voltage of the solar cell?[7] Evidently, to clarify the role of the driving force is a crucial question for understanding the operation of organic solar cells.[7,8]

Our current study was stimulated by the work of Ward et al.[9] They conducted time-resolved photoluminescence measurements on donor−acceptor blends, in which the LUMO energies of the acceptor were varied systematically. From their studies, they inferred the rate of charge transfer in the donor−acceptor pair and found an apparent correlation between the driving force and the charge transfer rate that they interpreted to be in agreement with the classical Marcus theory. Specifically, they concluded that the charge transfer rate is maximal when the driving force is $\Delta G_0 = -0.4$ eV but that the rate decreases significantly for driving forces above and below this optimum value. However, recent experiments on non-fullerene-type acceptors have been shown to lead to efficient solar cells, even if the driving force, measured as the energy difference between the donor LUMO and the acceptor LUMO, is close to zero.[10,11]

These considerations and the unclear role of ΔG_0 result from an approach where the electron transfer is a priori considered treatable in a classical Marcus type framework. Marcus' theory was originally developed and proved successful to describe

Received: September 15, 2017
Published: September 20, 2017

DOI: 10.1021/acs.jpcc.7b09213
J. Phys. Chem. C 2017, 121, 22739−22752

energy or electron transfer between an individual molecular donor and an individual molecular acceptor in solution.[12−14] However, in its original, classical form, it is not generally suitable to describe the transport of charges through a thin film of an organic semiconductor.[15−17] The latter may be seen as a sequence of electron transfer events between chemically identical donor and acceptor sites. The reason for this shortcoming is that in disordered systems the direct quantum mechanical tunneling between initial and final states takes more weight compared to the thermally activated process than predicted by classical Marcus theory.[18−20] It is therefore uncertain whether classical Marcus theory is the most appropriate approach to describe the electron transfer from a donor material to an acceptor material when the two materials form a disordered thin film in an organic solar cell. In fact, more sophisticated quantum mechanical descriptions have recently been suggested.[21−26] Nevertheless, Marcus theory is frequently used to account for the photogeneration of charges.[8,27−29] The question that we are discussing in this paper is, therefore, *whether classical Marcus theory gives a suitable description for electron transfer in a thin donor−acceptor type film and, associated with this, what the role of the driving force* ΔG_0 *is in promoting the electron transfer.*

We address this issue by measuring the electron transfer rate through time-resolved photoinduced absorption of thin films made of blends of a polymer donor and the fullerene acceptor PCBM over a broad range of temperatures. The measured rates (or their lower limits) are compared with the transfer rates that are expected on the basis of the molecular parameters. For our study, we employed PCBM as a prototypical, widely used acceptor and combined it with the donor polymer PTB7 that was also investigated by Ward et al.[9] As a second, representative donor polymer, we chose PCPDTBT.[30,31] Both PTB7 and PCPDTBT have moderate driving forces when combined with PCBM. As an example of a polymer with a high driving force, we also investigated the rigid MeLPPP. All chemical structures are shown in Figure 1.

2. EXPERIMENTAL SECTION

2.1. Materials and Sample Preparation. PTB7 (poly-({4,8-bis[(2-ethylhexyl)oxy]benzo[1,2-*b*:4,5-*b*′]dithiophene-2,6-diyl)-{3-fluoro-2-[(2-ethylhexyl)carbonyl]thieno[3,4-*b*]-thiophene-2,5-diyl}}) was purchased from 1-Material and has a molecular weight M_w of 23 kDa. The solvents, $PC_{60}BM$ and PCPDTBT (poly{[4,4-bis(2-ethylhexyl)-cyclopenta(2,1-*b*;3,4-*b*′)dithiophene-2,6-diyl]-*alt*-(2,1,3-benzothiadiazole-4,7-diyl}) were obtained from Sigma-Aldrich. Methylated ladder-type poly(para-phenylene) polymer (MeLPPP) (M_w = 83 kDa) was synthesized in the group of U. Scherf.[32,33] To prepare thin films for optical measurements, a 36 g/L chloroform solution of MeLPPP blended with PCBM (1:1 by weight) and of neat MeLPPP was spin-coated under a nitrogen atmosphere onto spectrosil B substrates at 700 and 800 rpm, respectively. PCPDTBT and PTB7 films were spin-coated onto quartz substrates at 700 rpm from 20 g/L chlorobenzene solutions. No further annealing step was performed in order to keep phase separation as low as possible. Doped films were obtained by immersing the neat polymer films in acetonitrile solution of $FeCl_3$ (0.1%) for about 10 min. In Figure 1, we display the difference in absorption between the film prior to and after the doping process. The UV/vis absorption was measured using a Cary 5000 UV−vis-NIR spectrophotometer. Photoluminescence spectra (PL) are recorded with a JASCO FP-8600 spectrofluorometer.

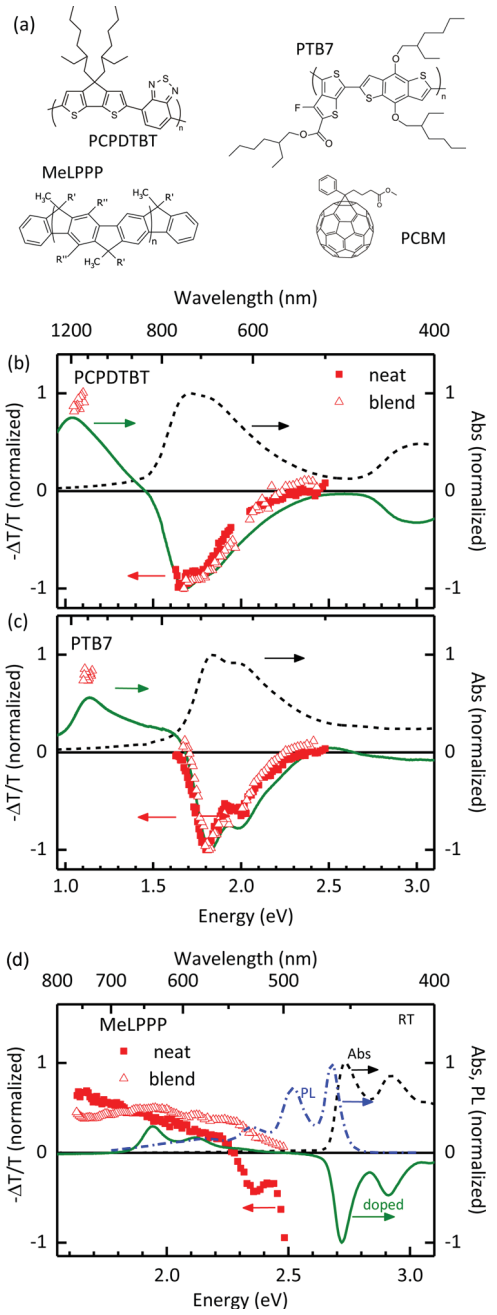

Figure 1. (a) Chemical structures of the donor polymers and the fullerene acceptor. (b−d) Spectra of blends and neat films of PCPDTBT, PTB7, and MeLPPP. The black dashed line shows the absorption of the neat neutral donor, and the green solid line indicates the changes obtained in absorption upon doping the neat donor. The symbols show the photoinduced absorption obtained for the neat donor film (solid squares) and for the blend (open triangles) at 2 ps after the excitation pulse (1 ps for neat PTB7). For MeLPPP, the photoluminescence (PL) is also indicated as a blue dash-dotted line.

2.2. Femtosecond Transient Absorption Measurements. Transient absorption measurements were performed using a RegA9000 regenerative amplifier system from Coherent Inc. (pulse length 210 fs) with a 100 kHz repetition rate. About 12% of the output intensity is used for generation of the probe light between 480 and 750 nm in a YAG-crystal. The remaining

DOI: 10.1021/acs.jpcc.7b09213
J. Phys. Chem. C 2017, 121, 22739−22752

intensity of the output intensity is used to pump an OPA (Coherent Inc.) for the pump beam at 3.1 eV (400 nm) and 1.94 eV (640 nm). The pump fluence is in the range 10−30 μJ/cm^2. The spectra are recorded by using a lock-in amplifier (SR830, Stanford Research) and a monochromator (spectral resolution 3 nm) with a Si-diode for the Vis region or a InGaAs-diode for the NIR region. The measurements were performed on thin films placed in a cryostat under a helium atmosphere and at temperatures as indicated in the figure captions.

2.3. CT Measurements. In order to determine the energy of the charge transfer (CT) state and the associated reorganization energy in MeLPPP:PCBM blends, we measured the external quantum efficiency (EQE) and electroluminescence (EL) in bulk heterojunction solar cell devices of the structure ITO-covered glass/MoO_3 (15 nm)/blend or neat film/Al (100 nm). Blends had a thickness of 110 nm, spun from chloroform at 15 mg mL^{-1}. For reference, solar cells with pristine MeLPPP (chloroform, 7.5 mg mL^{-1}) and PCBM layers (chloroform, 15 mg mL^{-1}), respectively, were fabricated accordingly. The thicknesses of the MeLPPP and PCBM films were 60 and 30 nm, respectively. The thicknesses of the active layer of the solar cells were controlled with a Dektak (Veeco) profilometer directly on a device.

EQE measurements were performed using a lock-in amplifier (SR830) at a reference frequency of 130 Hz and using monochromatic illumination from a 150 W tungsten lamp (Osram). For EL measurements, the solar cells were biased at 3V using a Keithley source-measure unit (SMU 237). The luminescence of the sample was recorded by a CCD camera (Andor iDus) coupled to a monochromator (Oriel). For both EQE and EL measurements, the sample was kept in an appropriate vacuum condition sample holder at room temperature. CT and reorganization energies were determined from a simultaneous Gaussian fit to the reduced EQE and EL spectra according to Vandewal et al.[34] The reduced EQE and EL are given by reduced EQE = E·EQE(E) and reduced EL = EL(E)/E.

3. RESULTS

3.1. Experimentally Determined Transfer Rates. In order to compare theoretically predicted rates with experimentally observed ones, the rates of charge transfer—or their lower bounds—need to be determined. We focused therefore on measuring the appearance of the absorption due to the cation that forms on the donor when the electron transfers onto the acceptor. Thus, a first step is to determine the spectral position of this absorption. For this, we measured the absorption of the respective neat donor polymer films after oxidizing them chemically using $FeCl_3$. The spectra and the other optical properties of the used materials are shown in Figure 1. The low-bandgap polymers PCPDTBT and PTB7 (Figure 1b,c) have their main absorption peak between 2.5 eV (500 nm) and 1.6 eV (800 nm). It is straightforward to assign the reduction of absorption in the spectra of the chemically oxidized neat samples as well as in the pump−probe spectra of the neat samples and blends to the ground state bleach (GSB) of the respective donor polymers. The difference in the absorption of the neat films before and after the chemical oxidation process is the absorption due to the thus formed cations on the polymers. The cation spectra show broad absorption bands centered at 1.0 eV (1200 nm) for PCPDTBT and 1.1 eV (1100 nm) for PTB7, which is also in agreement with literature.[35−37] At these energies, we can also observe a clear pump−probe signal with positive sign in the blends, yet not in the neat films, which we can therefore attribute to the absorption of the polymer cation formed after photoinduced electron transfer to PCBM.

Figure 1d contains the corresponding spectra for MeLPPP. The absorption is structured and lies in the blue part of the visible spectrum, with the first absorption peak situated at 2.7 eV (454 nm). In addition to the GSB at the same energy, there is a structured absorption with a 0−0 peak at about 1.9 eV (640 nm) and a vibronic replica at 2.1 eV (580 nm) in the cation absorption spectra obtained from the chemically oxidized films. The pump−probe spectrum at early times (2 ps) for the neat film consists of a stimulated emission (SE) band above 2.25 eV (below 550 nm) corresponding to the photoluminescence (PL) spectrum (blue line, in Figure 1d). A broad induced absorption band appears below 2.25 eV (above 550 nm) further increasing into the NIR beyond the investigated spectral range, which we attribute to the excited state absorption of the singlet exciton.[38] The SE contribution is nearly absent in the pump−probe spectrum of the blend. Instead, there is an additional absorption feature at the position of the polymer cation absorption with a maximum at about 1.9 eV (650 nm), which is also in accordance with the literature.[38,39]

Having identified the spectral position of the cation absorption, we can now monitor its evolution. Figure 2 shows charge transfer dynamics of the cation absorption at room temperature and at 12 K in the low-bandgap polymers and in their blends with PCBM. For control purposes, the appearance of the GSB is also monitored. For both blends, we observe that the appearance of the cation absorption occurs within our temporal resolution (220 fs in vis, 400 fs in NIR due to technical reasons, indicated by the gray and red shaded areas around time zero position) for room temperature measurement as well as at low temperatures. The same holds for the neat polymer films, yet the signals decay faster than in the blend. Conversely, the cation absorption signals of the blend films at 12 K show an additional offset due to an increased lifetime[40] that exceeds the laser repetition time of 10 μs.

Figure 3 displays the dynamics of the MeLPPP:PCBM system at early times for different temperatures between 250 and 12 K. The transients are taken at the wavelength of the cation absorption signal at 640 nm (1.9 eV). Within the entire temperature range probed, we see an ultrafast charge transfer which is faster than our temporal resolution. Furthermore, there is no initial offset. The exciton signal probed at 730 nm (1.7 eV) decays with a time constant of about 5 ps, which is mainly assigned to the diffusion of singlets to the interface which are not directly created at the interface. Small contributions of this 5 ps decay can also be seen in the cation signal at 250 and 200 K. We attribute this to a contribution from the overlapping exciton signal leaking into the cation signal, which disappears at lower temperatures (see Figure 3).

From these data, we can nominally derive the rise time for the cation signal. We find that the corresponding rate is in the range of (2−5) × 10^{12} s^{-1}. Thus, for all three materials and all temperatures probed, the rise time is within the resolution limit of our instrument. This resolution limit varies slightly for different probe wavelengths.

3.2. Transfer Rates according to Marcus Theory. We now consider whether our experimental values are consistent with Marcus theory. The Marcus transfer rate is given by[41,42]

DOI: 10.1021/acs.jpcc.7b09213
J. Phys. Chem. C 2017, 121, 22739−22752

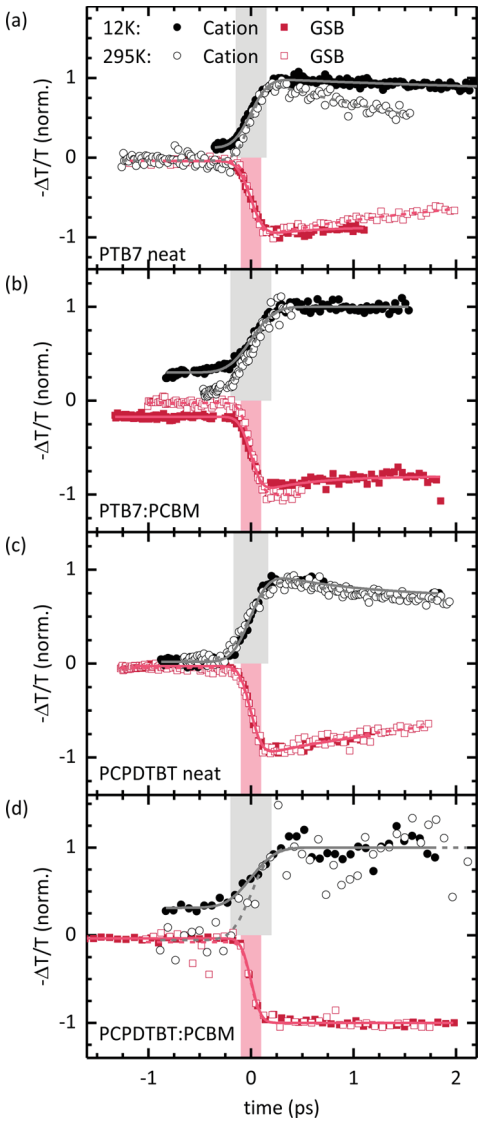

Figure 2. Normalized pump−probe transients in thin films, taken at the wavelength of the ground state bleach (GSB) and the cation absorption. The temporal resolution is indicated by the colored boxes at zero time delay; the solid lines correspond to fits. (a) Neat PTB7; (b) PTB7:PCBM, both GSB at 1.77 eV (700 nm), cation at 1.11 eV (1120 nm); (c) neat PCPDTBT; (d) PCPDTBT:PCBM, both GSB at 1.75 eV (710 nm), cation at 1.11 eV (1120 nm).

$$k_{\mathrm{Marcus}}(T) = \frac{|J_{\mathrm{DA}}|^2}{\hbar}\sqrt{\frac{\pi}{\lambda k_{\mathrm{B}}T}}\exp\left[-\frac{(\lambda + \Delta G_0)^2}{4\lambda k_{\mathrm{B}}T}\right] \quad (1)$$

with the electronic coupling strength J_{DA}, reorganization energy λ, and driving force ΔG_0. This equation is based on thermal equilibrium under the assumption that the quantum nature of the acoustic phonons (with energies of a few meV) does not need to be considered explicitly, i.e., $k_BT \gg \hbar\omega$, and can be treated classically.[43] This is typically the case for temperatures above 100 K.

In order to calculate the rate, we therefore require knowledge of the driving force ΔG_0, the reorganization energy λ, and the electronic coupling J_{DA} between donor and acceptor molecules. The rate is particularly sensitive to the relative magnitude of λ and ΔG_0, as the two quantities tend to have different signs, so that their difference enters the argument of the exponential function. As a simple approximation for the driving force, it is

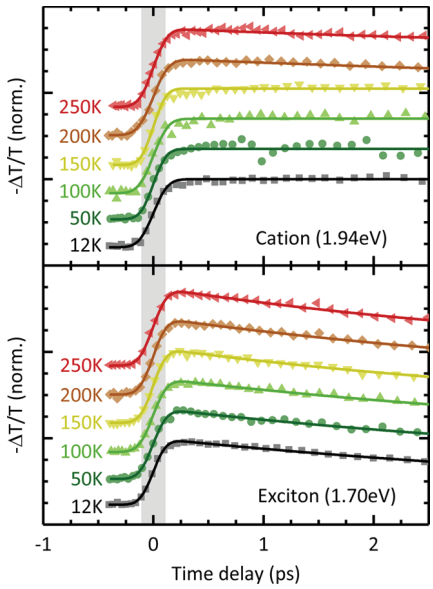

Figure 3. Normalized pump−probe transients of the cation absorption and the exciton absorption in MeLPPP:PCBM blend films excited at 3.1 eV (400 nm) at different temperatures.

common to take the difference in electron affinities.[44] This is sufficient for many cases. Here, we would like to determine ΔG_0 as accurately as possible. Therefore, we consider the difference between the energy of the photoexcited donor and the final charge-transfer state to be ΔG_0:[45]

$$-\Delta G_0 = E_{S1} - E_{CT} \quad (2)$$

This is illustrated in Figure 4 for ease of reference for the cases of $\Delta G_0 = 0$, $\Delta G_0 = -\lambda$, and $\Delta G_0 \ll -\lambda$. To find the values of ΔG_0 for our compounds, we determined E_{S1} from the intersection between the absorption and emission spectra, each normalized to unity at the peak of the first band. For PCPDTBT and PTB7, we took the values for E_{CT} and λ from

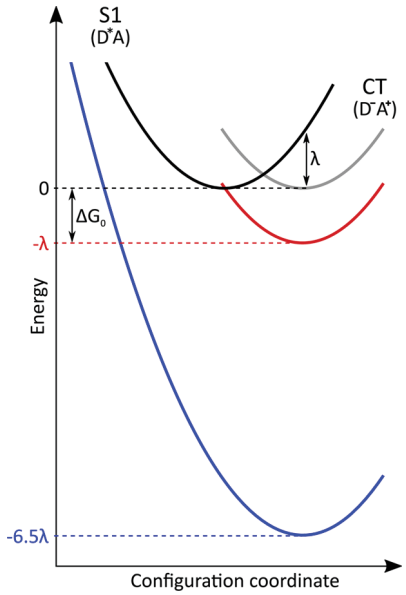

Figure 4. Energy diagram for an electron transfer process in the Marcus picture with vanishing driving force (gray), $\Delta G_0 \approx -\lambda$ (red) and $\Delta G_0 \approx -6.5\ \lambda$ (blue).

DOI: 10.1021/acs.jpcc.7b09213
J. Phys. Chem. C 2017, 121, 22739−22752

Table 1. Summary of the Input Parameters Used to Calculate the Charge Transfer Rate according to eq 1 for the Three Blends Considered[a]

	PCPDTBT:PCBM	PTB7:PCBM	MeLPPP:PCBM
E_{S1} (eV)	1.50 ± 0.10[47,48]	1.67 ± 0.05[49−51]	2.70 ± 0.05[52]
E_{CT} (eV)	1.30 ± 0.05[b]	1.35 ± 0.05[49,53,54]	1.57 ± 0.05
$-\Delta G_0$ (eV)	0.21 ± 0.11	0.32 ± 0.07	1.13 ± 0.07
λ (eV)	0.30 ± 0.10[b,45]	0.35 ± 0.05[9,45]	0.17 ± 0.03
$\lambda + \Delta G_0$ (eV)	0.09 ± 0.15	0.03 ± 0.09	−0.96 ± 0.08
J_{DA} (eV)[45,55]	0.03 ± 0.02	0.03 ± 0.02	0.03 ± 0.02

[a] E_{S1} is the energy of the singlet excited state, E_{CT} is the energy of the CT state, $-\Delta G_0$ denotes the driving force, λ is the reorganization energy associated with the charge transfer, and J_{DA} is the electronic coupling. [b] See the Supporting Information, Figure S3.

published data as listed in Table 1. These values result from fitting the photocurrent spectra (EQE) and electroluminescence (EL) as outlined by Vandewal,[34,46] where 2λ then corresponds to the difference between the maxima in the CT state absorption and emission and E_{CT} is taken from their intersection. Static disorder can contribute to the width of these bands, so that the obtained values are an upper limit. This method determines the reorganization energy between the neutral ground state and the CT state, whereas we consider the formation of the CT state via the excited state. In principle, these values are different. However, they are expected to be very similar, as the reorganization energy for the fullerene acceptor is small due to its rigidity.[56,57]

Table 1 lists the driving force thus obtained, along with the pertaining parameters. For the MeLPPP system, we needed to experimentally determine E_{CT} and λ. Therefore, we measured the EL of the MeLPPP:PCBM blend to compare against the EL spectrum of the neat MeLPPP and PCBM. The EL of neat MeLPPP was consistent with ref 58. It is more than 1 eV separated from the blend EL and therefore does not need to be considered further. Figure 5a shows the EL of the blend along with the EL from neat PCBM, taken from ref 59 and normalized to fit the high energy tail. The difference between the two spectra, shown as a blue line, is assigned to the EL of the CT state. In Figure 5b, the CT EL is compared to the EQE spectrum of the blend. We fitted the CT emission and the low energy tail of the EQE, respectively, according to $\mathrm{EL}(E) \propto \frac{1}{E\sqrt{4\pi\lambda k_B T}} \exp\left(-\frac{(E_{CT}-\lambda-E)^2}{4\lambda k_B T}\right)$ and $\mathrm{EQE}(E) \propto \frac{1}{E\sqrt{4\pi\lambda k_B T}} \exp\left(-\frac{(E_{CT}+\lambda-E)^2}{4\lambda k_B T}\right)$, as outlined in ref 34, using identical parameters for the CT emission and the fit to the low energy tails of the EQE. Here, E denotes the photon energy and $k_B T$ denotes the product of Bolzmann constant and temperature. From this procedure, we arrive at E_{CT} = 1.57 ± 0.05 eV and λ = 0.17 ± 0.03 eV.

To calculate the charge transfer rate according to Marcus, we still require the value of the electronic coupling. This can only be derived by calculations. Leng and co-workers report a value of 30 meV for PCPDTBT:PCBM,[45] and Liu and co-workers report 20−30 meV for P3HT:PCBM.[55] On the basis of these studies, we adopt a value of J = 30 ± 20 meV for all compounds. All values required to calculate the transfer rate are summarized in Table 1. A detailed discussion to each value and its error margin is given in the Supporting Information (SI 1.1). For reference, we have also considered which driving force ΔG_0^{IP}, and concomitantly which transfer rate, would result if the

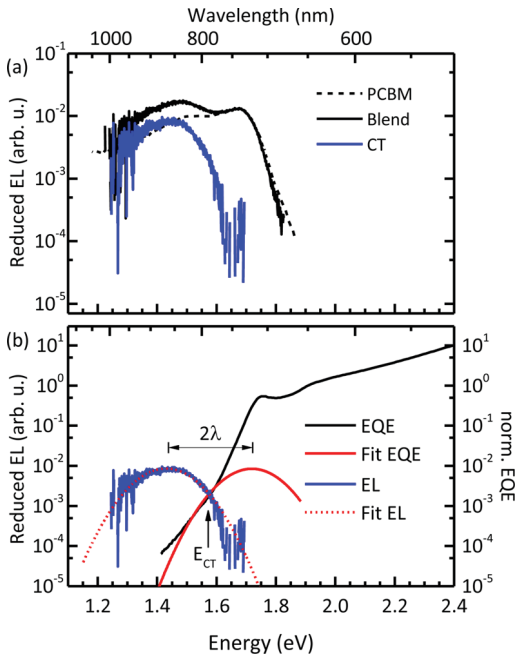

Figure 5. (a) Reduced EL of MeLPPP:PCBM (black solid line) and pristine PCBM (black dashed line). The difference of the two spectra corresponds to the CT emission (blue solid line). The spectra of pristine PCBM were reprinted with permission from ref 59. Copyright (2009) American Chemical Society. (b) Reduced EQE and EL spectra of MeLPPP:PCBM (black solid lines). The blue line corresponds to the CT-EL spectrum, as shown in part a. Red lines indicate simultaneous Gaussian fits to the CT region of EQE (solid) and EL (dotted) according to Vandewal et al.[34]

difference in the ionization potential of the donors, derived from refs 45 and 60 for PCPDTBT, as well as ref 50 for PTB7, and the fullerene EA of 3.8 ± 0.1 eV was considered.[2,61,62] It turns out that this does not impact the overall conclusions, as detailed in the Supporting Information (SI 1.2).

By comparing the values of ΔG_0 and λ, one can see that for PCPDTBT:PCBM and PTB7:PCBM $\Delta G_0 \cong -\lambda$, whereas for MeLPPP:PCBM $\Delta G_0 \cong -6.5\lambda$. These two cases are illustrated in Figure 4. Evidently, rather high transfer rates can be expected in the former case, while transfer should become difficult in the latter case, which is the Marcus inverted regime. Table 2 summarizes the transfer rates calculated according to eq 1 with the mean values of parameters of Table 1.

4. ANALYSIS

4.1. Electron Transfer in the Marcus Normal Regime.

It is worthwhile to discuss the range of values that may be obtained by using eq 1 from the experimentally found input parameters. We shall first focus on PCPDTBT and PTB7. The usual preconception is that a thermally activated charge transfer can be described by Marcus theory,[8,27] and that the expected charge transfer rate slows down upon cooling due to the exponential term. It turns out that, for the low-bandgap polymers we investigated, PCPDTBT and PTB7, the magnitude of the reorganization energy λ and of the driving force ΔG_0 are, within the experimental error, about equal, while their signs are opposite. As a result, the argument of the exponential function is close to zero, with some variation on both sides of zero due to the experimental error margins. The fact that $\Delta G_0 + \lambda \approx \pm 0$ has two consequences. First, it results in a rather large range of values that can be obtained within the

DOI: 10.1021/acs.jpcc.7b09213
J. Phys. Chem. C 2017, 121, 22739−22752

Table 2. Transfer Rates Determined according to eq 1 for Different Temperatures, along with the Experimentally Measured Lower Limits for the Transfer Rates[a]

temperature (K)	PCPDTBT	PTB7	MeLPPP
		Expected from Marcus Theory in s^{-1}	
295	2×10^{13}	3×10^{13}	3×10^{-10}
200	2×10^{13}	3×10^{13}	3×10^{-21}
150	2×10^{13}	3×10^{13}	2×10^{-32}
100	2×10^{13}	4×10^{13}	3×10^{-55}
12	4×10^{10}	7×10^{13}	$<10^{-300}$
		Experimental Values in s^{-1} (Lower Limits)	
295	$(2.9 \pm 1.8) \times 10^{12}$	$(2.6 \pm 0.2) \times 10^{12}$	$(4.1 \pm 0.2) \times 10^{12}$
12	$(2.2 \pm 0.7) \times 10^{12}$	$(2.4 \pm 0.1) \times 10^{12}$	$(4.5 \pm 0.2) \times 10^{12}$

[a]Minimum and maximum transfer rates resulting from the uncertainties of the parameters are given in the Supporting Information (Table S2).

limits of the input parameters. Second, the temperature dependence of the transfer rate does not necessarily reduce upon cooling, in contrast to the common expectation. Rather, it may be nearly independent of temperature or even increase upon cooling, when the overall temperature dependence is controlled by the nonexponential prefactor. Figure 6 illustrates the temperature dependence that results from eq 1 for PCPDTBT and for PTB7 in addition to the temperature dependence obtained when using the mean values for the input parameters λ, ΔG_0, and J_{DA}. Figure 6 also shows, as shaded areas, the range of accessible values when the input parameters λ, ΔG_0, and J_{DA} are varied within their range of uncertainty (compare Table S2 in the Supporting Information). While we show the functional dependence of eq 1 for values down to 10 K, one needs to bear in mind that the *mathematical* application of eq 1 below about 100 K does not necessarily carry any *physical* meaning as detailed below. The gray shaded area indicates the range of rates that are beyond our instrumental time resolution.

The values of the singlet energy, CT state energy, and reorganization energy found for PCPDTBT and PTB7 in combination with PCBM are typical for many low-bandgap polymers. It is therefore instructive to consider how sensitively the transfer rates depend on the driving force and reorganization energy. Figure 7 shows calculated Marcus rates (eq 1) as a function of driving force for an electronic coupling of J_{DA} = 30 meV and two different values of reorganziation energy, λ = 0.30 eV and λ = 0.35 eV. This corresponds to the

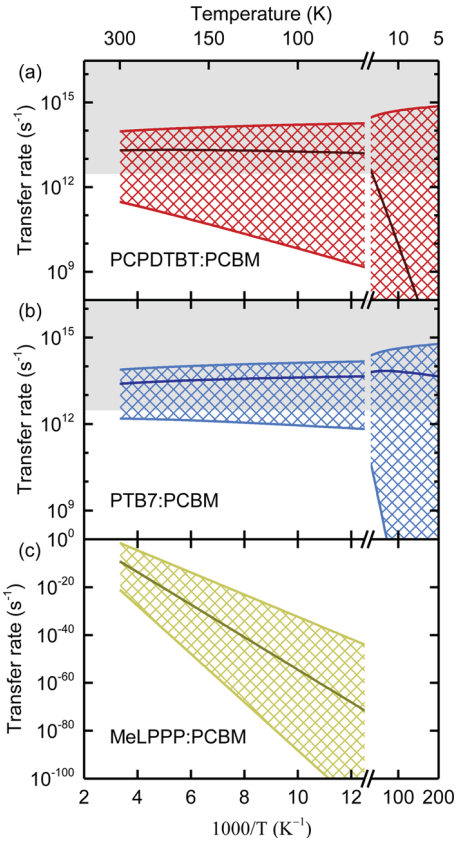

Figure 6. Arrhenius plots of the Marcus-type electron transfer rate according to eq 1, calculated using the mean values for each parameter (dark solid line). The fastest and slowest rates accessible within the error range of the parameters are shown as light solid lines bordering the patterned range of accessible values. The gray shaded area indicates values that are beyond our instrumental resolution.

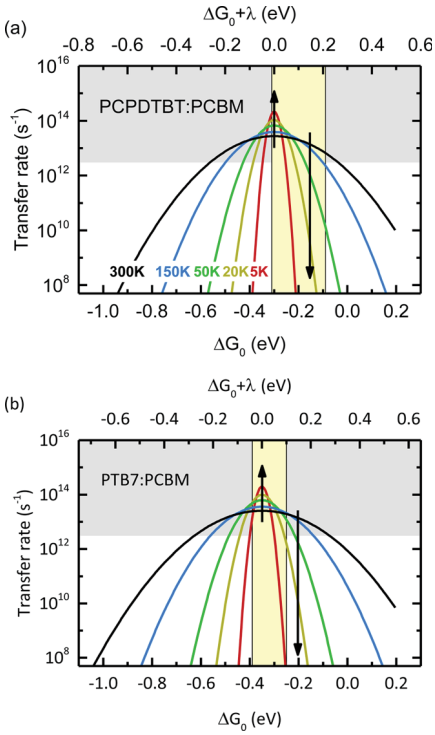

Figure 7. Marcus-type electron transfer rates according to eq 1 as a function of driving force for temperatures of 300, 150, 50, 20, and 5 K (a) for PCPDTBT:PCBM and (b) for PTB7:PCBM. The gray shaded area indicates values that are beyond our instrumental resolution. The yellow shaded area indicates the parameter range for the driving force.

DOI: 10.1021/acs.jpcc.7b09213
J. Phys. Chem. C 2017, 121, 22739−22752

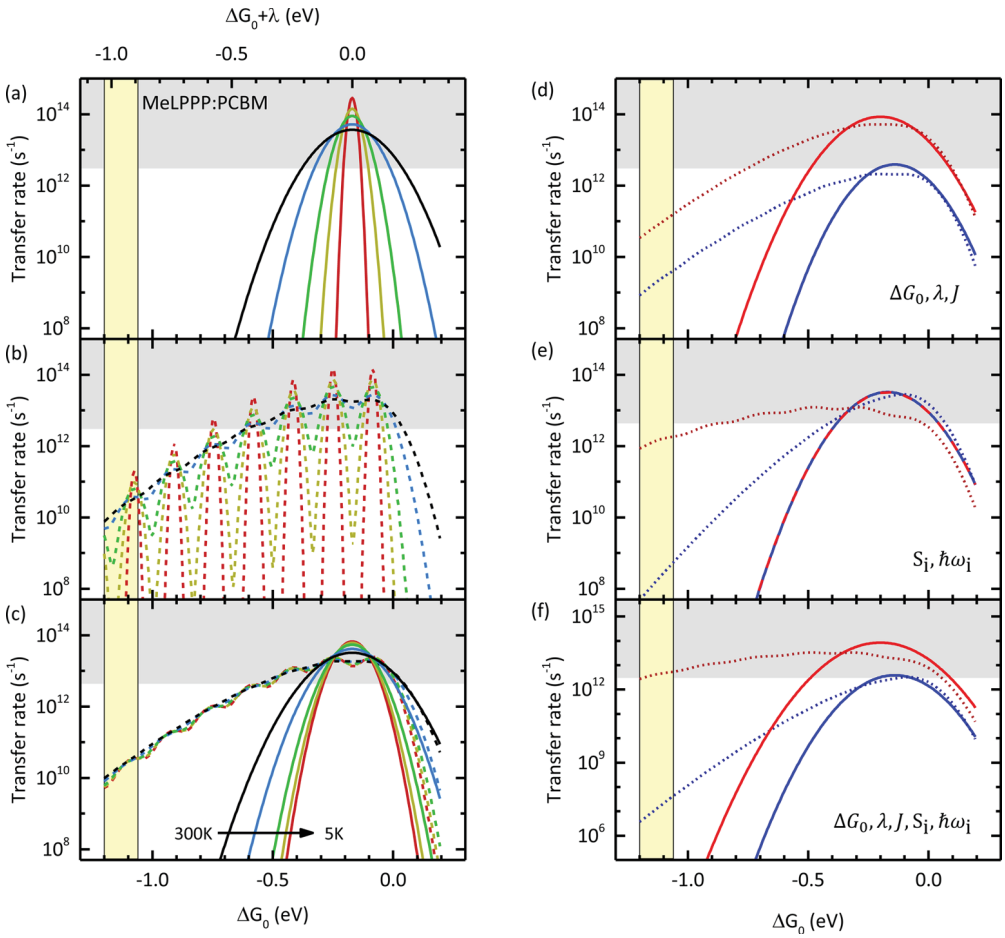

Figure 8. Electron transfer rates for MeLPPP:PCBM calculated with λ = 0.17 eV and J_{DA} = 30 meV for different temperatures (300, 150, 50, 20, and 5 K). The gray shaded area indicates values that are beyond our instrumental resolution. The yellow shaded area indicates the parameter range for the driving force. (a) Using Marcus theory (eq 1), (b) using MLJ theory (eq 3), (c) including disorder in eq 1 (solid lines) and in eq 3 (dashed lines). (d–f) Maximizing (red lines) and minimizing (blue lines) electron transfer rates at 300 K including disorder using Marcus theory (solid lines) and MLJ theory (dotted lines) by varying (d) ΔG_0, λ, and J_{DA}, (e) S_i and $\hbar\omega_i$, and (f) all parameters.

parameter sets for PCPDTBT:PCBM and PTB7:PCBM. The resulting rates are displayed for different temperatures in the range from 300 to 5 K. Evidently, for a driving force close to zero, Marcus theory predicts a strong reduction of the transfer rate with decreasing temperature and values that are accessible with many pump–probe setups. This temperature dependence agrees with the notion one has when considering the corresponding energy levels in Figure 4. However, for driving forces close to λ, the transfer rate increases upon cooling. This is because the exponential term in eq 1 vanishes, so that the $T^{-0.5}$ dependence in the prefactor dominates. Furthermore, the rate increases to values that push the time resolution of common pump–probe setups to their limits. In Figure 7, the yellow area indicates the error range we found for the driving force ΔG_0. This illustrates how for PCPDTBT:PCBM both an increasing as well as a decreasing transfer rate upon cooling would be consistent with the experimental data. Essentially the same applies for PTB7:PCBM. It becomes further evident that, for both materials, the rate expected according to Marcus as well as its temperature dependence should exceed our experimental resolution. While this is indeed what we observe (cf. Table 2), it can neither confirm nor disprove the applicability of eq 1.

The lower limit we experimentally find by pump–probe spectroscopy for the transfer rate in PTB7:PCBM, about 2.6 × 10^{12} s^{-1}, is at variance with the transfer rate of 8 × 10^{11} s^{-1} reported by Ward et al. on the basis of photoluminescence quenching experiments.[9] The latter value would have been well within our experimental range. Ward et al. find their value can be fitted with Marcus theory, using values of λ = 0.4 eV and ΔG_0 = −0.2 eV. From their data, we calculate a corresponding coupling strength J_{DA} of 9 meV. While their reorganization energy and driving force are close to the ones we found of λ = 0.35 ± 0.05 eV and ΔG_0 = −0.32 ± 0.07 eV, their required electronic coupling is low compared to the value range of J_{DA} = 0.03 ± 0.02 eV that is reported in other publications.[45,55]

In summary, while PCPDTBT and PTB7 are donor materials which are widely used for solar cells and have values for ΔG_0 and λ that are typical for the low bandgap polymer/fullerene couples used in solar cells, they are not suitable to assess the validity of the Marcus approach in thin films as well as similar donor–acceptor systems. The reason for this lies in the fact that ΔG_0 and λ are approximately of equal magnitude yet opposite sign, so that the resulting rate may rise, remain constant, or decrease with decreasing temperature, depending sensitively on whether the two parameters sum up to the positive or negative side of zero. In addition, for a moderate coupling strength of J_{DA} = 30 meV, the resulting transfer times are below 100 fs, thus rendering detection difficult. From Figure 7, it is also evident that the applicability of Marcus

DOI: 10.1021/acs.jpcc.7b09213
J. Phys. Chem. C 2017, 121, 22739–22752

theory may be probed more reliably for donor−acceptor systems that have a driving force close to zero, as has been reported for some blends made with nonfullerene acceptors.[10,11] There, slower transfer rates, in particular upon cooling, can be expected if Marcus theory applies.

4.2. Electron Transfer in the Marcus Inverted Regime. We now turn to the material system with a more significant difference between ΔG_0 and λ, that is MeLPPP combined with PCBM. We compare the values expected on the basis of Marcus theory against the experimental value. Figure 8a shows the transfer rates calculated using eq 1 for the values given in Table 1, with the yellow shaded area indicating the error range of ΔG_0. Evidently, for MeLPPP:PCBM, the transfer should be very slow, at most near 10^{-2} s^{-1} (see Figure 6 and Table S2 in the Supporting Information). However, from solar cell measurements, we know that the transfer actually occurs with a finite yield.[63] Furthermore, if the transfer occurred indeed on a long time scale, we should see some signal at negative delay times from the previous pulse, as the laser repetition rate is 100 kHz. This is not the case (see Figure 3). Rather, we observe that the signal for MeLPPP appears within the rise-time of the laser. Therefore, we conclude that the electron transfer is indeed many orders of magnitude faster than what classical Marcus theory would predict (see also Table 2).

This can be understood when considering Figure 4. For MeLPPP, the driving force is more than 6 times larger than the reorganization energy. Thus, the system is well into the so-called Marcus inverted regime. Under such conditions, the probability of tunneling from the D*A to the D^+A^- potential energy surface can become significant.[64,65] This tunneling process is taken into account in the extension of Marcus theory by Marcus, Levich, and Jortner (MLJ). We have therefore considered whether our results are consistent with the MLJ equation[43]

$$k_{LJ}(T) = \frac{|J_{DA}|^2}{\hbar}\sqrt{\frac{\pi}{\lambda_o k_B T}}\sum_{\nu=0}^{\infty}\frac{e^{-S_i}S_i^{\nu}}{\nu!} \times \exp\left[-\frac{(\Delta G_0 + \lambda_o + \nu\hbar\omega_i)^2}{4\lambda_o k_B T}\right] \quad (3)$$

In this approach, one differentiates between the high-frequency intramolecular vibrations $\hbar\omega_i$, for which $\hbar\omega_i \gg k_B T$, and the low-frequency, environmental phonons with $\hbar\omega_o \ll k_B T$. We adopt the subscripts i and o to differentiate the inner (=intramolecular) and outer (=environmental) contributions. While the contributions of the intramolecular vibrations are explicitly included with their associated Huang−Rhys parameter S_i, the influence of the surrounding medium is incorporated through the reorganization energy λ_o.

Figure 8b shows the rates calculated by eq 3 assuming a mean vibrational energy of $\hbar\omega_i$ = 165 meV for donor and acceptor, a Huang−Rhys parameter S_i of 1, and an estimated outer reorganization energy $\lambda_o \approx 0.5\lambda \approx 0.09$ meV. Estimating the outer reorganization energy is not trivial.[65,66] Theoretical calculations for similar systems show that this estimate gives reasonable results.[28] The dependence of eq 3 on these parameters will be discussed further below. Two features are noteworthy. First, the dependence of the transfer rates on the driving force ΔG_0 is significantly reduced compared to Figure 8a. Second, there is a resonance (of 165 meV) on the energy dependence of the rate with a narrowing line width at lower temperatures. Thus, at lower temperatures, the transfer rate would be very sensitive to small energy variations. Furthermore, there would be a temperature dependence of the transfer rates, in contrast to what we experimentally observe (see Figure 3), unless by chance a stationary point on the curve is hit.

So far, we have neglected that there is some statistical energetic disorder in the sample, so that ΔG_0 may feature a statistical distribution. We have therefore considered how the rates obtained by eqs 1 and 3 change if we allow for a statistical variation in ΔG_0. We implemented disorder by convoluting eqs 1 and 3 below with a Gaussian disorder distribution $g(\epsilon) = \frac{1}{\sqrt{2\pi}\sigma}\exp\left(-\frac{\epsilon^2}{2\sigma^2}\right)$ with a width of σ = 50 meV according to

$$k(T) = \int_{-\infty}^{\infty}\frac{|J_{DA}|^2}{\hbar}\sqrt{\frac{\pi}{\lambda k_B T}}\exp\left[-\frac{(\lambda + \Delta G_0 - \epsilon)^2}{4\lambda k_B T}\right] \times\frac{1}{\sqrt{2\pi}\sigma}\exp\left[-\frac{\epsilon^2}{2\sigma^2}\right]d\epsilon \quad (4)$$

for eq 1 and a corresponding expression for eq 3. This results in

$$k(T) = \frac{|J_{DA}|^2}{\hbar}\sqrt{\frac{2\pi}{2\lambda k_B T + \sigma^2}}\exp\left[-\frac{(\lambda + \Delta G_0)^2}{4\lambda k_B T + 2\sigma^2}\right] \quad (5)$$

for eq 1 and an analogous expression for eq 3. This procedure corresponds to considering the statistical mean over many individual single electron transfer events that differ slightly in ΔG_0. In passing, we note that this differs in nature from considering a sequence of electron transfer rates at thermal equilibrium in a Gaussian density of states, where a different expression results for the ensemble average as detailed in refs 18−20. As can be seen in Figure 8c, energetic disorder results in a weaker temperature dependence of the Marcus-based transfer rates at lower temperatures (eq 1). For the MLJ-based transfer rates (eq 3), the inclusion of disorder first smears out the oscillatory dependence of k on ΔG_0, and second, it removes the temperature dependence almost entirely, consistent with our experimental findings. From this first evaluation, it seems that a MLJ-type approach that includes the effects of statistical disorder seems more appropriate to account for the experimental rate.

We now consider how the MLJ rates at room temperature depend on the choice of input parameters. The curves in Figure 8a−c were obtained using the mean values in Table 1 for ΔG_0 and λ, as well as an effective vibrational frequency $\hbar\omega_i$ of 165 meV with S_i = 1, and the approximation of $\lambda_o \approx 0.5\lambda$. Changing the values of the reorganization energy λ, driving force ΔG_0, and coupling strength J_{DA} to the maximum and minimum values in Table 1 shifts both the MLJ rates and the Marcus rates on the ordinate and abscissa yet causes only very minor changes in the slope of the curves (Figure 8d). In contrast, considering a different vibrational energy and vibrational coupling by varying $\hbar\omega_i$ from 150 to 200 meV and S_i from 0.5 to 2 modifies the dependence of the MLJ rate on the driving force (Figure 8e). Both the slope and the ΔG_0 value for which the MLJ rate is at maximum are modified. In particular, the slope is rather sensitive to the value of S_i, so that an increase in S_i leads to high transfer rates in the Marcus inverted regime. The reason for this is that the dissipation of the excess energy between the S_1 and the CT state is enhanced for larger vibrational energies and stronger coupling to the vibrations, which increases the electron transfer rate. This is akin to the energy gap law for nonradiative

DOI: 10.1021/acs.jpcc.7b09213
J. Phys. Chem. C 2017, 121, 22739−22752

decay.[67,68] The maximum range of transfer rates that is consistent with the most fortunate or unfortunate combination of input parameters is shown in Figure 8f. When considering Figure 8d–f, one can see that the measured transfer rate for the MeLPPP:PCBM system is consistent with MLJ theory, provided that the vibrational dissipation of energy is not too weak, i.e., $S_i \geq 1$, and disorder is included. We recall that the yellow bar in Figure 8 indicates the ΔG_0 range for the MeLPPP:PCBM system, and that we found the electron transfer to occur with a rate that exceeds 4×10^{12} s^{-1}. It is somewhat disconcerting that such a fast rate is only in agreement with the MLJ rate if all parameters combine in the most advantageous way within their error range, and we furthermore take $S_i = 1$. This is larger than the effective Huang–Rhys parameter observed in the absorption or emission spectra of MeLPPP, which is around 0.6.[69,70] This suggests that there may be further contributions that facilitate such a fast rate, such as particularly strong electronic or vibrational coupling between the photoexcited, initial S_1 state and the charge separated, final CT state.[21,22,29,71,72] Another contribution could be ultrafast hole transfer from photoexcited PCBM molecules, as their absorbance at the pump energy (3.1 eV) is in a similar range to that of MeLPPP. Fullerenes have a tightly bound S_1 state at about 1.7 eV, as well as a sequence of charge-transfer states from about 2.3 eV onward.[73] After absorption at 3.1 eV, fast internal conversion will occur within the manifold of CT states down to 2.3 eV, or even down to the Frenkel-type 1.7 eV state. If hole transfer takes place from the more delocalized interfullerene charge transfer state at 2.3 eV, the associated driving force is approximately 0.7 eV (see the Supporting Information). While this is well in the Marcus inverted regime, an ultrafast transfer is reasonable within the boundaries predicted by the MLJ equation, as evident by considering the upper and lower limits for the transfer rates in Figure 8f. Alternatively, hole transfer could occur from the 1.7 eV state, where the driving force of 0.1–0.2 eV is rather low, so that an ultrafast transfer is even compatible with a Marcus-type process.

It is therefore instructive to consider other systems such as P3HT:PCBM, where both electron and hole transfer are reported to occur on ultrafast time scales (50 fs for electron transfer[21] and less than 250 fs for hole transfer[74]), although these processes are well in the Marcus inverted regime, as detailed in the Supporting Information, implying that these fast processes cannot be described by Marcus theory. Figure 9 shows the dependence of the transfer rate for electron and hole transfer for P3HT:PCBM calculated according to the Marcus and Marcus–Levich–Jortner equations. The effect of disorder is already implemented, as described above with $\sigma = 75$ meV, and we used $J_{DA} = 0.02$ eV, $\lambda_o = 0.27$ eV, $S_i = 1$, and $\hbar\omega_i = 180$ meV as detailed in the Supporting Information.

Regarding the temperature dependence of the electron transfer, we did not observe any significant reduction for the rate of electron transfer from MeLPPP to PCBM upon cooling. This is in good agreement with a description in the framework of the MLJ theory for a disordered system. The use of the MLJ theory is required for the MeLPPP:PCBM system, as its large driving force places this donor–acceptor couple well into the Marcus inverted regime. Regarding the low-bandgap donors PCPDTBT and PTB7 with the acceptor PCBM, all three cases of an accelerating, constant, and decreasing rate with temperature are, in principle, compatible with Marcus theory and the range of experimentally determined input parameters.

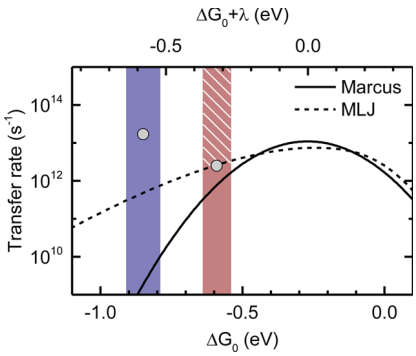

Figure 9. Calculated transfer rates for P3HT:PCBM in the framework of Marcus theory (solid line) and MLJ (dased line). The boxes indicate the driving force for electron transfer (blue) and hole transfer (red). The gray dots indicate measured transfer rates from refs 21 and 74 in which the value for hole transfer is resolution limited (indicated by the dashed area).

If MLJ theory is applied to these materials (see Figures S1 and S2 in the Supporting Information) and a statistical energetic disorder is considered, no temperature dependence should result. Experimentally, we observed rates faster than our detection limit, which is consistent with theoretical expectations.

5. DISCUSSION

5.1. The Role of the Driving Force, Based on Marcus and MLJ Theory. Thus, in summary, we find temperature-independent electron transfer rates in excess of 2×10^{12} s^{-1} for all three donor:fullerene blends investigated. For PCPDTBT:PCBM and PTB7:PCBM, this experimental lower limit is consistent with the values that can be expected mathematically from Marcus theory on the basis of the input parameters. However, as shall be discussed in detail below, this fast rate renders the applicability of Marcus theory (as well as MLJ theory) itself questionable. However, for MeLPPP:PCBM, the experimentally observed lower limit for the transfer rate cannot be accounted for by Marcus theory. It can be reconciled with the value expected from Marcus–Levich–Jortner theory, which considers tunneling from the S_1 state to the CT-state surface followed by dissipation of energy through coupling to high-frequency vibrations. Numerically, the experimental rate just about agrees with the value predicted by MLJ theory provided that the errors of all input parameters combine most fortunately and a strong vibrational coupling is assumed. Alternatively, ultrafast hole transfer from PCBM to MeLPPP could account for the experimental data, in agreement with MLJ theory if the transfer takes place from a more delocalized CT state on the fullerene, or in numerical agreement with Marcus theory if the hole transfers from the S_1 of the PCBM. Therefore, we finally considered the P3HT:PCBM system, where the reported values for electron transfer disagree with both Marcus or MLJ theory. Hole transfer can also not be reconciled with Marcus theory yet can just about be brought in numerical agreement with rates predicted by MLJ theory.

These results raise two issues. First, if we presume that the mixed classical/quantum-chemical description by Marcus, Levich, and Jortner is a suitable framework to describe the electron transfer in thin donor–acceptor blend films, what could be concluded regarding the importance of the driving force? Second, do the fast rates that we observed, and that have been observed by many others for similar systems

DOI: 10.1021/acs.jpcc.7b09213
J. Phys. Chem. C 2017, 121, 22739–22752

before,[10,21,35,75−77] actually allow for a description as a nonadiabatic transfer? We shall address these questions in sequence.

Figure 10 shows how the electron transfer rates evolve with driving force for a MLJ equation and, for comparison, a Marcus

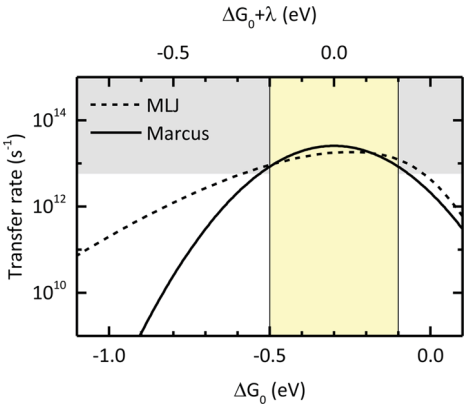

Figure 10. Electron transfer rates for eq 1 (Marcus) and eq 3 (MLJ) for PCPDTBT:PCBM with energetic disorder using J_{DA} = 30 meV, λ = 0.3 eV, S_i = 1, $\hbar\omega_i$ = 165 meV, and σ = 50 meV. The gray shaded area indicates values that are beyond our instrumental resolution. The yellow shaded area indicates the parameter range for the driving force.

equation. We include disorder and take a typical value of 0.3 eV for the reorganization energy λ in donor polymer:fullerene systems. For donor−acceptor combinations, a typical driving force ΔG_0 is in the range from −0.1 to −0.5 eV, indicated by yellow shading in Figure 10. Larger values are not common, as they compromise the open circuit voltage.[7,8] It is evident that (i) $\Delta G_0 \approx -\lambda$, (ii) the transfer rate is only weakly dependent on ΔG_0, and (iii) it occurs faster than 10^{13} s^{-1}. How does this impact the efficiency of electron transfer? The efficiency of electron transfer from the photoexcited donor can be calculated as $\phi_{ET} = k_{ET}/(k_{ET} + \tau_S^{-1})$, with τ_S being the lifetime of the photoexcited donor in the absence of the acceptor. If we take 0.5 ns to be a typical lifetime for a S_1 state in the donor, we find that electron transfer occurs with essentially 99.98% efficiency for $k_{ET} = 10^{13}$ s^{-1}, i.e., for any ΔG_0 in the range from −0.1 to −0.5 eV. For driving forces exceeding −0.6 eV, i.e., 2λ, the dependence of the forward transfer rate on ΔG_0 is still weak to moderate due to the fairly flat slope of the MLJ curve. Even for an electron transfer rate of 10^{11} s^{-1}, obtained with the MLJ curve for ΔG_0 = −1 eV, the resulting electron transfer efficiency is still 83%. Thus, on the basis of a MLJ equation, *the driving force is irrelevant for the forward electron transfer from donor to acceptor* which occurs with virtually 100% efficiency for ΔG_0 in the range from −0.1 to −0.5 eV.

This conclusion appears to be at variance with some experimental results indicating that the yield of photogeneration does depend on driving force and is—at least qualitatively—in agreement with Marcus theory.[8,27] This paradox is solved by considering that the overall yield of photogeneration is the product of the primary yield of the formation of the CT state and the yield of its subsequent dissociation into free charges. The latter is controlled by the competition between CT separation and loss. The loss rate may include several pathways, such as direct radiative or nonradiative recombination to the ground state,[78,79] recombination via an intermediate triplet state,[80,81] or back transfer to the initial singlet state.[82] The yield of CT separation is then determined by the trade-off between the processes of endothermic escape and exothermic geminate recombination, which both can depend on the released excess energies but in a counteracting way. For example, when comparing the transfer from one donor to different acceptors, an increase in ΔG_0 implies a reduction of the CT state energy and concomitantly a higher nonradiative decay rate from the CT state.[79] On the other hand, a large ΔG_0 can be of advantage for the escape from the CT state. It has been suggested that this allows for the generation of (vibrationally cold) states at the top of the disorder-controlled density of CT states, with associated high initial electron/hole mobility that have a faster rate of CT state dissociation.[83] *As a result of these competing processes, there can seem to be an apparent optimal driving force that is, however, not related to the actual charge transfer rate from the photoexcited donor to the acceptor* and a description in terms of Marcus theory.

5.2. Implications of Fast Transfer Rates Regarding Marcus and MLJ Theory. We now turn to the second issue, the implications of the fast transfer rate. Both the Marcus and MLJ equations consider a nonadiabatic electron transfer; i.e., the frequency of vibrations is fast compared to the time required for the electron transfer.[84] Essentially, this corresponds to the requirement that thermal equilibrium is established. At room temperature, low energy vibrations can be easily excited, e.g., with a thermal energy of 26 meV. This energy corresponds to a vibrational frequency of about 6.3 × 10^{12} Hz, implying that a time well in excess of $(6.3 \times 10^{12}$ Hz$)^{-1}$ = 160 fs is required for nonadiabatic electron transfer. At lower temperatures, this time increases accordingly. Processes with transfer times shorter than a few 100 fs (i.e., rates larger than 10^{12}−10^{13} s^{-1}) are therefore not suitably described by a Marcus or Marcus−Levich−Jortner type picture. In fact, donor−acceptor systems where Marcus theory was experimentally confirmed to apply had electron transfer rates in the range 10^6−10^{10} s^{-1}.[14] These were donor and acceptor couples separated by a spacer and measured in solution. The donor−acceptor couples investigated here are neither separated by a spacer nor measured in solution, where the outer reorganization energy can be significant. Rather, our samples are in a solid film, which reduces external reorganization effects. In all cases, including the P3HT:PCBM system, the transfer rates were experimentally found in excess of 3 × 10^{12} s^{-1}.

This is at variance with the value of 8 × 10^{11} s^{-1} reported by Ward et al. for the PTB7:PCBM system,[9] yet it agrees with frequent literature reports that electron transfer in thin film conjugated polymer:fullerene systems frequently occurs in less than a couple of hundred femtoseconds.[35,76,85,86]

Thus, even if these transfer rates may, for example, be numerically consistent with nonadiabatic electron transfer rates such as those by Marcus or MLJ, the thermal equilibrium which is presumed in deriving these expressions cannot be established on the fast time scales that are observed. Consequently, it is necessary to look beyond such descriptions and to apply models that include adiabatic and coherent mechanisms of electron transfer.[21−23,76,86−88] On these short time scales, coupling to nuclear motion is an essential part to the description of electron transfer in solid state donor−acceptor blends.[21] Similarly, the delocalization of the electron wave function over the acceptor molecules and the associated density of accepting states become crucial.[86−88] That density of states can also depend on the morphology of the donor−acceptor blend. The importance of high intermolecular coupling and

DOI: 10.1021/acs.jpcc.7b09213
J. Phys. Chem. C 2017, 121, 22739−22752

charge delocalization has recently been highlighted by Jakowetz et al. in experiments involving pump−push−probe spectroscopy.[76] Also, suitable quantum chemical approaches are being developed in contemporary theoretical work.[21−23]

CONCLUSION

In summary, we have shown that forward charge transfer from donor to acceptor occurs at time scales below 250 fs for PCPDTBT, PTB7, and MeLPPP blended with PCBM, even though the temperature range was varied from 300 to 12 K and the driving force ranges from −0.2 to −1.1 eV. This corresponds to the regimes from $\Delta G_0 \approx -\lambda$, where Marcus-type electron transfer rates are at maximum to the Marcus-inverted regime $\Delta G_0 \approx -6.5\lambda$. At such fast time scales, the efficiency of electron transfer exceeds 99.9%, presuming a lifetime of the donor singlet state of about 500 ps. By carefully considering the experimentally determined range of input parameters to eqs 1 and 3, we find that (i) these transfer rates can be *numerically* consistent with Marcus theory for PCPDTBT:PCBM and PTB7:PCBM, even at low temperatures. In contrast, for MeLPPP:PCBM, tunneling and coupling to vibrations would need to be included explicitly by MLJ theory. An analysis of values reported for P3HT:PCBM confirms this further. (ii) For realistic input parameters, ΔG_0 has no significant impact on the rate or efficiency of electron transfer from the photoexcited donor to the cold CT state. Overall, however, we note that, at such short time scales, theoretical approaches beyond the nonadiabatic transfer are required.

Our findings suggest that the most promising strategy for the design of efficient solar cells may be to accept a low driving force in favor of optimizing the open-circuit voltage, and then to aim at enhancing the subsequent charge separation rate from the relaxed CT state. Approaches for that include optimizing the packing between the acceptor or donor molecules so as to enhance interchromophore coupling, charge delocalization, and charge mobility as well as reducing the reorganization energy.[66,72,73,76,89]

ASSOCIATED CONTENT

Supporting Information

The Supporting Information is available free of charge on the ACS Publications website at DOI: 10.1021/acs.jpcc.7b09213.

(i) A detailed discussion of input parameters for evaluation of eqs 1 and 3, (ii) an extension of Table 2 including maximum and minimum calculated transfer rates, (iii) additional figures comparing transfer rates using eqs 1 and 3 for PCPDTBT:PCBM and PTB7:PCBM, (iv) an evaluation of transfer rates for hole transfer in the MeLPPP:PCBM system, and for both electron and hole transfer in the P3HT:PCBM system, and (v) reorganization energy and CT state energy for PCPDTBT:PCBM (PDF)

AUTHOR INFORMATION

Corresponding Author

*E-mail: Anna.Koehler@uni-bayreuth.de.

ORCID

Anna Köhler: 0000-0001-5029-4420

Author Contributions

‖T.U., S.W.: Both authors contributed equally.

Notes

The authors declare no competing financial interest.

ACKNOWLEDGMENTS

We are grateful to Stavros Athanasopoulos for helpful discussions and suggestions. We further thank Dieter Neher and his research group for providing the reorganization energy and CT state energy for PCPDTBT:PCBM, shown as Figure S3 in the Supporting Information. Financial support is acknowledged from the Deutsche Forschungsgemeinschaft through GRK1640 (Photophysics of Synthetic and Biological Multichromophoric Systems), from the Marie-Curie Innovative Training Network (ITN) INFORM, and from the Bayerisches Staatsministerium für Bildung und Kultus, Wissenschaft und Kunst through the grant "Solar Technologies go Hybrid" as well as the program "MINT-Lehramt plus".

REFERENCES

(1) Bässler, H.; Köhler, A. "Hot or Cold": How Do Charge Transfer States at the Donor-Acceptor Interface of an Organic Solar Cell Dissociate? *Phys. Chem. Chem. Phys.* **2015**, *17*, 28451−28462.

(2) Albrecht, S.; Vandewal, K.; Tumbleston, J. R.; Fischer, F. S.; Douglas, J. D.; Frechet, J. M.; Ludwigs, S.; Ade, H.; Salleo, A.; Neher, D. On the Efficiency of Charge Transfer State Splitting in Polymer:Fullerene Solar Cells. *Adv. Mater.* **2014**, *26*, 2533−2539.

(3) Deibel, C.; Strobel, T.; Dyakonov, V. Role of the Charge Transfer State in Organic Donor−Acceptor Solar Cells. *Adv. Mater.* **2010**, *22*, 4097−4111.

(4) Hood, S. N.; Kassal, I. Entropy and Disorder Enable Charge Separation in Organic Solar Cells. *J. Phys. Chem. Lett.* **2016**, *7*, 4495−4500.

(5) Shoaee, S.; Clarke, T. M.; Huang, C.; Barlow, S.; Marder, S. R.; Heeney, M.; McCulloch, I.; Durrant, J. R. Acceptor Energy Level Control of Charge Photogeneration in Organic Donor/Acceptor Blends. *J. Am. Chem. Soc.* **2010**, *132*, 12919−12926.

(6) Pensack, R. D.; Asbury, J. B. Barrierless Free Carrier Formation in an Organic Photovoltaic Material Measured with Ultrafast Vibrational Spectroscopy. *J. Am. Chem. Soc.* **2009**, *131*, 15986−15987.

(7) Veldman, D.; Meskers, S. C. J.; Janssen, R. A. J. The Energy of Charge-Transfer States in Electron Donor-Acceptor Blends: Insight into the Energy Losses in Organic Solar Cells. *Adv. Funct. Mater.* **2009**, *19*, 1939−1948.

(8) Hendriks, K. H.; Wijpkema, A. S.; van Franeker, J. J.; Wienk, M. M.; Janssen, R. A. Dichotomous Role of Exciting the Donor or the Acceptor on Charge Generation in Organic Solar Cells. *J. Am. Chem. Soc.* **2016**, *138*, 10026−10031.

(9) Ward, A. J.; Ruseckas, A.; Kareem, M. M.; Ebenhoch, B.; Serrano, L. A.; Al-Eid, M.; Fitzpatrick, B.; Rotello, V. M.; Cooke, G.; Samuel, I. D. W. The Impact of Driving Force on Electron Transfer Rates in Photovoltaic Donor-Acceptor Blends. *Adv. Mater.* **2015**, *27*, 2496−2500.

(10) Liu, J.; Chen, S.; Qian, D.; Gautam, B.; Yang, G.; Zhao, J.; Bergqvist, J.; Zhang, F.; Ma, W.; Ade, H.; et al. Fast Charge Separation in a Non-Fullerene Organic Solar Cell with a Small Driving Force. *Nat. Energy* **2016**, *1*, 16089.

(11) Kawashima, K.; Tamai, Y.; Ohkita, H.; Osaka, I.; Takimiya, K. High-Efficiency Polymer Solar Cells with Small Photon Energy Loss. *Nat. Commun.* **2015**, *6*, 10085.

(12) Marcus, R. A.; Sutin, N. Electron Transfers in Chemistry and Biology. *Biochim. Biophys. Acta, Rev. Bioenerg.* **1985**, *811*, 265−322.

(13) Marcus, R. A. Exchange Reactions and Electron Transfer Reactions Including Isotopic Exchange. Theory of Oxidation-Reduction Reactions Involving Electron Transfer. Part 4.-a Statistical-Mechanical Basis for Treating Contributions from Solvent, Ligands, and Inert Salt. *Discuss. Faraday Soc.* **1960**, *29*, 21−31.

(14) Miller, J. R.; Calcaterra, L. T.; Closs, G. L. Intramolecular Long-Distance Electron Transfer in Radical Anions. The Effects of Free

Energy and Solvent on the Reaction Rates. *J. Am. Chem. Soc.* **1984**, *106*, 3047−3049.
(15) Hoffmann, S. T.; Athanasopoulos, S.; Beljonne, D.; Bässler, H.; Köhler, A. How Do Triplets and Charges Move in Disordered Organic Semiconductors? A Monte Carlo Study Comprising the Equilibrium and Nonequilibrium Regime. *J. Phys. Chem. C* **2012**, *116*, 16371−16383.
(16) Bässler, H.; Köhler, A. Charge Transport in Organic Semiconductors. In *Unimolecular and Supramolecular Electronics I: Chemistry and Physics Meet at Metal-Molecule Interfaces*; Metzger, R. M., Ed.; Springer: Berlin, Heidelberg, 2012; pp 1−65.
(17) Köhler, A.; Bässler, H. Electronic and Optical Processes of Organic Semiconductors. *Electronic Processes in Organic Semiconductors*; Wiley-VCH: Weinheim, Germany, 2015; pp 193−305.
(18) Fishchuk, I. I.; Kadashchuk, A.; Hoffmann, S. T.; Athanasopoulos, S.; Genoe, J.; Bässler, H.; Köhler, A. Unified Description for Hopping Transport in Organic Semiconductors Including Both Energetic Disorder and Polaronic Contributions. *Phys. Rev. B: Condens. Matter Mater. Phys.* **2013**, *88*, 125202.
(19) Fishchuk, I. I.; Kadashchuk, A.; Sudha Devi, L.; Heremans, P.; Bässler, H.; Köhler, A. Triplet Energy Transfer in Conjugated Polymers. Ii. A Polaron Theory Description Addressing the Influence of Disorder. *Phys. Rev. B: Condens. Matter Mater. Phys.* **2008**, *78*, 045211.
(20) Sudha Devi, L.; Al-Suti, M. K.; Dosche, C.; Khan, M. S.; Friend, R. H.; Köhler, A. Triplet Energy Transfer in Conjugated Polymers. I. Experimental Investigation of a Weakly Disordered Compound. *Phys. Rev. B: Condens. Matter Mater. Phys.* **2008**, *78*, 045210.
(21) Falke, S. M.; Rozzi, C. A.; Brida, D.; Maiuri, M.; Amato, M.; Sommer, E.; De Sio, A.; Rubio, A.; Cerullo, G.; Molinari, E.; et al. Coherent Ultrafast Charge Transfer in an Organic Photovoltaic Blend. *Science* **2014**, *344*, 1001−1005.
(22) Bredas, J.-L.; Sargent, E. H.; Scholes, G. D. Photovoltaic Concepts Inspired by Coherence Effects in Photosynthetic Systems. *Nat. Mater.* **2016**, *16*, 35−44.
(23) Bittner, E. R.; Silva, C. Noise-Induced Quantum Coherence Drives Photo-Carrier Generation Dynamics at Polymeric Semiconductor Heterojunctions. *Nat. Commun.* **2014**, *5*, 3119.
(24) Tamura, H.; Burghardt, I. Potential Barrier and Excess Energy for Electron−Hole Separation from the Charge-Transfer Exciton at Donor−Acceptor Heterojunctions of Organic Solar Cells. *J. Phys. Chem. C* **2013**, *117*, 15020−15025.
(25) Tamura, H.; Burghardt, I.; Tsukada, M. Exciton Dissociation at Thiophene/Fullerene Interfaces: The Electronic Structures and Quantum Dynamics. *J. Phys. Chem. C* **2011**, *115*, 10205−10210.
(26) Tamura, H.; Martinazzo, R.; Ruckenbauer, M.; Burghardt, I. Quantum Dynamics of Ultrafast Charge Transfer at an Oligothiophene-Fullerene Heterojunction. *J. Chem. Phys.* **2012**, *137*, 22A540.
(27) Coffey, D. C.; Larson, B. W.; Hains, A. W.; Whitaker, J. B.; Kopidakis, N.; Boltalina, O. V.; Strauss, S. H.; Rumbles, G. An Optimal Driving Force for Converting Excitons into Free Carriers in Excitonic Solar Cells. *J. Phys. Chem. C* **2012**, *116*, 8916−8923.
(28) Liu, T.; Troisi, A. Absolute Rate of Charge Separation and Recombination in a Molecular Model of the P3ht/Pcbm Interface. *J. Phys. Chem. C* **2011**, *115*, 2406−2415.
(29) Savoie, B. M.; Rao, A.; Bakulin, A. A.; Gelinas, S.; Movaghar, B.; Friend, R. H.; Marks, T. J.; Ratner, M. A. Unequal Partnership: Asymmetric Roles of Polymeric Donor and Fullerene Acceptor in Generating Free Charge. *J. Am. Chem. Soc.* **2014**, *136*, 2876−2884.
(30) Peet, J.; Kim, J. Y.; Coates, N. E.; Ma, W. L.; Moses, D.; Heeger, A. J.; Bazan, G. C. Efficiency Enhancement in Low-Bandgap Polymer Solar Cells by Processing with Alkane Dithiols. *Nat. Mater.* **2007**, *6*, 497−500.
(31) Boland, P.; Lee, K.; Namkoong, G. Device Optimization in Pcpdtbt:Pcbm Plastic Solar Cells. *Sol. Energy Mater. Sol. Cells* **2010**, *94*, 915−920.
(32) Scherf, U.; Müllen, K. Polyarylenes and Poly(Arylenevinylenes), 7. A Soluble Ladder Polymer Via Bridging of Functionalized Poly(P-Phenylene)-Precursors. *Makromol. Chem., Rapid Commun.* **1991**, *12*, 489−497.
(33) Scherf, U.; Bohnen, A.; Müllen, K. Polyarylenes and Poly(Arylenevinylene)S, 9 the Oxidized States of a (1,4-Phenylene) Ladder Polymer. *Makromol. Chem.* **1992**, *193*, 1127−1133.
(34) Vandewal, K.; Tvingstedt, K.; Gadisa, A.; Inganäs, O.; Manca, J. V. Relating the Open-Circuit Voltage to Interface Molecular Properties of Donor:Acceptor Bulk Heterojunction Solar Cells. *Phys. Rev. B: Condens. Matter Mater. Phys.* **2010**, *81*, 125204.
(35) Grancini, G.; Maiuri, M.; Fazzi, D.; Petrozza, A.; Egelhaaf, H. J.; Brida, D.; Cerullo, G.; Lanzani, G. Hot Exciton Dissociation in Polymer Solar Cells. *Nat. Mater.* **2012**, *12*, 29−33.
(36) Szarko, J. M.; Rolczynski, B. S.; Lou, S. J.; Xu, T.; Strzalka, J.; Marks, T. J.; Yu, L.; Chen, L. X. Photovoltaic Function and Exciton/Charge Transfer Dynamics in a Highly Efficient Semiconducting Copolymer. *Adv. Funct. Mater.* **2014**, *24*, 10−26.
(37) Etzold, F.; Howard, I. A.; Forler, N.; Cho, D. M.; Meister, M.; Mangold, H.; Shu, J.; Hansen, M. R.; Müllen, K.; Laquai, F. The Effect of Solvent Additives on Morphology and Excited-State Dynamics in Pcpdtbt:Pcbm Photovoltaic Blends. *J. Am. Chem. Soc.* **2012**, *134*, 10569−10583.
(38) Müller, J. G.; Lupton, J. M.; Feldmann, J.; Lemmer, U.; Scharber, M. C.; Sariciftci, N. S.; Brabec, C. J.; Scherf, U. Ultrafast Dynamics of Charge Carrier Photogeneration and Geminate Recombination in Conjugated Polymer:Fullerene Solar Cells. *Phys. Rev. B: Condens. Matter Mater. Phys.* **2005**, *72*, 195208.
(39) Wohlgenannt, M.; Jiang, X. M.; Vardeny, Z. V. Spin-Dependent Exciton Formation Rates in Π-Conjugated Oligomers and Polymers. Synth. *Synth. Met.* **2003**, *137*, 1069−1071.
(40) Luzzati, S.; Scharber, M.; Catellani, M.; Giacalone, F.; Segura, J. L.; Martin, N.; Neugebauer, H.; Sariciftci, N. S. Long-Lived Photoinduced Charges in Donor−Acceptor Anthraquinone-Substituted Thiophene Copolymers. *J. Phys. Chem. B* **2006**, *110*, 5351−5358.
(41) Marcus, R. A. Electron Transfer Reactions in Chemistry. Theory and Experiment. *Rev. Mod. Phys.* **1993**, *65*, 599−610.
(42) Kestner, N. R.; Logan, J.; Jortner, J. Thermal Electron Transfer Reactions in Polar Solvents. *J. Phys. Chem.* **1974**, *78*, 2148−2166.
(43) Jortner, J. Temperature Dependent Activation Energy for Electron Transfer between Biological Molecules. *J. Chem. Phys.* **1976**, *64*, 4860−4867.
(44) Dennler, G.; Scharber, M. C.; Brabec, C. J. Polymer-Fullerene Bulk-Heterojunction Solar Cells. *Adv. Mater.* **2009**, *21*, 1323−1338.
(45) Leng, C.; Qin, H.; Si, Y.; Zhao, Y. Theoretical Prediction of the Rate Constants for Exciton Dissociation and Charge Recombination to a Triplet State in Pcpdtbt with Different Fullerene Derivatives. *J. Phys. Chem. C* **2014**, *118*, 1843−1855.
(46) Vandewal, K.; Tvingstedt, K.; Gadisa, A.; Inganas, O.; Manca, J. V. On the Origin of the Open-Circuit Voltage of Polymer-Fullerene Solar Cells. *Nat. Mater.* **2009**, *8*, 904−909.
(47) Scharsich, C.; Fischer, F. S. U.; Wilma, K.; Hildner, R.; Ludwigs, S.; Köhler, A. Revealing Structure Formation in Pcpdtbt by Optical Spectroscopy. *J. Polym. Sci., Part B: Polym. Phys.* **2015**, *53*, 1416−1430.
(48) Jarzab, D.; Cordella, F.; Gao, J.; Scharber, M.; Egelhaaf, H.-J.; Loi, M. A. Low-Temperature Behaviour of Charge Transfer Excitons in Narrow-Bandgap Polymer-Based Bulk Heterojunctions. *Adv. Energy Mater.* **2011**, *1*, 604−609.
(49) Kraus, H.; Heiber, M. C.; Vath, S.; Kern, J.; Deibel, C.; Sperlich, A.; Dyakonov, V. Analysis of Triplet Exciton Loss Pathways in Ptb7:Pc71bm Bulk Heterojunction Solar Cells. *Sci. Rep.* **2016**, *6*, 29158.
(50) Carsten, B.; Szarko, J. M.; Son, H. J.; Wang, W.; Lu, L.; He, F.; Rolczynski, B. S.; Lou, S. J.; Chen, L. X.; Yu, L. Examining the Effect of the Dipole Moment on Charge Separation in Donor-Acceptor Polymers for Organic Photovoltaic Applications. *J. Am. Chem. Soc.* **2011**, *133*, 20468−20475.
(51) Liang, Y.; Xu, Z.; Xia, J.; Tsai, S. T.; Wu, Y.; Li, G.; Ray, C.; Yu, L. For the Bright Future-Bulk Heterojunction Polymer Solar Cells with Power Conversion Efficiency of 7.4%. *Adv. Mater.* **2010**, *22*, E135−E138.

DOI: 10.1021/acs.jpcc.7b09213
J. Phys. Chem. C 2017, 121, 22739−22752

(52) Hoffmann, S. T.; Scheler, E.; Koenen, J.-M.; Forster, M.; Scherf, U.; Strohriegl, P.; Bässler, H.; Köhler, A. Triplet Energy Transfer in Conjugated Polymers. Iii. An Experimental Assessment Regarding the Influence of Disorder on Polaronic Transport. *Phys. Rev. B: Condens. Matter Mater. Phys.* **2010**, *81*, 165208.
(53) Peng, Z.; Xia, Y.; Gao, F.; Xiong, K.; Hu, Z.; James, D. I.; Chen, J.; Wang, E.; Hou, L. A Dual Ternary System for Highly Efficient Ito-Free Inverted Polymer Solar Cells. *J. Mater. Chem. A* **2015**, *3*, 18365−18371.
(54) Gerhard, M.; Arndt, A. P.; Howard, I. A.; Rahimi-Iman, A.; Lemmer, U.; Koch, M. Temperature- and Energy-Dependent Separation of Charge-Transfer States in Ptb7-Based Organic Solar Cells. *J. Phys. Chem. C* **2015**, *119*, 28309−28318.
(55) Liu, T.; Cheung, D. L.; Troisi, A. Structural Variability and Dynamics of the P3ht/Pcbm Interface and Its Effects on the Electronic Structure and the Charge-Transfer Rates in Solar Cells. *Phys. Chem. Chem. Phys.* **2011**, *13*, 21461−21470.
(56) Hoke, E. T.; Vandewal, K.; Bartelt, J. A.; Mateker, W. R.; Douglas, J. D.; Noriega, R.; Graham, K. R.; Fréchet, J. M. J.; Salleo, A.; McGehee, M. D. Recombination in Polymer:Fullerene Solar Cells with Open-Circuit Voltages Approaching and Exceeding 1.0 V. *Adv. Energy Mater.* **2013**, *3*, 220−230.
(57) Guldi, D. M.; Prato, M. Excited-State Properties of C60 Fullerene Derivatives. *Acc. Chem. Res.* **2000**, *33*, 695−703.
(58) Tasch, S.; Niko, A.; Leising, G.; Scherf, U. Highly Efficient Electroluminescence of New Wide Band Gap Ladder-Type Poly(Para-Phenylenes). *Appl. Phys. Lett.* **1996**, *68*, 1090−1092.
(59) Tvingstedt, K.; Vandewal, K.; Gadisa, A.; Zhang, F.; Manca, J.; Inganäs, O. Electroluminescence from Charge Transfer States in Polymer Solar Cells. *J. Am. Chem. Soc.* **2009**, *131*, 11819−11824.
(60) Clarke, T.; Ballantyne, A.; Jamieson, F.; Brabec, C.; Nelson, J.; Durrant, J. Transient Absorption Spectroscopy of Charge Photogeneration Yields and Lifetimes in a Low Bandgap Polymer/Fullerene Film. *Chem. Commun.* **2008**, *1*, 89−91.
(61) Faist, M. A.; Kirchartz, T.; Gong, W.; Ashraf, R. S.; McCulloch, I.; de Mello, J. C.; Ekins-Daukes, N. J.; Bradley, D. D. C.; Nelson, J. Competition between the Charge Transfer State and the Singlet States of Donor or Acceptor Limiting the Efficiency in Polymer:Fullerene Solar Cells. *J. Am. Chem. Soc.* **2012**, *134*, 685−692.
(62) He, Y.; Chen, H.-Y.; Hou, J.; Li, Y. Indene−C60 Bisadduct: A New Acceptor for High-Performance Polymer Solar Cells. *J. Am. Chem. Soc.* **2010**, *132*, 1377−1382.
(63) Arif, M.; Yang, K.; Li, L.; Yu, P.; Guha, S.; Gangopadhyay, S.; Förster, M.; Scherf, U. Harvesting Triplet Excitons for Application in Polymer Solar Cells. *Appl. Phys. Lett.* **2009**, *94*, 063307.
(64) Coropceanu, V.; Cornil, J.; da Silva Filho, D. A.; Olivier, Y.; Silbey, R.; Brédas, J.-L. Charge Transport in Organic Semiconductors. *Chem. Rev.* **2007**, *107*, 926−952.
(65) Brédas, J.-L.; Beljonne, D.; Coropceanu, V.; Cornil, J. Charge-Transfer and Energy-Transfer Processes in Π-Conjugated Oligomers and Polymers: A Molecular Picture. *Chem. Rev.* **2004**, *104*, 4971−5004.
(66) Vandewal, K.; Benduhn, J.; Schellhammer, K. S.; Vangerven, T.; Rückert, J. E.; Piersimoni, F.; Scholz, R.; Zeika, O.; Fan, Y.; Barlow, S.; et al. Absorption Tails of Donor:C60 Blends Provide Insight into Thermally Activated Charge-Transfer Processes and Polaron Relaxation. *J. Am. Chem. Soc.* **2017**, *139*, 1699−1704.
(67) Freed, K. F.; Jortner, J. Multiphonon Processes in the Nonradiative Decay of Large Molecules. *J. Chem. Phys.* **1970**, *52*, 6272−6291.
(68) Englman, R.; Jortner, J. The Energy Gap Law for Radiationless Transitions in Large Molecules. *Mol. Phys.* **1970**, *18*, 145−164.
(69) Hoffmann, S. T.; Bässler, H.; Köhler, A. What Determines Inhomogeneous Broadening of Electronic Transitions in Conjugated Polymers? *J. Phys. Chem. B* **2010**, *114*, 17037−17048.
(70) Khan, A. L. T.; Sreearunothai, P.; Herz, L. M.; Banach, M. J.; Köhler, A. Morphology-Dependent Energy Transfer within Polyfluorene Thin Films. *Phys. Rev. B: Condens. Matter Mater. Phys.* **2004**, *69*, 085201.
(71) Janković, V.; Vukmirović, N. Origin of Space-Separated Charges in Photoexcited Organic Heterojunctions on Ultrafast Time Scales. *Phys. Rev. B: Condens. Matter Mater. Phys.* **2017**, *95*, 075308.
(72) Kocherzhenko, A. A.; Lee, D.; Forsuelo, M. A.; Whaley, K. B. Coherent and Incoherent Contributions to Charge Separation in Multichromophore Systems. *J. Phys. Chem. C* **2015**, *119*, 7590−7603.
(73) Hahn, T.; Tscheuschner, S.; Saller, C.; Strohriegl, P.; Boregowda, P.; Mukhopadhyay, T.; Patil, S.; Neher, D.; Bässler, H.; Köhler, A. Role of Intrinsic Photogeneration in Single Layer and Bilayer Solar Cells with C60 and Pcbm. *J. Phys. Chem. C* **2016**, *120*, 25083−25091.
(74) Cook, S.; Katoh, R.; Furube, A. Ultrafast Studies of Charge Generation in Pcbm:P3ht Blend Films Following Excitation of the Fullerene Pcbm. *J. Phys. Chem. C* **2009**, *113*, 2547−2552.
(75) Chen, K.; Barker, A. J.; Reish, M. E.; Gordon, K. C.; Hodgkiss, J. M. Broadband Ultrafast Photoluminescence Spectroscopy Resolves Charge Photogeneration Via Delocalized Hot Excitons in Polymer:-Fullerene Photovoltaic Blends. *J. Am. Chem. Soc.* **2013**, *135*, 18502−18512.
(76) Jakowetz, A. C.; Bohm, M. L.; Zhang, J.; Sadhanala, A.; Huettner, S.; Bakulin, A. A.; Rao, A.; Friend, R. H. What Controls the Rate of Ultrafast Charge Transfer and Charge Separation Efficiency in Organic Photovoltaic Blends. *J. Am. Chem. Soc.* **2016**, *138*, 11672−11679.
(77) Kozlov, O. V.; Pavelyev Vlad, G.; de Gier Hilde, D.; Remco Havenith, W. A.; van Loosdrecht Paul, H. M.; Hummelen Jan, C.; Pshenichnikov Maxim, S. Ultrafast Electron and Hole Transfer in Bulk Heterojunctions of Low-Bandgap Polymers. *Org. Photonics Photovolt.* **2016**, *4*, 24−34.
(78) Vandewal, K.; Albrecht, S.; Hoke, E. T.; Graham, K. R.; Widmer, J.; Douglas, J. D.; Schubert, M.; Mateker, W. R.; Bloking, J. T.; Burkhard, G. F.; et al. Efficient Charge Generation by Relaxed Charge-Transfer States at Organic Interfaces. *Nat. Mater.* **2013**, *13*, 63−68.
(79) Benduhn, J.; Tvingstedt, K.; Piersimoni, F.; Ullbrich, S.; Fan, Y.; Tropiano, M.; McGarry, K. A.; Zeika, O.; Riede, M. K.; Douglas, C. J.; et al. Intrinsic Non-Radiative Voltage Losses in Fullerene-Based Organic Solar Cells. *Nat. Energy* **2017**, *2*, 17053.
(80) Kraffert, F.; Steyrleuthner, R.; Albrecht, S.; Neher, D.; Scharber, M. C.; Bittl, R.; Behrends, J. Charge Separation in Pcpdtbt:Pcbm Blends from an Epr Perspective. *J. Phys. Chem. C* **2014**, *118*, 28482−28493.
(81) Rao, A.; Chow, P. C. Y.; Gelinas, S.; Schlenker, C. W.; Li, C.-Z.; Yip, H.-L.; Jen, A. K. Y.; Ginger, D. S.; Friend, R. H. The Role of Spin in the Kinetic Control of Recombination in Organic Photovoltaics. *Nature* **2013**, *500*, 435−439.
(82) Morteani, A. C.; Sreearunothai, P.; Herz, L. M.; Friend, R. H.; Silva, C. Exciton Regeneration at Polymeric Semiconductor Heterojunctions. *Phys. Rev. Lett.* **2004**, *92*, 247402.
(83) Melianas, A.; Pranculis, V.; Xia, Y.; Felekidis, N.; Inganäs, O.; Gulbinas, V.; Kemerink, M. Photogenerated Carrier Mobility Significantly Exceeds Injected Carrier Mobility in Organic Solar Cells. *Adv. Energy Mater.* **2017**, *7*, 1602143.
(84) May, V.; Kühn, O. Electron Transfer. *Charge and Energy Transfer Dynamics in Molecular Systems*; Wiley-VCH Verlag GmbH & Co. KGaA: Berlin, Germany, 2011; pp 309−433.
(85) Bakulin, A. A.; Rao, A.; Pavelyev, V. G.; van Loosdrecht, P. H. M.; Pshenichnikov, M. S.; Niedzialek, D.; Cornil, J.; Beljonne, D.; Friend, R. H. The Role of Driving Energy and Delocalized States for Charge Separation in Organic Semiconductors. *Science* **2012**, *335*, 1340−1344.
(86) Herrmann, D.; Niesar, S.; Scharsich, C.; Köhler, A.; Stutzmann, M.; Riedle, E. Role of Structural Order and Excess Energy on Ultrafast Free Charge Generation in Hybrid Polythiophene/Si Photovoltaics Probed in Real Time by near-Infrared Broadband Transient Absorption. *J. Am. Chem. Soc.* **2011**, *133*, 18220−18233.
(87) Kästner, C.; Vandewal, K.; Egbe, D. A. M.; Hoppe, H. Revelation of Interfacial Energetics in Organic Multiheterojunctions. *Adv. Sci.* **2017**, *4*, 1600331.

DOI: 10.1021/acs.jpcc.7b09213
J. Phys. Chem. C 2017, 121, 22739−22752

(88) Zimmerman, J. D.; Xiao, X.; Renshaw, C. K.; Wang, S.; Diev, V. V.; Thompson, M. E.; Forrest, S. R. Independent Control of Bulk and Interfacial Morphologies of Small Molecular Weight Organic Heterojunction Solar Cells. *Nano Lett.* **2012**, *12*, 4366−4371.
(89) Tscheuschner, S.; Bässler, H.; Huber, K.; Köhler, A. A Combined Theoretical and Experimental Study of Dissociation of Charge Transfer States at the Donor−Acceptor Interface of Organic Solar Cells. *J. Phys. Chem. B* **2015**, *119*, 10359−10371.

DOI: 10.1021/acs.jpcc.7b09213
J. Phys. Chem. C 2017, 121, 22739−22752

Supporting Information

The Impact of Driving Force and Temperature on the Electron Transfer in Donor-Acceptor Blend Systems

Thomas Unger[1#], Stefan Wedler[1#], Frank-Julian Kahle[1], Ullrich Scherf [3], Heinz Bässler[2], Anna Köhler[1,2*]

[1]Experimental Physics II, University of Bayreuth, 95447 Bayreuth, Germany.

[2]Bayreuth Institut of Macromolecular Research (BIMF), University of Bayreuth, 95447 Bayreuth, Germany.

[3]Makromolekulare Chemie, Bergische Universität Wuppertal, 42119 Wuppertal

*e-Mail: Anna.Koehler@uni-bayreuth.de

[#] both authors contributed equally

I Energy levels from literature

1.1 Parameters for Marcus theory

The description of electron transfer rates in the framework of classical Marcus theory is based on the driving force ΔG_0, the reorganization energy λ and the electronic coupling J_{DA}. We estimate the driving force ΔG_0 as the difference between the energy of the singlet state E_{S1} and the energy of the charge transfer state E_{CT}. In what follows we shall discuss the values we used for these energies, which are summarized in Table 1 in the main text.

Singlet energy E_{S1}

PCPDTBT: We take a value of 1.5 ± 0.10 eV, consistent with the spectra and calculations reported by Scharsich et al.[1]and Jarzab et al.[2] In both cases the value is taken from the intersection of absorption and emission spectra.

PTB7: We take a value of 1.67 ± 0.05 eV. Kraus et al. reported 1.65 eV [3] (from the intersection of absorption and emission spectra), while 1.68 eV are reported by Son et al. [4] (taken from the onset of absorption), and Liang et al. [5] (taken from the onset of absorption).

MeLPPP: We take a value of 2.7 eV ± 0.05 eV from the intersection of absorption and emission spectra reported by Hoffmann et al. [6]

Energy of the charge transfer state E_{CT}

PCPDTBT: For PCPDTBT, Kurpiers et al. reported the CT-Energy in blends with PCBM to be 1.30 eV (see section V). We thus consider a CT energy of 1.30 ± 0.05 eV to be a reliable estimate.

PTB7: Peng et al. fitted the EQE data to give a CT energy of about 1.4 eV.[7] Based on the open-circuit voltage, Kraus et al. estimate a CT energy of 1.3 eV,[3] consistent with a value of 1.32 eV reported by Gerhard et al. [8] We thus consider a mean value of 1.35 ± 0.05 eV

MeLPPP: There are no reports in literature to the best of our knowledge. We performed EQE- and EL-measurements to determine E_{CT} as detailed in the manuscript.

Reorganization energy λ

PCPDTBT: For PCPDTBT, Kurpiers et al. reported the reorganization energy to be 0.22 eV from fitting the EQE and EL and considering the Stokes' shift (see section V). As this DFT calculations by Leng et al. further yield a value of 0.4 eV for C-PCPDTBT.[9] For our calculations, we adopted a value of 0.30 ± 0.10 eV.

PTB7: Fits to the EQE by Peng et al. give λ = 0.3 eV.[7] This may be compared to a value of 0.4 eV that is reported by Ward et al.[10] We consider thus that λ = 0.35 ± 0.05 eV is a reasonable estimate.

MeLPPP: See main manuscript.

Electronic coupling J_{DA}

Leng and coworkers considered the electron transfer from PCPDTBT to PCBM. Their DFT calculations give a value of about 20 meV for J_{DA}.[9] For other material systems, similar values are obtained. For example, for the combination of P3HT with PCBM, electronic couplings from 20 to 30 meV are reported, depending on the intermolecular distance.[11] We estimate thus that J_{DA}=30±20 meV gives a reliable parameter range for all materials considered.

1.2 Alternative estimation for ΔG_0 from electronic frontier orbitals

A common estimate of the driving force is to take the ionization potential IP of the donor molecule, to subtract the electron affinity EA of the acceptor molecule and to subtract the singlet energy E_{S1} of the donor molecule, $-\Delta G_0 = (\mathrm{IP} - \mathrm{EA}) - E_{S1}$. In this section we estimate ΔG_0 by this method. First we discuss the energy values taken from literature before we summarize them and the resulting ΔG_0 in table S1. This method results in very similar values for ΔG_0 within the reported parameter ranges. In addition, the resulting transfer rates according to Marcus theory (eq 1 in the main text) and the possible range of their values are included in Table S1 as well.

EA PCBM

As detailed in Hahn et al.,[12] based on the gas phase electron affinity and the polarization energy, the value of the electron affinity of the fullerene C60 is expected to be at about 3.7 eV. Values reported for PCBM on the basis of cyclic voltammetry range around 3.7-3.9 eV.[13-15] We therefore use a value of **3.8±0.1** eV.

Ionization Potential IP

PCPDTBT: DFT calculations by Leng et al. using CAM-B3LYP results in 5.0 eV.[9] UPS measurements with PCPDTBT on different substrates give values of 5.1 eV on PEDT:PSS, 4.9 eV on ITO and 4.8 eV on gold.[16] In CV measurements, both oxidation and reduction are shown reversibly, giving a value of 5.3 eV.[17] We consider that **5.05 ± 0.1** eV is a realistic value for the IP of PCPDTBT, having taken the standard deviation of the values to estimate the error.

PTB7: A value of 5.15 eV is reported by cyclic voltammetry measurements.[4] We estimate an error of 0.1 eV.

MeLPPP: The ionization potential of MeLPPP was determined to be 5.3 ± 0.05 eV by UPS.[18]

Table S1: Input parameters and the resulting Marcus transfer rate, based on considering $-\Delta G_0 = (\mathrm{IP} - \mathrm{EA}) - E_{S1}$. Values and estimated errors are taken from literature as described in the text.

		PCPDTBT	PTB7	MeLPPP
	IP (eV)	5.05±0.10	5.15±0.05	5.3±0.1
	E_{S1} (eV)	1.50 ± 0.10[1,2]	1.67 ± 0.05[3-5]	2.7±0.05
	$-\Delta G_0$ (eV)	0.25±0.17	0.32±0.12	1.2±0.15
Temperature (K)		Marcus transfer rate (s^{-1})		
295	min	2.2×10^{11}	1.0×10^{12}	9.8×10^{-33}
	mean	$\mathbf{2.6 \times 10^{13}}$	$\mathbf{2.5 \times 10^{13}}$	$\mathbf{8.2 \times 10^{-14}}$
	max	9.4×10^{13}	7.7×10^{13}	3.5×10^{-2}
200	min	7.9×10^{10}	7.6×10^{11}	7.2×10^{-54}
	mean	$\mathbf{3.0 \times 10^{13}}$	$\mathbf{3.0 \times 10^{13}}$	$\mathbf{2.2 \times 10^{-26}}$
	max	1.1×10^{14}	9.4×10^{13}	2.0×10^{-9}
150	min	2.6×10^{10}	5.4×10^{11}	9.1×10^{-76}
	mean	$\mathbf{3.3 \times 10^{13}}$	$\mathbf{3.4 \times 10^{13}}$	$\mathbf{2.0 \times 10^{-39}}$
	max	1.3×10^{14}	1.1×10^{14}	6.0×10^{-17}
100	min	2.7×10^{9}	2.5×10^{11}	1.3×10^{-119}
	mean	$\mathbf{3.7 \times 10^{13}}$	$\mathbf{4.1 \times 10^{13}}$	$\mathbf{1.5 \times 10^{-65}}$
	max	1.6×10^{14}	1.3×10^{14}	4.9×10^{-32}
12	min	1.8×10^{-14}	4.2×10^{2}	
	mean	$\mathbf{1.8 \times 10^{13}}$	$\mathbf{6.8 \times 10^{13}}$	$< \mathbf{10^{-300}}$
	max	4.7×10^{14}	3.8×10^{14}	

II Minimum and maximum transfer rate in the framework of Marcus theory

Table S2: Transfer rates determined according to eq 1 in the manuscript for different temperatures, along with the experimentally measured lower limits for the transfer rates. The minimum and maximum values result from the parameter ranges as discussed above.

Temperature (K)		PCPDTBT	PTB7	MeLPPP
		expected from Marcus theory in s^{-1}		
295	min	2.9×10^{11}	1.5×10^{12}	2.4×10^{-22}
	mean	$\mathbf{2.0 \times 10^{13}}$	$\mathbf{2.5 \times 10^{13}}$	$\mathbf{2.6 \times 10^{-10}}$
	max	9.4×10^{13}	7.7×10^{13}	1.5×10^{-2}
200	min	1.2×10^{11}	1.4×10^{12}	1.5×10^{-38}
	mean	$\mathbf{2.1 \times 10^{13}}$	$\mathbf{3.0 \times 10^{13}}$	$\mathbf{3.1 \times 10^{-21}}$
	max	1.1×10^{14}	9.4×10^{13}	5.8×10^{-10}
150	min	4.8×10^{10}	1.3×10^{12}	2.4×10^{-55}
	mean	$\mathbf{2.0 \times 10^{13}}$	$\mathbf{3.4 \times 10^{13}}$	$\mathbf{1.5 \times 10^{-32}}$
	max	1.3×10^{14}	1.1×10^{14}	1.1×10^{-17}
100	min	6.7×10^{9}	9.0×10^{11}	5.9×10^{-89}
	mean	$\mathbf{1.8 \times 10^{13}}$	$\mathbf{4.1 \times 10^{13}}$	$\mathbf{3.1 \times 10^{-55}}$
	max	1.6×10^{14}	1.3×10^{14}	4.1×10^{-33}
12	min	3.1×10^{-11}	1.6×10^{7}	
	mean	$\mathbf{4.4 \times 10^{10}}$	$\mathbf{6.8 \times 10^{13}}$	$\mathbf{< 10^{-300}}$
	max	4.7×10^{14}	3.8×10^{14}	
		experimental values in s^{-1}		
295		$(2.9 \pm 1.8) \times 10^{12}$	$(2.6 \pm 0.2) \times 10^{12}$	$(4.1 \pm 0.2) \times 10^{12}$
12		$(2.2 \pm 0.7) \times 10^{12}$	$(2.4 \pm 0.1) \times 10^{12}$	$(4.5 \pm 0.2) \times 10^{12}$

III Comparison of transfer rates for the low-bandgap polymer:PCBM blends

3.1 PCPDTBT:PCBM

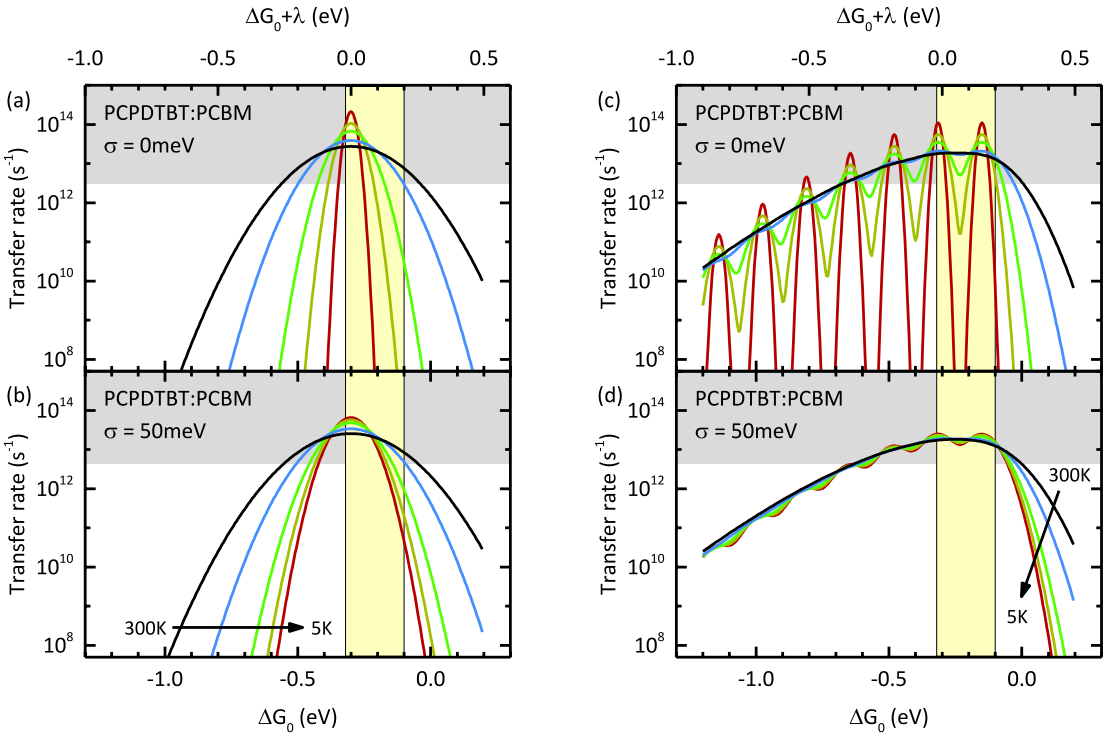

Fig. S1
Marcus rates (a,b) and Marcus-Levich-Jortner rates (c,d) of the PCPDTBT:PCBM blend as a function of driving force for different temperatures (300K, 150K, 50K, 20K and 5K) without disorder (a,c) and with energetic disorder of $\sigma = 50\mathrm{meV}$ (b,d). The grey shaded area indicates values that are beyond our instrumental resolution. The yellow shaded indicates the parameter range for the driving force.

3.2 PTB7:PCBM

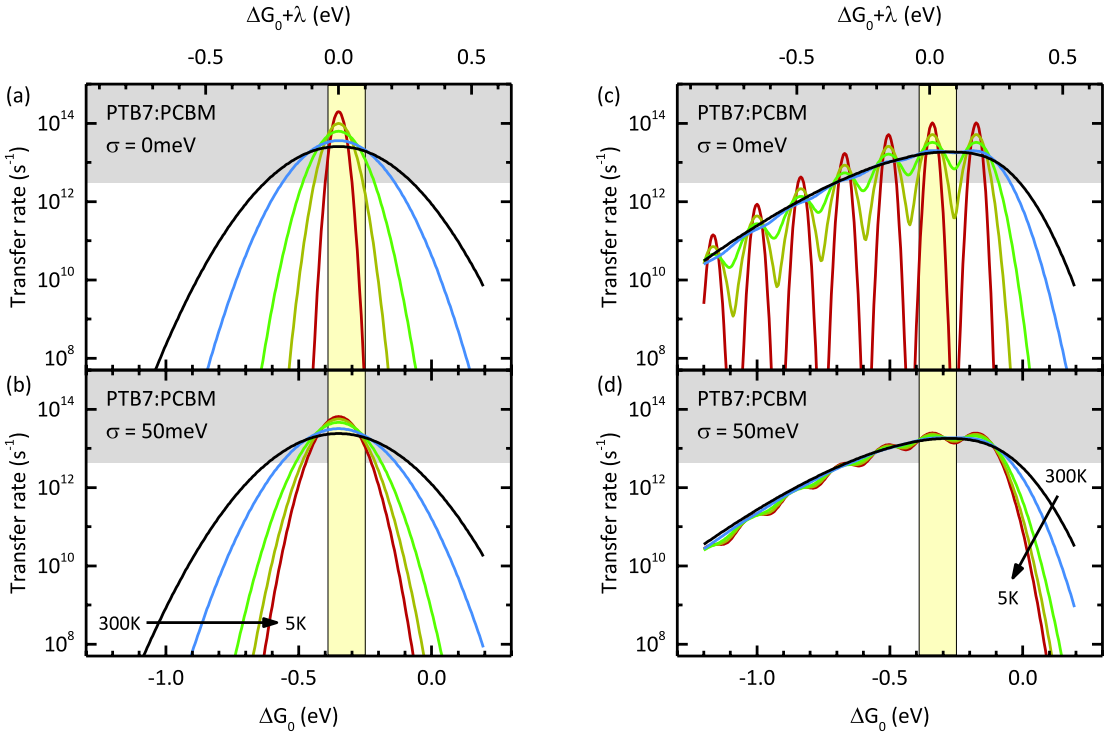

Fig. S2
Marcus rates (a,b) and Marcus-Levich-Jortner rates (c,d) of the PTB7:PCBM blend as a function of driving force for different temperatures (300K, 150K, 50K, 20K and 5K) without disorder (a,c) and with energetic disorder of $\sigma = 50\mathrm{meV}$ (b,d). The grey shaded area indicates values that are beyond our instrumental resolution. The yellow shaded indicates the parameter range for the driving force.

IV Hole transfer from photoexcited acceptor to donor

4.1 MeLPPP:PCBM

We use the same method for the calculation of the driving force for hole transfer ΔG_0^{HT} as for electron transfer. For this purpose we need the singlet energy E_{S1} of PCBM. Veldman et al report a value of 1.70 eV taken from the onset of absorption.[19] Coffey et al give a value of 1.76 eV determined by absorption and photoluminescence spectroscopy.[20] We therefore use a value of $\mathbf{1.73 \pm 0.05}$ eV. Using our measurement value of 1.57 ± 0.05 eV for the CT energy, we calculate the driving force to $-\Delta G_0^{\mathrm{HT}} = 160 \pm 70$ meV.

If hole transfer takes place from the CT manifold with energies of 2.3 eV and above as detailed by Hahn et al,[12] the driving force increases to $-\Delta G_0^{\mathrm{HT}} = 0.73$ eV, which is well in the Marcus inverted regime.

4.2 The case of P3HT:PCBM

We again need the energy values of the singlet state and the CT state to consider the expected transfer rates in the framework of Marcus and MLJ.

Reported values of the singlet energy are 2.06 eV using Franck Condon analysis of absorption by Herrman et al,[21] 1.91 eV using the onset of absorption by Veldman et al[19] and 2.0 eV using absorption and photoluminescence spectroscopy by Ohkita et al.[22] We use a value of $\boldsymbol{E_{S1} = 1.99 \pm 0.06}$ **eV**.

Vandewal et al performed EL/EQE measurements[23] and report a value of **1.14 eV** for the **CT** state energy as well as a **reorganization energy** of **0.27 eV**. Their value for the reorganization energy matches with the result from Alberga et al, which was calculated using MD simulations.[24]

The value of the **electronic coupling** is reported to be around 10 to 30 meV by Liu et al.[11, 25] We use **20 ± 10 meV**.

Further parameters for calculations in the MLJ framework are $\boldsymbol{\sigma = 75}$ **meV** for the energetic disorder, a **Huang Rhys parameter of 1** and a vibrational energy of $\boldsymbol{\hbar\omega = 180}$ **meV** as reported by Hermann et al.[21]

Using the energies of the singlet state as well as the CT state as discussed above, we calculate the driving force for electron transfer $-\Delta G_0^{\mathrm{ET}} = 850 \pm 60$ meV and for hole transfer $-\Delta G_0^{\mathrm{HT}} = 590 \pm 50$ meV. Both transfer types take place well in the Marcus inverted regime, being triple (twice) the reorganization energy for electron (hole) transfer.

Having established the input values, we calculate the transfer rates for the P3HT:PCBM blend system in Figure 9 in the manuscript. The possible ranges for the driving forces are indicated by blue (electron transfer) and red (hole transfer) boxes. Falke et al measured an electron transfer time between 50 and 60 fs (sub-20 fs resolution),[26] and Cook et al give a resolution limited value of 250 fs for the hole transfer,[27] which are drawn in Figure 9 in the manuscript as well. Both transfer times are much too fast compared to the expectations of Marcus theory.

V Reorganisation energy and CT energy of PCPDTBT:PCBM

Figure S3 shows the electroluminescence and the external quantum efficiency for a blend solar cell made of PCPDTBT:PCBM. This Figure is part of the manuscript 'On the Activation Energy of Free Charge Formation in Polymer-Fullerene Solar Cells and the Role of "Hot" Generation Pathways' by Jona Kurpiers, Thomas Ferron, Steffen Roland, John A. Love, Tobias Thiede, Frank Jaiser, Steve Albrecht, Anne Katholing, Sylvia Janietz, Antonio Facchetti, Brian A. Collins and Dieter Neher., which was kindly provided to us by the authors prior to publication.

The EQE and EL measurements were performed and analysed as described for the MeLPPP:PCBM system.

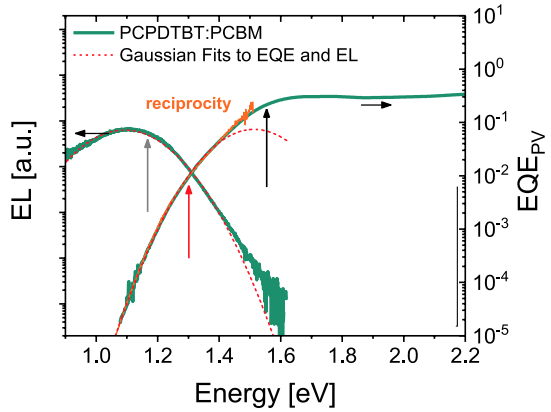

Fig S3:
EL and EQE measurements for PCPDTBT:PCBM. Red dotted lines indicate simultaneous Gaussian fits to the CT-region of EQE and EL according to Vandewal et al.[23] This results in a reorganization energy of 220 meV and a CT energy of 1.30 eV.

References

1. Scharsich, C.; Fischer, F. S. U.; Wilma, K.; Hildner, R.; Ludwigs, S.; Köhler, A., Revealing Structure Formation in Pcpdtbt by Optical Spectroscopy. *J. Polym. Sci. B Polym. Phys.* **2015**, *53*, 1416-1430.
2. Jarzab, D.; Cordella, F.; Gao, J.; Scharber, M.; Egelhaaf, H.-J.; Loi, M. A., Low-Temperature Behaviour of Charge Transfer Excitons in Narrow-Bandgap Polymer-Based Bulk Heterojunctions. *Adv. Energy Mater.* **2011**, *1*, 604-609.
3. Kraus, H.; Heiber, M. C.; Vath, S.; Kern, J.; Deibel, C.; Sperlich, A.; Dyakonov, V., Analysis of Triplet Exciton Loss Pathways in Ptb7:Pc71bm Bulk Heterojunction Solar Cells. *Sci. Rep.* **2016**, *6*.
4. Carsten, B.; Szarko, J. M.; Son, H. J.; Wang, W.; Lu, L.; He, F.; Rolczynski, B. S.; Lou, S. J.; Chen, L. X.; Yu, L., Examining the Effect of the Dipole Moment on Charge Separation in Donor-Acceptor Polymers for Organic Photovoltaic Applications. *J. Am. Chem. Soc.* **2011**, *133*, 20468-20475.
5. Liang, Y.; Xu, Z.; Xia, J.; Tsai, S. T.; Wu, Y.; Li, G.; Ray, C.; Yu, L., For the Bright Future-Bulk Heterojunction Polymer Solar Cells with Power Conversion Efficiency of 7.4%. *Adv. Mater.* **2010**, *22*, E135-E138.
6. Hoffmann, S. T.; Scheler, E.; Koenen, J.-M.; Forster, M.; Scherf, U.; Strohriegl, P.; Bässler, H.; Köhler, A., Triplet Energy Transfer in Conjugated Polymers. Iii. An Experimental Assessment Regarding the Influence of Disorder on Polaronic Transport. *Phys. Rev. B* **2010**, *81*.
7. Peng, Z.; Xia, Y.; Gao, F.; Xiong, K.; Hu, Z.; James, D. I.; Chen, J.; Wang, E.; Hou, L., A Dual Ternary System for Highly Efficient Ito-Free Inverted Polymer Solar Cells. *J. Mater. Chem. A* **2015**, *3*, 18365-18371.
8. Gerhard, M.; Arndt, A. P.; Howard, I. A.; Rahimi-Iman, A.; Lemmer, U.; Koch, M., Temperature- and Energy-Dependent Separation of Charge-Transfer States in Ptb7-Based Organic Solar Cells. *J. Phys. Chem. C* **2015**, *119*, 28309-28318.
9. Leng, C.; Qin, H.; Si, Y.; Zhao, Y., Theoretical Prediction of the Rate Constants for Exciton Dissociation and Charge Recombination to a Triplet State in Pcpdtbt with Different Fullerene Derivatives. *J. Phys. Chem. C* **2014**, *118*, 1843-1855.
10. Ward, A. J.; Ruseckas, A.; Kareem, M. M.; Ebenhoch, B.; Serrano, L. A.; Al-Eid, M.; Fitzpatrick, B.; Rotello, V. M.; Cooke, G.; Samuel, I. D. W., The Impact of Driving Force on Electron Transfer Rates in Photovoltaic Donor-Acceptor Blends. *Adv. Mater.* **2015**, *27*, 2496-2500.
11. Liu, T.; Cheung, D. L.; Troisi, A., Structural Variability and Dynamics of the P3ht/Pcbm Interface and Its Effects on the Electronic Structure and the Charge-Transfer Rates in Solar Cells. *Phys. Chem. Chem. Phys.* **2011**, *13*, 21461-21470.
12. Hahn, T.; Tscheuschner, S.; Saller, C.; Strohriegl, P.; Boregowda, P.; Mukhopadhyay, T.; Patil, S.; Neher, D.; Bässler, H.; Köhler, A., Role of Intrinsic Photogeneration in Single Layer and Bilayer Solar Cells with C60 and Pcbm. *J. Phys. Chem. C* **2016**, *120*, 25083-25091.
13. Faist, M. A.; Kirchartz, T.; Gong, W.; Ashraf, R. S.; McCulloch, I.; de Mello, J. C.; Ekins-Daukes, N. J.; Bradley, D. D. C.; Nelson, J., Competition between the Charge Transfer State and the Singlet States of Donor or Acceptor Limiting the Efficiency in Polymer:Fullerene Solar Cells. *J. Am. Chem. Soc.* **2012**, *134*, 685-692.
14. He, Y.; Chen, H.-Y.; Hou, J.; Li, Y., Indene−C60 Bisadduct: A New Acceptor for High-Performance Polymer Solar Cells. *J. Am. Chem. Soc.* **2010**, *132*, 1377-1382.
15. Albrecht, S.; Vandewal, K.; Tumbleston, J. R.; Fischer, F. S.; Douglas, J. D.; Frechet, J. M.; Ludwigs, S.; Ade, H.; Salleo, A.; Neher, D., On the Efficiency of Charge Transfer State Splitting in Polymer:Fullerene Solar Cells. *Adv. Mater.* **2014**, *26*, 2533-2539.
16. Aygül, U.; Peisert, H.; Frisch, J.; Vollmer, A.; Koch, N.; Chassé, T., Electronic Properties of Interfaces between Pcpdtbt and Prototypical Electrodes Studied by Photoemission Spectroscopy. *ChemPhysChem* **2011**, *12*, 2345-2351.
17. Mühlbacher, D.; Scharber, M.; Morana, M.; Zhu, Z.; Waller, D.; Gaudiana, R.; Brabec, C., High Photovoltaic Performance of a Low-Bandgap Polymer. *Adv. Mater.* **2006**, *18*, 2884-2889.

18. Schwarz, C.; Tscheuschner, S.; Frisch, J.; Winkler, S.; Koch, N.; Bässler, H.; Köhler, A., Role of the Effective Mass and Interfacial Dipoles on Exciton Dissociation in Organic Donor-Acceptor Solar Cells. *Physical Review B* **2013**, *87*.
19. Veldman, D.; Meskers, S. C. J.; Janssen, R. A. J., The Energy of Charge-Transfer States in Electron Donor-Acceptor Blends: Insight into the Energy Losses in Organic Solar Cells. *Adv. Funct. Mater.* **2009**, *19*, 1939-1948.
20. Coffey, D. C.; Larson, B. W.; Hains, A. W.; Whitaker, J. B.; Kopidakis, N.; Boltalina, O. V.; Strauss, S. H.; Rumbles, G., An Optimal Driving Force for Converting Excitons into Free Carriers in Excitonic Solar Cells. *J. Phys. Chem. C* **2012**, *116*, 8916-8923.
21. Herrmann, D.; Niesar, S.; Scharsich, C.; Köhler, A.; Stutzmann, M.; Riedle, E., Role of Structural Order and Excess Energy on Ultrafast Free Charge Generation in Hybrid Polythiophene/Si Photovoltaics Probed in Real Time by near-Infrared Broadband Transient Absorption. *J. Am. Chem. Soc.* **2011**, *133*, 18220-18233.
22. Ohkita, H., et al., Charge Carrier Formation in Polythiophene/Fullerene Blend Films Studied by Transient Absorption Spectroscopy. *J. Am. Chem. Soc.* **2008**, *130*, 3030-3042.
23. Vandewal, K.; Tvingstedt, K.; Gadisa, A.; Inganäs, O.; Manca, J. V., Relating the Open-Circuit Voltage to Interface Molecular Properties of Donor:Acceptor Bulk Heterojunction Solar Cells. *Phys. Rev. B* **2010**, *81*.
24. Alberga, D.; Perrier, A.; Ciofini, I.; Mangiatordi, G. F.; Lattanzi, G.; Adamo, C., Morphological and Charge Transport Properties of Amorphous and Crystalline P3ht and Pbttt: Insights from Theory. *Phys. Chem. Chem. Phys.* **2015**, *17*, 18742-18750.
25. Liu, T.; Troisi, A., Absolute Rate of Charge Separation and Recombination in a Molecular Model of the P3ht/Pcbm Interface. *J. Phys. Chem. C* **2011**, *115*, 2406-2415.
26. Falke, S. M., et al., Coherent Ultrafast Charge Transfer in an Organic Photovoltaic Blend. *Science* **2014**, *344*, 1001-1005.
27. Cook, S.; Katoh, R.; Furube, A., Ultrafast Studies of Charge Generation in Pcbm:P3ht Blend Films Following Excitation of the Fullerene Pcbm. *J. Phys. Chem. C* **2009**, *113*, 2547-2552.

10 The Role of PbI_2 on $CH_3NH_3PbI_3$ Perovskite Stability, Device Parameters and Degradation

Tanaji Gujar, Thomas Unger, Martina Fried, Andreas Schönleber, Sander van Smaalen, Anna Köhler und Mukundan Thelakkat

Veröffentlicht in
Physical Chemistry Chemical Physics (2018)

(DOI: 10.1039/c7cp04749e)

PCCP

PAPER

View Article Online
View Journal

Cite this: DOI: 10.1039/c7cp04749e

The role of PbI_2 in $CH_3NH_3PbI_3$ perovskite stability, solar cell parameters and device degradation†

Tanaji P. Gujar,[a] Thomas Unger,[b] Andreas Schönleber,[c] Martina Fried,[a] Fabian Panzer,[b] Sander van Smaalen,[c] Anna Köhler[b] and Mukundan Thelakkat*[a]

Received 14th July 2017,
Accepted 21st November 2017

DOI: 10.1039/c7cp04749e

rsc.li/pccp

We report a systematic investigation on the role of excess PbI_2 content in $CH_3NH_3PbI_3$ perovskite film properties, solar cell parameters and device storage stability. We used the CH_3NH_3I vapor assisted method for the preparation of PbI_2-free $CH_3NH_3PbI_3$ films under a N_2 atmosphere. These pristine $CH_3NH_3PbI_3$ films were annealed at 165 °C for different time intervals in a N_2 atmosphere to generate additional PbI_2 in these films. From XRD measurements, the excess of PbI_2 was quantified. Detailed characterization using scanning electron microscopy, X-ray diffraction, UV-Visible and photoluminescence for continuous aging of $CH_3NH_3PbI_3$ films under ambient condition (50% humidity) is carried out for understanding the influence of different PbI_2 contents on degradation of the $CH_3NH_3PbI_3$ films. We find that the rate of degradation of $CH_3NH_3PbI_3$ is accelerated due to the amount of PbI_2 present in the film. A comparison of solar cell parameters of devices prepared using $CH_3NH_3PbI_3$ samples having different PbI_2 contents reveals a strong influence on the current density–voltage hysteresis as well as storage stability. We demonstrate that $CH_3NH_3PbI_3$ devices do not require any residual PbI_2 for a high performance. Moreover, a small amount of excess PbI_2, which improves the initial performance of the devices slightly, has undesirable effects on the $CH_3NH_3PbI_3$ film stability as well as on device hysteresis and stability.

Introduction

Organometal halide perovskite solar cells have achieved great progress in the last few years. The power conversion efficiency (PCE) of $CH_3NH_3PbI_3$ perovskite based thin film photovoltaic devices has already reached a high value of 22% in just a few years.[1] This rapid progress was achieved by optimizing both the material and device architecture and understanding the underlying photoinduced charge separation mechanisms of these devices.[2–11] Major efforts have been made to achieve high efficiency using various approaches comprising passivation of defects[12] and tuning and controlling numerous parameters in perovskite layers such as the surface morphology,[13] grain size,[14] different halogen ratio[15,16] and different cation compositions (mixture of CH_3NH_3/$HC(NH_2)_2$).[17] Additionally, both the charge extraction layers, the electron transport layer (ETL)[7] and the hole transport layer (HTL),[18] have also been studied and optimized.

Several recent papers reveal that one of the preferred techniques to improve the PCE of $CH_3NH_3PbI_3$ is using excess PbI_2, which is not converted to $CH_3NH_3PbI_3$. For example, Chen *et al.* demonstrated the role of PbI_2 in $CH_3NH_3PbI_3$ for the improvement of device performance by annealing after preparing pristine $CH_3NH_3PbI_3$ using the CH_3NH_3I (MAI)-vapor assisted method.[12] Kim *et al.* demonstrated that 5.7 wt% PbI_2 in the $(CH(NH_2)_2PbI_3)_{0.85}(CH_3NH_3PbBr_3)_{0.15}$ perovskite prepared using the solvent engineering method improved the PCE as well as reduced the hysteresis.[17] Roldan-Carmona *et al.* observed that 10 wt% additional PbI_2 in $CH_3NH_3PbI_3$ using the solvent engineering method is beneficial for the improvement of PCE of devices.[19] It was also reported that 2 wt% residual PbI_2 in $CH_3NH_3PbI_3$ is beneficial to improve the device efficiency.[20] Moreover, the benefits of PbI_2 in $CH_3NH_3PbI_3$ towards an improved performance can be inferred from the fact that most of the high PCE perovskite solar cells prepared using a variety of methods exhibited unintentionally a small amount of excess PbI_2.[21,22] Jacobsson *et al.*[23] also confirmed that the hysteresis index in $(CH(NH_2)_2PbI_3)_{0.85}(CH_3NH_3PbBr_3)_{0.15}$ devices is higher for samples having a residual PbI_2 content compared to the PbI_2-deficient samples. Based on this, it was suggested that excess PbI_2 in $CH_3NH_3PbI_3$ can help to passivate defects at

[a] Applied Functional Polymers, Macromolecular Chemistry I, University of Bayreuth, 95447 Bayreuth, Germany. E-mail: Mukundan.Thelakkat@uni-bayreuth.de
[b] Experimental Physics II, University of Bayreuth, 95447 Bayreuth, Germany
[c] Laboratory of Crystallography, University of Bayreuth, 95447 Bayreuth, Germany

† Electronic supplementary information (ESI) available. See DOI: 10.1039/c7cp04749e

surfaces and grain boundaries[12] and a small amount of residual PbI_2 in the perovskite supports reduction of charge recombination and improves open circuit voltage (V_{oc}) and the fill factor (FF).[17] It has also been suggested that the small amount of excess PbI_2 in the perovskite influences the morphology and increases the size as well as the uniformity of perovskite crystals using the solvent engineering method.[19,24]

On the other hand, it is noteworthy that for PbI_2-free $CH_3NH_3PbI_3$ solar cells using a modified MAI-vapor assisted method for $CH_3NH_3PbI_3$ crystallization, we clearly demonstrated a reproducible performance with ~15% PCE.[25] Li *et al.* have a similar observation that a high PCE of 14.2% can be achieved for PbI_2-free $CH_3NH_3PbI_3$ prepared using a low pressure MAI-vapor assisted method.[26] While considering the excess PbI_2 for high PCE perovskite solar cells, one should not overlook the fact that PbI_2 in perovskites exhibits intrinsic instability under illumination.[27] Liu *et al.* demonstrated that residual PbI_2 accelerates the degradation of $CH_3NH_3PbI_3$ films upon exposure to illumination.[27] Encapsulated devices have the same stability performance like excess PbI_2-free $CH_3NH_3PbI_3$ devices. Thus, the influence of PbI_2 in perovskite films on solar cells is moderately known but their influence on degradation or stability is ambiguous. It is therefore of great interest to study systematically the effect of PbI_2 in $CH_3NH_3PbI_3$ not only on the PCE of solar cells, but also on their photophysics and stability, since both long term stability and a high PCE are essential for practical applications. For a comprehensive investigation of the effect of PbI_2, it is necessary to consider separately the effects caused by PbI_2 in $CH_3NH_3PbI_3$ on absorption/emission, morphology, decomposition of the perovskite layer, device parameters and the overall device stability. Thus the open questions that we address are (1) what is the influence of residual PbI_2 on the stability of the perovskite films and morphology? (2) Can we observe any quantifiable trend in the PL properties and PbI_2 content? (3) How far is the beneficial effect of PbI_2 counteracting the performance and stability of the devices? and (4) Is it possible to separate the different positive and negative effects to make conclusion on the net effect of residual PbI_2?

We used the MAI-vapor assisted method for the preparation of $CH_3NH_3PbI_3$ films under a N_2 atmosphere.[25] With this method we guarantee uniform film formation with similar grain sizes and high reproducibility and stability of the $CH_3NH_3PbI_3$ films.[25,28] There are three ways to introduce PbI_2 in such films: (a) by prolonged thermal annealing of a PbI_2-free film[12] or (b) by purposefully adding non-stoichiometric amounts of precursors to obtain residual non-converted PbI_2 in the final perovskite[17,19] or (c) partial conversion of PbI_2 to $CH_3NH_3PbI_3$.[21,22] We adopted the first method to obtain samples with different amounts of PbI_2 by annealing the samples at 165 °C for different time intervals in a N_2 atmosphere. Characterization using scanning electron microscopy (SEM), X-ray diffraction (XRD), UV-Visible and photoluminescence (PL) with aging of $CH_3NH_3PbI_3$ films under ambient conditions (50% humidity) is carried out for understanding the influence of residual PbI_2 on the stability of $CH_3NH_3PbI_3$ itself. A comparison of solar cell parameters for the different $CH_3NH_3PbI_3$ samples with varying PbI_2 contents is also performed. We demonstrate that a solar cell device with a very small amount of excess PbI_2 can exhibit a slightly higher PCE, but this small amount of excess PbI_2 has undesirable effects on the $CH_3NH_3PbI_3$ film stability, current density–voltage (J/V) hysteresis and device stability. The presence of a small amount of excess PbI_2 results in the faster degradation of the $CH_3NH_3PbI_3$ layer in a humid air atmosphere and the degradation rate increases with the amount of additional PbI_2 in $CH_3NH_3PbI_3$ films. Thus, this work gives insights into the overall consequences of residual PbI_2 on different aspects of $CH_3NH_3PbI_3$ solar cells. This work confirms the initial positive influence of excess PbI_2 on $CH_3NH_3PbI_3$ solar cell devices but simultaneously also proves that it accelerates film degradation and therefore limits device lifetime.

Experimental section

Materials

All starting materials were purchased from Sigma-Aldrich and used as received. Spiro-OMeTAD was purchased from Merck Chemicals.

MAI synthesis

MAI was synthesized by reacting 24 mL of methylamine (33 wt% in absolute ethanol) and 10 mL of hydroiodic acid (57 wt% in water) in a round-bottom flask at room temperature (RT) for 2 h under Ar with stirring. The raw precipitate was recovered by removing the solvent in a rotary evaporator at 40 °C. The raw product was washed with ethyl ether, dried in a vacuum at RT and redissolved in absolute ethanol. The pure MAI recrystallized upon cooling is filtered and dried at RT in a vacuum oven for 24 h. The purity of MAI is very crucial for the synthesis of a pure perovskite.

Device fabrication

Fluorine doped tin oxide (FTO)-coated glass sheets (17 $\Omega\ \square^{-1}$) were etched with zinc powder and HCl (2 M) to obtain the required electrode pattern. The substrates were then cleaned with a detergent followed by sonication in deionized water, acetone and ethanol for 10 min each, and dried with clean dry air. A 50 nm compact-TiO_2 (c-TiO_2) blocking layer was deposited by spray pyrolysis of titanium(IV) bis(acetoacetonato)–di(isopropanoxylate) diluted in ethanol at 450 °C on FTO-coated glass substrates and annealed at 450 °C for 1 h. After cooling, the substrates were transferred in a glovebox under a N_2 atmosphere. For $CH_3NH_3PbI_3$ formation, we adapted a published procedure[12,25,28] and optimized it as follows. PbI_2 (1 M) was dissolved in *N*,*N*-dimethyl formamide overnight under stirring conditions at 100 °C and 80 μL solution was spin coated on the FTO/c-TiO_2 substrates at 2000 rpm for 50 s, and dried at 100 °C for 5 min. 100 mg MAI powder was spread out around the PbI_2 coated substrates with a Petri dish covering on the top and heated at 165 °C for 13 h for full conversion. Subsequently, the as-prepared samples were annealed at 165 °C for different time intervals to generate residual PbI_2. The HTL deposition solution comprised of

2,2′,7,7′-tetrakis-(*N*,*N*-di-*p*-methoxyphenylamine) 9,9′-spirobifluorene (spiro-OMeTAD) in chlorobenzene (102.85 mg mL^{-1}), 40 mL of 4-*tert*-butylpyridine and 37 mL (520 mg mL^{-1}) solution of bis(trifluoromethane) sulfonimide lithium salt (LiTFSI) in acetonitrile. This solution was spin coated at 2000 rpm for 30 s under N_2 conditions and stored in dry air overnight. No oxidants were used. This was followed by thermal deposition of gold to form the back contact. The active areas of the devices fabricated in this work are 0.09 and 0.16 cm^2.

Characterization

The structural and phase characterization of the $CH_3NH_3PbI_3$ layer deposited on the FTO/c-TiO_2 substrate was carried out in the reflection mode XRD using a Panalytical X'pert pro diffractometer with Cu Kα_1 radiation (λ = 0.15405 nm), operated at 40 kV and 40 mA. The diffractograms were recorded in the 2θ range of 10 to 45° with a 2θ step size of 0.008°. UV-Vis absorption spectra were collected using a V-630 UV-Vis Jasco Spectrophotometer coupled with an integrating sphere. The surface morphology and cross-section were characterized by field emission SEM using a Zeiss 1530 instrument with an accelerating voltage of 3.0 kV. PL spectra and PL quantum yield were recorded of $CH_3NH_3PbI_3$ deposited on quartz substrates with an integrating sphere coupled *via* optical fiber to a Oriel spectrograph MS125 and a Andor Idus CCD camera. The excitation source is a 485 nm laser diode LDH-D-C-485, PicoQuant GmbH. The used intensity was about 450 mW cm^{-2}. Each sample is measured after 2 min of laser exposure in order to account for the "soaking effect".[29,30] The exposure time is kept constant for all measurements. The influence of the soaking effect was investigated for each sample at day 1 (see Fig. S1 in the ESI†). The *J*/*V* plots of solar cell devices were obtained using an Oriel solar simulator under AM 1.5, 1000 W m^{-2} conditions. The *J*/*V* data under these conditions were obtained using a Keithley model 2400 source meter. All *J*/*V* measurements were performed in a N_2 atmosphere. Both forward (from −1 V to +2 V) and backward (from +2 V to −1 V) sweeps were recorded to understand the hysteresis. All the devices were measured at a sweep rate of 100 mV s^{-1}. Each device was equilibrated by multiscans in reverse mode under illumination till the short circuit current density (J_{sc}) was stabilized. Each device type was fabricated in two batches (4 devices each) and analyzed to understand the scattering of device parameters.

Results and discussion

XRD analysis of the residual PbI_2 content and the influence on the morphology

For generation of PbI_2 in $CH_3NH_3PbI_3$ films, we used thermal annealing of pure $CH_3NH_3PbI_3$ films at 165 °C for different time intervals (0, 15, 30, 45 and 60 min) and the five samples obtained are mentioned in the following as A, B, C, D and E, respectively. To monitor the generation of PbI_2 by annealing and to verify the comparative amount of PbI_2 in the processed $CH_3NH_3PbI_3$ material, XRD experiments have been performed

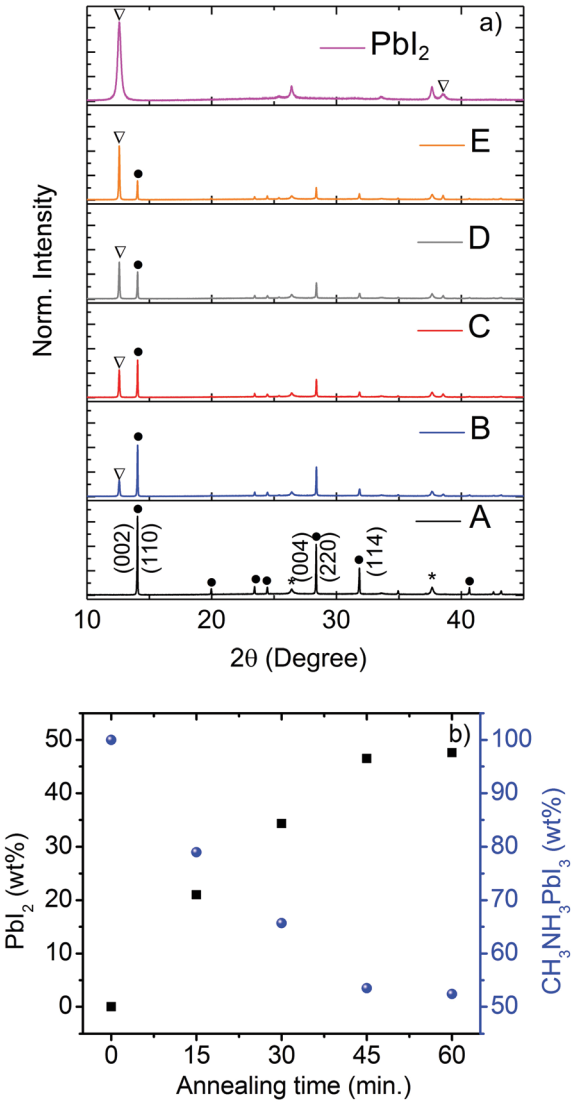

Fig. 1 (a) XRD patterns of $CH_3NH_3PbI_3$ samples on compact TiO_2 annealed at 165 °C for (A) 0 min, (B) 15 min, (C) 30 min, (D) 45 min and (E) 60 min; (b) PbI_2 wt% and $CH_3NH_3PbI_3$ wt% with annealing time. XRD peaks are labeled for $CH_3NH_3PbI_3$ (black dot), PbI_2 (open triangle) and substrate (black star).

for all samples including pure PbI_2 (Fig. 1a). The X-ray patterns confirm the presence of the tetragonal perovskite phase of $CH_3NH_3PbI_3$ in all of the prepared films. In sample A, XRD pattern shows that the films composed of a single pristine perovskite phase with strong diffraction peaks (110), (220) and (114), characteristic of $CH_3NH_3PbI_3$ in the tetragonal phase. No peaks of PbI_2 could be detected. The PbI_2 phase in the pure perovskite can be identified by the characteristic PbI_2 peak located at 2θ ~ 12.7°. Accordingly, for sample B, a small PbI_2 peak becomes apparent at 2θ of 12.7°. With increasing annealing time, the characteristic PbI_2 peak increases in intensity from sample B to E on the concomitant expense of the intensity of the (110) peak of the perovskite at about 15°. Fig. 1b shows that the amount of PbI_2 present in the pervoskite films and PbI_2 wt% rapidly increase with an increase in the annealing time,

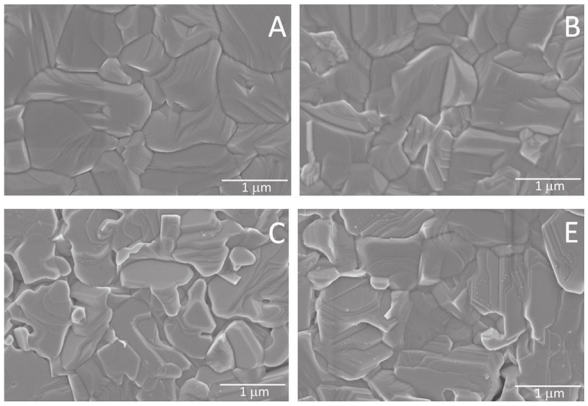

Fig. 2 SEM images of $CH_3NH_3PbI_3$ samples A, B, C and E at magnification 10 KX. The SEM image of sample D is very similar to that of sample E and is shown in Fig. S4 (ESI†).

confirming this interconversion during thermal annealing. An increase of PbI_2 amounts in the films as obtained from XRD is confirmed by PbI_2 wt% calculated from optical measurements and both values agree very well. As per XRD measurements, the samples A to E have 0, 21, 34, 46 and 48 wt% PbI_2 respectively. Detailed calculations of PbI_2 wt% in $CH_3NH_3PbI_3$ films from XRD and optical spectroscopy (Fig. S2 and S3) are explained in the ESI.†

SEM images obtained from the surface analysis of the $CH_3NH_3PbI_3$ films A, B, C and E are shown in Fig. 2, which illustrate the changes in the grain-size upon annealing. Since there is no detectable difference for samples D and E, the image of sample D is given in Fig. S4 (ESI†). From the surface view of sample A, it is clear that the $CH_3NH_3PbI_3$ films are composed of micrometer-sized grains that exhibit a densely packed morphology and are free from pinholes/pores. The average grain size is 1000 nm. From sample B to E, compactness of the samples decreases as well as edges of grains vanish from sample B to E. Especially in sample E, one can observe loss of matter at the grain boundaries, which suggest that with a prolonged annealing time, the PbI_2 content increases by evaporation of MAI at grain boundaries and probably at the surface of the film as well. The cross-sectional SEM of samples A to E (Fig. S4, ESI†) does not show any clear separation/gap between the grains in the bulk of the film. According to Chen *et al.*, $CH_3NH_3PbI_3$ decomposed upon prolonged annealing at 150 °C and conversion from $CH_3NH_3PbI_3$ to PbI_2 occurred where CH_3NH_3I species escaped from the perovskite film to form the PbI_2 phase mostly at grain boundaries and at the relevant interfaces.[12] Xie *et al.* also confirmed the existence of PbI_2 on the surface formed by decomposition of $CH_3NH_3PbI_3$ by annealing at 150 °C.[31] However, in our case it seems most decomposition happens at the surface, but it is difficult to exactly depict the location regarding the presence/distribution of PbI_2 in these films just from SEM analysis.

Influence of PbI_2 on the optical properties

Fig. 3a shows the absorption spectra of samples A to E. The initial thicknesses of all samples were similar and lie in the range of 300 to 325 nm. The position of band-edge absorption

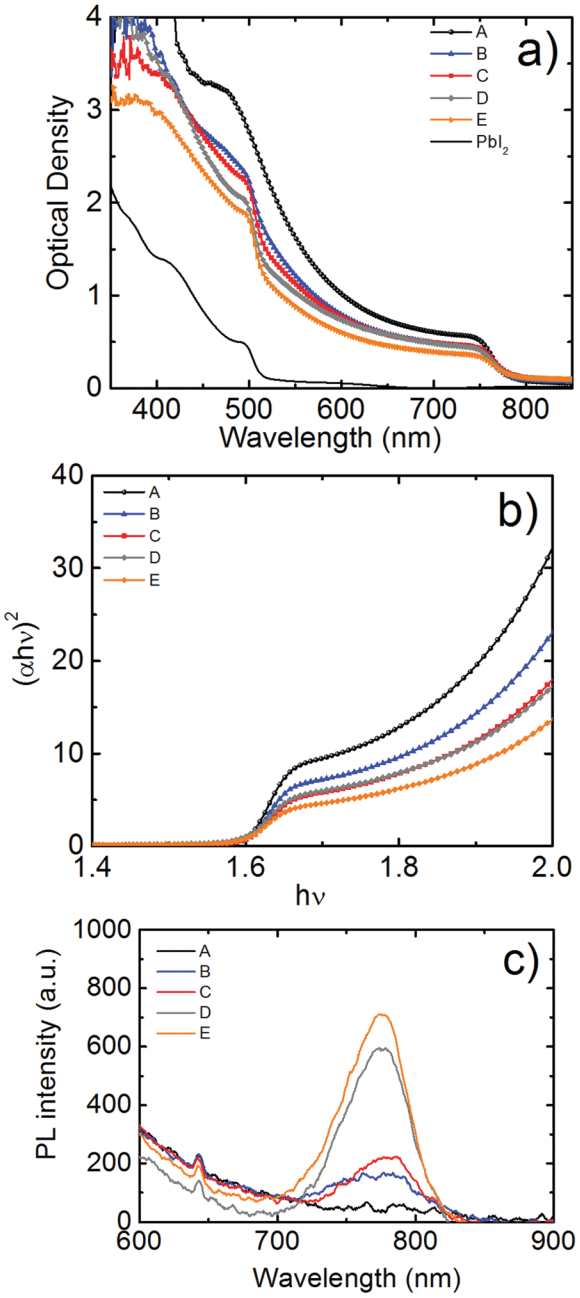

Fig. 3 (a) UV-Visible absorption spectra of samples A to E and PbI_2 film; (b) plots of $(\alpha h\nu)^2$ against $h\nu$ of all $CH_3NH_3PbI_3$ samples; (c) steady-state photoluminescence (PL) for all samples.

of all samples is almost the same but the absolute absorbance at 700 nm for samples A to E indicates that the optical density decreases. It is obvious that, from samples A to E, the $CH_3NH_3PbI_3$ amount in the film decreases with an increase in the PbI_2 content. In the absorption graph for samples B to E, a kink (shoulder) is observed at 500 nm and its intensity increased from sample B to E. Upon comparison to the PbI_2 absorption (Fig. 3a), this is indicative of an increased amount of the PbI_2 content in the $CH_3NH_3PbI_3$ films. To obtain the band gap (E_g), these data were further analyzed using the classical Tauc relation, for direct optical gap semiconductors: $\alpha = A(h\nu - E_g)^n/h\nu$, where α is the absorption

coefficient, A is the proportionality constant, n = 0.5 for direct band gap materials and $h\nu$ = photon energy. The plots of $(\alpha h\nu)^2$ *versus* $h\nu$ of the $CH_3NH_3PbI_3$ films are shown in Fig. 3b. This graph gives E_g, when a straight portion of $(\alpha h\nu)^2$ against the $h\nu$ plot is extrapolated to the point α = 0. For all samples it is around 1.6 eV, thus independent of the excess PbI_2 content and consistent with recent literature reports.[32,33]

Fig. 3c shows the steady-state PL spectra of the different samples on quartz substrates without any protection layers on top and measured in humid air (50% humidity). While sample A does not show any PL, the PL intensity increases from sample B to E and the peak position stays constant around 780 nm (1.59 eV).

Influence of PbI_2 on degradation of perovskite films

A second series of XRD measurements were performed to explore the film stability and the degree of degradation of the pristine $CH_3NH_3PbI_3$ and PbI_2 containing $CH_3NH_3PbI_3$ films over time in humid air. Fig. 4 shows the typical XRD patterns of $CH_3NH_3PbI_3$ samples A (no PbI_2), B (least PbI_2) and E (highest PbI_2) over time in a controlled 50% humid atmosphere. For sample A, strong characteristic peaks of the $CH_3NH_3PbI_3$ tetragonal structure are observed on the first day, after 15 days and after 30 days of storage. There is no observable change in the XRD pattern between the pristine $CH_3NH_3PbI_3$ film and the $CH_3NH_3PbI_3$ film after 15 days of storage at 50% humidity as well as after 30 days. For sample B, the diffraction characteristic peaks of the $CH_3NH_3PbI_3$ structure (at 2θ = 14.2°) along with PbI_2 characteristic peak at a 2θ value of 12.7° are observed on day 1. After storage of 15 days in 50% humidity, the intensity of the (110) peak at a 2θ value of 14.2° is slightly decreased and the PbI_2 peak intensity is increased. After 30 days of storage, the peak intensity of PbI_2 is significantly increased with a radical decrease of the $CH_3NH_3PbI_3$ (110) peak intensity. For sample E (the highest PbI_2 content with respect to $CH_3NH_3PbI_3$), the $CH_3NH_3PbI_3$ diffraction characteristic (110) peak intensity is lower than the PbI_2 characteristic peak on the first day. The (110) peak intensity is drastically decreased with an increase in the PbI_2 peak after 15 days of storage of sample E. After 30 days, the PbI_2 peak intensity is increased and $CH_3NH_3PbI_3$ peaks appear with a very low intensity.

The degradation mechanism of $CH_3NH_3PbI_3$ in the presence of water, high and low relative humidity has been already suggested by different authors in reactions (1)–(3) below.[34–40]

According to the literature, pure $CH_3NH_3PbI_3$ likely reacts with water from humid air and forms non-soluble PbI_2 and aqueous CH_3NH_3I (reaction (1)).[35,36] At higher (>80%) humidity $CH_3NH_3PbI_3$ reacts with water and forms $(CH_3NH_3)_4PbI_6{\cdot}2H_2O$ (reaction (2)).[34,37,38] In the presence of lower (<50%) humidity $CH_3NH_3PbI_3$ decomposes into CH_3NH_2, HI, PbI_2 with an irreversible reaction as given in eqn (3).[39,40]

$$CH_3NH_3PbI_3(s) \xrightarrow{H_2O(aq)} PbI_2(s) + CH_3NH_3I(aq) \quad (1)$$

$$4CH_3NH_3PbI_3 + 2H_2O \xrightleftharpoons{H_2O(>80\%)} (CH_3NH_3)_4PbI_6\cdot 2H_2O + 3PbI_2 \quad (2)$$

$$(CH_3NH_3PbI_3)_n \xrightarrow{H_2O\,(Low\,humidity)} \left[(CH_3NH_3PbI_3)_{n-1}(PbI_2)(HI)\right] + CH_3NH_2(g) \quad (3)$$

$$(CH_3NH_3PbI_3)_n + PbI_2 \xrightarrow{H_2O(\leq 50\%\,HR)} \left[(CH_3NH_3PbI_3)_{n-y}(PbI_2)_{y+1}(HI)_y\right] + yCH_3NH_2(g) \quad (4)$$

In our experiment, the $CH_3NH_3PbI_3$ films (sample A) are highly air-stable robust materials that do not show any PbI_2

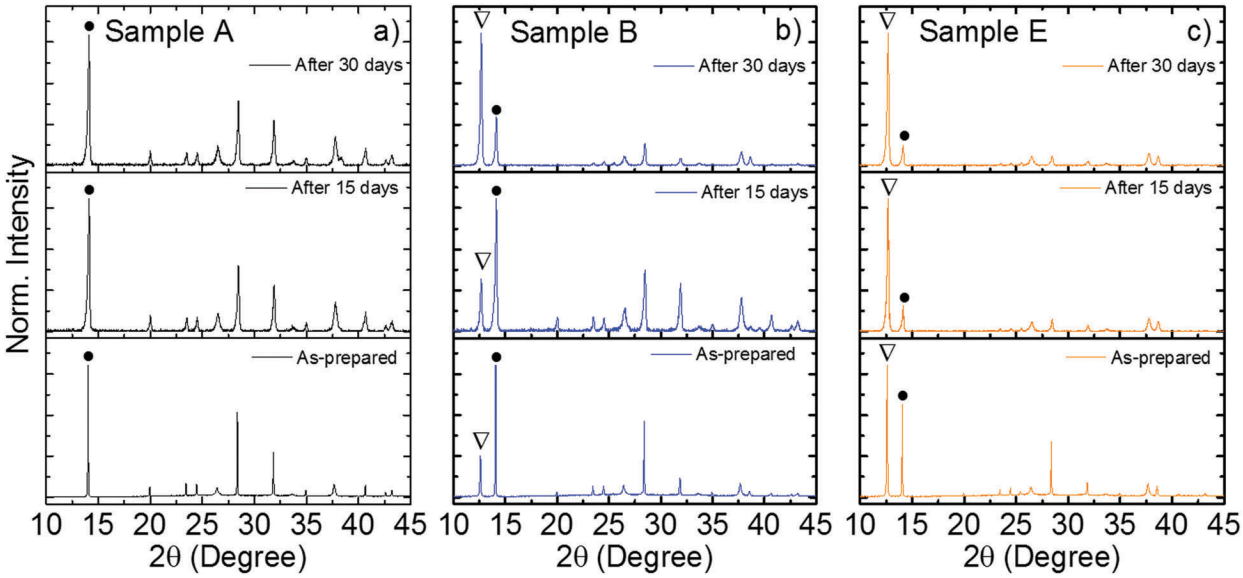

Fig. 4 XRD patterns of pure and PbI_2 containing $CH_3NH_3PbI_3$ samples obtained upon air exposure for different periods (at 50% humidity), (a) samples A, (b) sample B and (c) sample E. The peaks assigned: black dot for $CH_3NH_3PbI_3$ and open triangle for PbI_2.

peaks due to degradation for up to 30 days, similar to the observations of Christians *et al.*[34] However, when PbI_2 is present in $CH_3NH_3PbI_3$, most probably a non-reversible reaction (4) takes place producing volatile (CH_3NH_2). Thus, as observed in our experiments, this degradation process is faster for the excess PbI_2 content in $CH_3NH_3PbI_3$ compared to the PbI_2-free $CH_3NH_3PbI_3$ samples. Based on these observations, it is clear that PbI_2 acts as a catalyst for the degradation of $CH_3NH_3PbI_3$ as we suggest in the reaction (4).

To understand the stability of the $CH_3NH_3PbI_3$ films stored under ambient condition with 50% humidity, we tracked the normalized absorbance of the film at 700 nm for samples A, B, C, D and E for a month (Fig. 5a). The complete spectral change for each sample is given in Fig. S5 (ESI†). Absorbance measurements made on $CH_3NH_3PbI_3$ films with different amounts of PbI_2 content generated by annealing of the $CH_3NH_3PbI_3$ sample show the typical spectral features of $CH_3NH_3PbI_3$ with PbI_2 on first day. Thus the rate of decrease of the absorbance intensity at 700 nm increases from sample B to E and it is the highest for sample E. To summarize the changes in absorption with storage time, we have additionally plotted the change in optical absorbance with storage time in 50% humidity for the two extreme cases; for sample A without any residual PbI_2 and E having an appreciable amount of PbI_2 (Fig. 5b). For sample A, overlap of the optical spectra for the first 15 days is observed and only a negligible change is observed after 30 days. The optical absorption curves in Fig. 5a and Fig. S5a (ESI†) do not show characteristic peaks from PbI_2, however the absorption curves show a slight decline after 30 days, even though no degradation could be confirmed in XRD studies. Thus we believe that the observed negligible decline of absorbance after 30 days could be due to the surface interaction of the perovskite with humidity in those samples during optical measurements. Additionally, at the very first degradation stage, where only negligible PbI_2 is present, PbI_2 may not be detected by our used XRD set up, but it may be sensitive enough for optical measurements. In contrast, for sample E the decrease is much stronger and the shoulder at 500 nm (arising out of PbI_2 absorption, see Fig. 3a) gets more pronounced with storage time. Sample A shows the least change in the optical spectra. The increased rate of absorbance loss indicates that PbI_2 in the samples B to E accelerates the rate of degradation.

The PL emission studies on samples without and with PbI_2 content give further insight into the role of PbI_2 in degradation. All the samples were stored under the same conditions of 50% humidity for about 60 days. We observed that samples A to E show different evolutions in the integrated PL intensity over time (Fig. 5c). The pure $CH_3NH_3PbI_3$ (sample A) with hardly any initial PL emission (Fig. 3c) continuously increased in the PL intensity with a storage time of up to 58 days.

For sample B, PL emission is observed from the first day onwards and it increased up to 38 days; and afterwards decreased continuously. A similar trend is observed for sample C, yet the PL peak emission is reached already after 20 days. Sample D (not shown here) and E have similar PL emission spectra over time. For both samples, PL emission decreased from the first day onwards. The integrated intensity first increases and reaches its maximum even before 20 days for both D and E samples. The peak position shifts to shorter times with increasing excess PbI_2 and the peak intensity reduces. This indicates that whenever samples have some amount of PbI_2, it

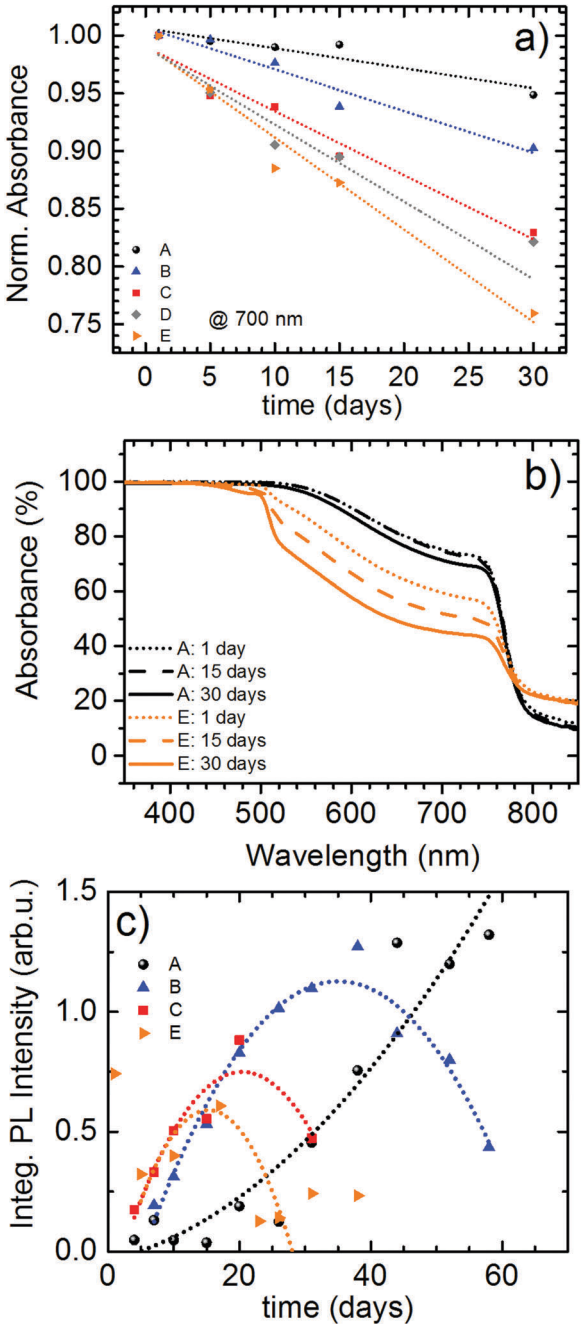

Fig. 5 (a) Normalized absorbance at 700 nm of $CH_3NH_3PbI_3$ samples A to E stored under 50% RH as a function of time (for 0–30 days); dotted lines are linear fits to guide the eye. (b) Comparative decay of UV-Visible absorption of samples A and E stored under 50% relative humidity for 0, 15 and 30 days. (c) Integrated PL intensity for the different samples over storage time under 50% relative humidity. Dotted lines are 2nd order polynomial fits to serve as guide to the eye (see ESI,† Table S2 for fit parameters).

helps to increase PL emission, but also deteriorates the PL efficiency for a long term. The actual mechanisms of PbI_2 in PL enhancement are still topics of ongoing discussion. As widely accepted in the literature, the main mechanism is related to trap-filling effects.[41] Degradation of the perovskite structure is accompanied by a blue shift of the PL peak position, which is also seen here (see S6 in ESI†).[42] Moreover, the evolution of the PL intensity with time correlates with the content of PbI_2. This suggests that a small fraction of PbI_2 reduces non-radiative recombination, a higher fraction leads to a decrease in the PL intensity. The relative change in PL is a sensitive tool that indicates the degradation of the $CH_3NH_3PbI_3$ films.

Influence of the PbI_2 content on solar cell parameters and hysteresis

To comparatively study the influence of the PbI_2 content on the photovoltaic parameters, simple planar devices (glass/FTO/c-TiO_2/$CH_3NH_3PbI_3$/spiro-OMeTAD/Au) without any mesoporous TiO_2 layers were prepared using samples A, B, C, D and E under N_2 and investigated. The *J*/*V* plots of the best devices are illustrated in Fig. 6. All of the data presented here are obtained in the reverse scan from +2.0 to −1.0 V at 100 mV s^{-1}. The solar cell parameters of the best-performing devices and average PCE values (of 8 devices for each type from 2 batches) are listed in Table 1. The scattering of solar cell parameters for devices with samples A to E is given in Table S3 (ESI†). The device based on sample A exhibits a J_{sc} of 15.18 mA cm^{-2}, a V_{oc} of 0.90 V, and 69% FF with a maximum PCE of 10.80% (average: 9.12% and constant output PCE at V_{MPP} = 9.4%). For B, where even though a small amount of $CH_3NH_3PbI_3$ has been consumed for the formation of PbI_2, the J_{sc} (17.22 mA cm^{-2}) and V_{oc} (0.94 V) values are improved and consequently a higher PCE of 11.00% (average: 10.17%) is obtained. For devices based on samples C to E (with an increase in the PbI_2 content), J_{sc} decreases from 16.15 to 13.30 mA cm^{-2}, V_{oc} from 0.94 to 0.87 V as well as the FF from 66.88 to 56.37%. The decrease of J_{sc} from sample B to E is obvious because of a considerable reduction of the $CH_3NH_3PbI_3$ material in the active layer by decomposition and formation of PbI_2 upon annealing. It can be observed from Fig. 6 that $CH_3NH_3PbI_3$ solar cells fabricated from both samples, A without PbI_2 as well as B with PbI_2, exhibit excellent performance. The difference in average values for all the parameters is not considerable, even though the sample B exhibits the best performance. This is in agreement with numerous reports, which suggested to add a small amount of PbI_2 to improve the solar cell performance. Furthermore, the series and shunt resistances (R_s and R_{sh}) of the various devices were determined from illuminated *J*/*V* curves at V_{oc} and J_{sc}, respectively, and are listed in Table 1. From sample A to C, the R_s value decreased from 8.33 to 5.78 Ω cm^2, and it again increases from sample C to E, with an increase in the PbI_2 content. This has an obvious detrimental effect on charge transport as observed in the low J_{sc} and FF values. Among samples A to D, the device using sample A has the lowest R_{sh} value, which suggests that sample A has the highest carrier recombination within the device for the given geometry and contacts.

For perovskite solar cells containing perovskite/TiO_2 interfaces, the *J*/*V* data obtained depend on the scan rate, forward or backward sweep directions as well as the voltage of equilibration under illumination. This observed hysteresis causes usually drastic changes in the FF depending on the measurement protocol. Consequently the PCE calculated from the reverse scan (from +2.0 to −1.0 V) seems to be higher than that for the forward scan (from −1.0 to +2.0 V). In this regard, various measurement protocols have been recommended.[43,44] For the device application point of view, it is important to know why perovskite solar cells have hysteresis and how it can be reduced. Therefore, we examined, if there is an influence of generated PbI_2 on *J*/*V* hysteresis. In the course of *J*/*V* studies of devices with increasing PbI_2 content, we observe an enhancement in photovoltaic hysteresis (Fig. 6). From sample A to E, a decrease in J_{sc} mainly results from decreasing absorption due to gradual increasing conversion of $CH_3NH_3PbI_3$ to PbI_2. But the FF in the reverse scan increases as

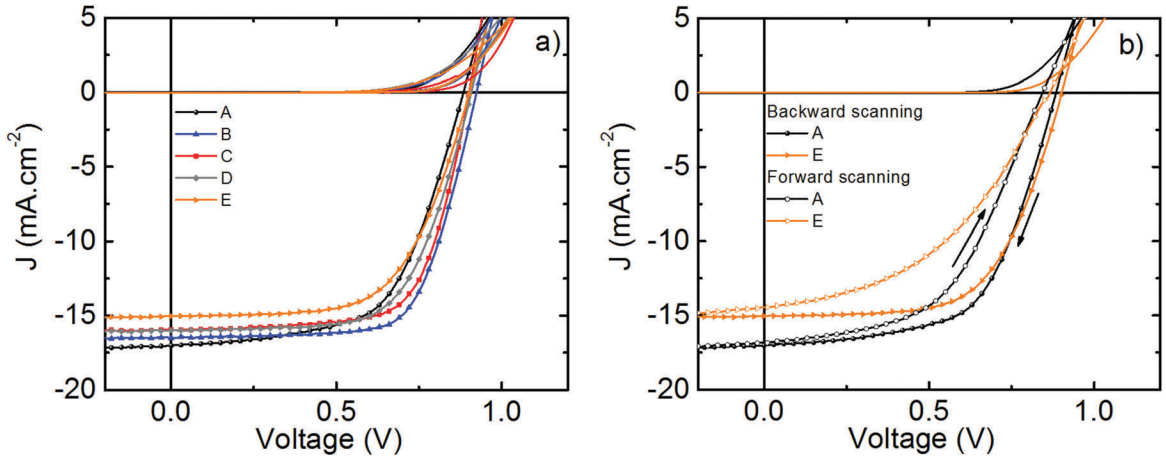

Fig. 6 (a) *J*/*V* characteristics of $CH_3NH_3PbI_3$ solar cell for samples A to E, (b) influence of scanning directions on *J*/*V* characteristics of the $CH_3NH_3PbI_3$ solar cell for samples A and E. For the forward bias from −1 V to +2 V and for the reverse bias from +2 V to −1 V measured under simulated AM 1.5 100 mW cm^{-2} sun light at scan rate 100 mV s^{-1}; the hysteresis indices for $CH_3NH_3PbI_3$ solar cells employing samples A to E with increasing PbI_2 content are given in Table 1. The *J*/*V* assigned: filled symbol for reverse scan and open symbol for forward scan.

Table 1 Photovoltaic parameters of the devices prepared from different $CH_3NH_3PbI_3$ samples. The devices were measured directly after preparation under a nitrogen atmosphere. The average of 8 devices is given in brackets for all parameters. All the devices were measured under 100 mW cm^{-2} AM 1.5 irradiation at a scan rate of 100 mV s^{-1} in reverse bias. HI: hysteresis index

Samples	J_{sc} (mA cm^{-2}) $\pm\sigma$	V_{oc} (V)	FF (%)	PCE (%)	R_s (Ω cm^2)	R_{sh} (Ω cm^2)	HI
A (0 min)	16.7 (15.1 ± 0.8)	0.94 (0.92 ± 0.03)	68 (65 ± 4)	10.8 (9.1 ± 1.1)	8.33	831	0.22
B (15 min)	17.2 (16.3 ± 0.8)	0.94 (0.94 ± 0.02)	68 (67 ± 2)	11.0 (10.2 ± 0.5)	7.41	2219	0.27
C (30 min)	16.6 (16.2 ± 0.4)	0.95 (0.94 ± 0.01)	67 (64 ± 4)	10.6 (9.7 ± 0.7)	5.78	1875	0.34
D (45 min)	14.9 (14.8 ± 0.3)	0.90 (0.90 ± 0.02)	68 (61 ± 6)	9.1 (8.2 ± 0.7)	7.87	7013	0.40
E (60 min)	12.81 (13.3 ± 0.8)	0.92 (0.87 ± 0.04)	59 (56 ± 6)	7.0 (6.5 ± 0.5)	8.33	2146	0.43

a consequence of the sweep direction. Additionally, we observed an increase of hysteresis from sample A to E. Hysteresis is measured in terms of the dimensionless hysteresis index factor as defined by Sanchez *et al.* to compare the different solar cells by taking the photocurrent values at 50% of V_{oc}.[45] Kim *et al.* modified this index by considering the fact that hysteresis has a pronounced effect of change in photocurrent at 80% of V_{oc}.[46] We used following hysteresis index to correlate the PbI_2 content in $CH_3NH_3PbI_3$ with *J*/*V* hysteresis as calculated from eqn (5).

$$\text{Hysteresis index} = \frac{J_R(0.8V_{oc}) - J_F(0.8V_{oc})}{J_R(0.8V_{oc})} \quad (5)$$

where $J_R(0.8V_{oc})$ and $J_F(0.8V_{oc})$ are photocurrent values for reverse and forward scans at 80% of the V_{oc} value. The corresponding hysteresis indices for devices A to E are shown in Table 1. Upon comparing devices with similar J_{sc} and PCE (devices A and B), the hysteresis index is smaller for device A without PbI_2. It is higher for devices C, D and E. For comparable devices, thus the hysteresis index increased with an increase in the PbI_2 content in $CH_3NH_3PbI_3$. Here, prolongation of the annealing time may enhance the density of the defects and deteriorate the interface of $TiO_2/CH_3NH_3PbI_3$, which would also result in the hysteresis. Yu *et al.*[47] observed that the hysteresis index in $CH_3NH_3PbI_3$ devices is higher for samples having the residual PbI_2 content compared to samples without residual PbI_2. Jacobsson *et al.*[23] also observed that the hysteresis was generally higher in the PbI_2-rich samples whereas it was rather small in the stoichiometric and in most of the PbI_2-deficient samples which was attributed to difference in ion migration at the grain boundaries. Meanwhile, there's hysteresis for pure $CH_3NH_3PbI_3$ solar cells, indicating that there is still hysteresis in the devices even though the PbI_2 is absent. Although the origin of hysteresis effects is still unclear, one of the suggested reasons for this hysteretic behavior is dominantly associated with the perovskite material itself.[48] We firmly believe that by reducing the concentration of defects and their migration, the hysteresis can be suppressed considerably.

Device storage stability

The solar cell devices were stored under a N_2 atmosphere at room temperature without any further encapsulation. The *J*/*V* characteristics were measured for samples A to E for more than a month and the corresponding solar cell parameters are presented in Fig. 7. In general, the influence on V_{oc} and the FF as a function of time is not predominant and not considerably different for the different devices. But both J_{sc} and PCE exhibit

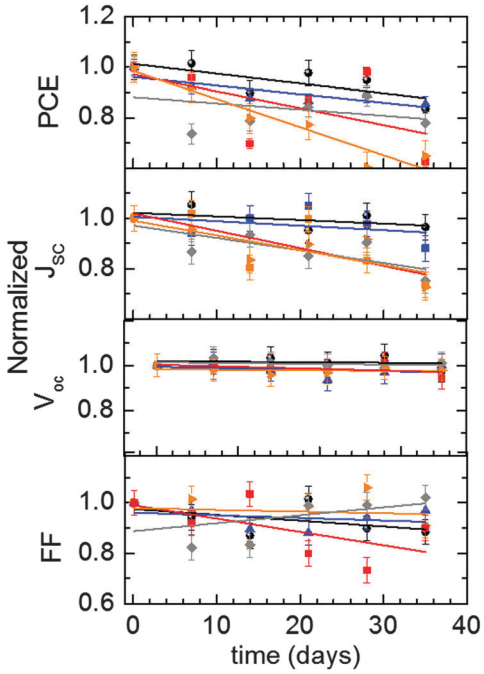

Fig. 7 Stacked plot of the normalized average performance parameters with different storage times for solar cells prepared from samples A (black dot), B (blue triangle), C (red square), D (gray square) and E (orange triangle).

considerable differences. For device A, J_{sc} increased from 15.18 to 16.10 mA cm^{-2} and V_{oc} increased from 0.91 to 0.96 V, resulting in a slight improvement of the PCE from 9.4 to 9.6% for the first seven days. After 14 days, the overall PCE slightly decreased to 9.03%. At the end of 35 days (840 h), the device parameters J_{sc}, V_{oc}, FF and PCE are almost constant and show a negligible decrease, which demonstrates the excellent durability of PbI_2-free samples.

For device B, J_{sc} shows a minor decrease (17 to 16.5 mA cm^{-2}) and V_{oc} remains almost the same, resulting in a slight decrease of the PCE from 11.00 to 9.88% for the first seven days. After 14 days, the overall PCE decreased drastically to 8.60%. At the end of 35 days, all the device parameters J_{sc}, V_{oc}, FF and PCE decreased up to 12% of their original values. For devices C to E, J_{sc} was decreased and V_{oc} fluctuated in the range of 0.91 to 0.94 V, resulting in a slight decrease of the PCE for all devices for the first seven days. After 14 days, the overall PCE decreased drastically with time. J_{sc} of sample A remains almost constant and consequently the PCE after 30 days remains almost constant.

But for the devices C, D and E, J_{sc} decreases up to 70% and accordingly PCE also goes down (in device C about 56% of the starting value). We did see a negative influence of the PbI_2 content on device storage stability of $CH_3NH_3PbI_3$ devices stored in a N_2 atmosphere. In contrast, Liu *et al.* did not observe any drastic decrease of the performance for encapsulated $CH_3NH_3PbI_3$ with and without residual PbI_2 devices.[27]

Conclusions

We have demonstrated that different amounts of excess PbI_2 generated by annealing of pure $CH_3NH_3PbI_3$ prepared using the MAI-vapor assisted method have detrimental effects on the $CH_3NH_3PbI_3$ film stability, even though $CH_3NH_3PbI_3$ devices with small excess PbI_2 can exhibit a higher power conversion efficiency. The XRD, absorbance spectroscopy and PL measurement techniques were employed for a qualitative fundamental study on the stability of $CH_3NH_3PbI_3$ films with and without PbI_2. We show that the $CH_3NH_3PbI_3$ samples without PbI_2 degrade very slowly compared to $CH_3NH_3PbI_3$ with additional PbI_2. The rate of degradation is increased with an increase in the PbI_2 content in $CH_3NH_3PbI_3$. Pure $CH_3NH_3PbI_3$ without additional PbI_2 shows a positive impact on the material stability as well as device storage stability, suggesting a route toward perovskite solar cells with prolonged device lifetimes and resistance to humidity. We have shown that storage stability of the devices in N_2 atmospheres and the degree of *J*/*V* hysteresis (difference in the *J*/*V* curves depending on scan directions) in solar cells are dependent on the PbI_2 content in $CH_3NH_3PbI_3$. This study provides elucidation of fundamental pathways in the perovskite film decomposition process, which can be avoided to get more stable materials and more commercially sustainable devices.

Conflicts of interest

There are no conflicts to declare.

Acknowledgements

Financial support by the German Federal Ministry of Education and Research BMBF (Project: 03SF0484C), the German National Science Foundation DFG (SFB 840, TH 807/6-1 and GRK 1640) and the Bavarian State Ministry of Science, Research, and the Arts for the Collaborative Research Network ''Solar Technologies go Hybrid'', are gratefully acknowledged.

References

1 NREL Solar Cells Efficiency Chart, www.nrel.gov/ncpv/images/efficiency_chart.jpg, 04/2017.
2 A. Ng, Z. Ren, Q. Shen, S. H. Cheung, H. C. Gokkaya, G. Bai, J. Wang, L. Yang, S. K. So, A. B. Djurišić, W. W.-f. Leung, J. Hao, W. K. Chan and C. Surya, *J. Mater. Chem. A*, 2015, **3**, 9223–9231.
3 K.-L. Wu, A. Kogo, N. Sakai, M. Ikegami and T. Miyasaka, *Chem. Lett.*, 2015, **44**, 321–323.
4 T. Leijtens, G. E. Eperon, S. Pathak, A. Abate, M. M. Lee and H. J. Snaith, *Nat. Commun.*, 2013, **4**, 2885.
5 Y. Han, S. Meyer, Y. Dkhissi, K. Weber, J. M. Pringle, U. Bach, L. Spiccia and Y.-B. Cheng, *J. Mater. Chem. A*, 2015, **3**, 8139–8147.
6 Y. H. Lee, J. Luo, R. Humphry-Baker, P. Gao, M. Grätzel and M. K. Nazeeruddin, *Adv. Funct. Mater.*, 2015, **25**, 3925–3933.
7 H. Zhou, Q. Chen, G. Li, S. Luo, T. B. Song, H. S. Duan, Z. Hong, J. You, Y. Liu and Y. Yang, *Science*, 2014, **345**, 542–546.
8 S. Lv, S. Pang, Y. Zhou, N. P. Padture, H. Hu, L. Wang, X. Zhou, H. Zhu, L. Zhang, C. Huang and G. Cui, *Phys. Chem. Chem. Phys.*, 2014, **16**, 19206–19211.
9 F. X. Xie, D. Zhang, H. Su, X. Ren, K. S. Wong, M. Gratzel and W. C. H. Choy, *ACS Nano*, 2015, **9**, 639–646.
10 Y. Zhou, M. Yang, W. Wu, A. L. Vasiliev, K. Zhu and N. P. Padture, *J. Mater. Chem. A*, 2015, **3**, 8178–8184.
11 W. Nie, H. Tsai, R. Asadpour, J. C. Blancon, A. J. Neukirch, G. Gupta, J. J. Crochet, M. Chhowalla, S. Tretiak, M. A. Alam, H. L. Wang and A. D. Mohite, *Science*, 2015, **347**, 522–525.
12 Q. Chen, H. Zhou, T. B. Song, S. Luo, Z. Hong, H. S. Duan, L. Dou, Y. Liu and Y. Yang, *Nano Lett.*, 2014, **14**, 4158–4163.
13 G. E. Eperon, V. M. Burlakov, P. Docampo, A. Goriely and H. J. Snaith, *Adv. Funct. Mater.*, 2014, **24**, 151–157.
14 J. Chen, T. Shi, X. Li, B. Zhou, H. Cao and Y. Wang, *Appl. Phys. Lett.*, 2016, **108**, 053302.
15 G. E. Eperon, S. D. Stranks, C. Menelaou, M. B. Johnston, L. M. Herz and H. J. Snaith, *Energy Environ. Sci.*, 2014, **7**, 982–988.
16 P. Docampo, F. C. Hanusch, S. D. Stranks, M. Döblinger, J. M. Feckl, M. Ehrensperger, N. K. Minar, M. B. Johnston, H. J. Snaith and T. Bein, *Adv. Energy Mater.*, 2014, **4**, 1400355.
17 Y. C. Kim, N. J. Jeon, J. H. Noh, W. S. Yang, J. Seo, J. S. Yun, A. Ho-Baillie, S. Huang, M. A. Green, J. Seidel, T. K. Ahn and S. I. Seok, *Adv. Energy Mater.*, 2016, **6**, 1502104.
18 J. Liu, S. Pathak, T. Stergiopoulos, T. Leijtens, K. Wojciechowski, S. Schumann, N. Kausch-Busies and H. J. Snaith, *J. Phys. Chem. Lett.*, 2015, **6**, 1666–1673.
19 C. Roldán-Carmona, P. Gratia, I. Zimmermann, G. Grancini, P. Gao, M. Graetzel and M. K. Nazeeruddin, *Energy Environ. Sci.*, 2015, **8**, 3550–3556.
20 D. H. Cao, C. C. Stoumpos, C. D. Malliakas, M. J. Katz, O. K. Farha, J. T. Hupp and M. G. Kanatzidis, *APL Mater.*, 2014, **2**, 091101.
21 J. Burschka, N. Pellet, S. J. Moon, R. Humphry-Baker, P. Gao, M. K. Nazeeruddin and M. Gratzel, *Nature*, 2013, **499**, 316–319.
22 W. A. Laban and L. Etgar, *Energy Environ. Sci.*, 2013, **6**, 3249–3253.
23 T. J. Jacobsson, J. P. Correa-Baena, E. Halvani Anaraki, B. Philippe, S. D. Stranks, M. E. Bouduban, W. Tress, K. Schenk, J. Teuscher, J. E. Moser, H. Rensmo and A. Hagfeldt, *J. Am. Chem. Soc.*, 2016, **138**, 10331–10343.
24 J. Xiong, B. Yang, R. Wu, C. Cao, Y. Huang, C. Liu, Z. Hu, H. Huang, Y. Gao and J. Yang, *Org. Electron.*, 2015, **24**, 106–112.

25 T. P. Gujar and M. Thelakkat, *Energy Technol.*, 2016, **4**, 449–457.
26 Y. Li, J. K. Cooper, R. Buonsanti, C. Giannini, Y. Liu, F. M. Toma and I. D. Sharp, *J. Phys. Chem. Lett.*, 2015, **6**, 493–499.
27 F. Liu, Q. Dong, M. K. Wong, A. B. Djurišić, A. Ng, Z. Ren, Q. Shen, C. Surya, W. K. Chan, J. Wang, A. M. C. Ng, C. Liao, H. Li, K. Shih, C. Wei, H. Su and J. Dai, *Adv. Energy Mater.*, 2016, **6**, 1502206.
28 F. Panzer, S. Baderschneider, T. P. Gujar, T. Unger, S. Bagnich, M. Jakoby, H. Bässler, S. Hüttner, J. Köhler, R. Moos, M. Thelakkat, R. Hildner and A. Köhler, *Adv. Opt. Mater.*, 2016, **4**, 917–928.
29 P. Docampo, J. M. Ball, M. Darwich, G. E. Eperon and H. J. Snaith, *Nat. Commun.*, 2013, **4**, 2761.
30 S. D. Stranks, V. M. Burlakov, T. Leijtens, J. M. Ball, A. Goriely and H. J. Snaith, *Phys. Rev. Appl.*, 2014, **2**, 034007.
31 H. Xie, X. Liu, L. Lyu, D. Niu, Q. Wang, J. Huang and Y. Gao, *J. Phys. Chem. C*, 2016, **120**, 215–220.
32 C. Wehrenfennig, M. Liu, H. J. Snaith, M. B. Johnston and L. M. Herz, *Energy Environ. Sci.*, 2014, **7**, 2269–2275.
33 D. Bi, A. M. El-Zohry, A. Hagfeldt and G. Boschloo, *ACS Photonics*, 2015, **2**, 589–594.
34 J. A. Christians, P. A. Miranda Herrera and P. V. Kamat, *J. Am. Chem. Soc.*, 2015, **137**, 1530–1538.
35 G. Niu, W. Li, F. Meng, L. Wang, H. Dong and Y. Qiu, *J. Mater. Chem. A*, 2014, **2**, 705–710.
36 B. Philippe, B.-W. Park, R. Lindblad, J. Oscarsson, S. Ahmadi, E. M. J. Johansson and H. Rensmo, *Chem. Mater.*, 2015, **27**, 1720–1731.
37 J. Yang, B. D. Siempelkamp, D. Liu and T. L. Kelly, *ACS Nano*, 2015, **9**, 1955–1963.
38 A. M. A. Leguy, Y. Hu, M. Campoy-Quiles, M. I. Alonso, O. J. Weber, P. Azarhoosh, M. van Schilfgaarde, M. T. Weller, T. Bein, J. Nelson, P. Docampo and P. R. F. Barnes, *Chem. Mater.*, 2015, **27**, 3397–3407.
39 L. Zhang and P. H. L. Sit, *J. Phys. Chem. C*, 2015, **119**, 22370–22378.
40 J. M. Frost, K. T. Butler, F. Brivio, C. H. Hendon, M. van Schilfgaarde and A. Walsh, *Nano Lett.*, 2014, **14**, 2584–2590.
41 H. He, Q. Yu, H. Li, J. Li, J. Si, Y. Jin, N. Wang, J. Wang, J. He, X. Wang, Y. Zhang and Z. Ye, *Nat. Commun.*, 2016, **7**, 10896.
42 D. Yamashita, T. Handa, T. Ihara, H. Tahara, A. Shimazaki, A. Wakamiya and Y. Kanemitsu, *J. Phys. Chem. Lett.*, 2016, **7**, 3186–3191.
43 J. A. Christians, J. S. Manser and P. V. Kamat, *J. Phys. Chem. Lett.*, 2015, **6**, 852–857.
44 E. Zimmermann, K. K. Wong, M. Müller, H. Hu, P. Ehrenreich, M. Kohlstädt, U. Würfel, S. Mastroianni, G. Mathiazhagan, A. Hinsch, T. P. Gujar, M. Thelakkat, T. Pfadler and L. Schmidt-Mende, *APL Mater.*, 2016, **4**, 091901.
45 R. S. Sanchez, V. Gonzalez-Pedro, J. W. Lee, N. G. Park, Y. S. Kang, I. Mora-Sero and J. Bisquert, *J. Phys. Chem. Lett.*, 2014, **5**, 2357–2363.
46 H. S. Kim and N. G. Park, *J. Phys. Chem. Lett.*, 2014, **5**, 2927–2934.
47 H. Yu, H. Lu, F. Xie, S. Zhou and N. Zhao, *Adv. Funct. Mater.*, 2016, **26**, 1411–1419.
48 M. L. Petrus, J. Schlipf, C. Li, T. P. Gujar, N. Giesbrecht, P. Müller-Buschbaum, M. Thelakkat, T. Bein, S. Hüttner and P. Docampo, *Adv. Energy Mater.*, 2017, 1700264.

Supporting information for Physical Chemistry Chemical Physics

The Role of PbI_2 on $CH_3NH_3PbI_3$ Perovskite Stability, Solar Cell Parameters and Device Degradation

Tanaji P. Gujar[a], Thomas Unger[b], Andreas Schönleber[c], Martina Fried[a], Fabian Panzer[b], Sander van Smaalen[c], Anna Köhler[b] and Mukundan Thelakkat[a,*]

[a]*Applied Functional Polymers, Macromolecular Chemistry I, University of Bayreuth, 95447 Bayreuth, Germany.*

[b]*Experimental Physics II, University of Bayreuth, 95447 Bayreuth, Germany.*

[c]*Laboratory of Crystallography, University of Bayreuth, 95447 Bayreuth, Germany.*

*e-mail: Mukundan.Thelakkat@uni-bayreuth.de

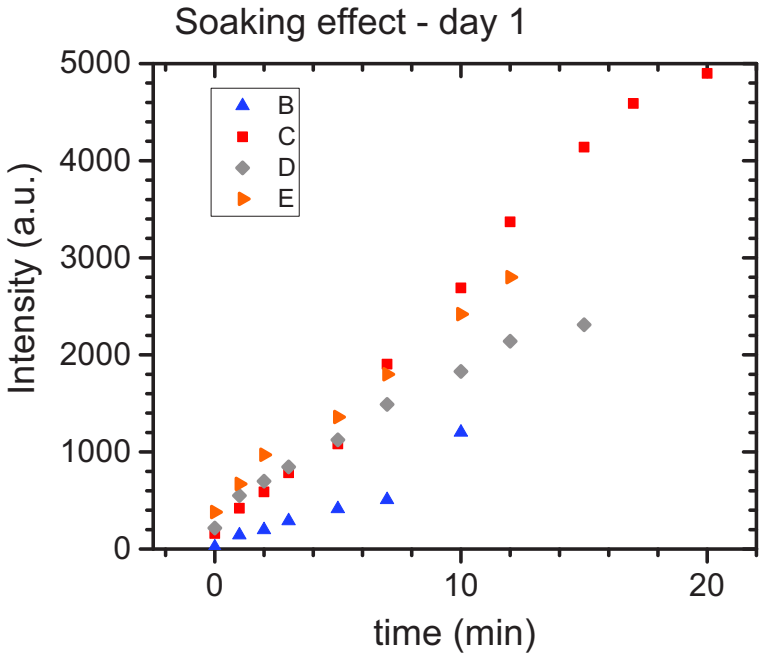

Figure S1. PL peak intensity for samples B to E with light soaking with 485 nm laser light (LDH-D-C-485, PicoQuant GmbH) with an intensity of about 450 $mWcm^{-2}$.

Calculation of PbI_2 content from optical absorption using reference measurements

We prepared six reference samples from PbI_2 and after complete conversion to $CH_3NH_3PbI_3$, we measured the optical density of these reference films. By comparing the optical density at 520 nm of these reference films and our samples A to E, a correlation of the real amount of $CH_3NH_3PbI_3$ in each sample could be obtained. From these calculated values, the amount of PbI_2 in A to E (in nm) is further calculated by using the calibration curve shown in fig.S2 a) using the conversion factor of 1.78 (slope of curve).

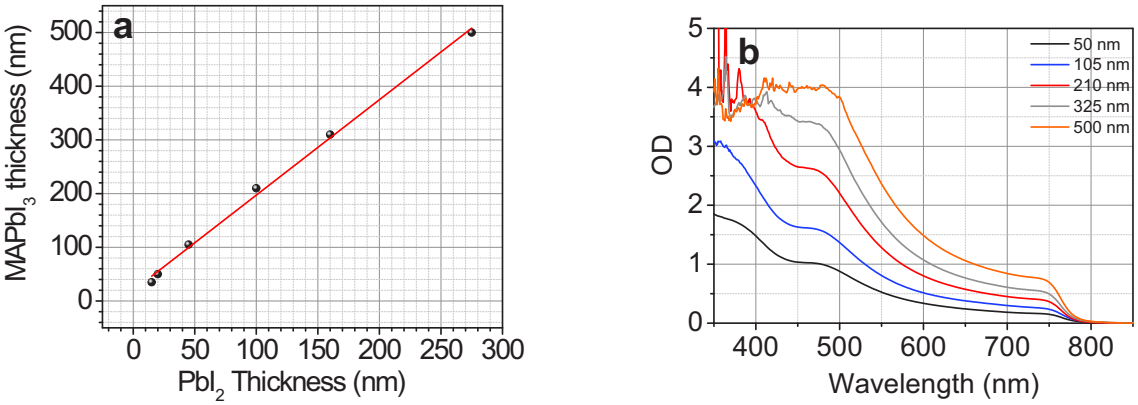

Figure S2. (a) Final perovskite film thickness as a function of the thickness of the precursor PbI_2 film, as measured by dektak profilometry; (b) absorbance spectra of these reference films from (a).

Comparing the thicknesses PbI_2 and $CH_3NH_3PbI_3$, it can be seen that the thickness of the perovskite is almost twice that of the PbI_2 precursor (slope= 1.78). Thus the calibration curve presented in Fig. S2a) gives an excellent method to calculate the amount of $CH_3NH_3PbI_3$ thickness arising from a definite thickness of PbI_2. Figure S2 b shows the absorption spectra of the perovskite films for different film thickness of $CH_3NH_3PbI_3$.

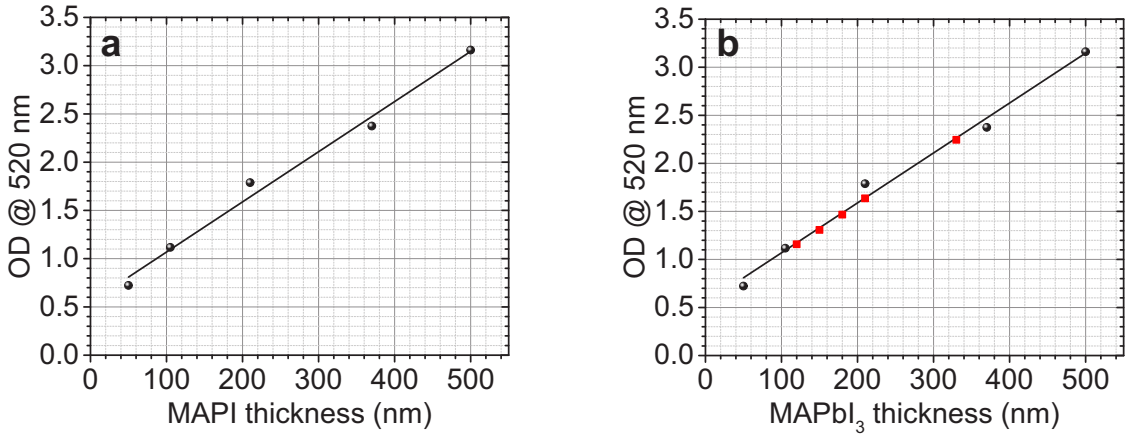

Figure S3. (a) Optical density at 520 nm as a function of the thickness $CH_3NH_3PbI_3$ reference films and (b) optical density values of samples A, B, C, D and E at 520 nm plotted as red points. Plot b) clearly shows that we can assess the amount of real $CH_3NH_3PbI_3$ existing in the films.

In fig. S3 a), the optical density at 520 nm of the reference films are increasing monotonically with $CH_3NH_3PbI_3$ thickness. The linear increase in optical density demonstrates the excellent control over film thickness. We extrapolated the optical density on graph a) and obtained thickness of $CH_3NH_3PbI_3$ and PbI_2 and listed in Table S1.

Table S1. Extraction of PbI_2 wt% from annealed $CH_3NH_3PbI_3$ films. All samples have initial thickness of about 330 nm of $CH_3NH_3PbI_3$.

Sample	$CH_3NH_3PbI_3$ thickness (nm) calculated from OD	$CH_3NH_3PbI_3$ thickness consumed (nm)	Calculated PbI_2 thickness (nm)[a]	Calculated PbI_2 (wt%)	
				from absorption	from XRD
A	330	0	0	0	0
B	210	120	67.54	24.34	21
C	180	150	84.43	31.93	34.3
D	150	180	101.31	40.31	46.5
E	120	210	118.20	49.62	47.6

[a] calculated from fig. S2 a) using the conversion factor of 1.78

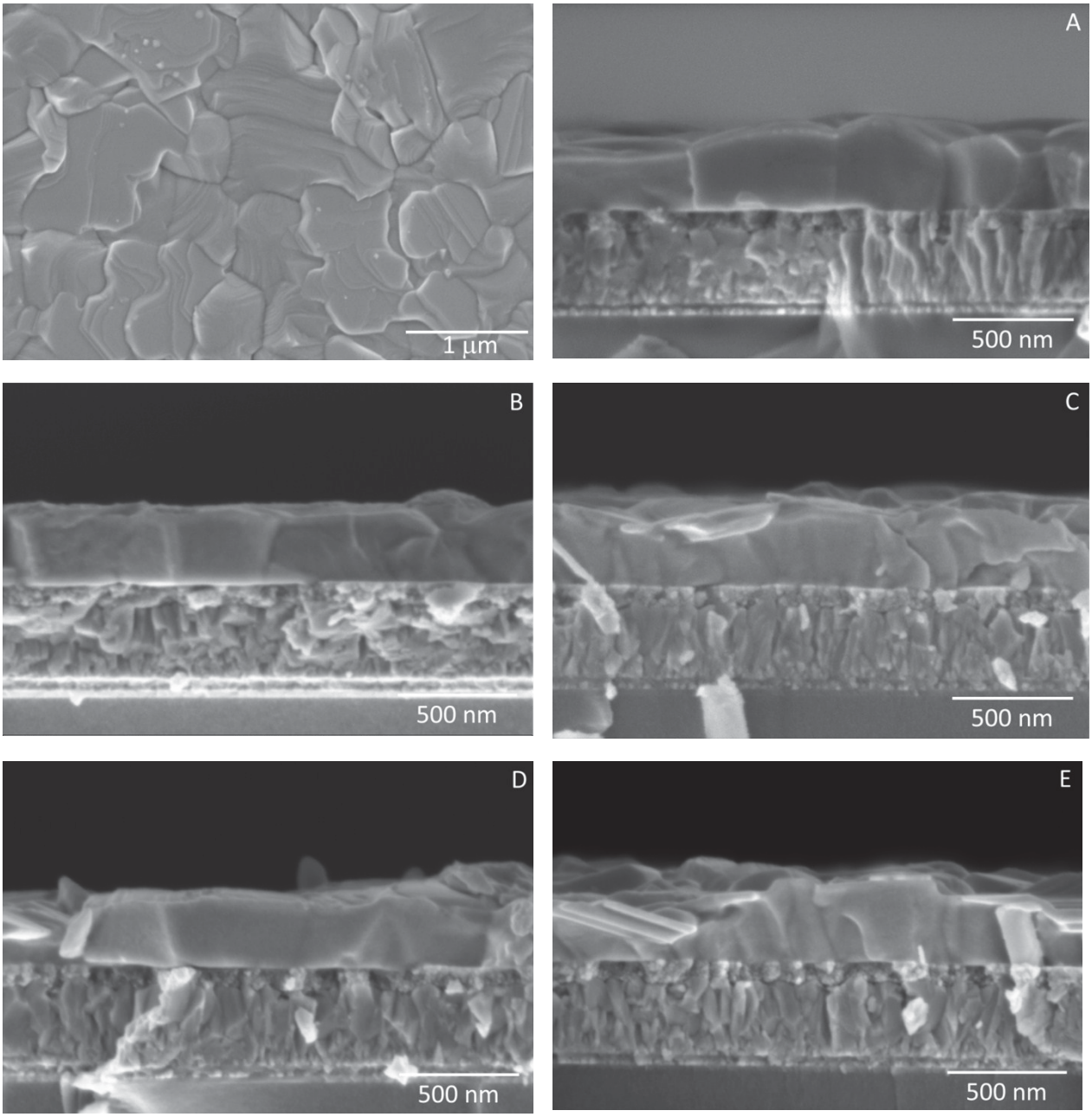

Figure S4. Surface SEM of sample D and cross-section SEM of samples A to E.

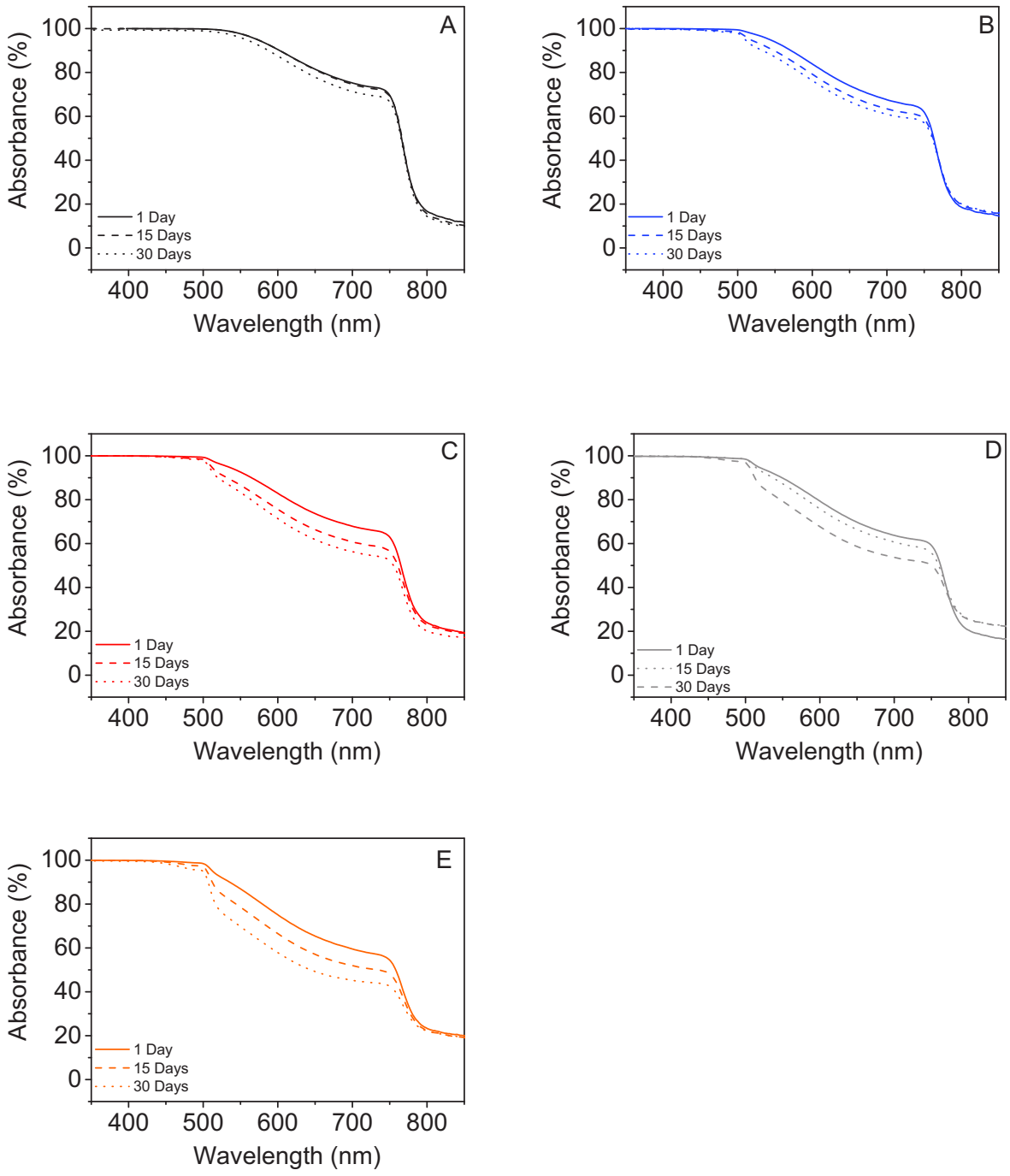

Figure S5. UV-Visible absorption spectra of the $CH_3NH_3PbI_3$ layers for different period of air exposure (at 50% humidity) for samples A, B, C, D and E.

Table S2. Polynomial fit parameters y=a*x^2+b*x+c

Sample	a	b	C
A	330	6243	-30589
B	-1174	82547	-345213
C	-2453	97215	-219069
E	-2692	73276	512

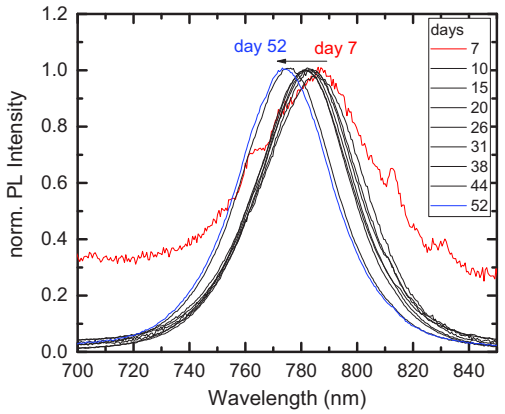

Figure S6. Normalized PL emission spectra for sample B stored under 50% % relative humidity for 7-52 days

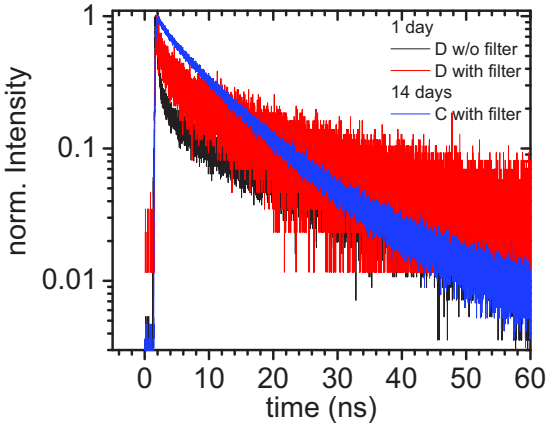

Figure S7. TRPL transients for sample D with (red line) and without (black line) filter for the laser scatter. Blue line shows sample C aged for 14 days period in air exposure (at 50% humidity).

Figure S8. a) The influence of scan rate and b) hysteresis along with c) steady state output at V_{mmp} of device A are shown.

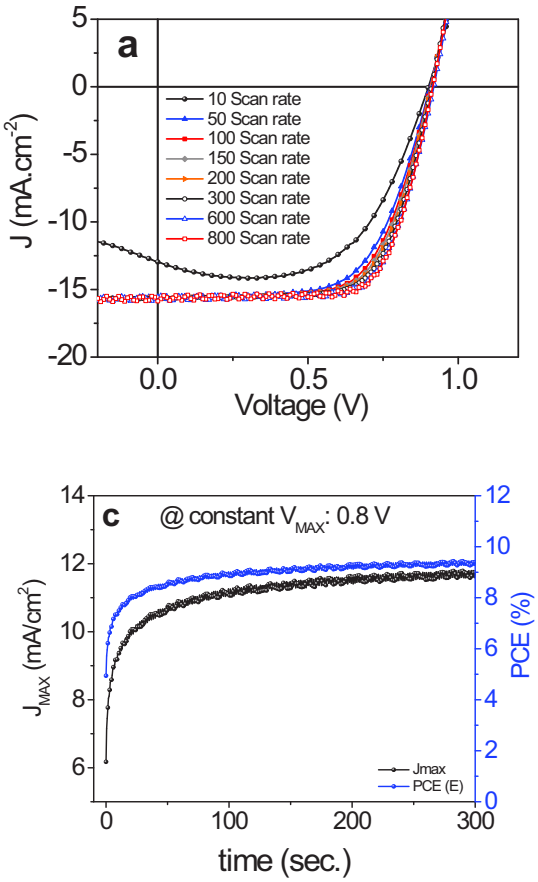

Table S3. Statistics regarding photovoltaic parameters of 8 devices (2 batches of 4 each) measured under 100 mW.cm^{-2} simulated AM1.5G illumination for sample A, B, C, D and E at scan rate 100 mV.S^{-1}.

Sample	Cell	J_{sc} [mA.cm^{-2}]	V_{oc} [V]	FF [%]	PCE [%]
A	1	15.14	0.93	66.08	9.32
	2	14.00	0.896	57.08	7.16
	3	14.74	0.94	67.00	9.33
	4	16.72	0.94	68.43	10.80
	5	15.38	0.94	66.76	9.69
	6	14.48	0.88	61.80	7.92
	7	15.18	0.90	69.03	9.39
	8	15.08	0.90	69.36	9.37
	Average	15.10	0.92	65.28	9.12

Sample	Cell	J_{sc} [mA.cm^{-2}]	V_{oc} [V]	FF [%]	PCE [%]
B	1	15.16	0.94	67.32	9.64
	2	17.22	0.94	67.70	11.00
	3	15.05	0.90	69.38	9.36
	4	16.19	0.93	66.71	10.06
	5	16.72	0.93	65.93	10.28
	6	16.75	0.93	65.73	10.26
	7	16.33	0.95	65.68	10.19
	8	16.70	0.95	66.56	10.56
	Average	16.26	0.94	66.88	10.17

Sample	Cell	J_{sc} [mA.cm^{-2}]	V_{oc} [V]	FF [%]	PCE [%]
C	1	15.46	0.940	62.13	9.03
	2	15.75	0.950	65.67	9.83
	3	16.75	0.93	66.31	10.35
	4	16.13	0.950	57.58	8.82
	5	16.21	0.94	65.43	9.97
	6	16.17	0.95	66.38	10.20
	7	16.59	0.95	67.11	10.58
	8	16.13	0.94	58.66	8.90
	Average	16.15	0.94	63.66	9.71

Sample	Cell	J_{sc} [mA.cm^{-2}]	V_{oc} [V]	FF [%]	PCE [%]
D	1	14.63	0.900	52.65	6.93
	2	15.39	0.920	55.96	7.92
	3	14.48	0.884	61.80	7.92
	4	14.59	0.920	62.05	8.33
	5	14.74	0.90	64.19	8.48

	6	14.79	0.90	67.56	8.96
	7	14.85	0.90	68.43	9.11
	8	14.97	0.92	56.06	7.72
	Average	14.81	0.90	61.09	8.17

Sample	Cell	J_{sc} [mA.cm^{-2}]	V_{oc} [V]	FF [%]	PCE [%]
E	1	13.95	0.840	58.74	6.88
	2	14.33	0.810	47.49	5.51
	3	13.46	0.830	54.19	6.05
	4	12.56	0.860	58.00	6.27
	5	14.50	0.872	54.35	6.87
	6	12.81	0.920	59.01	6.96
	7	14.63	0.900	52.65	6.93
	8	10.19	0.91	66.51	6.15
	Average	13.30	0.87	56.37	6.45

Method to determine the percentage of PbI_2 content in $CH_3NH_3PbI_3$ by XRD

K^{th} peak of phase i

L^{th} peak of phase j

$$\frac{I_{iK}}{I_{jL}} = \frac{G_{iK}}{G_{jL}} \cdot \frac{v_i}{v_j} = \frac{G_{iK}}{G_{jL}} \frac{\rho_i}{\rho_j} \cdot \frac{x_i}{x_j}$$

v_i is the volume concentration and x_i the mass concentration of phase i

with $G_i(hkl) = L_i(\theta) \cdot P_i(\theta) \cdot y_i H_i |F_i(hjk)|^2$

Polarization factor for Bragg-Brentano geometry with incident beam monochromator $P(\theta)$

$2\theta_M$ Bragg angle of monochromator $\theta_M = 13.640°$, $2\theta_M = 27{,}28°$, $cos^2(2\theta_M) = 0.789$

$$L(\theta) = \frac{1}{sin^2(\theta)\cos(\theta)} \qquad P(\theta) = \frac{1 + cos^2(2\theta_M)cos^2(2\theta)}{1 + cos^2(2\theta)_M}$$

$$\frac{I_{MAPbI_3}}{I_{PbI_2}} = \frac{G_{iK}}{G_{jL}}$$

$$\frac{I_{MAPbI_3}}{I_{PbI_2}} = \left(\frac{L_{MAPbI_3}(\theta)}{L_{PbI_2}(\theta)} \cdot \frac{P_{MAPbI_3}(\theta)}{P_{PbI_2}(\theta)} \frac{H_{MAPbI_3}}{H_{PbI_2}} \frac{\left|F_{MAPbI_3}\right|^2}{\left|F_{PbI_2}\right|^2} \right) \left(\frac{\rho_{MAPbI_3}}{\rho_{PbI_2}} \right)^{-1} \frac{x_{MAPbI_3}}{x_{PbI_2}}$$

L() is the Lorentz factor, P is the polarization factor, H(hkl) is the plane multiplicity, F(hkl) is the structure factor of the plane (hkl),

PbI_2:	001	$2\theta = 12.645°$
		$\theta = 6.323°$
$CH_3NH_3PbI_3$:	110	$2\theta = 14.110°$
	002	$\theta = 7.055°$

$$\frac{L_{MAPbI_3}}{L_{PbI_2}} = \left(\frac{82.949}{66.796} \right)^{-1} = \frac{1}{1.242} = 0.805$$

Polarization factor P(θ) with $\theta_M = 13.640°$

$$P(\theta) = \frac{1 + 0.7899 * cos^2(2\theta)}{1.7899}$$

$P_{MAPbI_3}(7.055°) = 0.9738$ $P_{PbI_2}(6.323) = 0.9789$ $\frac{P_{MAPbI_3}}{P_{PbI_2}} = \frac{0.9738}{0.9789} = 0.995$

$H_{MAPbI_3} \cdot |F_{MAPbI_3}|^2 = H_{MAPbI_3}(110) \cdot |F_{MAPbI_3}(110)|^2 + H_{MAPbI_3}(002) \cdot |F_{MAPbI_3}(002)|^2$

$= 4 * 313^2 + 2 * 338^2 = 620364$

$H_{PbI_2} \cdot |F_{PbI_2}|^2 = H_{MAPbI_2}(001) \cdot |F_{MAPbI_2}(001)|^2 = 2 * 287^2 = 164738$

Ration of densities

$$\frac{\rho_{MAPbI_3}}{\rho_{PbI_2}} = \frac{4.17\,{}^{g}/_{cm^3}}{6.16\,{}^{g}/_{cm^3}} = 0.677$$

$$\frac{I_{MAPbI_3}}{I_{PbI_2}} = \frac{G_{MAPbI_3}}{G_{PbI_2}} \cdot \left(\frac{\rho_{MAPbI_3}}{\rho_{PbI_2}}\right)^{-1} \frac{x_{MAPbI_3}}{x_{PbI_2}} \rightarrow \frac{x_{MAPbI_3}}{x_{PbI_2}} = \frac{I_{MAPbI_3}}{I_{PbI_2}} \left(\frac{G_{MAPbI_3}}{G_{PbI_2}}\right)^{-1} \frac{\rho_{MAPbI_3}}{\rho_{PbI_2}}$$

$$\frac{x_{MAPbI_3}}{x_{PbI_2}} = \frac{I_{MAPbI_3}}{I_{PbI_2}} \cdot 3.016 \cdot 0.677 = \frac{I_{MAPbI_3}}{I_{PbI_2}} \cdot 2.042$$

$$x_{\mathrm{PbI_2}} = \frac{x_{\mathrm{PbI_2}}}{x_{\mathrm{MAPbI_3}} + x_{\mathrm{PbI_2}}} = \frac{1}{\frac{x_{\mathrm{MAPbI_3}}}{x_{\mathrm{PbI_2}}} + 1} \quad \text{with} \quad x_{\mathrm{MAPbI_3}} + x_{\mathrm{PbI_2}} = 1$$

Sample	rel. Intensities	mass ratio $\frac{x_{MAPbI_3}}{x_{PbI_2}}$	PbI_2 content x_{PbI_2}
A	$I_{MAPbI_3} = 9.1795$ $I_{PbI_2} = -$	-	-
B	$I_{MAPbI_3} = 9.975$ $I_{PbI_2} = 5.4007$	3.7715	0.21
C	$I_{MAPbI_3} = 7.5424$ $I_{PbI_2} = 8.0434$	1.9148	0.343
D	$I_{MAPbI_3} = 5.7247$ $I_{PbI_2} = 10.1689$	1.1496	0.445
E	$I_{MAPbI_3} = 7.865$ $I_{PbI_2} = 14.5852$	1.1011	0.476

11 Emission Enhancement and Intermittency in Polycristalline Organolead Halide Perovsktite Films

Cheng Li, Yu Zhong, Carlos Andres Melo Luna, Thomas Unger, Konstantin Deichsel, Anna Gräser, Jürgen Köhler, Anna Köhler, Richard Hildner und Sven Hüttner

Veröffentlicht in
Molecules 21 (2016), 1081

(DOI: 10.3390/molecules21081081)

molecules

MDPI

Article

Emission Enhancement and Intermittency in Polycrystalline Organolead Halide Perovskite Films

Cheng Li [1], Yu Zhong [1], Carlos Andres Melo Luna [2,3], Thomas Unger [4], Konstantin Deichsel [2], Anna Gräser [1], Jürgen Köhler [2], Anna Köhler [4], Richard Hildner [2] and Sven Huettner [1,*]

1 Organic and Hybrid Electronics, Macromolecular Chemistry I, University of Bayreuth, Universitätstr. 30, Bayreuth 95447, Germany; cheng.li@uni-bayreuth.de (C.L.); s2yuzhon@stmail.uni-bayreuth.de (Y.Z.); anna.graeser@uni-bayreuth.de (A.G.)

2 Experimental Physics IV and Bayreuth Institute of Macromolecular Research, University of Bayreuth, Universitätstr. 30, Bayreuth 95447, Germany; Carlos.Melo@uni-bayreuth.de (C.A.M.L.); konstantin.deichsel@gmx.de (K.D.); juergen.koehler@uni-bayreuth.de (J.K.); richard.hildner@uni-bayreuth.de (R.H.)

3 Centre for Bioinformatics and Photonics—CIBioFi, Calle 13 No. 100-00, Edificio 320 No. 1069 and Departamento de Fisica, Universidad del Valle, Cali 760032, Colombia

4 Experimental Physics II, University of Bayreuth, Universitätstr. 30, Bayreuth 95447, Germany; thomas.unger@uni-bayreuth.de (T.U.); anna.koehler@uni-bayreuth.de (A.K.)

* Correspondence: sven.huetttner@uni-bayreuth.de; Tel.: +49-921-554-440

Academic Editor: Pablo Docampo

Received: 15 June 2016; Accepted: 9 August 2016; Published: 18 August 2016

Abstract: Inorganic-organic halide organometal perovskites have demonstrated very promising performance for opto-electronic applications, such as solar cells, light-emitting diodes, lasers, single-photon sources, etc. However, the little knowledge on the underlying photophysics, especially on a microscopic scale, hampers the further improvement of devices based on this material. In this communication, correlated conventional photoluminescence (PL) characterization and wide-field PL imaging as a function of time are employed to investigate the spatially- and temporally-resolved PL in $CH_3NH_3PbI_{3-x}Cl_x$ perovskite films. Along with a continuous increase of the PL intensity during light soaking, we also observe PL blinking or PL intermittency behavior in individual grains of these films. Combined with significant suppression of PL blinking in perovskite films coated with a phenyl-C61-butyric acid methyl ester (PCBM) layer, it suggests that this PL intermittency is attributed to Auger recombination induced by photoionized defects/traps or mobile ions within grains. These defects/traps are detrimental for light conversion and can be effectively passivated by the PCBM layer. This finding paves the way to provide a guideline on the further improvement of perovskite opto-electronic devices.

Keywords: perovskite solar cells; photoluminescence; intermittency; Auger recombination; ion migration; passivation; blinking; Methylammonium Lead Halide; methylammonium lead iodide

1. Introduction

Together with the unprecedented development of solution-processed inorganic-organic halide organometal perovskite-based solar cells (e.g., $CH_3NH_3PbI_{3-x}Cl_x$ and $CH_3NH_3PbI_3$), with power conversion efficiency (PCE) evolving from 3.8% [1] to 20.1% [2], the characterization of these materials has also made significant breakthroughs in the last few years [3]. A number of different methods are employed, ranging from crystallographic study [4,5], photo-physical investigation [6–8], to electrical characterization [9,10], etc. Presently, both scientific and technical interests concentrate on how to further improve PCE and decrease the energy loss during the light conversion process. However, till

now, there is still lack of a general guideline and evaluation to characterize the quality of perovskite films, especially at a microscopic scale.

Among various characterization approaches, photoluminescence (PL) measurements [6,11], in particular wide-field PL imaging [12–15], have been demonstrated to be powerful tools to reveal the underlying physics in perovskite materials, such as the distribution of defects, charge carrier lifetimes, analyzing recombination processes, etc. In general, PL characteristics of perovskite films are closely connected with its quality, in terms of the charge carrier lifetime and the recombination pathway [16]. In detail, a slow PL decay, or long carrier lifetime, is associated with less unintentional doping or defect states inside a domain, which lead to unfavorable non-radiative carrier recombination pathways [14]. Charge carrier recombination is considered as a combination of (1) trap-/defect-assisted (Shockley–Read–Hall recombination, via the sub-bandgap traps) (first order); (2) free electron-hole bimolecular (second order) and (3) Auger recombination (third order) [17,18]. Among them, radiative bimolecular recombination would be preferable as it facilitates approaching the maximum PCE, i.e., the Shockley–Queisser limit [19].

Although individual perovskite nanoparticles have been intensively studied by confocal PL microscopy [13,20,21], the knowledge on the perovskite film (i.e., ensemble of perovskite grains) [15] is still far from being fully understood. This is mainly due to the complex boundary conditions, broad distribution of particle sizes and trap sites [14]. In this communication, therefore, we apply both conventional PL characterization and the spatially-/temporally-resolved PL imaging to investigate perovskite films, revealing the possible factors hindering PCE towards the Shockley–Queisser limit.

2. Result and Discussion

The $CH_3NH_3PbI_{3-x}Cl_x$ perovskite films, which are investigated in this communication, are prepared by spin-coating of a mixed halide precursor solution (CH_3NH_3I:$PbCl_2$ = (3:1)) on quartz glass substrates, followed by a thermal annealing step in a nitrogen glovebox. The detailed fabrication process has been described in previous work [22]. The morphology of the film is shown in Figure 1. A uniform perovskite film is deposited on quartz substrate with only minor pinhole density due to gas release during annealing [23] (Figure 1a). We also employ atomic force microscopy (AFM) to investigate the microscopic structure of the film, shown in Figure 1b,c. It is evident that the perovskite film is comprised of densely-packed grains, which are ranging from 100 nm to 800 nm in size.

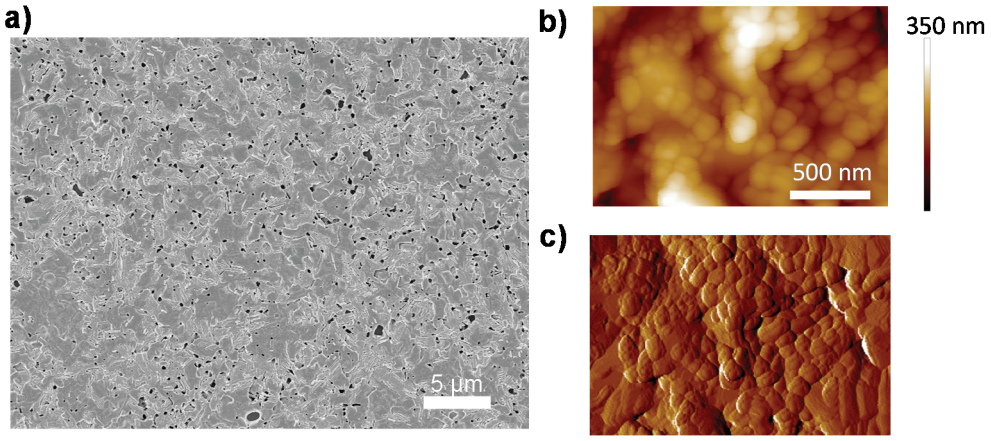

Figure 1. Morphology characteristics of a $CH_3NH_3PbI_{3-x}Cl_x$ perovskite film. (**a**) Scanning electron microscopy (SEM) image; (**b**) atomic force microscopy (AFM) morphology image; and (**c**) AFM phase image. The color bar in (**b**) indicates height.

The UV-VIS optical absorption and PL spectra of $CH_3NH_3PbI_{3-x}Cl_x$ perovskite thin film, measured with commercial spectrophotometers at room temperature are shown in the inset of Figure 2a.

The absorption edge is located at around 769 nm, which is consistent with previous other papers [24]. For the PL properties, being excited by a 532-nm laser, the emission peak is centered at around 780 nm. This small Stokes-shift (energy difference between optical absorption and emission), unlike the one in organic materials, is attributed to the small vibrational relaxation in perovskite [6]. Incorporating this perovskite film into a typical perovskite solar cell architecture (Figure S1) results in a performance as shown in Figure 2a. From the light current-voltage (J–V) curve measurement, we obtain the open circuit voltage V_{oc} = 1.06 V, short circuit current J_{sc} = 18.9 mA/cm^2 and fill factor FF = 62.3%, and, hence, the PCE is calculated as 12.5%.

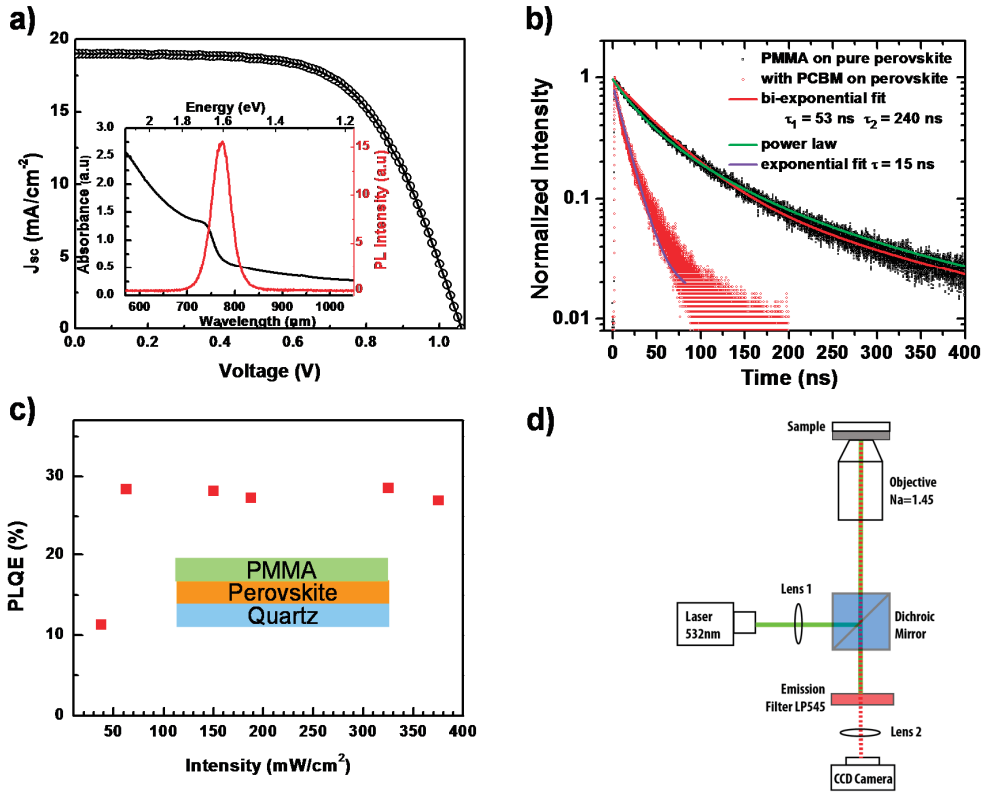

Figure 2. (**a**) Light current-voltage (J–V) curve measurement of a perovskite solar cell. The inset shows the photoluminescence (PL) and UV-VIS absorption spectra of a perovskite film; (**b**) Time-resolved photoluminescence measurement on a perovskite film with (red dots) and without (black dots) a PCBM quencher layer, together with fit lines; (**c**) Photoluminescence quantum efficiency (PLQE) of a perovskite thin film as a function of laser intensity. The inset shows the schematic of the device; (**d**) Schematic diagram of the PL imaging microscope.

By monitoring the PL decay after photoexcitation, we can investigate the charge carrier recombination kinetics. Figure 2b presents the normalized time-resolved PL behavior of this perovskite film under pulsed laser excitation at 485 nm, with and without a phenyl-C61-butyric acid methyl ester (PCBM) layer, respectively. The PL decay of the pure perovskite film cannot be described by a mono-exponential decay. Rather, it can be described using a power-law dependence. The best bi-exponential fit would give a dominant short decay component of about 52 ns.

Solid lines in Figure 2b represent the fits to bi-exponential decays, power-law decays and to exponential decay. For the quenched PL decay with PCBM, a diffusion model as described by Stranks et al. [6] should actually be applied. If one uses, for simplicity, an exponential fit, a decay time of 15 ns is obtained. We also carry out steady-state photoluminescence quantum efficiency (PLQE) measurements [25] on perovskite films with a PMMA layer as a function of the excitation intensity using a wavelength of 485 nm to study the recombination. As shown in Figure 2c, in the

initial low excitation intensity regime, PLQE rises with the laser intensity. We consider that this increase is associated with the possible trap-filling process, as well as the increase of exciton density as the photogenerated species [17,26]. In detail, due to the low temperature solution processing of the perovskite film, there can be various defect states within the crystallized bulk and surface, such as vacancies, interstitials, substitutions, etc. [27–29]. These defects can act as trap-assisted recombination (Shockley–Read–Hall recombination) centers, via which the free charge carriers can undergo non-radiative recombination processes [30]. These recombination centers would lead to shorter carrier life times and a lower open circuit voltage (V_{oc}). When illuminated, these sub-bandgap traps would be filled and stabilized by photogenerated electrons/holes, reducing the non-radiative recombination probability and consequently increasing V_{oc} under light soaking [31,32]. For the higher excitation intensity, the PLQE would reach a saturated value, indicating that all traps associated with the non-radiative recombination have been filled [17,26,33]. This scenario is consistent with our experimental data. However, we note that the PLQE is still quite low, around 30%, which is supposed to approach unity according to the detailed balance model [19,34]. This implies that besides the trap-assisted recombination, there exists an additional non-radiative recombination pathway. To understand the detailed mechanism, which suppresses the further increase of PL intensity, we employ spatially- and temporally-resolved PL microscopy to investigate the perovskite film locally on the level of individual grains.

The detailed experimental setup, which is displayed in Figure 2d, has been described in a previous paper [35]. Briefly, we employed a home-built microscope, which can be operated using wide-field illumination, and a charge-coupled device (CCD) camera as detector to image the PL of large areas (diameter ~60 μm) of a sample. We measured typically sequences of up to 2000 PL images with exposure times as short as 50 ms per image, which allows us to follow temporal changes of the PL intensity from the perovskite film under continuous laser illumination at a wavelength of 532 nm. Here, to rule out the possible influence of environmental effects on the perovskite films, i.e., oxygen and water molecules [36,37], we spin-coated a polymethyl methacrylate (PMMA) layer with a ~200-nm thickness on the top of the perovskite film as the protection layer. In addition, the PMMA layer was in direct contact with the immersion oil of the microscope objective during the whole PL characterization, which further prevents oxygen from diffusing into the film.

Figure 3a is an example of a wide-field PL image out of a sequence of images from a perovskite film, which agrees generally with the SEM result, showing ensembles of grains on the film and the appearance of pinholes on the surface. Note that, due to the diffraction limit, grains with a size smaller than ~300 nm cannot be resolved with our microscope and, thus, appear as blurred structures. However, we still observe the existence of dark crystal grain/particle boundaries. The observation of dark grain boundaries (non-radiative recombination centers) has also been observed by higher resolution confocal microscopy, as demonstrated by deQuilettes et al. [14] for example.

Figure 3b shows the PL intensity as a function of time, obtained by extracting the integrated PL of the orange circled Area A in Figure 3a from each image of the sequence. We find that the PL intensity continuously increases during the light soaking process, as shown in Figure 3b. This increase, which agrees with the previous PLQE measurement, has also been reported in other papers [17,21,38] and is attributed to trap filling processes.

Here, we note that the time dependence of the PL intensity in Area A, shown in Figure 3b, is fitted well by a bi-exponential function with time constants of ~14 s and ~280 s and prefactors of 230 and 690, respectively. Higher excitation intensities render shorter time constants, which is shown in more detail in the Supplementary Materials (Figure S2). This implies that there exist two distinct trap-filling processes, that is a quick one and a much slower one. We propose that the quick process is associated with the direct filling of defect states in the perovskite film [20]. These defects originate from the symmetry breaking of the perfect bulk crystalline structure in the vicinity of the surface or grain boundary, where well-defined facets are lacking [29]; while, for the slower one, we assume that it is ascribed to the formation and migration of defect states in the

perovskite film under light illumination. Recently, more and more studies have been carried out in this field, investigating the roles of defect formation/migration on the hysteresis and long-term (seconds to minutes) phenomena [39–41]. Hoke et al. [42] observed the presence of an iodine-rich phase in mixed halide perovskite under light irradiation. Chen et al. [43] detected the light activation and accumulation of ions by light soaking, resulting in PL quenching in the perovskite film. Yuan et al. [44] attributed the degradation of perovskite structures to the ion migration via light or external electron beam. Hentz et al. [45] also observed the formation of an iodine-rich region induced by an external electron beam.

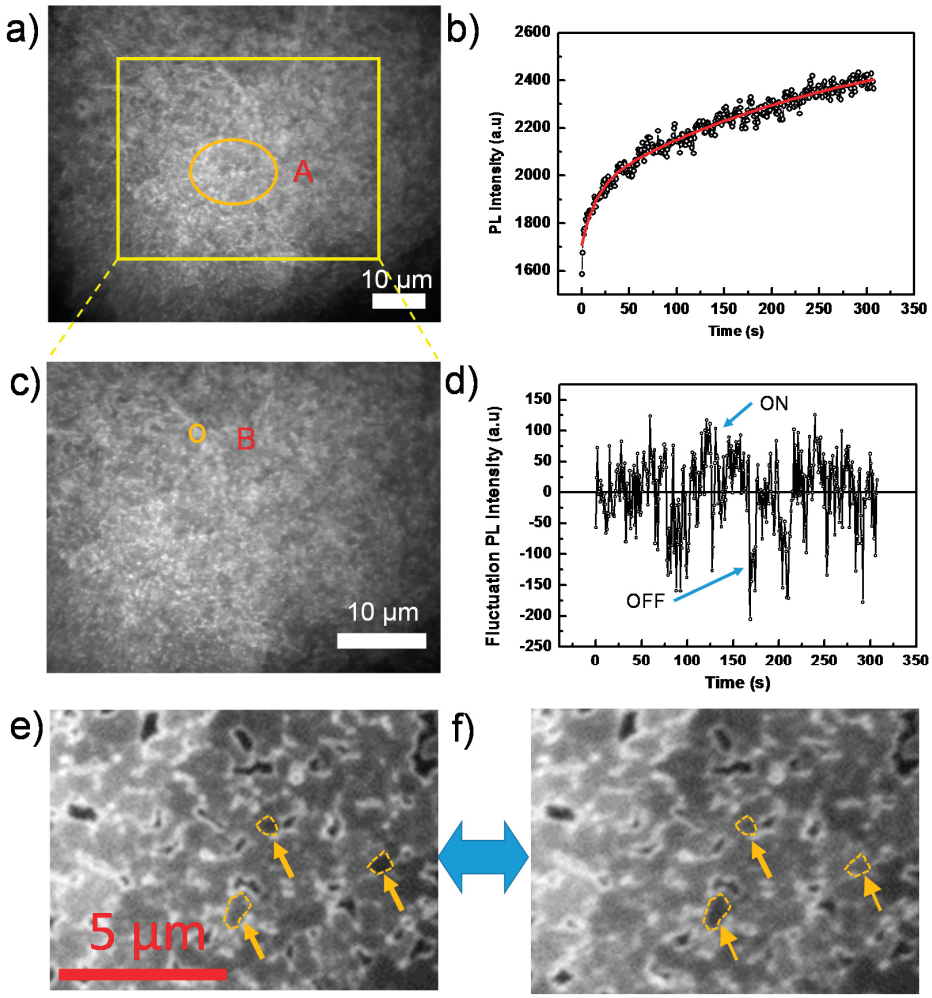

Figure 3. (**a**) Wide-field PL image of a perovskite film taken from a sequence of 400 consecutively-recorded images with an exposure time of 50 ms, an interval time of 500 ms and an excitation intensity of 44 mW/cm^2; (**b**) PL intensity trajectory extracted from Area A in the sequence of images in (**a**). The red line is the fit by an exponential function; (**c**) Enlarged view of the yellow square area of (**a**); (**d**) PL intensity trajectory extracted from Area B in (**c**) after subtraction of the exponentially increasing base line; (**e**,**f**) Individual grains in "ON" and "OFF" states, respectively, indicated by yellow arrows.

The overall continuous PL intensity enhancement, as shown in Figure 3b, is superimposed by strong PL intensity fluctuations beyond experimental noise. This behavior is reminiscent of random switching between ON (highly emissive state) and OFF (weakly emissive state) in the emission trajectory, which is known as blinking or PL intermittency [46]. The intermittency behavior is demonstrated in the Supplementary Materials (Figure S3), which shows the long-term OFF state. In addition, the video in the Supplementary Materials also clearly indicates the blinking behavior

confined within individual grains. Although the blinking behavior has been observed in perovskite nanocrystals [13,21,47], it is still not fully studied on compact films composed of the densely-packed perovskite grains [15].

To reveal the underling mechanism, we investigate individual grains, thus avoiding averaging over ensembles of grains in the film. Figure 3c displays an enlarged view of the yellow boxed area in Figure 3a, and an individual grain is highlighted by the orange circle labeled with B. As shown in Figure 3d, the PL intensity trajectory of this grain B, after subtraction of a continuous bi-exponentially-increasing baseline, shows a typical blinking behavior (see Supplementary Materials, Figure S3 for the individual grain in a shorter time scale), that is random distribution of ON/OFF states in the PL intensity trajectory. More individual grains exhibiting "ON" and "OFF" states are shown in Figure 3e,f, and the Supplementary Materials (Figure S3). Note that some ON or OFF states even last for more than 20 s, which indicates a significantly slow dynamic process.

To further investigate the detailed processes giving rise to blinking, we performed PL imaging on perovskite films coated with a PCBM layer, which acts as a PL quencher layer. Compared to the pure perovskite film, the overall PL intensity reduces significantly despite using higher excitation intensities (Figure 4a, which shows a PL image out of a sequence of images). This PCBM layer effectively separates the photogenerated charge carriers (free electron/hole or weakly bound excitons) [48], because PCBM serves as an electron acceptor and consequently quenches the radiative charge recombination (Figure S4). Figure 4b shows the integrated PL intensity of the yellow circled area in Figure 4a as a function of time, which can be well fitted by a bi-exponential function with time constants of 5.4 s and 14.6 s, respectively. This is consistent with the results displayed in Figure 2b, in which a faster (quenched) PL decay is due to the PCBM quencher layer. It is interesting to note that although the overall PL still increases as a function of time, the blinking amplitude significantly reduces below the noise level (the ratio between the fluctuation and the average emission intensity), both in the whole film and in individual grains, as shown in the inset of Figure 4b.

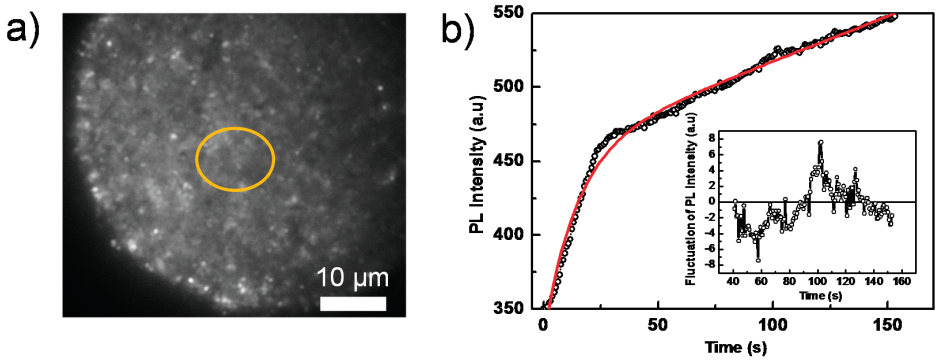

Figure 4. (**a**) Wide-field PL image of a perovskite film, covered with a PCBM quencher layer, taken from a sequence of 200 consecutively-recorded images with an exposure time of 100 ms, an interval time of 500 ms and an excitation intensity of 280 mW/cm^2; (**b**) PL intensity trajectory extracted from the yellow circled area in the sequence of images in (**a**). The red line is the fitting line by a bi-exponential function. The inset shows the relative fluctuations of the PL intensity after subtraction of the bi-exponential fit function.

Based on the previous results, combining both the conventional PL characterization and wide field PL imaging, we can reveal the underlying physics in the enhancement and quenching of the PL. Though there are several models to interpret the blinking behavior [46,49,50], the presence of OFF states in perovskite film/nanoparticles is commonly attributed to additional charges due to charge trapping process [15,20,21]. When there is no charge trapped in perovskite grains, shown in Figure 5a, the dominant decay process is bi-molecular recombination (for medium carrier densities) [17], which is radiative during the recombination process, denoted as the "ON" state. In contrast, when

photogenerated charges are trapped in the grain, either by surface or bulk defect states, the ionized surrounding enhances Auger recombination [15,51]. This recombination involves a recombination of an electron and a hole, followed by a process of energy transfer to a third carrier instead of photon emission, as shown in Figure 5b. This process is non-radiative and therefore renders the grains dark in PL imaging, denoted as the "OFF" state. When these trapped charges release, the PL emission recovers to the "ON" state. This Auger recombination statistically reduces the PL intensity in the whole film, resulting in the loss in V_{oc} and PCE [52,53].

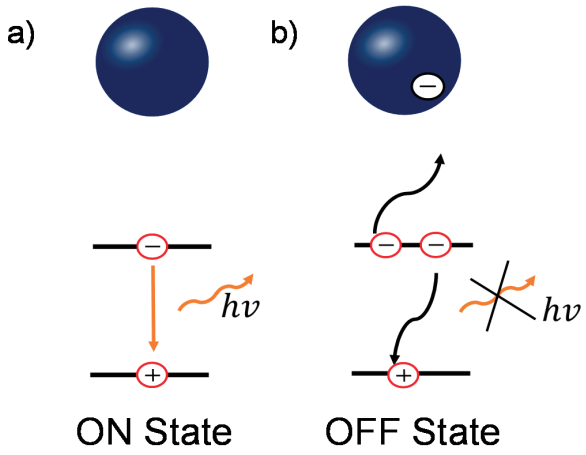

Figure 5. Schematic diagrams of the relationship between the charged grains and blinking behavior in perovskite. (**a**) In the uncharged states, the dominant recombination pathway is bi-molecular recombination; (**b**) In the charged states, the non-radiative three-carrier Auger recombination plays an important role. Blue ball represents an individual perovskite grain.

Note that the long durations of more than 20 s of "ON" and "OFF" states are similar to the slow response in electrical transient behavior, such as hysteresis and light-induced degradation [15,44]. This implies that it can be associated with the same mechanism, i.e., ion migration. These ions can be driven by the external electrical field and consequently accumulate, enhancing the Auger recombination locally [15]. In addition, these ions are also able to migrate between grains within the film [15,41].

When the perovskite film is covered with a PCBM quencher layer, the PL blinking is significantly suppressed (insets in Figure 4b). This is ascribed to two possible reasons: First, PCBM has been demonstrated to be a good candidate to passivate traps in perovskites, leading to a charge de-trapping process [54]. In addition, the insertion of PCBM suppresses the ionic migration among the grains of perovskite, leading to a further reduction of PL blinking [55]. Second, the Auger recombination is proportional to the third power of charge carrier density n^3 [16]. Owing to the effective charge transfer process at the perovskite/PCBM interface, the negative charge carrier density (n_e) inside the perovskite significantly decreases, giving rise to the decrease of the Auger recombination contribution.

3. Experimental Methods

CH_3NH_3I (MAI) was purchased from Tokyo Chemical Industry (TCI Deutschland GmbH, Eschborn, Germany), and all other chemicals were purchased from Sigma-Aldrich and used as received.

3.1. Perovskite Film Fabrication for PL Experiment

Glass substrates were washed and cleaned with acetone and isopropanol for 10 min each in ultrasonic baths. Then, these glass substrates were treated within an ozone chamber for approximately 10 min. Following that, in a nitrogen glovebox (both water and oxygen less than 10 ppm), the perovskite precursor, i.e., MAI and $PbCl_2$ (3:1) in anhydrous *N*,*N*-dimethylformamide (DMF), was spin-coated

on glass substrates at 3000 rpm for 60 s. Then, these as-spun films were annealed at 100 °C in the nitrogen atmosphere for 60 min. Subsequently, 20 mg/mL phenyl-C61-butyric acid methyl ester (PCBM) dissolved in chlorobenzene were coated on the film at 2000 rpm for 30 s as a quencher layer. In the end, 40 mg/mL poly(methyl methacrylate) (PMMA) dissolved in butyl acetate (anhydrous, 99%) was spin-coated on the perovskite film at 2000 rpm for 60 s acting as a protection layer.

3.2. Conventional PL Characterization

3.2.1. PLQE Measurements

Photoluminescence quantum yield (PLQE) was taken using an integrating sphere and a laser diode at a 485-nm wavelength (PicoQuant GmbH, Berlin, Germany). The spectra are spectrally corrected for grating, charge-coupled device (CCD) and fiber efficiencies.

3.2.2. Time-Correlated Single Photon Counting

PL transients are measured with a time-correlated single photon counting (TCSPC) setup (FluoTime 200, PicoQuant GmbH). The excitation source was a pulsed laser diode with a 485-nm wavelength with 2- to 10-MHz repetition rate and a pulse duration of about 140 ps.

3.3. PL Imaging Setup

The setup used for PL imaging of perovskite films is based on a home-built confocal microscope. The excitation source was a pulsed diode laser (LDH-P-FA-530L, 20-MHz repetition rate, 70-ps pulse duration, PicoQuant GmbH). This laser beam was spatially filtered and directed to the microscope equipped with an infinity-corrected high-numerical-aperture oil-immersion objective (Plan Apo, 60×, numerical aperture 1.45; Olympus, Japan). The perovskite film was placed in the focal plane of the objective, and the sample position was controlled by a piezo-stage (Tritor 102 SG, piezosystem Jena GmbH, Jena, Germany). In order to homogeneously illuminate a large area (diameter ~60 µm) of the films, we additionally inserted a wide-field lens in the excitation beam path that focuses the laser light into the back-focal plane of the objective.

The PL signal was collected by the same objective, passed a long-pass filter (LP545, AHF analysentechnik AG, Tübingen, Germany) to suppress residual laser light and was imaged onto a CCD camera (Orca-ER, Hamamatsu, Japan) by an objective lens. We have done an estimation on the noise level of the PL intensity measurement as follows. The laser power stability is better than 3% (r.m.s.); to be conservative, we use 3% in the following, i.e., $s_{Laser} = 0.03$. The CCD's dark current amounts to 0.03 electrons per pixel per second, i.e., with the used exposure times of <100 ms, this dark current is <0.003 electron per pixel per exposure. As will be clear from the numbers calculated below, this dark current is negligible and will not be considered further. The readout noise of the CCD-camera is 8 electrons (r.m.s.). The measured and displayed signals are given in AD counts (i.e., after signal amplification and AD conversion). The resulting conversion factor is 4.6 electrons per AD count according to the manufacturer. Finally, the created electrons have to be converted into detected photons to estimate the photon shot noise contributing to the signal. In the emission range of the samples around 800 nm, the quantum efficiency of the CCD amounts to 30%. For the data shown in Figure 3b,d, we estimate the noise level in the high signal regime starting at around 100 s. Here, the average signal is 2200 AD counts, corresponding to 10,120 electrons or 33,700 photons. For the readout noise, we then obtain $s_{CCD} = 0.0008$. From the number of detected photons, the shot noise is $s_{Shot} = 0.005$. Hence, in total, the noise level is $s = \sqrt{s_{Laser}^2 + s_{CCD}^2 + s_{Shot}^2} = 0.03$, which translates into 67 AD counts. Comparing this noise level to the observed signal fluctuations of about ±150 AD counts in Figure 3d, it is clear that these fluctuations cannot arise from noise. For the data shown in Figure 4, the situation is slightly different: using the displayed AD counts of around 500 in the high signal regime starting around 80 s, we obtain a noise level of 16 AD counts following the same

procedure as above. Hence, in the presence of the PCBM quencher layer, the observed fluctuations are largely determined by the noise level in these experiments.

4. Conclusions

In summary, by employing the conventional PL and wide-field PL image characterization, we have observed the enhancement and fluorescence intermittency (PL blinking) in a mixed halide perovskite film. We attribute the PL enhancement to the trap-filling process. In the meantime, we suggest the PL blinking behavior to the enhanced Auger non-radiative recombination due to the additional charges within the grain. These charges possibly originate from the photogenerated charge carriers trapped by defects or the mobile ionized defects (e.g., iodide ions or iodide vacancies). This photoionized process results in the PL blinking, hindering the approach towards the Shockley–Queisser limit. Therefore, this finding provides unique insight to a guideline on how to further improve the PCE of perovskite solar cells.

Supplementary Materials: Supplementary materials can be accessed at: http://www.mdpi.com/1420-3049/21/8/1081/s1.

Acknowledgments: Financial support by the Bavarian State Ministry of Science, Research and the Arts for the Collaborative Research Network "Solar Technologies go Hybrid" and Federal Ministry of Education and Research BMBF (03SF0484C) are gratefully acknowledged. Richard Hildner, Jürgen Köhler, Anna Köhler, Thomas Unger and Carlos Andres Melo Luna acknowledge additional funding from the German Research Foundation DFG (GRK1640 and HI1508/2). Carlos Andres Melo Luna acknowledges funding from the Colombian Department of Science, Technology and Innovation (Colciencias, Project 71003).

Author Contributions: Cheng Li, Yu Zhong, Richard Hildner and Sven Huettner initiated and designed the study. Cheng Li, Yu Zhong, Carlos Andres Melo Luna, Thomas Unger, Konstantin Deichsel and Anna Gräser carried out the experiments and analyzed the data. Cheng Li, Yu Zhong, Carlos Andres Melo Luna, Konstantin Deichsel and Anna Gräser carried out the PL imaging measurements under supervision of Jürgen Köhler and Richard Hildner; Thomas Unger carried out the PL related experiments under supervision of Anna Köhler; Cheng Li, Yu Zhong and Anna Gräser prepared and fabricated devices. Cheng Li, Thomas Unger, Richard Hildner and Sven Huettner prepared the manuscript. All authors discussed, revised and approved the manuscript.

Conflicts of Interest: The authors declare no conflict of interest.

References

1. Kojima, A.; Teshima, K.; Shirai, Y.; Miyasaka, T. Organometal Halide Perovskites as Visible-Light Sensitizers for Photovoltaic Cells. *J. Am. Chem. Soc.* **2009**, *131*, 6050–6051. [CrossRef] [PubMed]
2. Yang, W.S.; Noh, J.H.; Jeon, N.J.; Kim, Y.C.; Ryu, S.; Seo, J.; Seok, S.I. High-performance photovoltaic perovskite layers fabricated through intramolecular exchange. *Science* **2015**, *348*, 1234–1237. [CrossRef] [PubMed]
3. Stranks, S.D.; Snaith, H.J. Metal-halide perovskites for photovoltaic and light-emitting devices. *Nat. Nanotechnol.* **2015**, *10*, 391–402. [CrossRef] [PubMed]
4. Song, T.-B.; Chen, Q.; Zhou, H.; Luo, S.; Yang, Y.; You, J.; Yang, Y. Unraveling film transformations and device performance of planar perovskite solar cells. *Nano Energy* **2015**, *12*, 494–500. [CrossRef]
5. Chen, Q.; Zhou, H.; Hong, Z.; Luo, S.; Duan, H.-S.; Wang, H.-H.; Liu, Y.; Li, G.; Yang, Y. Planar Heterojunction Perovskite Solar Cells via Vapor-Assisted Solution Process. *J. Am. Chem. Soc.* **2014**, *136*, 622–625. [CrossRef] [PubMed]
6. Stranks, S.D.; Eperon, G.E.; Grancini, G.; Menelaou, C.; Alcocer, M.J.P.; Leijtens, T.; Herz, L.M.; Petrozza, A.; Snaith, H.J. Electron-hole diffusion lengths exceeding 1 micrometer in an organometal Trihalide Perovskite absorber. *Science* **2013**, *342*, 341–344. [CrossRef] [PubMed]
7. Grancini, G.; Srimath Kandada, A.R.; Frost, J.M.; Barker, A.J.; de Bastiani, M.; Gandini, M.; Marras, S.; Lanzani, G.; Walsh, A.; Petrozza, A. Role of microstructure in the electron–hole interaction of hybrid lead halide perovskites. *Nat. Photonics* **2015**, *9*, 695–701. [CrossRef] [PubMed]
8. Fang, H.-H.; Raissa, R.; Abdu-Aguye, M.; Adjokatse, S.; Blake, G.R.; Even, J.; Loi, M.A. Photophysics of Organic–Inorganic Hybrid Lead Iodide Perovskite Single Crystals. *Adv. Funct. Mater.* **2015**, *25*, 2378–2385. [CrossRef]

9. Almora, O.; Zarazua, I.; Mas-Marza, E.; Mora-Sero, I.; Bisquert, J.; Garcia-Belmonte, G. Capacitive Dark Currents, Hysteresis, and Electrode Polarization in Lead Halide Perovskite Solar Cells. *J. Phys. Chem. Lett.* **2015**, *6*, 1645–1652. [CrossRef] [PubMed]
10. Sanchez, R.S.; Gonzalez-Pedro, V.; Lee, J.-W.; Park, N.-G.; Kang, Y.S.; Mora-Sero, I.; Bisquert, J. Slow Dynamic Processes in Lead Halide Perovskite Solar Cells. Characteristic Times and Hysteresis. *J. Phys. Chem. Lett.* **2014**, *5*, 2357–2363. [CrossRef] [PubMed]
11. Xing, G.; Mathews, N.; Sun, S.; Lim, S.S.; Lam, Y.M.; Grätzel, M.; Mhaisalkar, S.; Sum, T.C. Long-range balanced electron- and hole-transport lengths in organic-inorganic $CH_3NH_3PbI_3$. *Science* **2013**, *342*, 344–347. [CrossRef] [PubMed]
12. Hameiri, Z.; Mahboubi Soufiani, A.; Juhl, M.K.; Jiang, L.; Huang, F.; Cheng, Y.-B.; Kampwerth, H.; Weber, J.W.; Green, M.A.; Trupke, T. Photoluminescence and electroluminescence imaging of perovskite solar cells. *Prog. Photovolt. Res. Appl.* **2015**, *23*, 1697–1705. [CrossRef]
13. Swarnkar, A.; Chulliyil, R.; Ravi, V.K.; Irfanullah, M.; Chowdhury, A.; Nag, A. Colloidal CsPbBr3 perovskite nanocrystals: Luminescence beyond traditional quantum dots. *Angew. Chem. Int. Ed.* **2015**, *54*, 15424–15428. [CrossRef] [PubMed]
14. Dane, W.D.; Vorpahl, S.M.; Stranks, S.D.; Nagaoka, H.; Eperon, G.E.; Ziffer, M.E.; Snaith, H.J.; Ginger, D.S. Impact of microstructure on local carrier lifetime in perovskite solar cells. *Science* **2015**, *348*, 683–686.
15. Wen, X.; Ho-Baillie, A.; Huang, S.; Sheng, R.; Chen, S.; Ko, H.-C.; Green, M.A. Mobile Charge-Induced Fluorescence Intermittency in Methylammonium Lead Bromide Perovskite. *Nano Lett.* **2015**, *15*, 4644–4649. [CrossRef] [PubMed]
16. Herz, L.M. Charge-Carrier Dynamics in Organic-Inorganic Metal Halide Perovskites. *Annu. Rev. Phys. Chem.* **2015**, *67*. [CrossRef] [PubMed]
17. Stranks, S.D.; Burlakov, V.M.; Leijtens, T.; Ball, J.M.; Goriely, A.; Snaith, H.J. Recombination Kinetics in Organic-Inorganic Perovskites: Excitons, Free Charge, and Subgap States. *Phys. Rev. Appl.* **2014**, *2*. [CrossRef]
18. Yamada, Y.; Nakamura, T.; Endo, M.; Wakamiya, A.; Kanemitsu, Y. Photocarrier Recombination Dynamics in Perovskite $CH_3NH_3PbI_3$ for Solar Cell Applications. *J. Am. Chem. Soc.* **2014**, *136*, 11610–11613. [CrossRef] [PubMed]
19. Miller, O.D.; Yablonovitch, E.; Kurtz, S.R. Intense internal and external fluorescence as solar cell approach the SQ efficiency limit. *IEEE J. Photovolt.* **2012**, *2*, 303–311. [CrossRef]
20. Tachikawa, T.; Karimata, I.; Kobori, Y. Surface charge trapping in organolead halide perovskites explored by single-particle photoluminescence imaging. *J. Phys. Chem. Lett.* **2015**, *6*, 3195–3201. [CrossRef]
21. Tian, Y.; Merdasa, A.; Peter, M.; Abdellah, M.; Zheng, K.; Ponseca, C.S.; Pullerits, T.; Yartsev, A.; Sundström, V.; Scheblykin, I.G. Giant photoluminescence blinking of perovskite nanocrystals reveals single-trap control of luminescence. *Nano Lett.* **2015**, *15*, 1603–1608. [CrossRef] [PubMed]
22. Li, C.; Tscheuschner, S.; Paulus, F.; Hopkinson, P.E.; Kießling, J.; Köhler, A.; Vaynzof, Y.; Huettner, S. Iodine Migration and its Effect on Hysteresis in Perovskite Solar Cells. *Adv. Mater.* **2016**, *28*, 2446–2454. [CrossRef] [PubMed]
23. Yu, H.; Wang, F.; Xie, F.; Li, W.; Chen, J.; Zhao, N. The Role of Chlorine in the Formation Process of "$CH_3NH_3PbI_{3-x}Cl_x$" Perovskite. *Adv. Funct. Mater.* **2014**, *24*, 7102–7108. [CrossRef]
24. Tan, Z.-K.; Moghaddam, R.S.; Lai, M.L.; Docampo, P.; Higler, R.; Deschler, F.; Price, M.; Sadhanala, A.; Pazos, L.M.; Credgington, D.; et al. Bright light-emitting diodes based on organometal halide perovskite. *Nat. Nanotechnol.* **2014**, *9*, 687–692. [CrossRef] [PubMed]
25. De Mello, J.C.; Wittmann, H.F.; Friend, R.H. An improved experimental determination of external photoluminescence quantum efficiency. *Adv. Mater.* **1997**, *9*, 230–232. [CrossRef]
26. Deschler, F.; Price, M.; Pathak, S.; Klintberg, L.E.; Jarausch, D.-D.; Higler, R.; Hüttner, S.; Leijtens, T.; Stranks, S.D.; Snaith, H.J.; et al. High Photoluminescence Efficiency and Optically Pumped Lasing in Solution-Processed Mixed Halide Perovskite Semiconductors. *J. Phys. Chem. Lett.* **2014**, *5*, 1421–1426. [CrossRef] [PubMed]
27. Yin, W.-J.; Shi, T.; Yan, Y. Unusual defect physics in $CH_3NH_3PbI_3$ perovskite solar cell absorber. *Appl. Phys. Lett.* **2014**, *104*. [CrossRef]
28. Baumann, A.; Väth, S.; Rieder, P.; Heiber, M.C.; Tvingstedt, K.; Dyakonov, V. Identification of Trap States in Perovskite Solar Cells. *J. Phys. Chem. Lett.* **2015**, *6*, 2350–2354. [CrossRef] [PubMed]

29. Wu, X.; Trinh, M.T.; Niesner, D.; Zhu, H.; Norman, Z.; Owen, J.S.; Yaffe, O.; Kudisch, B.J.; Zhu, X.-Y. Trap states in lead iodide perovskites. *J. Am. Chem. Soc.* **2015**, *137*, 2089–2096. [CrossRef] [PubMed]
30. Wetzelaer, G.-J.A.H.; Scheepers, M.; Sempere, A.M.; Momblona, C.; Ávila, J.; Bolink, H.J. Trap-Assisted Non-Radiative Recombination in Organic–Inorganic Perovskite Solar Cells. *Adv. Mater.* **2015**, *27*, 1837–1841. [CrossRef] [PubMed]
31. Zhao, C.; Chen, B.; Qiao, X.; Luan, L.; Lu, K.; Hu, B. Revealing Underlying Processes Involved in Light Soaking Effects and Hysteresis Phenomena in Perovskite Solar Cells. *Adv. Energy Mater.* **2015**, *5*. [CrossRef]
32. Deng, Y.; Xiao, Z.; Huang, J. Light-Induced Self-Poling Effect on Organometal Trihalide Perovskite Solar Cells for Increased Device Efficiency and Stability. *Adv. Energy Mater.* **2015**, *5*, 1500721. [CrossRef]
33. Noel, N.K.; Abate, A.; Stranks, S.D.; Parrott, E.S.; Burlakov, V.M.; Goriely, A.; Snaith, H.J. Enhanced Photoluminescence and Solar Cell Performance via Lewis Base Passivation of Organic–Inorganic Lead Halide Perovskites. *ACS Nano* **2014**, *8*, 9815–9821. [CrossRef] [PubMed]
34. Shockley, W.; Queisser, H.J. Detailed Balance Limit of Efficiency of p-n Junction Solar Cells. *J. Appl. Phys.* **1961**, *32*, 510–519. [CrossRef]
35. Haedler, A.T.; Kreger, K.; Issac, A.; Wittmann, B.; Kivala, M.; Hammer, N.; Kohler, J.; Schmidt, H.-W.; Hildner, R. Long-range energy transport in single supramolecular nanofibres at room temperature. *Nature* **2015**, *523*, 196–199. [CrossRef] [PubMed]
36. Tian, Y.; Peter, M.; Unger, E.; Abdellah, M.; Zheng, K.; Pullerits, T.; Yartsev, A.; Sundstrom, V.; Scheblykin, I.G. Mechanistic insights into perovskite photoluminescence enhancement: light curing with oxygen can boost yield thousandfold. *Phys. Chem. Chem. Phys.* **2015**, *17*, 24978–24987. [CrossRef] [PubMed]
37. Galisteo-López, J.F.; Anaya, M.; Calvo, M.E.; Míguez, H. Environmental Effects on the Photophysics of Organic–Inorganic Halide Perovskites. *J. Phys. Chem. Lett.* **2015**, *6*, 2200–2205. [CrossRef] [PubMed]
38. Tian, Y.; Merdasa, A.; Unger, E.; Abdellah, M.; Zheng, K.; McKibbin, S.; Mikkelsen, A.; Pullerits, T.; Yartsev, A.; Sundström, V.; et al. Enhanced Organo-Metal Halide Perovskite Photoluminescence from Nanosized Defect-Free Crystallites and Emitting Sites. *J. Phys. Chem. Lett.* **2015**, *6*, 4171–4177. [CrossRef] [PubMed]
39. Azpiroz, J.M.; Mosconi, E.; Bisquert, J.; de Angelis, F. Defect migration in methylammonium lead iodide and its role in perovskite solar cell operation. *Energy Environ. Sci.* **2015**, *8*, 2118–2127. [CrossRef]
40. Zhang, Y.; Liu, M.; Eperon, G.E.; Leijtens, T.C.; McMeekin, D.; Saliba, M.; Zhang, W.; de Bastiani, M.; Petrozza, A.; Herz, L.M.; et al. Charge selective contacts, mobile ions and anomalous hysteresis in organic-inorganic perovskite solar cells. *Mater. Horiz.* **2015**, *2*, 315–322. [CrossRef]
41. Yuan, Y.; Huang, J. Ion migration in organometal trihalide perovskite and its impact on photovoltaic efficiency and stability. *Acc. Chem. Res.* **2016**, *49*, 286–293. [CrossRef] [PubMed]
42. Hoke, E.T.; Slotcavage, D.J.; Dohner, E.R.; Bowring, A.R.; Karunadasa, H.I.; McGehee, M.D. Reversible photo-induced trap formation in mixed-halide hybrid perovskites for photovoltaics. *Chem. Sci.* **2015**, *6*, 613–617. [CrossRef]
43. Chen, S.; Wen, X.; Sheng, R.; Huang, S.; Deng, X.; Green, M.A.; Ho-Baillie, A. Mobile ion induced slow carrier dynamics in organic–inorganic perovskite $CH_3NH_3PbBr_3$. *ACS Appl. Mater. Interfaces* **2016**, *8*, 5351–5357. [CrossRef] [PubMed]
44. Yuan, H.; Debroye, E.; Janssen, K.; Naiki, H.; Steuwe, C.; Lu, G.; Moris, M.; Orgiu, E.; Uji-i, H.; de Schryver, F.; et al. Degradation of methylammonium lead iodide perovskite structures through light and electron beam driven ion migration. *J. Phys. Chem. Lett.* **2016**, *7*, 561–566. [CrossRef] [PubMed]
45. Hentz, O.; Zhao, Z.; Gradečak, S. Impacts of Ion Segregation on Local Optical Properties in Mixed Halide Perovskite Films. *Nano Lett.* **2016**, *16*, 1485–1490. [CrossRef] [PubMed]
46. Frantsuzov, P.; Kuno, M.; Janko, B.; Marcus, R.A. Universal emission intermittency in quantum dots, nanorods and nanowires. *Nat. Phys.* **2008**, *4*, 519–522. [CrossRef]
47. Park, Y.-S.; Guo, S.; Makarov, N.S.; Klimov, V.I. Room temperature single-photon emission from individual perovskite quantum dots. *ACS Nano* **2015**, *9*, 10386–10393. [CrossRef] [PubMed]
48. D'Innocenzo, V.; Grancini, G.; Alcocer, M.J.P.; Kandada, A.R.S.; Stranks, S.D.; Lee, M.M.; Lanzani, G.; Snaith, H.J.; Petrozza, A. Excitons versus free charges in organo-lead tri-halide perovskites. *Nat. Commun.* **2014**, *5*. [CrossRef] [PubMed]
49. Galland, C.; Ghosh, Y.; Steinbruck, A.; Sykora, M.; Hollingsworth, J.A.; Klimov, V.I.; Htoon, H. Two types of luminescence blinking revealed by spectroelectrochemistry of single quantum dots. *Nature* **2011**, *479*, 203–207. [CrossRef] [PubMed]

50. Anger, P.; Bharadwaj, P.; Novotny, L. Enhancement and Quenching of Single-Molecule Fluorescence. *Phys. Rev. Lett.* **2006**, *96*. [CrossRef] [PubMed]
51. Efros, A.L.; Rosen, M. Random telegraph signal in the photoluminescence intensity of a single quantum dot. *Phys. Rev. Lett.* **1997**, *78*, 1110–1113. [CrossRef]
52. Tvingstedt, K.; Malinkiewicz, O.; Baumann, A.; Deibel, C.; Snaith, H.J.; Dyakonov, V.; Bolink, H.J. Radiative efficiency of lead iodide based perovskite solar cells. *Sci. Rep.* **2014**, *4*. [CrossRef] [PubMed]
53. Tress, W.; Marinova, N.; Inganäs, O.; Nazeeruddin, M.K.; Zakeeruddin, S.M.; Graetzel, M. Predicting the open-circuit voltage of $CH_3NH_3PbI_3$ perovskite solar cells using electroluminescence and photovoltaic quantum efficiency spectra: the role of radiative and non-radiative recombination. *Adv. Energy Mater.* **2015**, *5*. [CrossRef]
54. Shao, Y.; Xiao, Z.; Bi, C.; Yuan, Y.; Huang, J. Origin and elimination of photocurrent hysteresis by fullerene passivation in $CH_3NH_3PbI_3$ planar heterojunction solar cells. *Nat. Commun.* **2014**, *5*. [CrossRef] [PubMed]
55. Xu, J.; Buin, A.; Ip, A.H.; Li, W.; Voznyy, O.; Comin, R.; Yuan, M.; Jeon, S.; Ning, Z.; McDowell, J.J.; et al. Perovskite-fullerene hybrid materials suppress hysteresis in planar diodes. *Nat. Commun.* **2015**, *6*. [CrossRef] [PubMed]

Sample Availability: Samples of the perovskite films are available from the authors on request.

Supplementary Materials: Emission Enhancement and Intermittency in Polycrystalline Organolead Halide Perovskite Films

Cheng Li, Yu Zhong, Carlos Andres Melo Luna, Thomas Unger, Konstantin Deichsel, Anna Gräser, Jürgen Köhler, Anna Köhler, Richard Hildner and Sven Huettner

1. Device Structure

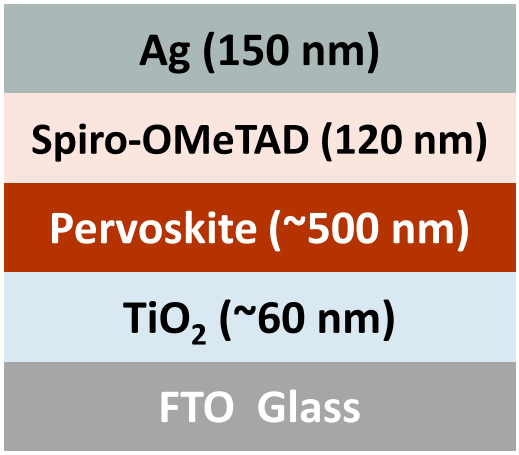

Figure S1. The schematic diagram of a typical perovskite solar cell.

2. Evolution of Photoluminescence at Different Excitation Intensities

A pure perovskite film on glass (like in Figure 3) was measured under low (44 mW/cm^2, Figure S2a,c) and higher excitation intensity (280 mW/cm^2; Figure S2b,d). Both curves were fitted by a bi-exponential function, showing a much faster increase process with time constants of 4 s and 120 s at the higher excitation intensity.

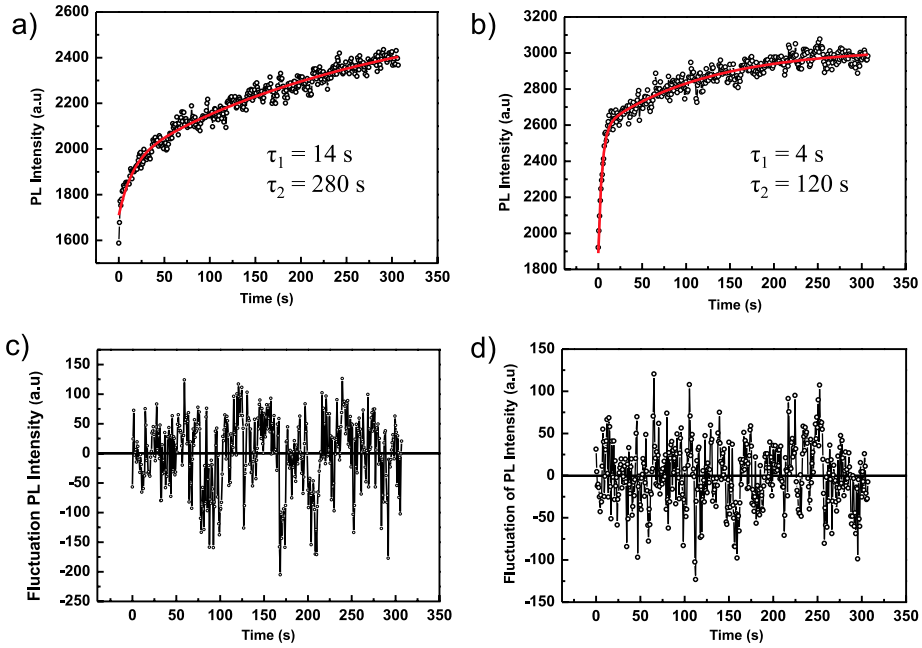

Figure S2. Comparison of PL intensity trajectory extracted from the same device in the sequence of images with excitation intensities of (**a**) 44 mW/cm^2 and (**b**) 280 mW/cm^2, respectively. The red lines are the corresponding bi-exponential fits; (**c**,**d**) are the fluctuation of the PL intensity under excitation intensities of 44 mW/cm^2 and 280 mW/cm^2, respectively.

3. Blinking in Detail

A video file is available for download, showing the PL intermittency in the pristine $CH_3NH_3PbI_{3-x}Cl_x$ perovskite film (excitation intensity 44 mW/cm²). The sequence is played 1.4x faster than real time. The diameter of the illumination spot is ~60μm.

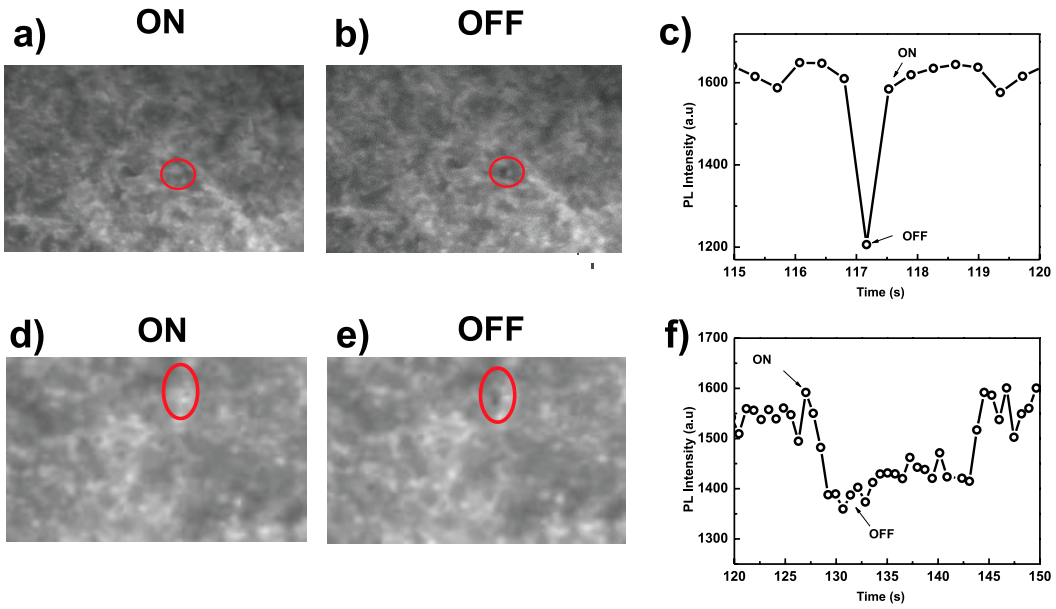

Figure S3. Different grains with PL blinking behaviors. (**a**) to (**c**) are one single grain with short OFF states; (**d**) to (**f**) are one single grain with longer OFF states.

4. Photoluminescence Quantum Efficiency

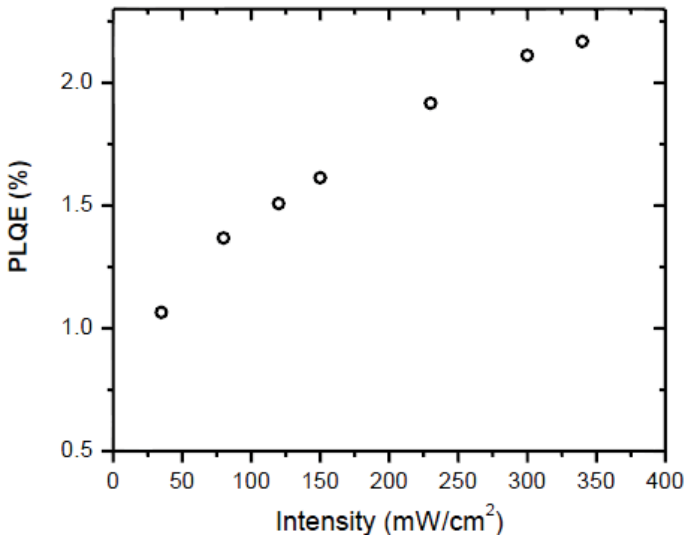

Figure S4. PLQE measurement of the perovskite/PCBM device, which exhibits PL quenching compared to the one without the PCBM quencher layer.

12 **Danksagung**

Als erstes möchte ich mich bei Frau Prof. Dr. Anna Köhler bedanken, die mir die Möglichkeit gegeben hat bei ihr am Lehrstuhl mich ausführlich dem interessanten Thema der zeitaufgelösten Spektroskopie zu widmen. Bei auftretenden Problemen hat sie stets ein offenes Ohr und hilfreiche Ratschläge für mich. Ich konnte mir immer ihrer Unterstüzung sicher sein. Darüber hinaus möchte ich mich für die riesige Unterstützung bei der Korrektur und Erarbeitung der Veröffentlichungen bedanken.

Dies gilt ebenso für Prof. Dr. Heinz Bässler. Vielen Dank für die Hilfe bei der Interpretation meiner Daten sowie für unsere interessanten und tiefgründigen Diskussionen über grundlegende Fragestellungen. Sein umfangreicher und tiefgründiger Erfahrungsschatz im wissenenschaftlichen Bereich, sowie abseits davon, erstaunen mich jedes mal aufs Neue.

Zu Beginn meiner Promotion, als die Einrichtung des Messaufbaus im Vordergrund stand, hat mir der Aufenthalt in München an der LMU in der Arbeitsgruppe von Prof. Eberhard Riedle (Lehrstuhl BMO) sehr weitergeholfen. Daher danke ich an dieser Stelle Prof. Riedle und seinen ehemaligen Doktoranden Maximilian Bradler und Matthias Wenninger für die wertvollen Tipps zum Thema ultraschneller Optik und transiente Absorptionsspektroskopie.

Auch möchte ich Nour Hafi von der Universität Braunschweig vom Lehrstuhl Biophysikalische Chemie danken für seine zahlreichen Tipps zur Justage des regenerativen Verstärkers und interessante Telefongespräche.

Natürlich danke ich auch Prof. Mukundan Thelakkat für die gute Zusammenarbeit als Mentor und als Projektpartner, der immer ein offenes Ohr für mich gehabt hat. Ebenfalls möchte ich Tanaji Gujar für die enge und unkomplizierte Zusammenarbeit danken sowie natürlich für die Präparation der Perowskit-Filme.

Mein Dank gilt auch Thomas Vogtmann für die Unterstützung in zahlreichen optischen und technischen sowie organisatorischen Dingen, Irene Bauer und Frank Schirmer für die kleinen, großen und schnellen Wunder bei der Problembewältigung im Labor und Michaela Fischer für die reibungslose organisatorische Unterstützung im Büroalltag. Auch Thomas Dabisch und Melanie Kummer sei gedankt für ihre Unterstützung.

Ich danke allen jetzigen und ehemaligen Doktoranden vom Lehrstuhl für ihre Unterstützung, die tolle Atmosphäre und die schöne Zeit am Lehrstuhl. Vielen Dank. Insbesondere danke ich meinen Bürokollegen Alex, Reichi, Stefan, Steffen und Julian für ihren steten Einsatz und den ein oder anderen längeren Feierabend.

Für die Erfahrung, die ich als Betreuer machen durfte, danke ich Marius Jacoby und Stefan Wedler. Mit Ihnen habe ich fachlich viel dazulernen können. Insbesondere danke ich Stefan, Alex, Fabi und Julian für das Lesen dieser Arbeit.

Außerdem möchte ich von ganzem Herzen meiner Freundin Aurélie danken, die mir mit viel Verständnis und Unterstützung immer zur Seite steht und mir jeden Tag neue Kraft schenkt.

Vor allem gilt mein ganz großer Dank meiner Familie, meinen Eltern und meiner Schwester, die mich all die Jahre unterstützt haben und in allen Lebenslagen immer für mich da sind.

Danke!

13 **Erklärung**

Hiermit erkläre ich mich einverstanden, dass die elektronische Fassung dieser Dissertation unter Wahrung meiner Urheberrechte und des Datenschutzes einer gesonderten Überprüfung hinsichtlich der eigenständigen Anfertigung der Dissertation unterzogen werden kann.

Hiermit versichere ich an Eides statt, dass ich die vorliegende Arbeit selbstständig verfasst und keine anderen als die von mir angegebenen Quellen und Hilfsmittel verwendet habe.

Hiermit erkläre ich, dass ich nicht bereits versucht habe eine Dissertation einzureichen oder mich einer Doktorprüfung zu unterziehen.

Hiermit erkläre ich, dass ich keine Hilfe von gewerblichen oder externen Promotionsberatern bzw. Promotionsvermittlern in Anspruch genommen habe und diese auch künftig nicht in Anspruch nehmen werde.

Bayreuth, den 3.08.2017

Thomas Unger

Liste der Veröffentlichungen

1 Thomas Unger, Fabian Panzer, Cristina Consani, Federico Koch, Tobias Brixner, Heinz Bässler and Anna Köhler,
Ultrafast Energy Transfer between Disordered and Highly Planarized Chains of Poly[2-methoxy-5-(2-ethylhexyloxy)-1,4-phenylenevinylene] (MEH-PPV),
ACS Macro Letters **4**, 412-416 (2015)

2 Cristina Consani, Federico Koch, Fabian Panzer, Thomas Unger, Anna Köhler and Tobias Brixner,
Relaxation dynamics and exciton energy transfer in the low-temperature phase of MEH-PPV,
The Journal of Chemical Physics **142**, 212429 (2015)

3 Kevin Wilma*, Thomas Unger*, Christoph Hunger, Manuel Hollfelder, S. Tuncel Kostakoğlu, A. G. Gürek, Mukundan Thelakkat, Jürgen Köhler, Anna Köhler, Stefan Gekle and Richard Hildner,
Excited State Dynamics and Conformations of a Cu(II)-Phthalocyanine-Perylenebisimide Dyad,
Physical Chemistry Chemical Physics **19**, 22169-22176 (2017)
**Diese Autoren haben gleich viel beigetragen.*

4 Thomas Unger*, Stefan Wedler*, Julian Kahle, Ullrich Scherf, Heinz Bässler, Anna Köhler
The Impact of Driving Force and Temperature on the Electron Transfer in Donor-Acceptor Blend Systems
The Journal of Physical Chemistry C **121**, 22739-22752 (2017)
**Diese Autoren haben gleich viel beigetragen.*

5 Tanaji P. Gujar, Thomas Unger Martina Fried, Andreas Schönleber, Sander van Smaalen, Anna Köhler, and Mukundan Thelakkat, *The Role of PbI_2 on Perovskite Stability, Device Parameters and Degradation,*
Physical Chemistry Chemical Physics (2018) DOI: 10.1039/c7cp04749e

6 Cheng Li, Yu Zhong, Carlos Andres Melo Luna, Thomas Unger, Konstantin Deichsel, Anna Gräser, Jürgen Köhler, Anna Köhler, Richard Hildner and Sven Hüttner,
Emission Enhancement and Intermittency in Polycristalline Organolead Halide Perovsktite Films,
Molecules **21**, 1081 (2016)

Veröffentlichungen die vor oder der Promotion entstanden sind aber nicht in dieser Arbeit enthalten sind

7 Tobias Hahn, Christina Saller, Irene Bauer, Thomas Unger, Anna Köhler and Peter Strohriegl,
Organic solar cells with crosslinked polymeric exciton blocking layer
Physica Status Solidi A **212**, 110, 2162-2168 (2015)

8 Fabian Panzer, Sebastian Baderschneider, Tanaji P. Gujar, Thomas Unger, Marius Jacoby, Sergey Bagnich, Heinz Bässler, Jürgen Köhler, Ralf Moos, Mukundan Thelakkat, Richard Hildner and Anna Köhler,
Reversible Laser Induced Amplified Spontaneous Emission from Coexisting Tetragonal and Orthorhombic Phases in Hybrid Lead Halide Perovskites,
Advanced Optical Materials **4**, 6, 917-928 (2016)

9 Sebastian T. Hoffmann, Frank Jaiser, Anna Hayer, Heinz Bässler, Thomas Unger, Stavros Athanasopoulos, Dieter Neher and Anna Köhler,
How Do Disorder, Reorganization, and Localization Influence the Hole Mobility in Conjugated Copolymers?;
Journal of the American Chemical Society **135**, 1772-1782 (2013)

10 Beatrice Ch. D. Salert, Hartmut Krueger, Sergey A. Bagnich, Thomas Unger, Frank Jaiser, Mahmoud Al-Sa'di, Dieter Neher, Anna Hayer and Thomas Eberle,
New Polymer Matrix System for Phosphorescent Organic Light-Emitting Diodes and the Role of the Small Molecular Co-host,
Journal of Polymer Science Part A: Polymer Chemistry **51**, 601-613 (2013)

11 Mahmoud Al-Sa'di, Frank Jaiser, Sergey Bagnich, Thomas Unger, James Blakesley, Andreas Wilke and Dieter Neher,
Electrical and Optical Simulations of a Polymer-Based Phosphorescent Organic Light-Emitting Diode with High Efficiency,
Journal of Polymer Science Part B: Polymer Physics **50**, 1567-1576 (2012)

12 Sergey A. Bagnich, Thomas Unger, Frank Jaiser, Dieter Neher, Manuel W. Thesen and Hartmut Krüger,
Efficient green electrophosphorescence based on ambipolar nonconjugated polymers: Evaluation of transport and emission properties,
Journal of Applied Physics **110**, 033724 (2011)